Study of 3D cellular microenvironments for the development of bone marrow in-vitro models

Roberto Riesco Alvarez

To cite this version:

Roberto Riesco Alvarez. Study of 3D cellular microenvironments for the development of bone marrow in-vitro models. Micro and nanotechnologies/Microelectronics. INSA de Toulouse, 2021. English. NNT : 2021ISAT0022 . tel-03623449

HAL Id: tel-03623449

https://theses.hal.science/tel-03623449

Submitted on 29 Mar 2022

THÈSE

En vue de l'obtention du

DOCTORAT DE L'UNIVERSITÉ DE TOULOUSE

Délivré par l'Institut National des Sciences Appliquées de Toulouse

Présentée et soutenue par

Roberto RIESCO ALVAREZ

Le 18 mai 2021

Étude de microenvironnements cellulaires 3D pour le développement des modèles in-vitro de la moelle osseuse

Ecole doctorale : **GEETS - Génie Electrique Electronique,Télécommunications et Santé : du système au nanosystème**

Spécialité : **MicroNano Systèmes**

Unité de recherche :
LAAS - Laboratoire d'Analyse et d'Architecture des Systèmes

Thèse dirigée par
Laurent MALAQUIN et Thierry LEICHLE

Jury
Mme Stéphanie DESCROIX, Rapporteur
M. Michael BROOK, Rapporteur
Mme Hélène ROUARD, Examinatrice
M. Bruno LE PIOUFLE, Examinateur
M. Christophe VIEU, Examinateur
M. Laurent MALAQUIN, Directeur de thèse
M. Thierry LEICHLE, Co-directeur de thèse

Study of 3D cellular microenvironments for the development of bone marrow in-vitro models

Roberto Riesco Álvarez

A thesis submitted for the degree of Doctor of Philosophy

INSA Toulouse

May 2021

Abstract

The cellular microenvironment is the local surrounding of a cell which contains physical and chemical cues. This information is processed by the cells to understand their environment and response to stimuli, further adapting their behavior. The study of cellular microenvironments is key to simulate the in-vivo conditions in in-vitro models. This work aims to reproduce the cellular microenvironment of the bone marrow, fabricating a model, which reproduces the complexity and heterogeneity of this tissue. Bone marrow is a gelatinous tissue located in the porous architecture of the trabecular bone that hosts hematopoietic stem cells (HSC) and mesenchymal stromal cells (MSCs). Its main function is the constant renewal of blood cells, called haematopoiesis. The rich topological architectures displayed in the trabecular bone have constituted a technological challenge for the reproduction of 3D cellular microenvironments and the development of tissue models.

The current state of 3D fabrication technologies has opened the possibility to reproduce such porous architectures accurately and to replicate the three bone marrow niches: endosteal niche (bone tissue), perivascular niche (endothelial tissue) and the adipose niche (adipose tissue).

Here, we developed two models of porous architectures based on different 3D fabrication technologies: designed architectures by stereolithography and free-form structures by a novel technique based on porous emulsion-templated polymers synthesized within high internal phase emulsions (HIPEs). These architectures were both integrated in fluidic systems, providing perfusion capabilities to the systems that were used to reproduce some characteristic cues of the bone marrow microenvironment. The perfusion cue gave us temporal control over the cell culture and allowed the stimulation of the cells by shear stress. Both models were tested using osteosarcoma cell lines and mesenchymal stromal cells.

Résumé

Le microenvironnement cellulaire est l'environnement local d'une cellule qui contient des informations physiques et chimiques. Ces informations sont traitées par les cellules pour comprendre leur environnement et répondre aux stimuli, ce qui leur permet d'adapter leur comportement. L'étude des micro-environnements cellulaires est essentielle pour simuler les conditions in-vivo dans des modèles in-vitro. Ce travail vise à reproduire le microenvironnement cellulaire de la moelle osseuse, en fabriquant un modèle qui reproduit la complexité et l'hétérogénéité de ce tissu. La moelle osseuse est un tissu gélatineux situé dans l'architecture poreuse de l'os trabéculaire qui héberge des cellules souches hématopoïétiques (CSH) et des cellules stromales mésenchymateuses (CSM). Sa principale fonction est le renouvellement constant des cellules sanguines, appelé hématopoïèse. La richesse des architectures topologiques de l'os trabéculaire a constitué un défi technologique pour la reproduction de micro-environnements cellulaires en 3D et le développement de modèles tissulaires.

L'état actuel des technologies de fabrication 3D a ouvert la possibilité de reproduire ces architectures poreuses avec précision et de reproduire les trois niches de la moelle osseuse: la niche endostéale (tissu osseux), la niche périvasculaire (tissu endothélial) et la niche adipeuse (tissu adipeux).

Ici, nous avons développé deux modèles d'architectures poreuses basés sur différentes technologies de fabrication 3D: des architectures conçues par stéréolithographie et des structures de forme libre par une nouvelle technique basée sur des polymères poreux en émulsion synthétisés dans des émulsions à phase interne élevée (HIPE). Ces architectures ont toutes deux été intégrées dans des systèmes fluidiques, offrant des capacités de perfusion aux systèmes qui ont été utilisés pour reproduire certains indices caractéristiques du microenvironnement de la moelle osseuse. La perfusion nous a donné un contrôle temporel sur la culture cellulaire et a permis la stimulation des cellules par une contrainte de cisaillement. Les deux modèles ont été testés en utilisant des lignées cellulaires d'ostéosarcomes et des cellules stromales mésenchymateuses.

Table of Contents

Table of abbreviations

Shortcut	Meaning
ABS	Acrylonitrile butadiene styrene
BJ	Binder jetting
BMSCs	Bone marrow mesenchymal stromal cells
BV/TV	Bone volume fraction
CAD	Computer-aid design
ColMA	Collagen Methacrylate
DIW	Direct ink writing
ECM	Extracellular matrix
FDM	Fused deposition modelling
GelMA	Gelatin Methacrylate
HIPEs	High internal phase emulsions
HIPS	High-impact polystyrene
HSC	Hematopoietic stem cells
LIPEs	Low internal phase emulsions
MFCS	Microfluidic flow control system
MIPEs	Mid internal phase emulsions
MSCs	Mesenchymal stromal cells
Nylon	Aliphatic polyamides
PA	Polyamides
PDF	Probability distribution functions
PDMS	Polydimethylsiloxane
PLA	Polylactic acid
PLLA	Poly(L-lactic acid)
polyHIPE	Polymeric High Internal Phase Emulsions
PPC	Poly(propylene carbonate)
PS	Polystyrenes
PU	Polyurethane
SaOS-2	Sarcoma osteogenic cell line
SEM	Scanning electron microscopy
SLA	Stereolithography
SLM	Selective laser melting
SLS	Selective sintering laser
TbSp	Trabecular separation
TbTh	Trabecular thickness
TPU	Thermoplastic polyurethane
µCT	X-ray micro-computed tomography

General introduction

The cellular microenvironment is the local surrounding of a cell which contains physical and chemical cues. This information is processed by the cells to understand their environment and response to stimuli, further adapting their behavior. The study of cellular microenvironments is key to simulate the in-vivo conditions in in-vitro models. The current models employed in biology and medicine to investigate tissues and develop drugs are mainly based on 2D configurations on hard substrates (such as polystyrene). These models misrepresent the natural habitat of cells and can induce biases in the cellular behavior that affects the conclusions of biological studies.

The motivation of this work is to reproduce the cellular microenvironment of the bone marrow, fabricating a model, which reproduces the complexity and heterogeneity of this tissue. Bone marrow is a gelatinous tissue located in the porous architecture of the trabecular bone that hosts hematopoietic stem cells (HSC) and mesenchymal stromal cells (MSCs). Its main function is the constant renewal of blood cells, called haematopoiesis. The rich topological architectures displayed in the trabecular bone have constituted a technological challenge for the reproduction of 3D cellular microenvironments and the development of tissue models. The current state of 3D fabrication technologies has opened the possibility to reproduce such porous architectures accurately and to replicate the three bone marrow niches: endosteal niche (bone tissue), perivascular niche (endothelial tissue) and the adipose niche (adipose tissue).

Here, we developed two models of porous architectures based on different 3D fabrication technologies: designed architectures by stereolithography and free-form structures by a novel technique based on porous emulsion-templated polymers synthesized within high internal phase emulsions (HIPEs). These architectures were both integrated in fluidic systems, providing perfusion capabilities to the systems that were used to reproduce some characteristic cues of the bone marrow microenvironment. The perfusion cue gave us temporal control over the cell culture and allowed the stimulation of the cells by shear stress.

General introduction

This manuscript is divided in five chapters, each one devoted to a specific aspect of the development and validation of our 3D bone marrow models:

In Chapter 1, we describe in the internal architecture of bone and its relationship with the key functionalities of bone marrow. Based on recent literature studies, we define a list of specific cues that have been identified as critical in the cellular microenvironment of the bone marrow and its homeostasis. We review aspects regarding topography, mechanical properties, cell adhesion and liquid movement. Then, we compare various bone marrow models found in the literature in order to contextualize our work.

In Chapter 2, we present an overview of the existing fabrication technologies available to generate 3D architectures, classifying them as designed architectures and free-form structures. From the material point of view, we discuss the interdependence between each material and its associated properties with each fabrication technique. Designed architectures require the use of a new photo-sensitive material that have been adapted to photopolymerization, while free-form structures are obtained through an original fabrication process using a well-known biocompatible material. We introduce the advantages and performances of each of our fabrication methods and characterize the resulting structures in the context of the trabecular bone microarchitectures.

In Chapter 3, we carry out the biological validation of the materials. We establish a full protocol to accomplish cell culture on DS3000, a new material suited to stereolithography, by evaluating its cytotoxicity and promoting cell adhesion. Then, we study cell culture in the developed 3D architectures using cells lines in static culture conditions.

In Chapter 4, we demonstrate the integration our porous architectures into fluidic devices to implement perfusion capabilities, turning them into bioreactors. We discuss the adaptations of the fabrication processes, characterize the morphology of the resulting architectures and propose a hydrodynamic characterization of the devices. Finally, we present the validation of dynamic cell culture first using cell lines and further human primary mesenchymal stromal cells.

In Chapter 5, we introduce the latest developments that were not completed because of the COVID-19 pandemic as a perspective for this work, and we provide a general conclusion of the manuscript.

This project is highly technological oriented and presents several innovations in terms of fabrication and experimental protocol. To make this manuscript easier to read and to facilitate the analysis of the technological aspects, the experimental protocols are directly included in the text within color boxes. We have sorted these protocols depending in if they are of general knowledge (green boxes) or original work (orange boxes).

I. Bone marrow cellular microenvironments

1. Biological context: bone marrow

The goal of this project is the development of new tools and technologies devoted to understand the processes taking place in the bone marrow. The bone marrow is a gelatinous tissue located in the cavernous regions of the trabecular bone. It is a fundamental part of mammalian organisms, providing a niche for hematopoietic stem cells (HSC) consisting of mesenchymal stromal cells (MSCs). HSCs are constantly renewed in the bone marrow in a process call haematopoiesis. An illustrative sketch of the bone marrow is shown in **Figure 1.1**. Here, we can see the structure of a long bone with different close-up views of the regions of the bone marrow, which are divided into red bone marrow and yellow bone marrow.

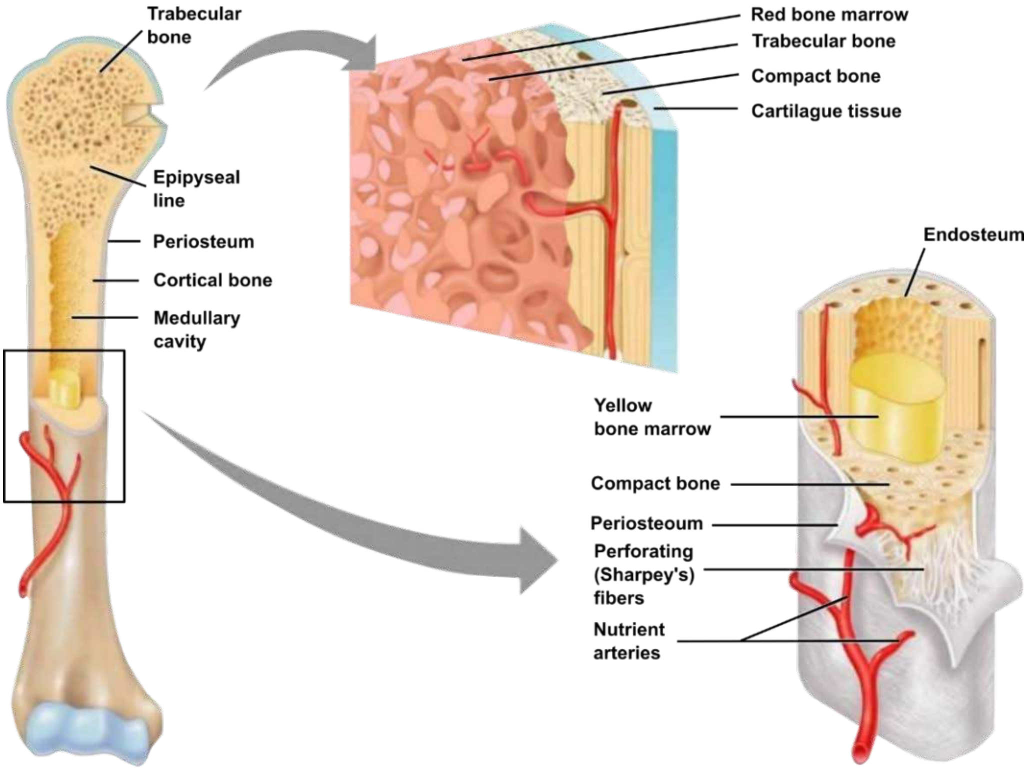

Figure 1.1. *Structure of a long bone (humerus of arm) with a sectioned part to show the internal microarchitecture. Enlarged view of a section showing the trabecular bone and the red bone marrow and cross-sectional view of the cortical part with the yellow bone marrow. Adapted from [1].*

Depending on the proportion of cells present in the tissue, bone marrow tends to be differentiated in two kinds of tissues, red bone marrow and yellow bone marrow. Red bone marrow is mainly composed of blood cells in different stages of differentiation as well as a network of reticular fibers, pericytes (perivascular MSC) and pro-hematopoietic stromal cells.

The main role of the bone marrow is the haematopoiesis, the production of blood components from hematopoietic stem cells (HSCs) which differentiate in three cellular lineages of blood: red blood cells, lymphoid and myeloid cells. Sequentially, these cells are differentiated into the immunity cells which constitutes the immune system such as the lymphocytes and monocytes among many others. The life span of blood cells is 100-120 days and therefore, this important tissue ensures their constant renewal, generating $4 - 5 \times 10^{11}$ cells per day [2]. The full lineages of cells produced in the bone marrow are shown in **Figure 1.2**. This image depicts the central role of bone marrow as a cell factory for the normal functioning of the human body.

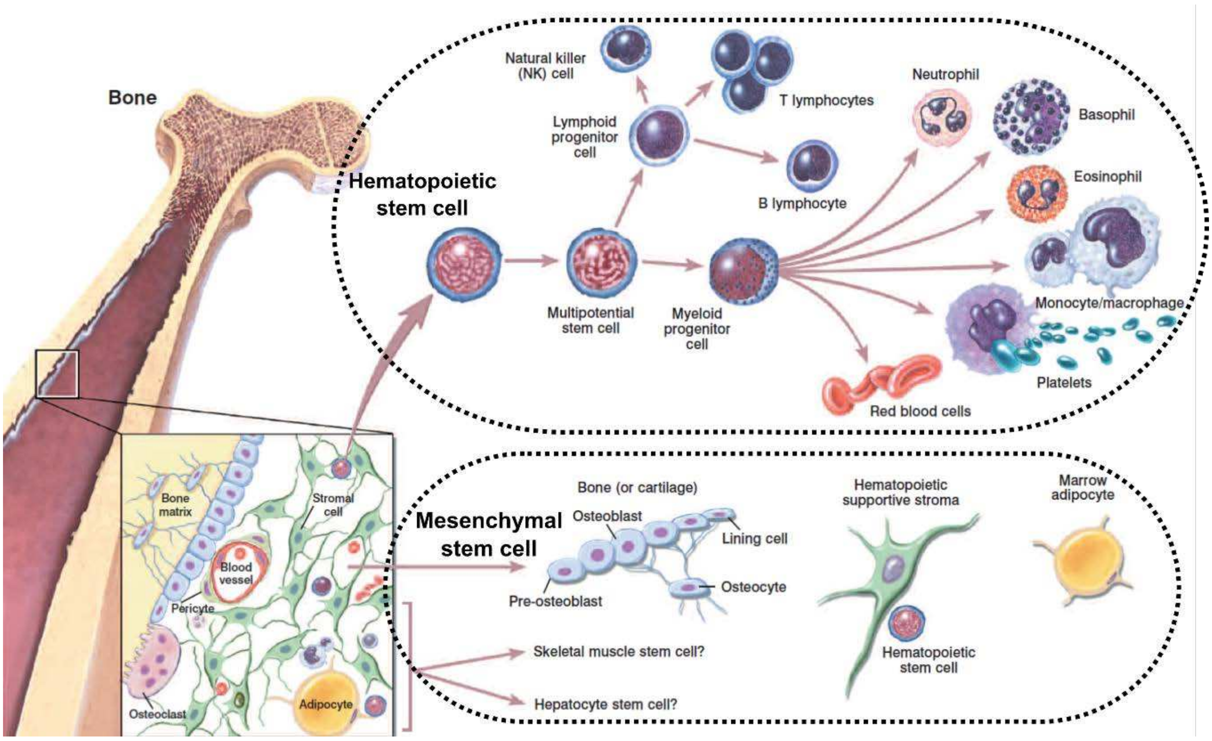

Figure 1.2. *Hematopoietic and stromal cell differentiation pathway of the cells located in the bone marrow. Adapted from [3].*

Moreover, the role of the trabecular bone and the bone marrow for connective tissue regeneration is even more important since they are the niche hosting MSCs. (mesenchymal stromal cells). MSCs are non-hematopoietic pluripotent cells that are at the base of bone marrow homeostasis. However, they are considered as great candidates for therapeutical use in regenerative medicine.

With age, the production of blood cells decreases due to altered haematopoiesis and the microenvironment is partially replaced with adipose tissue known as yellow bone marrow which composes the majority of the bone marrow tissue [4], [5]. If necessary, after serious injuries or pathological conditions, it can be reactivated to speed up the regeneration capabilities of the system. This punctual need for blood cells generates a stimulus in the bone marrow that is translated into an increase of the haematopoiesis in the red bone marrow. It also induces the proliferation of MSCs and their differentiation towards the support of the HSCs and the creation of the hematopoietic microenvironment [1], [5].

Due to the large diversity of cells and to the importance of the processes that take place in this tissue, the bone marrow is allocated in the cavities of the trabecular bone. This constitutes a large volume available to host the haematopoiesis and produces the large quantity of cells needed in the human body. The trabecular bone is a porous structure located in the bones generated by secreted collagen randomly organized, and further mineralized. This structure ensures the important role of providing support and protection i.e., a niche for hematopoietic and non-hematopoietic cells of the bone marrow. **Figure 1.3** presents the trabecular microarchitecture obtained by X-ray computed tomography by Pothuaud et al [6]. There, we can observe an irregular structure with high porosity. The resulting digital model was processed and analyzed to obtain quantitative values corresponding to the architecture. This data was obtained through the analysis of several samples of bone marrow corresponding to different bones in the body from different patients, and it is shown in **Table 1.1**.

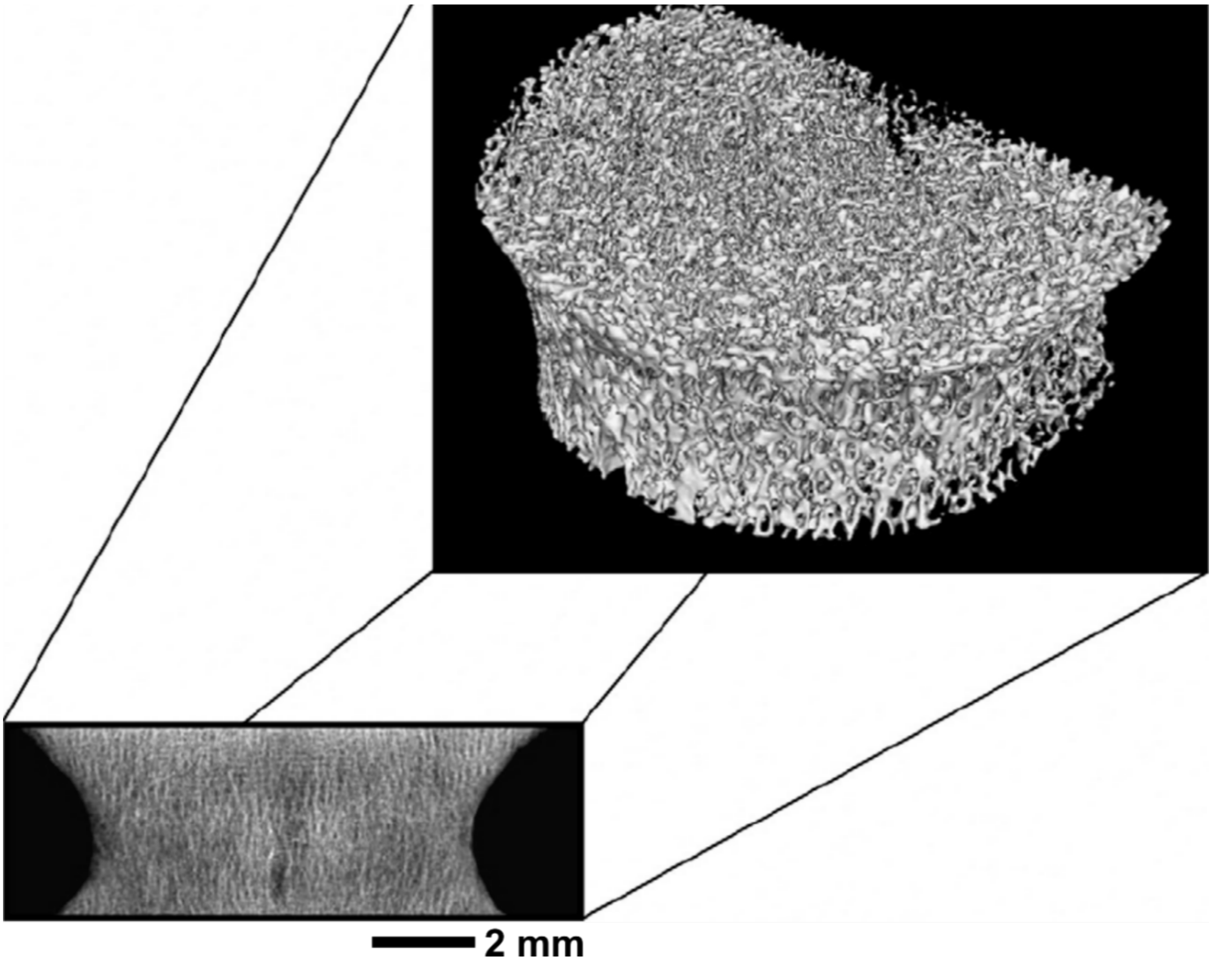

Figure 1.3. *Three-dimensional reconstruction of the trabecular bone microarchitecture obtained by X-ray microcomputed Tomography of an entire vertebral body. The specimen was 3D characterized by BV/TV*^{1} *= 31.8% and TbTh*^{2} *= 0.259 mm. Adapted from* [6].

Trabecular bone can be found in flat-bones and in the extremities and the central region of long bones. Mesenchymal stromal cells present the form of a dense weblike network, which provides support for the rest of cells. Osteoblastic differentiation is supposed to take place in the proximities of the inner bone surfaces, although the precise interface between osteo- and adipogenic lineage is still not clearly defined [7].

From a material point of view, the mechanical properties of bones have been extensively studied for centuries, being mentioned in Egyptian and Babylonic texts, and described in the first medical commentaries of the skeleton by the Renaissance physicians as the hardest part of the body. Nowadays, bone biomechanics focus on understanding the interconnections of the various kinds of internal organization and their formations and remodeling due to functional adaptations [8].

Table 1.1 *Descriptive statistic of the trabecular bone microarchitecture of several bones of the human body from different skeleton regions. Adapted from* [6].

Samples	BV/TV[a] (%)	TbTh[b] (µm)	TbSp[c] (µm)
Lumbar spine mean (n = 20)	30.6 ± 5.5	233 ± 14	551 ± 139
Femoral neck mean (n = 17)	26.2 ± 6.7	239 ± 23	750 ± 378
Ultradistal radius mean (n = 20)	28.4 ± 4.3	226 ± 18	584 ± 105

Measuring and classifying bone biomechanics is a topic treated in hundreds of studies with diverse outcomes. Literature presents an agreement in terms of relative mechanical properties of the different compartments in the bones but presents a vast range of absolute values due to the bias of the experimenter and the techniques employed, the treatment of biological samples and the large variations that these samples can present due to patient related divergences (**Figure 1.4**, **Table 1.2**).

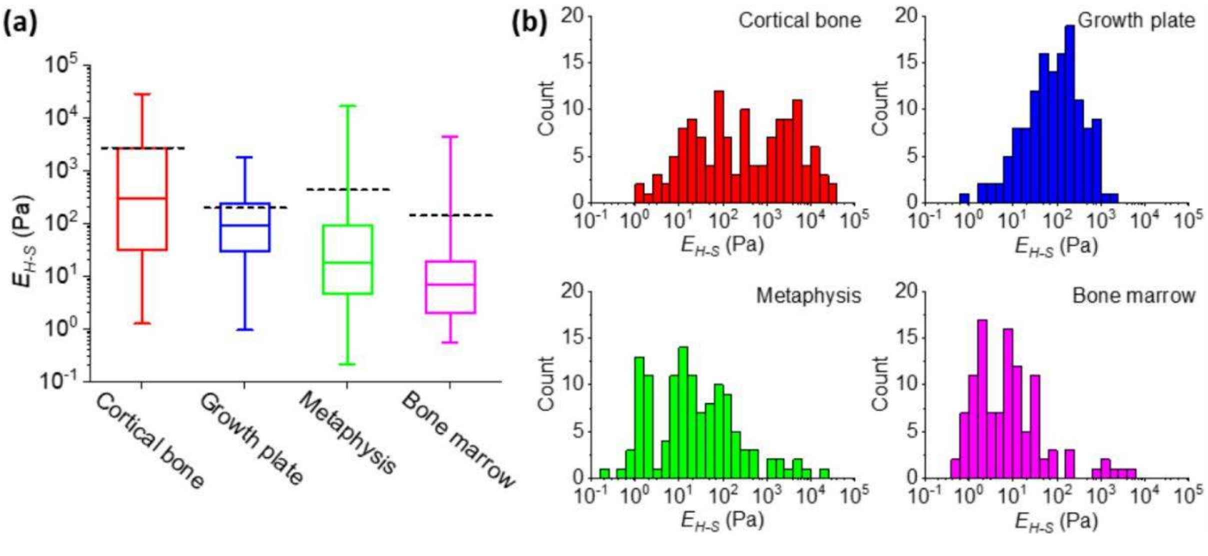

Figure 1.4. *Elastic properties of different regions of the bone calculated by atomic force microscopy using the Hertz-Sneddon model with fitted contact point and the histograms for each regions from [9].*

---

[a] *Bone volume fraction (BV/TV) is the volume of mineralized bone over total volume. We can understand it as the inversed value of the porosity.*

[b] *Trabecular thickness (TbTh) is the mean thickness of the strut composing the trabecular microarchitecture.*

[c] *Trabecular separation (TbSp) is the mean distance between the struts. It has a similar meaning than the pore size mean.*

***Table 1.2**. Comparison of the elastic modulus of the bone marrow employing different techniques to measure the Young's modulus [10].*

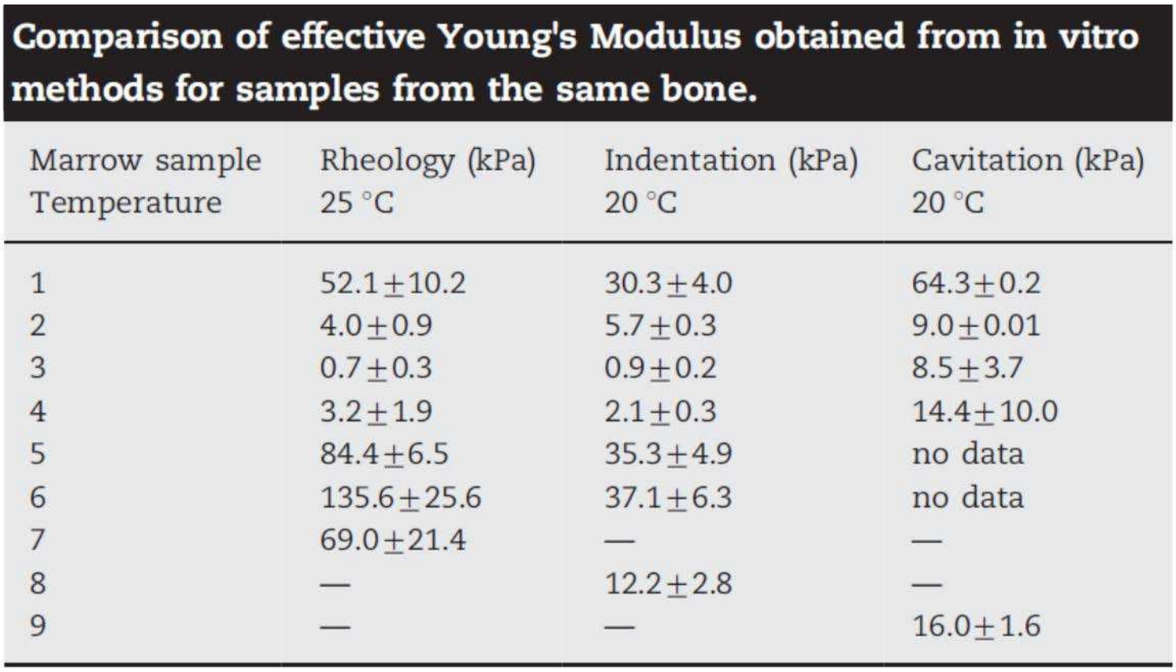

Comparison of effective Young's Modulus obtained from in vitro methods for samples from the same bone.

Marrow sample Temperature	Rheology (kPa) 25 °C	Indentation (kPa) 20 °C	Cavitation (kPa) 20 °C
1	52.1±10.2	30.3±4.0	64.3±0.2
2	4.0±0.9	5.7±0.3	9.0±0.01
3	0.7±0.3	0.9±0.2	8.5±3.7
4	3.2±1.9	2.1±0.3	14.4±10.0
5	84.4±6.5	35.3±4.9	no data
6	135.6±25.6	37.1±6.3	no data
7	69.0±21.4	—	—
8	—	12.2±2.8	—
9	—	—	16.0±1.6

R. Ashman and J. Rho measured the elastic modulus of the trabecular bone scaffold, after the removal of the bone marrow tissue from the cavities, measuring the modulus of the mineralized architecture. The values obtained were $E = 10.4 \pm 3.5\, GPa$, measured dry by tensile testing and $E = 14.8 \pm 1.4\, GPa$ by ultrasonic transmission [11]. The authors provide as well a review of literature data ranging from $0.75 - 20\, GPa$. On the other hand, the bone marrow tissue is reported to have a Young modulus ranging from $0.5 - 25\, kPa$. Those values show, no matter the study, that there is a large stiffness gap between the tissues, with a steep transition at the interface between the trabecular bone and the bone marrow tissue, which represent a major technological challenge for creating physiological models adapted to tissue engineering.

The modelling of the bone marrow tissue and its functions is critical in order to fully understand how it responds in different situations such as infections, haemopathy, radiotherapy or chemotherapy. This could help improving diagnosis and therapies to re-establish the bone marrow functions in treated patients. Latest studies have attempted to unveil the different compartments of the bone marrow, where the vast cellular and morphological heterogeneities are essential to reproduce *in-vitro* [12]. However, these models remain incomplete.

2. Cellular microenvironments

a. The motivations for in vitro models

Since the discovery of the cell culture techniques during the 19th Century by Wilhelm Roux, a large portion of the advances achieved in Biology has been mainly supported by *in-vitro* and *in-vivo* experiments. *In-vitro* experiments primarily involve the culture of cells on flat plastic or glass surfaces: Petri dishes or multi-well plates, and are nowadays referred to as two-dimensional cell culture. Cell seeded in such substrates, usually one kind at a time, adhere to the surfaces, produce their extracellular matrix and proliferate, organizing themselves in flat monolayers. In these procedures, we study the development, behavior or features of cells or microorganisms in a controlled environment out of their natural habitat. *In-vivo* studies are conducted in whole living organism, usually animals or humans. These give a more complete overview of the global impact of procedures or substances on the whole organism. Generally, the use of those models for, for instance, therapeutic targets is sequential, starting by *in-vitro* models, continuing with *in-vivo* animal models and finishing the trials on humans.

This progressive increment in the complexity of models has yielded a large amount of knowledge in the past decades. Nevertheless, the recent advances in new life science characterization techniques and the poor performance of certain experiments have urged scientists to reevaluate well-established knowledge to understand these miscarriages, especially regarding clinical test success ratios. The process of drug development involves certain strictly regulated phases in order to obtain approval for patient distribution shown in **Table 1.3** [13], [14].

New drug discoveries start with what is called pre-clinical trials, from the conception of the molecule to the *in-vitro* or/and *in-vivo* experiments that validate the effect of this new pharmacological compound. This first stage is key to filter thousands of potential drugs, on average 1 for each 5000 [15] prior to a move to clinical trials. These trials are devoted to the design of the drug, the validation of the possible beneficial effects and the evaluation of drug delivery, among relevant information to obtain clinical trial authorization. Phase 0 was established in 2006 by the “Exploratory IND study, Guidance document” of the FDA as an exploratory phase. It takes place at the beginning of phase 1 with the goal of scientific exploration to reduce the clinical failure, yet limiting human exposure to non-approved procedures/molecules.

Table 1.3. *Classification of the different stages of a drug discovery and the process to achieve distribution authorization by the pertinent regulatory organism.*

Phase	**Kind of proof**	**Goal**
Pre-clinical trial	*In-vitro* / *in-vivo* experiments	Gather information of dosing and toxicity levels
Phase 0 (optional)	10 people	Exploratory phase
Phase 1	20 - 100 healthy volunteers	Evaluation of safety and dosing
Phase 2	100 - 300 with specific condition	Evaluate the efficacy of the drug to deal with the disease
Phase 3	300 - 3000 with specific condition	Determine the therapeutic effect of a drug
Phase 4 (post-approval)	Anyone under physician treatment	Monitors long-term effect

As shown in **Figure 1.5**, according to the Biotechnology Innovation Organization [1], only the $9.6\,\%$ of the clinical trials goes from Phase I to approval. Aside of the increasing cost of carrying out such large-scale clinical tests due to the strict safety regulations enforced by states, one of the primary sources of trial failure in this context is the inability to demonstrate the drug efficacy, which reaches 30% in the case of dropout from Phase III to approval [16], [17]. Companies run hundreds of *in-vitro* experiments prior to engage with clinical tests in order to reduce the potential dropouts. Moreover, *in-vivo* models, such as mice or rats, can give biased data due to large differences in human physiology. The elevated number of mistrials could indicate that these models, *in-vitro* or in-*vivo,* are not pertinent and provide researchers with misleading information, resulting in the endorsement of the drug assays based on faulty data.

Beyond these economic considerations, scientists are more aware of their impact in the world and try to improve their practice by implementing new ethical guidelines. One of the ramping issues expressed and considered recently, is the use of animal models in science. These concerns have encouraged the development of alternative solutions to avoid as much as possible animal experimentations. In 2002, Paul Flecknell proposed the guideline "**3Rs: R**eplacement, **R**eduction and **R**efinement" [18], [19], a set of principles with the purpose of: first, develop new techniques and models aimed to substitute the use of animal models; second, reduce the number of animals used in the experiments by improving the design and analysis of those; and last, minimize the animal suffering by establishing ethical standards. These considerations are now well-established in the scientific community and they have strongly motivated the development of *in-vitro* models to meet these new integrity principles.

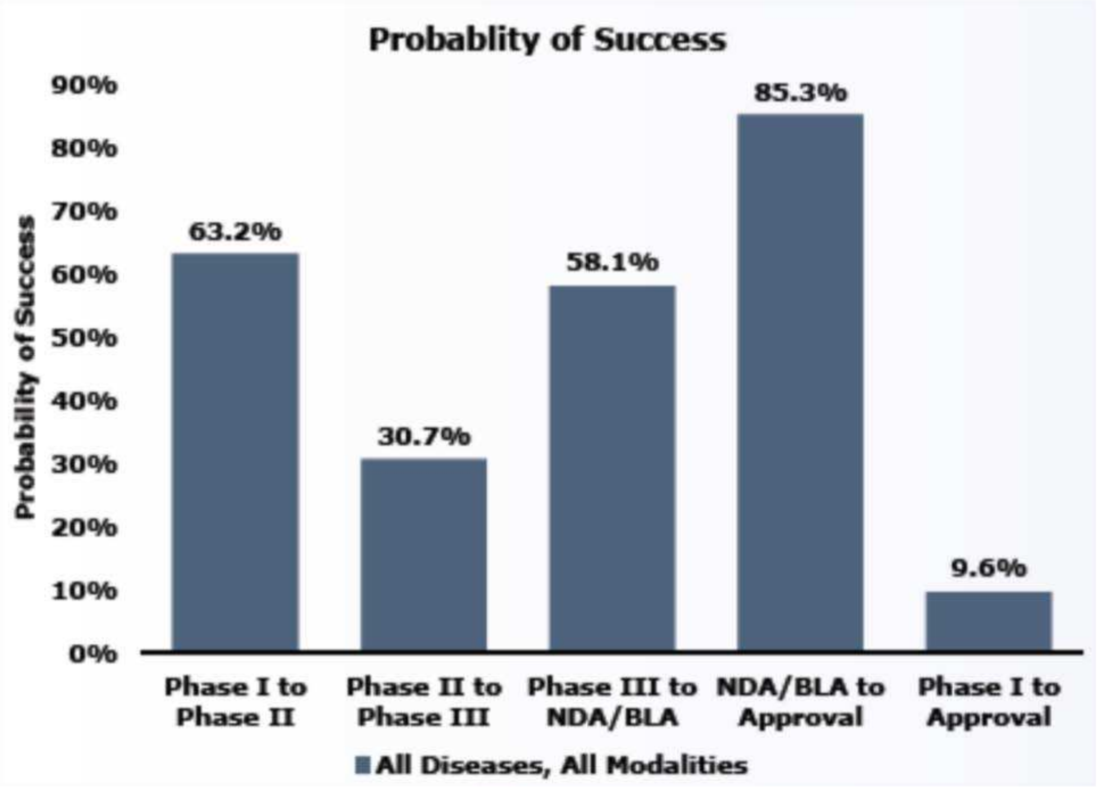

Figure 1.5. *Statistical data of the chance of success of a clinical trial, remarking the relevance of pertinent in-vitro models, in order to enhance the successful rate by highlighting the potential challenges in an earlier phase. Adapted from [20].*

To understand how an *in-vitro* experiment can be misleading, we need to analyze the fundamental characteristics of the tests and evaluate ways to close the gap moving from *in-vitro* to *in-vivo* experimentation. As previously discussed, *in-vitro* experiments refer to the study of cells or microorganisms in a controlled environment using cell culture techniques. The key of the success of such experiments lies in the understanding and the modelling of the new habitat where we carry out our observation, usually called microenvironment and how it differs from the natural environment.

b. The cellular microenvironment

By definition, the microenvironment of a cell gathers every cue and piece of information that a cell receives and uses to understand its surroundings and react according to it (**Figure 1.6**). It would provide a wide variety of information such as biochemical cues (growth factors, pH, nourishment), biophysical cues (rigidity, adhesion), and other harder to categorize such as architecture, surrounding cell neighbors or any kind of external stimuli. Cells use this information to perceive their habitat and regulate their physiology accordingly. For example, important functions such as proliferation and apoptosis are impacted by the supply of nourishment and oxygen, or by the amount of neighbors surrounding an individual cell. Therefore, we can assume that a flat glass or plastic surface, in static conditions, provides information for a cell that does not match its *in-vivo* habitat.

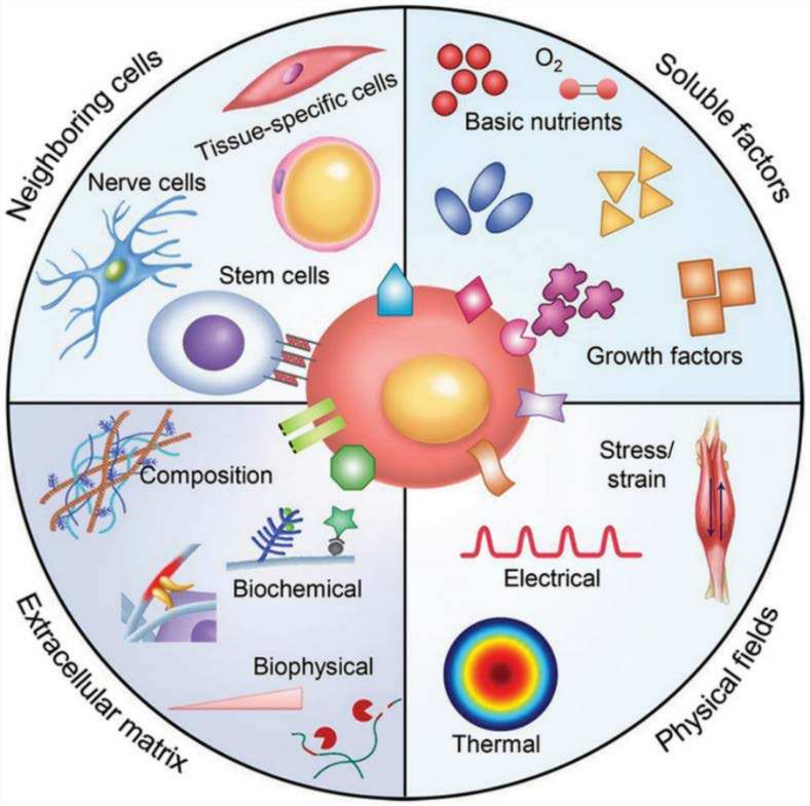

Figure 1.6. *Illustration presenting the different relevant signals produced by the cellular microenvironment and the sort of response carried out by the cells. Adapted from [21].*

The development of new technologies and biomaterials has made the study of the microenvironment a priority in many laboratories around the world. These technologies have permitted to isolate cues of the microenvironment and to study their implications. Much relevant knowledge has been made in the last years regarding isolated cues, and it is still important to understand the synergies and entanglements lying under the combination of few or several biophysical and biochemical cues as it occurs in the living organisms. [22]–[25].

The ultimate goal of these developments is to achieve the fabrication of relevant *in-vitro* models to provide robust and reproducible environments for the investigation of fundamental biological questions and their use in pharmacological studies. In the coming sections, we will have an overview of the main biophysical cues from the point of view of the bone marrow, having special focus on their impact on the MSCs behavior.

i. Tissue architecture

We define the tissue architecture as the spatial organization of both the cellular component and the extracellular matrix (ECM) composing the tissue. Because the interactions of the cells with their microenvironment depends strongly on the system morphology and internal organization, cells will adapt their behavior and interaction mechanisms differently as shown in **Figure 1.7**.

Topography is one of the most significant cues of the microenvironment, which has become relevant lately due to its impact in the tissue architecture, i.e., its spatial organization. Occasionally the terms topography and topology are used interchangeably when talking of 3D architectures, though there is a fundamental difference between them. Topography studies the geometry of a surface taking into account its shape and features, while topology is the mathematical study of the transformation of a space.

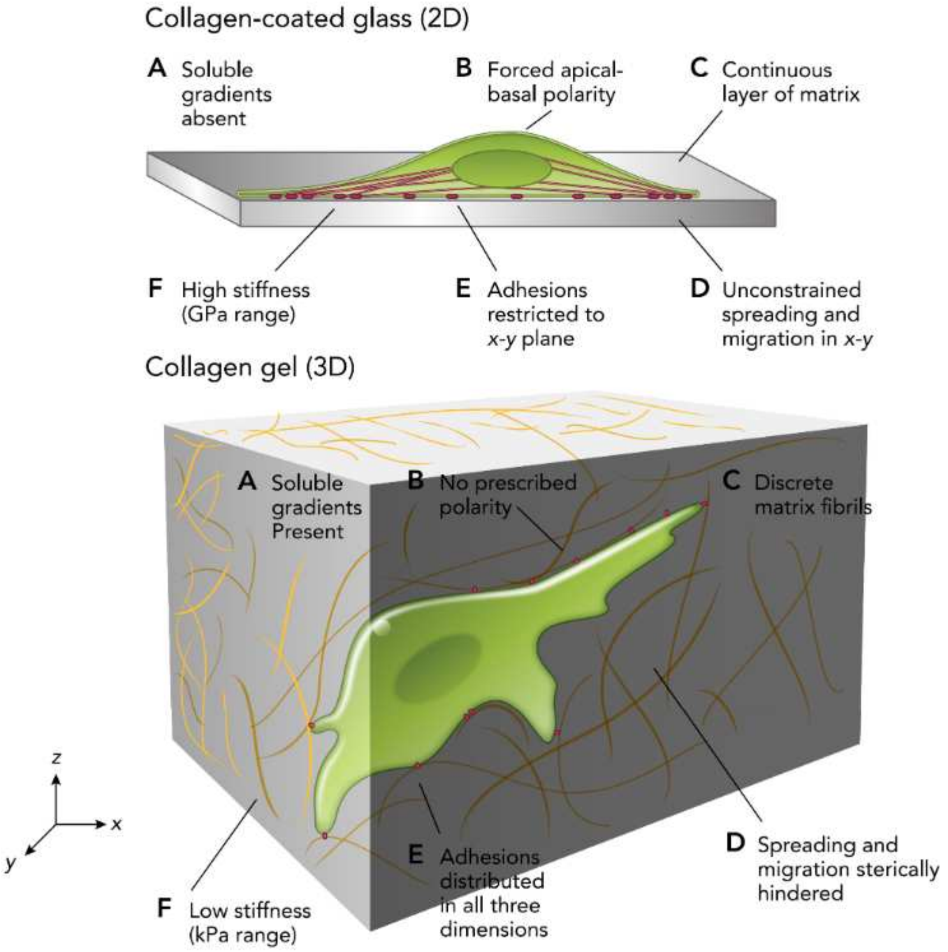

Figure 1.7. *Illustration of the transition between 2D and 3D cellular microenvironment. The images enumerate the main alterations caused by the dimensional progression of in-vitro models which presents a relevant impact to the cell behavior. Adapted from [26].*

When discussing the transition of 2D *in-vitro* models to 3D *in-vitro* models, the dimensional increment changes the way cells interact with each other and with their surroundings. **Figure 1.8A** represents a flat surface with two points (**P_1**, **P_2**) on it. The shortest distance between them is contained in the surface, representing a 2D *in-vitro* model. **Figure 1.8B**, presents a curved surface illustrating a modification in the dimensionality. In this configuration, the shortest distance *d* between **P_1** and **P_2**, is different than the shortest distance confined into the plane. This latter case represents a 3D model in which cells can interact between them using a superior dimension. Moreover, the increment of dimensions has a deeper impact from the mathematical point of view and it is translated to the 3D models by an increment in the surface density and the geometrical perimeters as illustrated in **Figure 1.8C-D**. The red dashed lines occupy a volume **V** which encloses the surface **s_1** or **s_2** in either configuration. By comparing both cases, we can understand that the surface $s_1 < s_2$. Biologically speaking, this is relevant due to the increase of surface available for cells to adhere, which impacts the cell density per unit of area and decreases the cell-cell distance.

With this simplified illustration, we then can explain the differences between topography and topology. From the external point of view of the experimenter, the modification of a surface into a 3D structure constitutes a change in the topography. While the cells are confined to the surface of that structure, this process modifies the systems by enabling another dimension to interact. Therefore, this represents a modification of their topology and it opens the possibility of interactions that were previously forbidden.

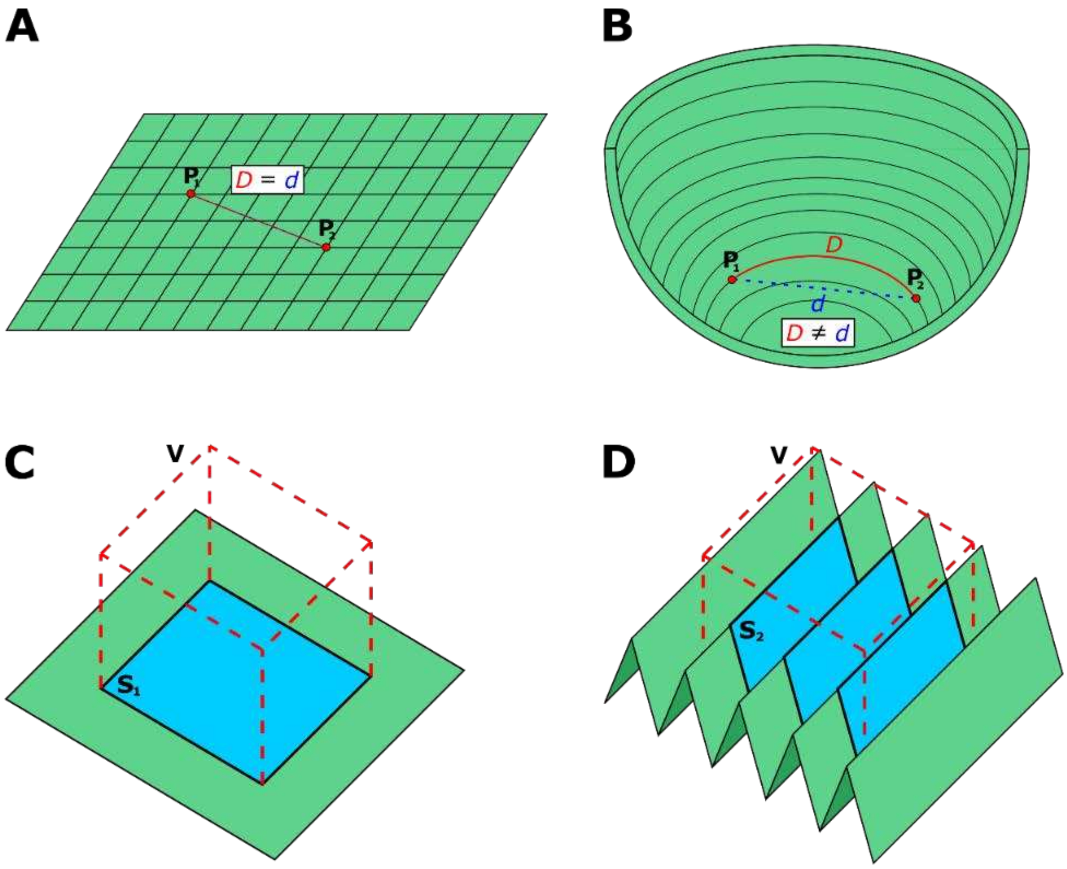

Figure 1.8. *Illustration showing the main modifications when the dimensionality of topographical structures evolves.* ***(a-b)*** *present how the inclusion of an extra dimension can change the minimal distance between two points by taking the path out of a planar confinement.* ***(c-d)*** *represent the packing of surface available when structures become three-dimensional by allowing the folding of the plane.*

The dimensional constraints may also force cells to restrict their migration movements to the plane, decreasing the degrees of freedom available to interact with other cells and explore their surroundings. Cell migration is indeed closely related to cell adhesion and cell-matrix interactions via the focal adhesion points. Those are anchoring spots at sub-cellular level composed by tens of different proteins (Integrin-like) that provide mechanical linkages between the cells, the ECM and the substrate. They are regulated via signaling events in the cellular microenvironment and they rule the cell migration and the tractions forces through actin filaments networks [27], [28]. In order to travel, cells deploy temporally pseudo-protrusions to examine new paths to migrate in the matrix, prior establishing definitive major protrusions. The number of protrusions established is tightly regulated by the focal adhesion proteins (FAK: focal adhesion kinase): numerous protrusions will lead to strong anchoring of the cell to the substrate, obstructing or impeding the cells to move; too few will result in an inefficiency to explore its surroundings. For instance, in 2D configuration, the apical-basal polarization tends to produce oriented and strongly expressed focal adhesion points, that are more prominent, the stiffer the material is, and that restrains cell migration. In 3D configuration, we observe fewer focal adhesion points that are less prominent and oriented in different directions in space.

In practice, the transition from 2D towards 3D induces others modifications in the cellular microenvironment caused by the technological method used to achieve 3D constructs. The generation of 3D microenvironments calls for specific materials enabling the realization of 3D architectures that often imply variations in chemical composition, adhesion properties and mechanical cues, impacting the overall characteristics of the system.

Moreover, the transition of biological *in-vitro* models towards the third dimension does not just raise technical issues and difficulties in managing a wide and variable range of cellular microenvironment parameters, but it also faces the challenge of characterizing closely bound features in 3D. A large number of characterization techniques employed in the field of biology are based on optical measurements optimized for planar configuration in fully transparent substrate at visible wavelengths. These are not suited to the complex 3D *in-vitro* models and new characterization methods have been developed to produce accurate measurements such as confocal microscopy or light sheet fluorescence microscopy.

Concerning the bone marrow, there is an extensive literature related to 3D cell culture of human bone marrow derived stromal cells (hBMSCs) [29]–[31]. Diverse techniques have been employed to fabricate 3D scaffolds with the purpose of mimicking the spatial organization of bone architectures [32]. The typical material employed is deeply linked to the fabrication technology. In this context, additive manufacturing offers a large range of compatible materials and it is probably one of the most popular solutions for the fabrication of such structures in this field. For instance, Mondal et al. [33] have fabricated 3D scaffolds in polylactic acid coated with hydroxyapatite nanoparticles, a known osteogenic material as presented in ***Figure 1.9***. The most popular materials for the fabrication of bone architectures are polymers such as polycaprolactone (PCL) [34], [35] or polylactic acid (PLA) [36], [37] and hydrogels such as polyacrylamide [34], gelatin [38] or collagen [39], in their natural forms, or methacrylated into gelatin methacrylate (GelMA) [40] and collagen methacrylate (ColMA) [41], among others [42]–[44].

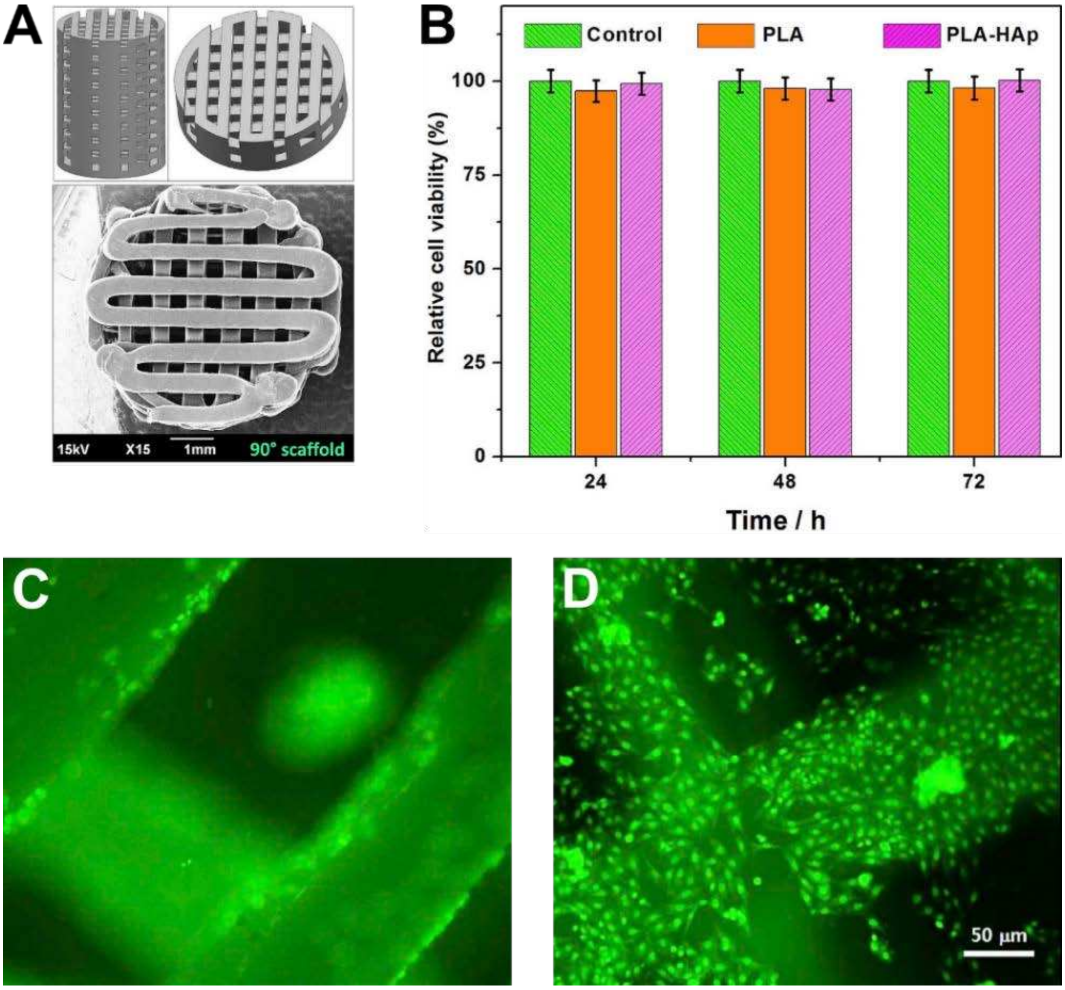

Figure 1.9. *3D PLA scaffolds coated with hydroxyapatite nanoparticles.* ***(a)*** *3D digital model and SEM image of a 3D printed scaffold fabricated in PLA and coated with hydroxyapatite nanoparticles.* ***(b)*** *MTT assay of PLA-HAp and PLA filaments of MG-63 cells on the scaffolds.* ***(c-d)*** *AO/PI live/death staining of MG-63 cells on the PLA scaffolds pristine* ***(c)*** *and hydroxyapatite-coated* ***(d)****. Adapted from [33].*

In combination with those, we highlight the use of particles to create composites based on hydroxyapatite [33], tricalcium phosphate [45] or titanium [46], [47], among others. As an example of a typical application of composite, Braham et al. [48] fabricated a 3D architecture using extrusion 3D printer and calcium phosphate cement to reproduce a pathologic bone marrow microenvironment (multiple myeloma), as shown in ***Figure 1.10***. Beside additive manufacturing, there are alternative methods to produce 3D scaffolds. Nevertheless, most of these techniques do not offer control of the produced architecture (in terms of organization, dimensions). Among those method, we must mention the electrospinning of non-woven nanofibers scaffolds commonly produced in material such as silk [49], [50], collagen [51] or PCL [52]. Other methods are solvent evaporation [53] and particle leaching [54], [55].

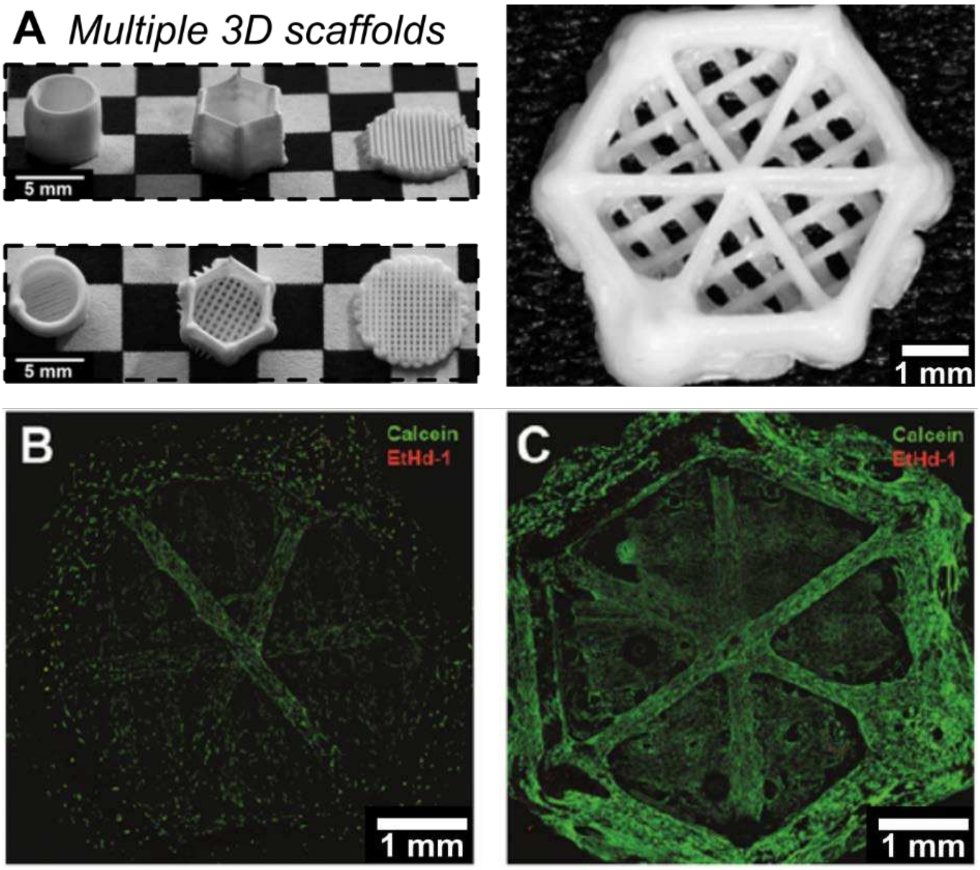

Figure 1.10. *Plotted CPC scaffolds.* ***(a) Left:*** *side view and top view of 3D constructs.* ***Right:*** *hexagonal porous scaffold chosen as the final format.* ***(b-c)*** *Alive and dead MSCs imaging on 3D scaffold at days 4* ***(b)*** *and days 7* ***(c)****. Adapted from [48].*

Kumar et al. have studied 3D scaffold structures in PCL with an attempt to isolate the impact of the topography from the adhesion and mechanical properties [56] (**Figure 1.11**). They studied the response of hBMSCs (gene expression) to the morphologies and roughness typical of scaffolds produced by each fabrication method: salt-leaching, gas-foaming, phase-separation, electrospinning nanofibers and 3D printing and 2D spun-coat films. They observed that the cell behavior is related to the cell shape permitted by each structure, and to the tensile strain that is induced over the cytoskeleton.

In order to complete a bone marrow model, we must consider the topology of the microenvironment as an ensemble of a porous architecture provided by the trabecular bone with the bone marrow tissue located in the cavities of this structure. This can be achieved by providing a three-dimensional scaffold onto which cells can adhere and graft ECM to develop intra-cavities and inter-cavities constructs for cells to develop, mimicking the bone marrow tissue inside the trabecular bone.

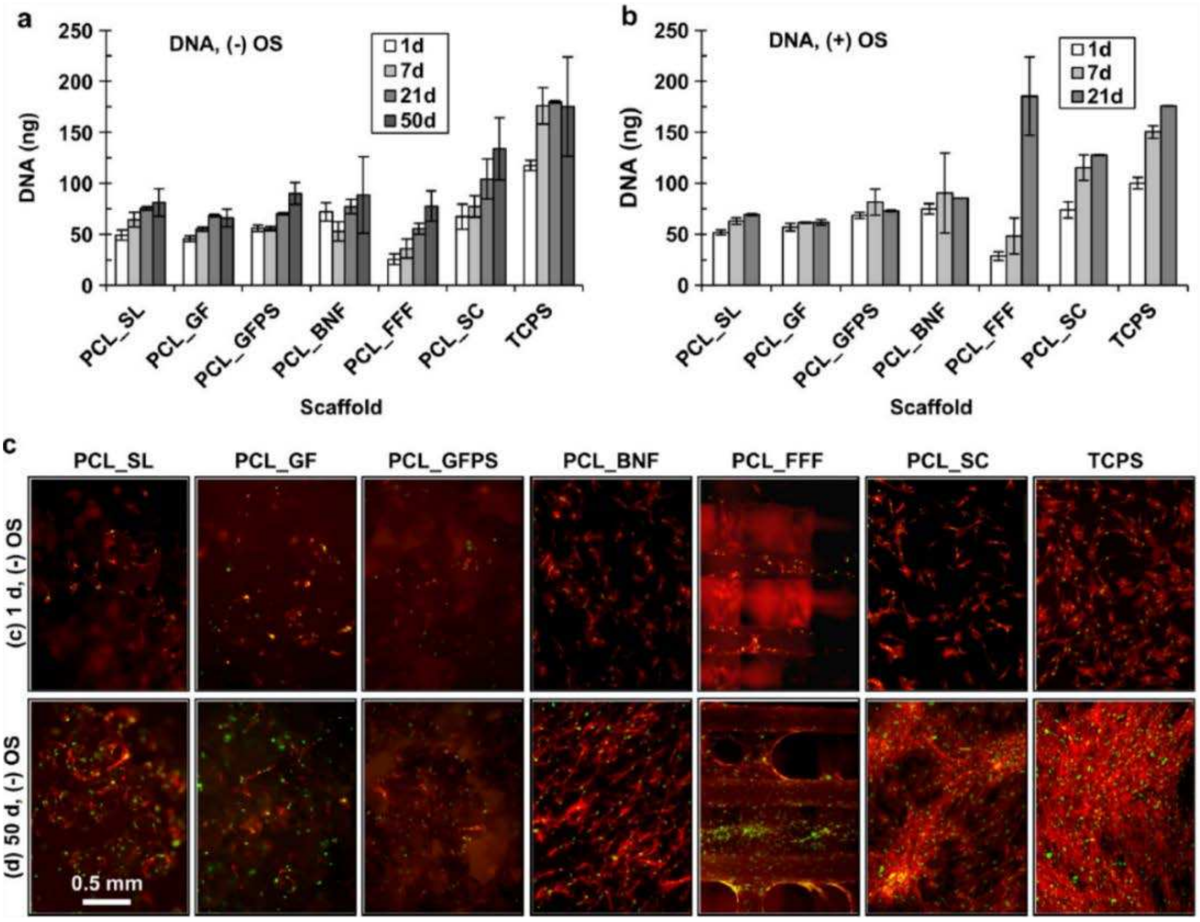

Figure 1.11. *hBMSC cell numbers measured by Picogreen DNA assay* ***(a)*** *without* ***(b)*** *with osteogenic inductor supplement.* ***(c)*** *Fluorescence characterization of 1D and 50D of cell culture of hBMSC in polycaprolactone scaffold produced with different fabrication technologies: salt-leaching, gas-foaming, phase-separation, electrospinning nanofibers and 3D printing and 2D spun-coat films. Nuclei are green (Sytox green) and actin is red (AlexaFluor 546 phalloidin). Scale bar applies to all images in (c). Adapted from [56].*

ii. Cell adhesion

As discussed, there is an important difference between 2D and 3D organizations due to the variations in cell-substrate interactions. In this paragraph our aim is to move from the description of cellular architectures at the tissue level towards the interaction mechanisms involved at the cellular level happening mainly by adhesion. The spatial distribution of the focal adhesion points modifies the distributions of the microtubes and the shape that the cytoskeleton adopts to attach to the structures, changing the shape of the cells.

In a 2D configuration, cells grow in a flat monolayer, spreading horizontally but constrained in the vertical direction. Additionally, the mechanical interactions to which the cells are exposed are limited in dimensionality: cell-cell interactions in the lateral directions and mechanical forces induced by the cell-substrate interactions vertically generate an asymmetrical condition. Consequently, cells tend to present a flat and elongated configuration leading to a forced apical-basal polarity. Though, natural for certain cell types, it is not for other cells that are surrounded by the ECM in their natural environment. Cell shape drives large variations in cellular function and modifies the cell behavior. Weaver et al. [57] showed how cell polarity decreased apoptosis sensitivity by modifying the expression of integrins in the cytoskeleton of the cells. The modifications in the microenvironment induced by the increase of dimensionality modifies also the signaling pathways of cells. Wang et al. [58] have proven that growth and adhesion are coupled in a 3D architecture as opposed to in monolayer cell cultures on 2D plastic substrates.

Various authors have engineered micropatterned adhesive islands in 2D substrates proving the impact of cell spreading on the function of cells [59]. Singhvi et al. [60] have demonstrated the used of micropatterned substrates to control cell growth in order to obtain reproducible cell populations by limiting the adhesive surface available. Chen et al. [61] went one step further establishing a link between the cell spreading and cell apoptosis, agreeing with the discoveries of the impact of cell polarity mentioned before. Moreover, McBeath et al. [59] were able to demonstrate the impact of cell shape on cell differentiation. MSC were seeded on adhesive islands of different sizes in order to limit their extension, showing that small and round MSC will differentiate into adipocytes and well-spread MSC into osteoblasts (**Figure 1.12**) due to the differences in tensile forces felt in the cytoskeleton, which activate the RhoA signal pathway, a main regulator of contractility in many cells. Additionally to the spreading surface of cells, the geometry of the shape has been shown to be a differentiation driving cue for MSC [62], proving that pointed featured shapes induce osteogenesis while rounded shapes promote adipogenesis. This is consistent with McBeth et al. finding that the increase or decrease of the tension in the cytoskeleton modifies the cell fate.

Cell adhesion is thus a strong cue to take into account when designing a cellular microenvironment. The question of the role of adhesion to reproduce a 3D bone marrow model has not yet been addressed, though there are studies investigating the impact of cell adhesion on the MSCs in 2D conditions. Adhesion is highly entangled with other cues, such as the scaffold topology and mechanical properties. Hence it is very challenging to design experiments devoted to understand the role of adhesion in complex architectures. Since cell adhesion is essential to the cell-substrate interaction, numerous studies have concluded that enhancing adhesion to the substrates would therefore promote the survival, proliferation and migration of cells [63]. On the other hand, this can be a double-edged sword when considering adhesion as a differentiation inductor cue for MSCs. It thus must be carefully considered when selecting the materials and coating for 3D *in-vitro* models.

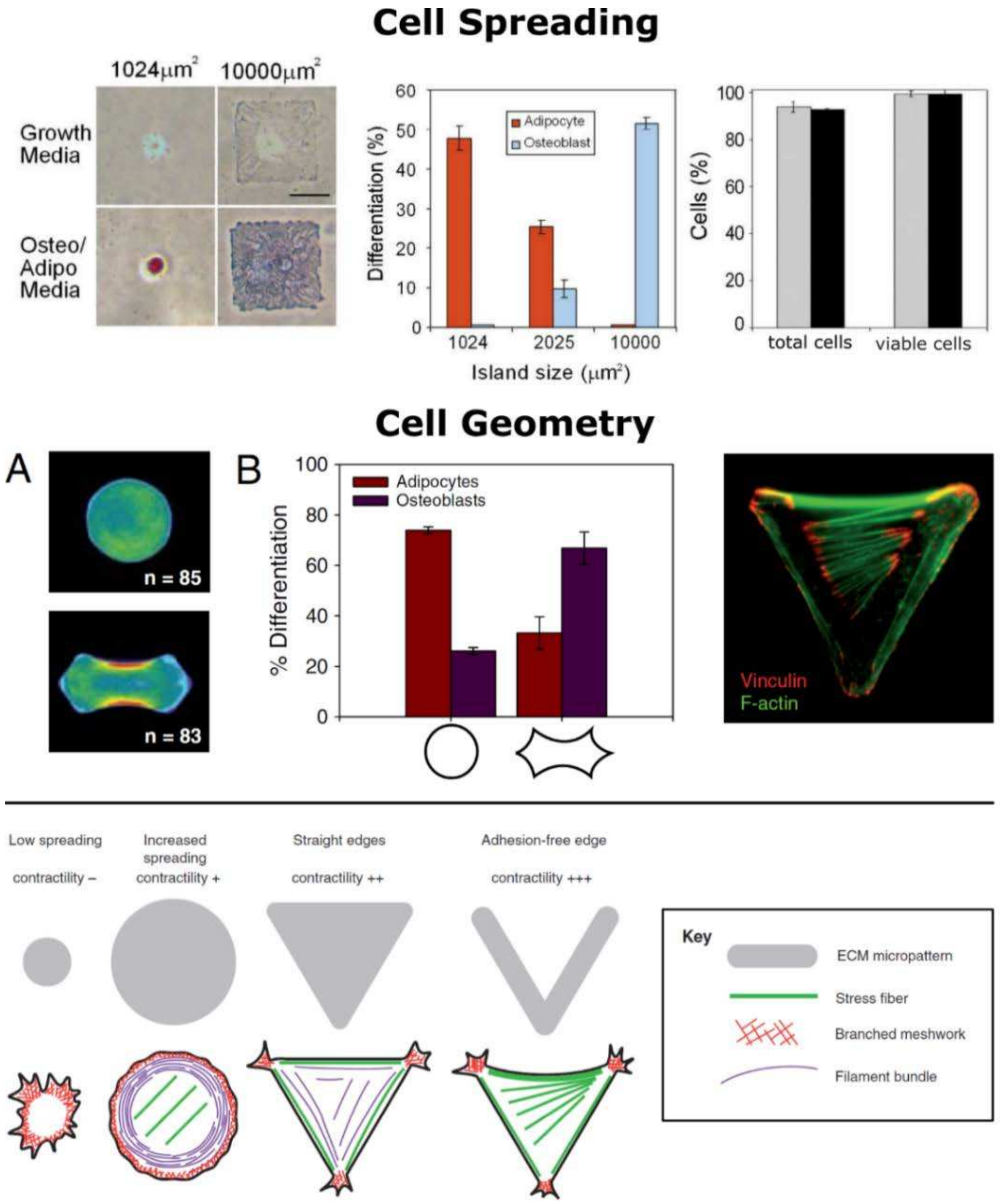

Figure 1.12. *Summary of the effect of adhesion and shape on the differentiation of MSC.* ***(a)*** *Cell spreading: patches of adhesion-promoter proteins of different sizes tends to induce different phenotype cells.* ***(b)*** *Cell geometry: the shape acquired by the cells when adhering has been proved as an important cue for cell differentiation.* ***(c)*** *Geometrical constrictions induce different levels of stress in the cytoskeleton of the cell, generating contractility and promoting certain phenotypes in the MSC [59], [62].*

iii. Mechanical properties

In tight relation with the cell adhesion onto the surface of a substrate goes the intrinsic properties of the material, more specifically, the mechanical properties of the substrate and ECM [64]. The mechanical properties of a biomimetic material have been a rising question brought by biologists and material scientists since the 80s, with a large relevance in the last decades due to the blooming of new technologies devoted to the fabrication of complex architectures for their application in biological studies. Mechanical properties, such as the Young modulus or the viscoelasticity, takes essential roles in the microenvironments to regulate fundamental biological processes such as cell growth, migration or differentiation [65]–[67]. Studying these parameters provides insight on how subcellular scale arrangement impacts cells behavior at the larger scales of tissues or organs. **Figure 1.13A** shows the large range of mechanical properties found in living organisms and the accurate reproduction of these features when building a biomimetic microenvironment represents a major challenge. MSCs have been shown to be mechanosensitive and mechanoresponsive cells which respond to the changes of the elastic modulus of their surroundings and alter their cytoskeleton contractility to keep the balance with the external mechanical forces exerted by the cell-ECM adhesions (***Figure 1.13B-C)***.

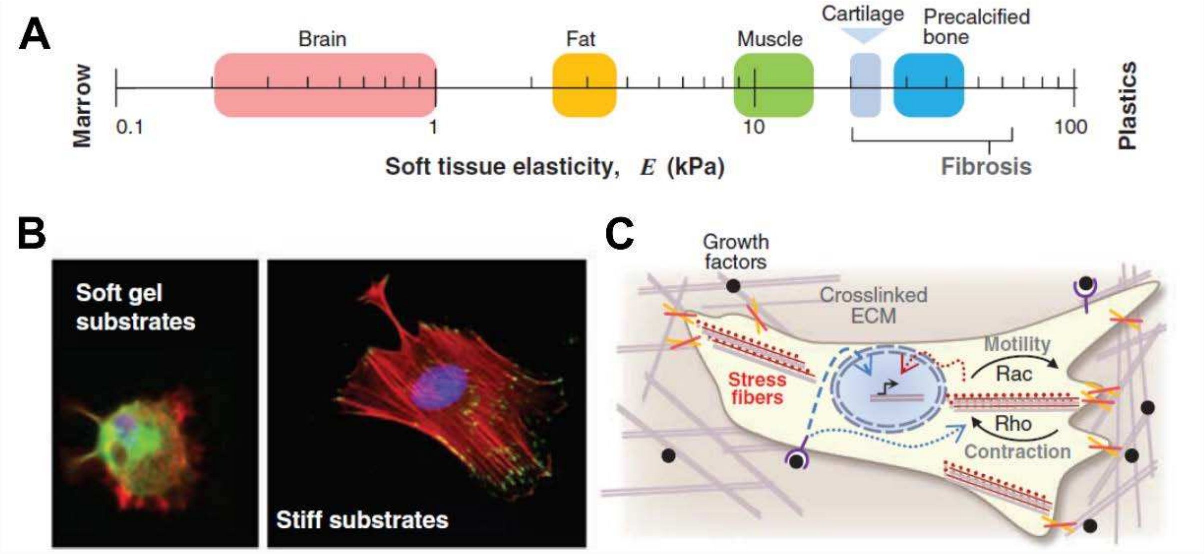

Figure 1.13. (a) *Tissue elasticity ranges from soft brain to pre-calcified bone,* $E \sim 20\ Pa\ to\ 30\ kPa$. ***(b)*** *In-vitro substrate mimicking soft and stiff microenvironments, showing that cells anchoring is stronger in stiff substrate than soft substrates.* ***(c)*** *Signals involved in regulating the stress in the cytoskeleton as a response to the microenvironment. Adapted from [68].*

Engler et al. [69] have proven that MSCs are able to respond to the elasticity of the microenvironment and differentiate. MSCs grown in gels that mimic the elastic modulus of muscles express myogenic markers, whereas MSCs cultured in rigid materials mimicking pre-calcified bones express osteogenic markers [69]. Though mechanical cues are not the only cellular fate inductors, cells already committed to a specific phenotype will appear less responsive to opposite soluble induction factors [70].

It is interesting to notice that cell density has a large impact on cell adhesion and behavior. It has been proved that cell assemblies can mechanically interact with the underlying soft substrate when they are seeded at high densities. This mechanism promotes cell spreading with prominent stress fibers and focal adhesion points similar to the ones found in cell cultured on stiff substrates [71]. Those findings indicate that cells are able to sense the tension caused by their neighbors and respond by spreading on the surface. These cell-cell interactions can override the impact of the low stiffness of soft substrates on the cellular morphology and function. Winet et al. [72] theorized that this spreading locally modifies the stiffness of the substrate, creating a gradient sensed by other cells (up to 5 cell length) and the formation of long-range patterns. Moreover, higher cell density has been associated to higher cell survival and the enhancing of certain cell functions [73] as it is shown in **Figure 1.14**.

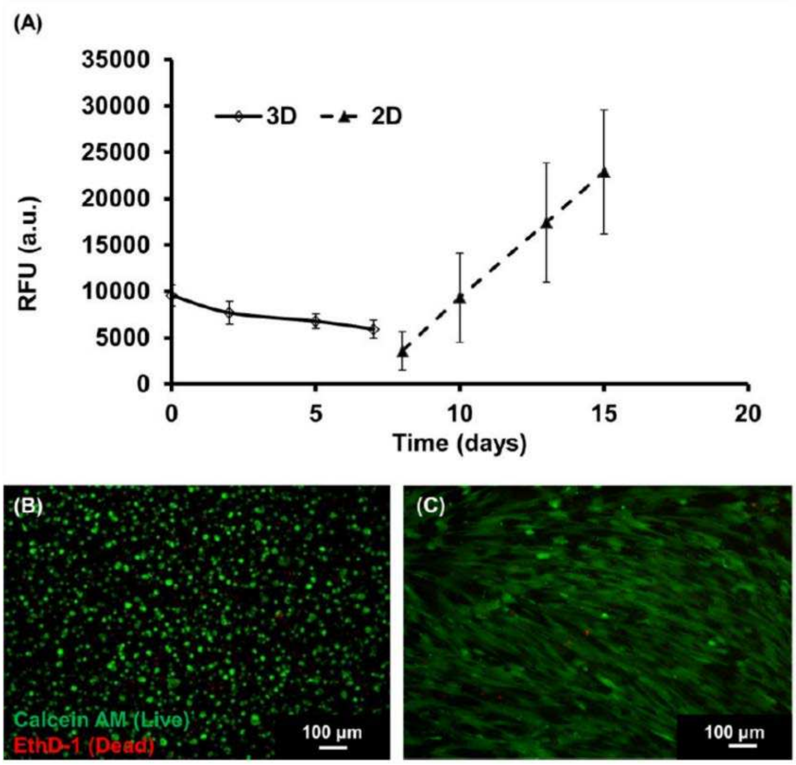

Figure 1.14. Evaluation of the reversibility of the apparent changes caused by the high cell density differences between 3D and 2D configurations. hMSCs were cultured in alginate matrices for 1 week in 3D culture and then replated in standard 2D conditions. **(a)** Metabolic activity for both cultures in 3D and 2D conditions. **(b)** Live/Dead viability assay performed in 3D configuration, and **(c)** in 2D configuration. Adapted from [73].

The combination of mechanical cues with topology [74] is not the only contributor to differentiation, but it plays a major role in cellular fate and must be taken into consideration when selecting materials for scaffold construction. Considering the bone marrow microenvironment, as explained in the biological context of the present work, we face a highly heterogenous systems in terms of stiffnesses associated with a large range of elastic moduli that presents a technological challenge to fabricate.

iv. Perfusion: shear stress and mass transport

Beside dimensionality, there are other relevant and striking differences between the 2D static *in-vitro* models used as gold standard in biology and the *in-vivo* models. In this part, we will focus on the dynamic aspects inherent to *in-vivo* models and the steps taken in last years to implement it in cell culture methods.

In the specific case of bone tissue, biomechanical stimuli play an important physiological role, providing fundamental conditions for the correct development of the tissue. Besides the predominant strain caused by the deformation on the internal structures due to the physical activity, fluid shear stress presents an underlying constant mechanical stimulus generated by the continuous interstitial fluid movement through the internal structure of the bone. Mechanical stress has been considered as one of the most relevant insight for bone remodeling for decades [75] or even a century if we consider the Wolff's law as a starting point at the end of 19th century [76]. This importance is evidenced in situations such as in spaceflights or in long periods of bed convalescence, where the lack of mechanical loading translates into the loss of bone mass.

When talking of static as opposed to dynamic cell culture, we mostly refer to the fact that culture medium, and therefore the soluble factors, remains immobile in the culture container. This situation presents a clear contrast with the *in-vivo* situation, which presents a dynamic flow of nourishment and the flush out of metabolic by-products. The intrinsic exchange of medium generates several differences in terms of mass transfer aspects and how cells receive information and how they react to this information, but furthermore, it implies as well the incorporation of previously inexistent biophysical cues such as shear stress.

Regarding bone marrow, fluid movement has various origins: first, there is a network of vascular vessels arriving from the cortical bone and passing through the bone marrow to supply nourishment for cell (**Figure 1.15A**). Bone possesses a unique vessel unit in the bone marrow called sinusoid that connects an arteria and a vein with a porous membrane to enable the transfer of hematopoietic and non-hematopoietic cells (**Figure 1.15B-C**) [77]. Second, there is a hydrostatic pressure drop across the cortical bone vessels that induces a radial flow [78]. Third, interstitial fluid movements in the cavities of the trabecular bone are caused by the mechanical load in the bones. Finally, additional fluid fluctuations can be caused by muscles contractions, temporarily occluding the circulatory system around the bones and increasing the bone marrow pressure [79]. A detailed explanation on blood and interstitial flow through the porosity of the bone tissue can be found in [80].

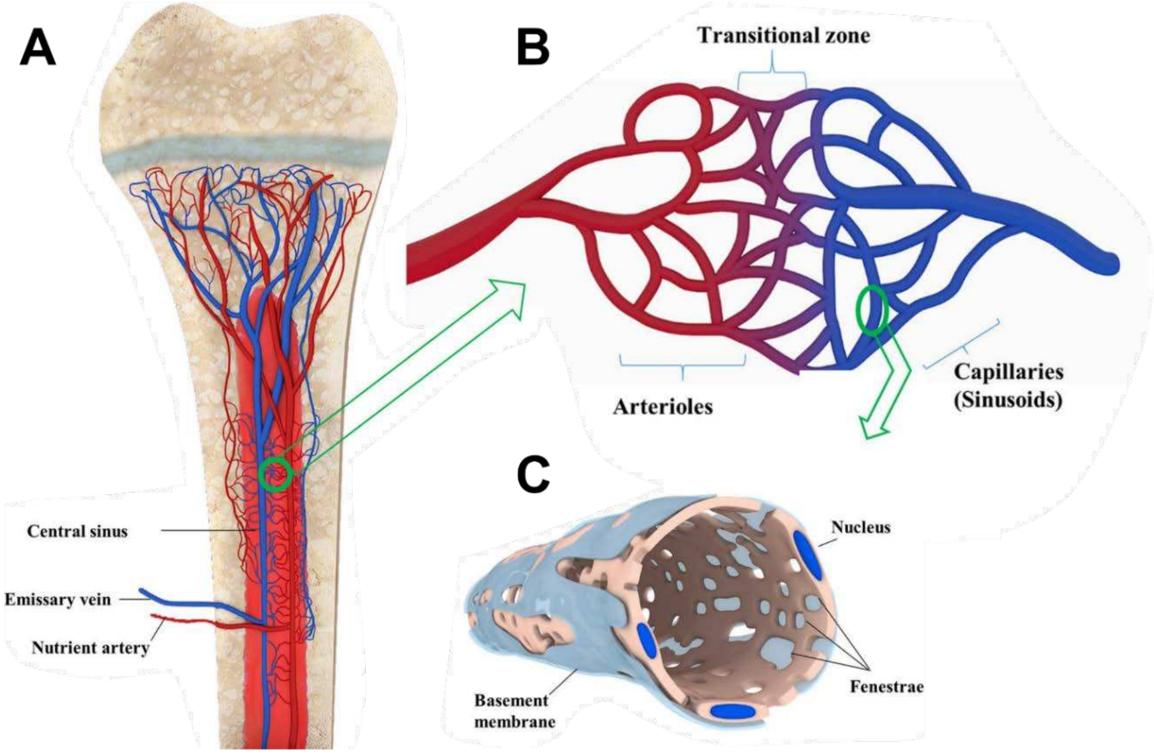

Figure 1.15. *A schematic illustration of blood supply of long bones.* ***(a)*** *Cross-section of the bone with the correspondent circulatory system and ramifications.* ***(b)*** *Magnified illustration of the joint of the arterial and venal systems happening in the bone marrow via the intersection a particular vessel construct call sinusoid.* ***(c)*** *Transversal section of a sinusoidal capillary that shows that the endothelium is fenestrated and also covered by an incomplete basement membrane to increase the permeability to large molecules and blood cells. Adapted from [77].*

The development of systems that provide control over the fluid flow and mass transfer mechanism (nutrients and waste products, retention of extracellular matrix component and signaling soluble factors) within the culture has been an axis of research in recent times. Bioreactors are generally defined as devices for which biological or biochemical processes happen in a controlled environment (pH, temperature, nourishment supply or waste removal), commonly implemented by inducing a fluid movement in the system.

Figure 1.16 presents numerous configurations of bioreactors, giving new alternatives for 3D tissue engineering applications. Spinner flasks, rotating wall bioreactors, hollow fiber membrane systems and perfusion rigs are the most common systems [81]. Perfusion appears to be the solution that presents the largest benefits due to the capability to incorporate 3D constructs and generate more homogeneous microenvironments with improved transport through the scaffolds.

The supply of oxygen and soluble nutrients, as well as the proper flushing of cellular wastes are limiting factors when developing *in-vitro* 3D tissues. In 3D systems, promoting mass transfer through advection and diffusion is essential to ensure cell viability. The clearest example is the necrotic cores that spheroids[d] exhibit when it exceed a certain size due to the shortage of oxygen and nutriments in the central core [82]. The perfusion of medium through engineered porous scaffold has presented a proper response to mass transport limitations by enabling a homogeneous flow within the cell architecture rather than improving the convection at the monolithic surface. For instance, direct perfusion bioreactors have proven to enhance matrix deposition in bone cells due to the increase of available nutriments (and the stimulation induced by the fluid movement) [83], [84].

---

[d] Spheroid: spherical cellular aggregates produced by culture a large density of cells under low-adhesion conditions, just a droplet suspension or anti-adhesive plastic supports.

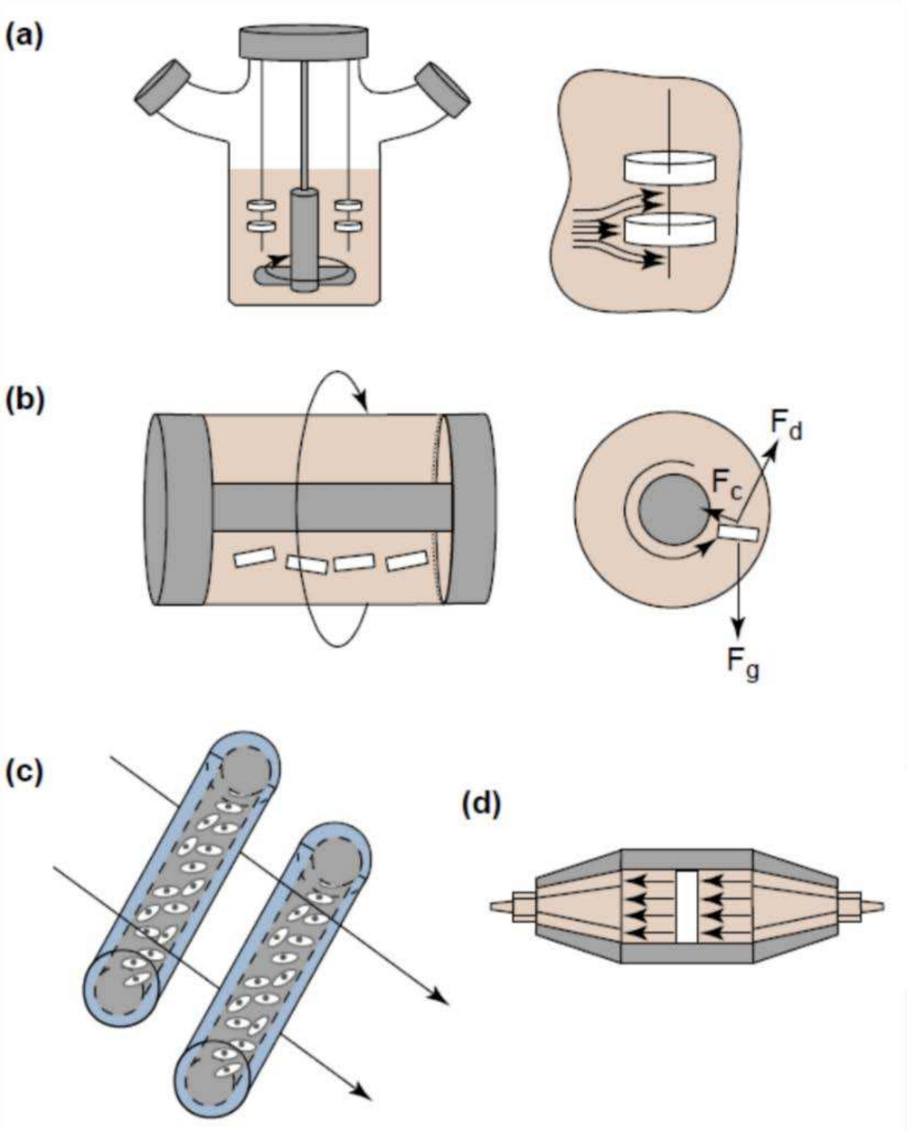

Figure 1.16. *Schematic illustration of different kinds of bioreactors used for tissue engineering applications.* ***(a)*** *In spinnerflask bioreactors, the scaffold is immerged in a container with a medium flow produced by stirring.* ***(b)*** *Rotating-wall vessels rotates the wall of a container to produce a microenvironment with large mass transport and low shear stress.* ***(c)*** *In hollow-fiber bioreactors, cells are embedded inside hollow fibers and the fluid flows around of the fibers.* ***(d)*** *In direct perfusion bioreactors, the fluid flows directly through the construct. Adapted from [81].*

Weinbaum et al. [85] have simulated the fluid shear stress in the channels of bone. The authors showed that the shear stress reaches 0.8-3 Pa under moderated physical load due to the fluid movement which alters the static regime of the bone tissue. **Figure 1.17** presents the work of Metzger et al. [86] related the pressure induces by a mechanical load over the trabecular bone microarchitecture and the shear stress induced within the bone marrow located in the trabecular structure. The authors measured the pressure gradients associated with the deformation of the architecture obtained by µCT and calculated the shear stress by computational fluid models. The shear stress in the trabecular bone ranges from 0 to 25 Pa.

The fluid movement component which is tangential to the surface generates a shear stress gradient perpendicular to the plane and proportional to the fluid viscosity. The flow pattern is thus important to consider when trying to reproduce the *in-vivo* environment: though there is not a clear agreement on which flow pattern is more physiologically relevant, a steady state flow seems to be more suited than pulsate patterns [79], [87]. Bioreactor systems have been employed to investigate the role of shear stress in the osteogenesis of MSC, in 2D and 3D, showing in both cases that the mechanical loading induces cell differentiation. Those studies suggest an increase in the expression of certain proteins related with osteoblastic-like cells such as ALP, PGE, OPN, OC, COX-2, Col1 and the mineralized matrix production when the shear stress is in the range of $0.5 \text{ to } 1\ Pa$ in 2D cultures and $1 \text{ to } 5 \times 10^{-2} Pa$ in 3D cultures [88]–[95]. The difference in order of magnitude (10-50 folds) found with the increase of dimensionality can be explained by the differences of cell attachment: flattened cells are predominant in 2D configuration, while bridged cells with 2 or more struts are found in 3D cell culture [96]. These values, that are below the expected values found *in-vivo,* suggest that the influence of the ECM and the mineralization of the tissue *in-vivo* might reduce the sensitivity of cells to the shear stress.

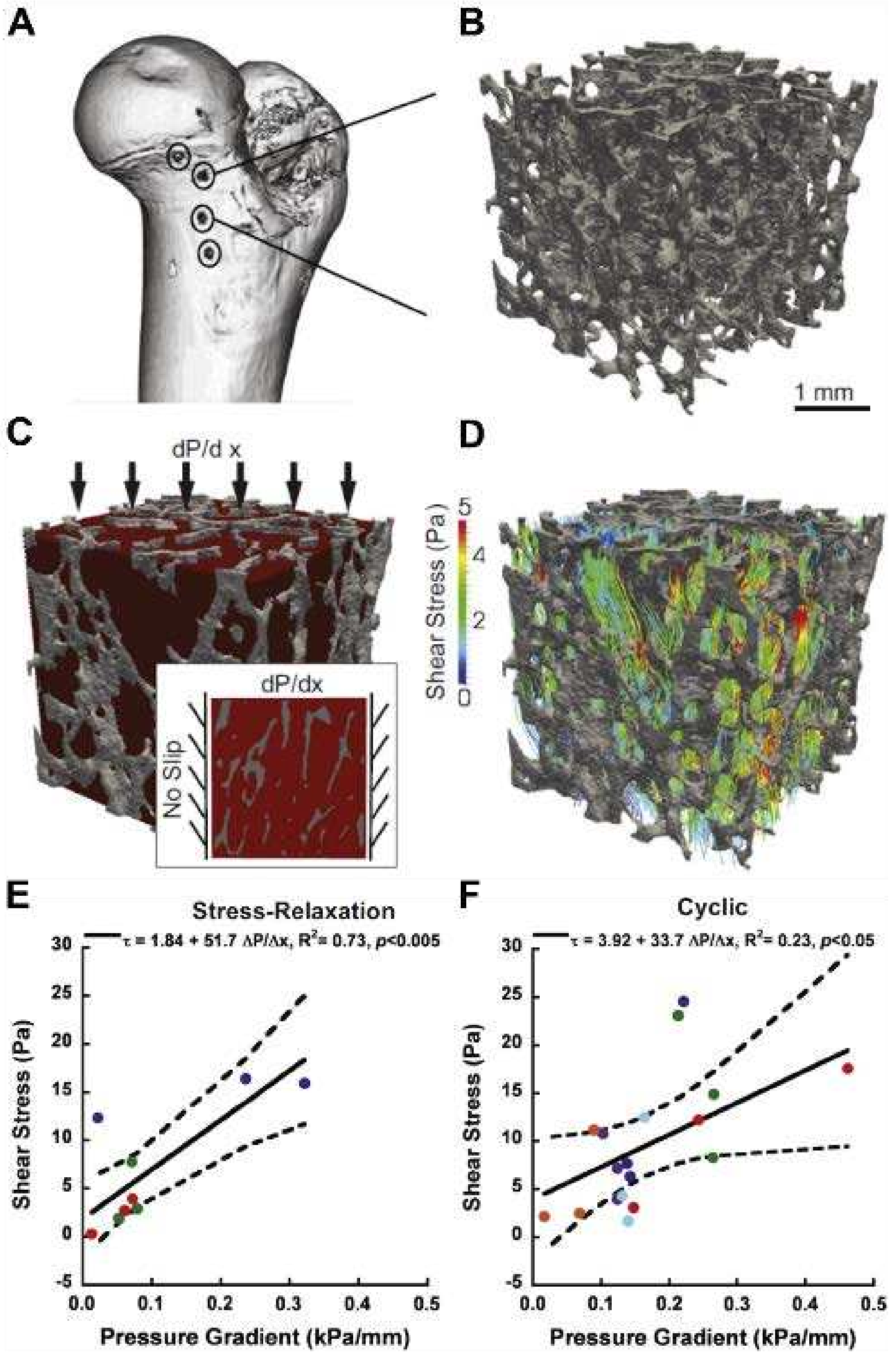

Figure 1.17. Mechanical characterization of the deformation and pressure generated in the trabecular bone characterized by μCT in combination with pressure transducers. **(a)** 3D reconstruction of a femoral head using μCT. **(b)** 4mm^3 cubic region selected between two pressure transducers to simulate the mechanical environment and **(c)** the generated mesh with approximately 1 million of tetrahedral finite element. **(d)** Shear stress streamlines of the bone marrow calculated by computational fluid dynamics models. **(e-f)** Volumetric- and time-averaged shear stress calculated during stress-relaxation and cyclic mechanical loading of the trabecular specimens. Adapted from [86].

3. Microphysiological systems

A microphysiological system (MPS), is by definition a minimalistic biological construct integrated in an *in-vitro* support which aims to reproduce certain relevant aspects of a specific organ or tissue in a controllable situation. MPS are designed to answer precise biological questions and to that aim they reproduce some of the most relevant features of the cellular microenvironment for that targeted situations and integrate well-defined biological functions. In **Figure 1.18**, we present some examples of MPS devoted to answer specific questions on the bone marrow physiology.

There have been several works focusing on the development of 3D MPS for the bone marrow in healthy conditions or as pathological models (acute myeloid leukemia, multiple myeloma, acute lymphoblastic, chronic myeloid leukemia, among others) (**Figure 1.18A**) [97]–[99]. The bone marrow structure can be understood as an assembly of three different compartments of different tissues: the endosteal niche (bone tissue), the perivascular niche (endothelial tissue) and the adipose niche (adipose tissue). Despite the insights that these models provided on the understanding of these niches on cell trafficking, cell differentiation, cell multipotency or even metastatic mechanisms, most of the studies carried out are focused on the truthful reproduction of a single niche, targeting an accurate model of a single compartment [97], [100]–[102]. Nevertheless, there have been some attempts to create devices that reproduce two separated niches and their interactions, as illustrated in **Figure 1.18B-C** [103], [104]. It is important to note that the three different compartments have not yet been reproduced in a single device [99]. These works have highlighted the difficulties in representing the distinct physical, chemical, and biological characteristics featured in the bone marrow. Besides, most of the multi-niche approaches are based on confining the different niches in separated compartments interacting via porous membranes or channels [105]. This spatial cellular distribution disrupts the heterogenous organization found the bone marrow and private cells from the cell-cell interaction information [103], [105]–[109].

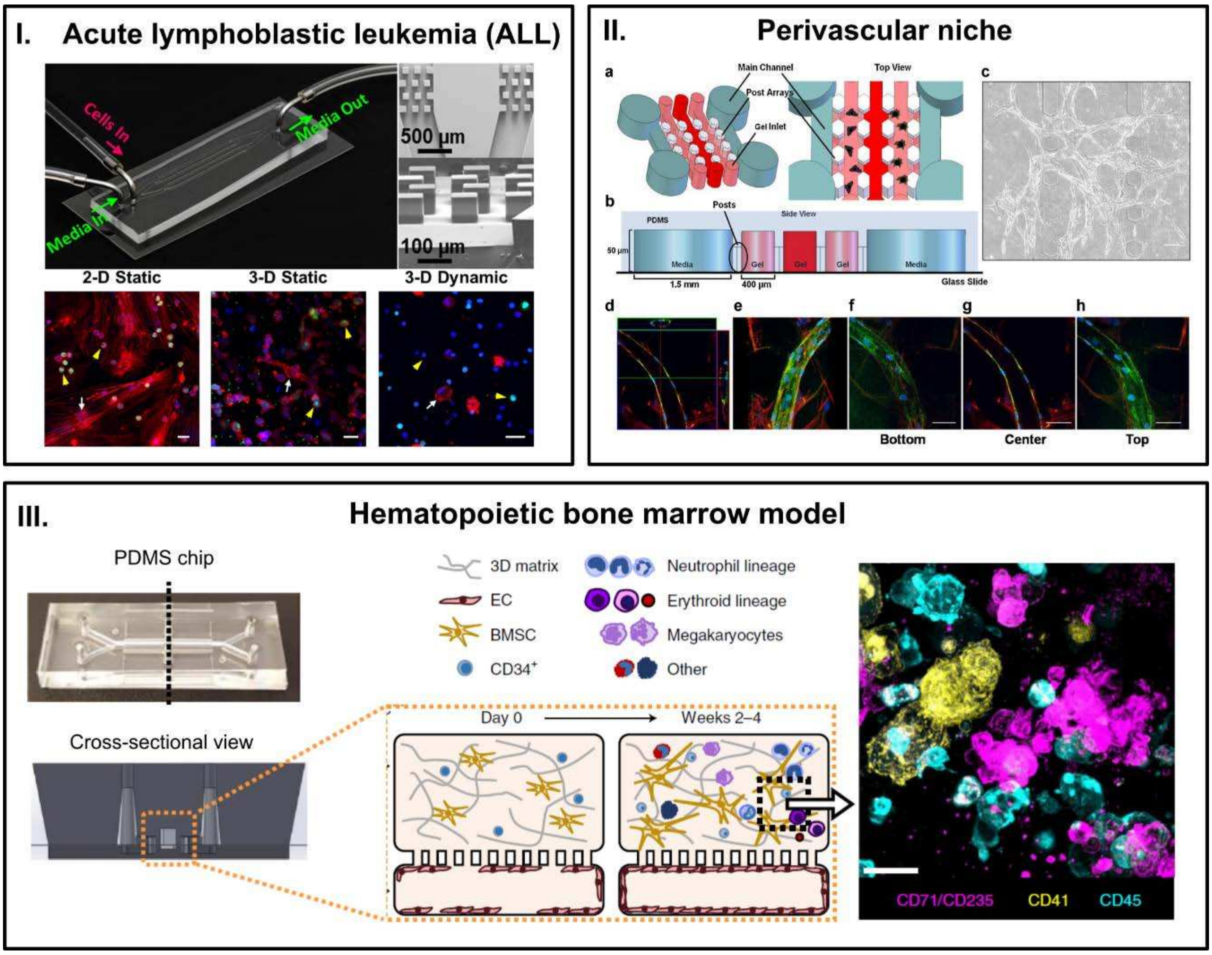

Figure 1.18. *Examples of microphysiological systems with multiple compartments developed for the study of bone marrow in metastatic or regenerative contexts.*

A. *3D microfluidic model of Acute lymphoblastic leukemia (ALL).* ***Up:*** *microfluidic platform consisting in 4 channels where collagen hydrogel is placed with MSC, Human osteoblast and SUP-B15 cancer cells. SEM images show the internal pillar of the channels to hold the hydrogel.* ***Down:*** *Confocal images of the co-cultured cells in 2D static conditions, 3D static conditions and 3D dynamic conditions at day 7. Adapted from [110].*

B. *Formation of capillary-like network in 3D fibrin gels.* ***(a)*** *Schematic representation of the microfluidic device showing two parallel main channels to provide media and nutrients to the gel channels in the center, which uses hexagonal pillars to hold the gels.* ***(b)*** *Side view of the PDMS device with the hydrogels in the channels.* ***(c)*** *Phase-contrast image at 14D of HUVECs and MSCs.* ***(d) – (h)*** *high magnification confocal images at 14D. Adapted from [100].*

C. *Design of primary human hematopoietic bone marrow model.* ***Left:*** *photograph of the PDMS microdevice and a vertical cross-section of the chip.* ***Middle:*** *schematic of the cross-sectional view at day 0 after seeding and within 2 weeks of the culture initiation.* ***Right:*** *Immunofluorescence image of a vertical cross-section through the gel in the upper channel of the BM chip taken at day 14. Adapted from [103].*

There are typically two approaches to mimic the hematopoietic niches: hydrogels materials or scaffolds. The first method aims at imposing a distribution of cells in the three dimensions by embedding the cells in a polymerizable soft material such as alginate, fibronectin or collagen [101], [103], [111]. But it lacks the microporous design provided by the trabecular bone *in-vivo*. In most of the cases, those materials provide a suitable microenvironment for the cell culture, yet because of the vast variety of materials and the tendency of simplifying the ECM found *in-vivo* with a single or duet-composition, the standardization of the hydrogel matrix as cellular microenvironment is difficult. Another striking divergency from the *in-vivo* conditions when using hydrogels as 3D support is the mechanical properties (those are soft materials, with elastic modulus ranging $\sim 1 - 1000\ Pa$).

Scaffolding approaches aim to mimic the complex architecture deployed by the trabecular bone, providing structural and mechanical cues that allow the system to host the different niches within their cavities. Typically, these structures are fabricated with stiff materials similar to the mineralized bone as polystyrene [102] or hydroxyapatite [104] (**Figure 1.19A**). Other approaches rely on the use of decellularized bone microarchitectures (**Figure 1.19B**) [102], [112]. This scaffolding approach is frequently used to reproduce the endosteal niche in combination with the adipose or vascular niche (mostly using endothelial cell lines). It is also worth to notice that most of those development are usually implemented on a microfluidic format, restraining the devices to the millimetric scale, often with one of the dimensions in the sub-millimetric scale (**Figure 1.19A-B).** Though, this is still considered as 3D architectures, the constrain of one axis to the submicrometric scale can induce anisotropies in the cellular distribution and can generate gradients of species in the medium.

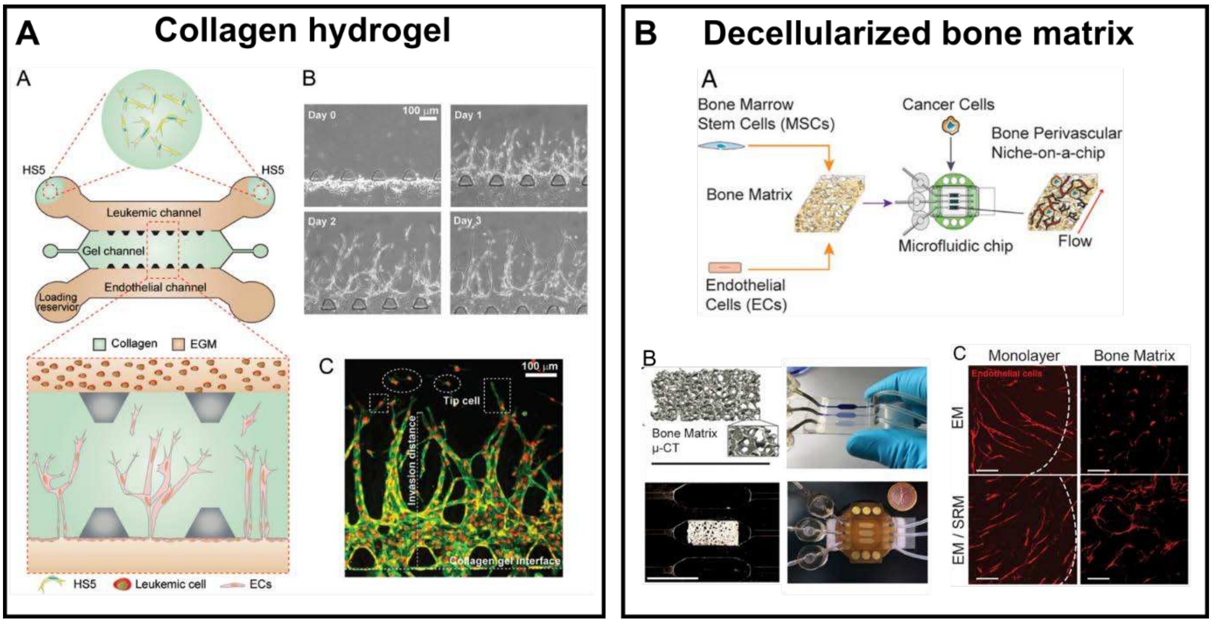

Figure 1.19. *Examples of 3D architectures in microphysiological systems.*

A. *Leukemic-cell-induced EC invasion and lumen formation in a 3D biomimetic angiogenesis device using collagen hydrogel as 3D matrix.* ***(a)*** *Schematic showing the 3D biomimetic device.* ***(b)*** *Representative phase-contrast images showing invasion of ECs in the collagen gel.* ***(c)*** *Confocal image in z -projection showing spouting and migrating ECs toward the leukemic.*

B. *Formation and maintenance of the niche-on-a-chip.* ***(a)*** *Schematic showing the bone perivascular (BoPV) niche device for studies of breast cancer colonization.* ***(b)*** *Bone tissue reconstruction based on micro-computed tomography and rectangular-shaped bone matrix in the microfluidic chip (6 mm x 3 mm x 1 mm). Overview of the microfluidic chip used to culture the BoPV niche.* ***(c)*** *Confocal images of RFP-labelled ECs forming vascular networks in monolayers or in the bone matrix. (Scale bar: 200 μm.)*

4. Objectives of this work

The discussed information presented in this chapter provides the framework of this project. In simple words, the main goal of this project is to establish the tools and technologies to develop a functional 3D *in-vitro* model with perfusion capacity and the potential to acquire a function. We aim to apply this technology for the realization of a microphysiological system of the bone marrow, thus containing functional hematopoietic niches.

We have overviewed the key features of the cellular microenvironment that characterize bone marrow and that are essential to be reproduced in a microphysiological system. Bone marrow features a complex and heterogeneous microenvironment composed of a structural part and a functional part (hematopoietic niche), respectively constituted by the porous architecture of the trabecular bone and by the cellular construct. Because of the complexity to reproduce the heterogeneities of the cellular microenvironment displayed in the bone marrow, the structural and functional parts are usually treated separately in order to simplify the technological developments. This leads to some inaccurate experimental environments that can mislead the biological hypothesis.

For the bone marrow, the porous structure where cells are located provides support for the correct development of the tissue and for the ECM grafting and the creation of the MSC network that holds the hematopoietic niche. The interconnection of porous cavities in the bone marrow ensures cell migration and establishes the different compartments that compose the niche (red bone marrow and yellow bone marrow).

Furthermore, reproducing the spatial distribution of mechanical cues raises a major challenge because of the abrupt transition at the interface between the trabecular bone and the bone marrow. We can consider the bone marrow as a 2-phases system with a stiff architecture composed of mineralized collagen (with a large Young modulus, about $\sim 0.2 - 1\ GPa$) grafted to a soft gel mainly composed of ECM and cells (with low stiffness ranging $\sim 0.5 - 50\ kPa$). Most of the examples found in the literature reproduce the cellular microenvironment constituted mainly by ECM from scratch, obviating the capacity of cells to segregate ECM and generate complex 3D structures that we can observe *in-vivo*.

Finally, fluid movements in the interstitial channels of the bone and in the cavities of the bone marrow induce shear stress and allow mass transfer. The latter is necessary to bring nourishment to the cells and to flush out the cellular by-product generated by the metabolic activity. The mechanical stress induced by the flow (shear stress) that stimulates cells constitutes an essential piece of the puzzle that represents the cellular microenvironment of the bone marrow.

The kind of environmental cues to be provided to the cells in order to induce a specific function will largely vary and depend on the final use of the model. These aspects are currently under investigation by our colleagues Nicolas Espagnolle and Melanie

Gadelorge from the *Etablissement Français du Sang* (EFS) and the RESTORE unit. They provided advices on the biological questions and the opportunity to work directly with human primary cells of the bone marrow.

This work aims at reproducing structural features of the trabecular bone and its specific microenvironment. In the following chapters, we will present two different technological approaches to achieve this goal via designed or free-form architectures. We will explore the possibility to induce different stimuli within the scaffold. Furthermore, we will implement fluidic perfusion through the integration of the scaffolds into commercial bioreactors or into a microfluidic chip in order to study the impact of the shear stress and the mass transport on cell culture.

References

[1] E. Marieb and K. Hoehn, *Human anatomy and Physiology 9th Edition*. 2013.

[2] R. Sender, S. Fuchs, and R. Milo, “Revised Estimates for the Number of Human and Bacteria Cells in the Body,” *PLOS Biol.*, vol. 14, no. 8, p. e1002533, Aug. 2016, doi: 10.1371/journal.pbio.1002533.

[3] A. Kahn, “Regenerative medicine,” *J. Soc. Biol.*, vol. 195, no. 1, pp. 5–7, 2001, doi: 10.1051/jbio/2001195010005.

[4] M. H. Ross and W. Pawlina, *Histology: A Text and Atlas with Correlated Cell and Molecular Biology, 7e*. 2016.

[5] O. Gurevitch, S. Slavin, and A. G. Feldman, “Conversion of red bone marrow into yellow - Cause and mechanisms,” *Med. Hypotheses*, vol. 69, no. 3, pp. 531–536, 2007, doi: 10.1016/j.mehy.2007.01.052.

[6] L. Pothuaud, P. Carceller, and D. Hans, “Correlations between grey-level variations in 2D projection images (TBS) and 3D microarchitecture: Applications in the study of human trabecular bone microarchitecture,” *Bone*, vol. 42, no. 4, pp. 775–787, Apr. 2008, doi: 10.1016/j.bone.2007.11.018.

[7] A. B. Castillo and C. R. Jacobs, “Mesenchymal stem cell mechanobiology,” *Current Osteoporosis Reports*, vol. 8, no. 2. Curr Osteoporos Rep, pp. 98–104, Jun. 2010, doi: 10.1007/s11914-010-0015-2.

[8] H. Roesler, “The history of some fundamental concepts in bone biomechanics,” *J. Biomech.*, vol. 20, no. 11–12, pp. 1025–1034, Jan. 1987, doi: 10.1016/0021-9290(87)90020-0.

[9] X. Chen *et al.*, “Mechanical Heterogeneity in the Bone Microenvironment as Characterized by Atomic Force Microscopy,” *Biophys. J.*, vol. 119, no. 3, pp. 502–513, Aug. 2020, doi: 10.1016/j.bpj.2020.06.026.

[10] L. E. Jansen, N. P. Birch, J. D. Schiffman, A. J. Crosby, and S. R. Peyton, “Mechanics of intact bone marrow,” *J. Mech. Behav. Biomed. Mater.*, vol. 50, pp. 299–307, Oct. 2015, doi: 10.1016/j.jmbbm.2015.06.023.

[11] J. Y. Rho, R. B. Ashman, and C. H. Turner, “Young’s modulus of trabecular and cortical bone material: Ultrasonic and microtensile measurements,” *J. Biomech.*, vol. 26, no. 2, pp. 111–119, Feb. 1993, doi: 10.1016/0021-9290(93)90042-D.

[12] V. W. C. Yu and D. T. Scadden, “Heterogeneity of the bone marrow niche,” *Current Opinion in Hematology*, vol. 23, no. 4. Lippincott Williams and Wilkins, pp. 331–338, Jul. 01, 2016, doi: 10.1097/MOH.0000000000000265.

[13] N. E. McKenzie, “The drug development process,” in *Fundamentals of Cancer Prevention*, 2005, pp. 131–138.

[14] EMA, “Note for Guidance on General Considerations for Clinical Trials,” *ICH E8*, no. September 1997, pp. 1–14, 1998, Accessed: Jan. 28, 2021. [Online]. Available: http://www.emea.eu.int.

[15] Ezekiel Emanuel, “The Solution to Drug Prices - The New York Times,” *The New York Times*, 2015. https://www.nytimes.com/2015/09/09/opinion/the-solution-to-drug-prices.html (accessed Jan. 28, 2021).

[16] T. J. Hwang, D. Carpenter, J. C. Lauffenburger, B. Wang, J. M. Franklin, and A. S. Kesselheim, “Failure of investigational drugs in late-stage clinical development and publication of trial results,” *JAMA Intern. Med.*, vol. 176, no. 12, pp. 1826–1833, Dec. 2016, doi: 10.1001/jamainternmed.2016.6008.

[17] D. B. Fogel, “Factors associated with clinical trials that fail and opportunities for improving the likelihood of success: A review,” *Contemporary Clinical Trials Communications*, vol. 11. Elsevier Inc, pp. 156–164, Sep. 01, 2018, doi: 10.1016/j.conctc.2018.08.001.

[18] P. Flecknell, “Replacement, Reduction and Refinement*,” in *Mainzer Vorsysponsium*, 2002.

[19] “3Rs Alternatives: Technologies and Approaches | Animal Welfare Information Center | NAL | USDA.” https://www.nal.usda.gov/awic/3rs-alternatives-technologies-and-approaches (accessed Mar. 24, 2021).

[20] D. W. Thomas, J. Burns, J. Audette, A. Carroll, C. Dow-Hygelund, and M. Hay, “Clinical Development Success Rates Pharma intelligence 2006 - 2015,” 2015. Accessed: Jan. 28, 2021. [Online]. Available: https://www.bio.org/sites/default/files/Clinical Development Success Rates 2006-2015 - BIO, Biomedtracker, Amplion 2016.pdf.

[21] G. Huang *et al.*, “Functional and Biomimetic Materials for Engineering of the Three-Dimensional Cell Microenvironment,” *Chemical Reviews*, vol. 117, no. 20. American Chemical Society, pp. 12764–12850, Oct. 25, 2017, doi: 10.1021/acs.chemrev.7b00094.

[22] Y. L. Han *et al.*, “Engineering physical microenvironment for stem cell based regenerative medicine,” *Drug Discovery Today*, vol. 19, no. 6. Elsevier Ltd, pp. 763–773, Jun. 01, 2014, doi: 10.1016/j.drudis.2014.01.015.

[23] J. Barthes, H. Özçelik, M. Hindié, A. Ndreu-Halili, A. Hasan, and N. E. Vrana, “Cell Microenvironment Engineering and Monitoring for Tissue Engineering and Regenerative Medicine: The Recent Advances,” *BioMed Research International*, vol. 2014. Hindawi Publishing Corporation, 2014, doi: 10.1155/2014/921905.

[24] R. Kumar, P. S. Godavarthy, and D. S. Krause, “The bone marrow microenvironment in health and disease at a glance,” *J. Cell Sci.*, vol. 131, no. 4, Feb. 2018, doi: 10.1242/jcs.201707.

[25] D. Vigetti, M. Götte, M. S. G. Pavão, and A. D. Theocharis, “Cellular microenvironment in human pathologies,” *BioMed Research International*, vol. 2013. 2013, doi: 10.1155/2013/946958.

[26] B. M. Baker and C. S. Chen, “Deconstructing the third dimension-how 3D culture microenvironments alter cellular cues,” *J. Cell Sci.*, vol. 125, no. 13, pp. 3015–3024, 2012, doi: 10.1242/jcs.079509.

[27] S. I. Fraley *et al.*, “A distinctive role for focal adhesion proteins in three-dimensional cell motility,” *Nat. Cell Biol.*, vol. 12, no. 6, pp. 598–604, Jun. 2010, doi: 10.1038/ncb2062.

[28] K. E. Kubow and A. R. Horwitz, “Reducing background fluorescence reveals adhesions in 3D matrices,” *Nature Cell Biology*, vol. 13, no. 1. Nature Publishing Group, pp. 3–5, Jan. 21, 2011, doi: 10.1038/ncb0111-3.

[29] N. Di Maggio, E. Piccinini, M. Jaworski, A. Trumpp, D. J. Wendt, and I. Martin, “Toward modeling the bone marrow niche using scaffold-based 3D culture systems,” *Biomaterials*, vol. 32, no. 2, pp. 321–329, 2011, doi: 10.1016/j.biomaterials.2010.09.041.

[30] S. Srouji, T. Kizhner, and E. Livne, “3D scaffolds for bone marrow stem cell support in bone repair.,” *Regen. Med.*, vol. 1, no. 4, pp. 519–528, 2006, doi: 10.2217/17460751.1.4.519.

[31] A. Raic, T. Naolou, A. Mohra, C. Chatterjee, and C. Lee-Thedieck, “3D models of the bone marrow in health and disease: Yesterday, today, and tomorrow,” *MRS Commun.*, vol. 9, no. 1, pp. 37–52, 2019, doi: 10.1557/mrc.2018.203.

[32] D. Tang, R. S. Tare, L.-Y. Yang, D. F. Williams, K.-L. Ou, and R. O. C. Oreffo, “Biofabrication of bone tissue: approaches, challenges and translation for bone regeneration,” *Biomaterials*, vol. 83, pp. 363–382, Mar. 2016, doi: 10.1016/J.BIOMATERIALS.2016.01.024.

[33] S. Mondal *et al.*, “Hydroxyapatite nano bioceramics optimized 3D printed poly lactic acid scaffold for bone tissue engineering application,” *Ceram. Int.*, vol. 46, no. 3, pp. 3443–3455, 2020, doi: 10.1016/j.ceramint.2019.10.057.

[34] M. de Ruijter *et al.*, “Out-of-Plane 3D-Printed Microfibers Improve the Shear Properties of Hydrogel Composites,” *Small*, vol. 14, no. 8, pp. 1–6, 2018, doi: 10.1002/smll.201702773.

[35] G. Kumar *et al.*, “The determination of stem cell fate by 3D scaffold structures through the control of cell shape,” *Biomaterials*, vol. 32, no. 35, pp. 9188–9196, Dec. 2011, doi: 10.1016/j.biomaterials.2011.08.054.

[36] C. T. Kao, C. C. Lin, Y. W. Chen, C. H. Yeh, H. Y. Fang, and M. Y. Shie, “Poly(dopamine) coating of 3D printed poly(lactic acid) scaffolds for bone tissue engineering,” *Mater. Sci. Eng. C*, vol. 56, pp. 165–173, 2015, doi: 10.1016/j.msec.2015.06.028.

[37] B. Ashwin *et al.*, “3D-poly (lactic acid) scaffolds coated with gelatin and mucic acid for bone tissue engineering,” *Int. J. Biol. Macromol.*, vol. 162, pp. 523–532, 2020, doi: 10.1016/j.ijbiomac.2020.06.157.

[38] M. C. Echave, P. Sánchez, J. L. Pedraz, and G. Orive, “Progress of gelatin-based 3D approaches for bone regeneration,” *J. Drug Deliv. Sci. Technol.*, vol. 42, pp. 63–74, 2017, doi: 10.1016/j.jddst.2017.04.012.

[39] R. F. Cox, A. Jenkinson, K. Pohl, F. J. O’Brien, and M. P. Morgan, “Osteomimicry of mammary adenocarcinoma cells in vitro; increased

expression of bone matrix proteins and proliferation within a 3D collagen environment,” *PLoS One*, vol. 7, no. 7, 2012, doi: 10.1371/journal.pone.0041679.

[40] M. Du *et al.*, “3D bioprinting of BMSC-laden methacrylamide gelatin scaffolds with CBD-BMP2-collagen microfibers,” *Biofabrication*, vol. 7, no. 4, p. 44104, 2015, doi: 10.1088/1758-5090/7/4/044104.

[41] T. Zhang *et al.*, “Photo-crosslinkable, bone marrow-derived mesenchymal stem cells-encapsulating hydrogel based on collagen for osteogenic differentiation,” *Colloids Surfaces B Biointerfaces*, vol. 174, no. November 2018, pp. 528–535, 2019, doi: 10.1016/j.colsurfb.2018.11.050.

[42] S. V. Murphy, A. Skardal, and A. Atala, “Evaluation of hydrogels for bio-printing applications,” *J. Biomed. Mater. Res. - Part A*, vol. 101 A, no. 1, pp. 272–284, 2013, doi: 10.1002/jbm.a.34326.

[43] V. B. Morris, S. Nimbalkar, M. Younesi, P. McClellan, and O. Akkus, “Mechanical Properties, Cytocompatibility and Manufacturability of Chitosan:PEGDA Hybrid-Gel Scaffolds by Stereolithography,” *Ann. Biomed. Eng.*, vol. 45, no. 1, pp. 286–296, 2017, doi: 10.1007/s10439-016-1643-1.

[44] J. Malda *et al.*, “25th anniversary article: Engineering hydrogels for biofabrication,” *Adv. Mater.*, vol. 25, no. 36, pp. 5011–5028, 2013, doi: 10.1002/adma.201302042.

[45] J. A. Inzana *et al.*, “3D printing of composite calcium phosphate and collagen scaffolds for bone regeneration,” *Biomaterials*, vol. 35, no. 13, pp. 4026–4034, 2014, doi: 10.1016/j.biomaterials.2014.01.064.

[46] A. M. Pobloth *et al.*, “Mechanobiologically optimized 3D titanium-mesh scaffolds enhance bone regeneration in critical segmental defects in sheep,” *Sci. Transl. Med.*, vol. 10, no. 423, 2018, doi: 10.1126/scitranslmed.aam8828.

[47] V. V. Popov *et al.*, “Design and 3D-printing of titanium bone implants: brief review of approach and clinical cases,” *Biomed. Eng. Lett.*, vol. 8, no. 4, pp. 337–344, 2018, doi: 10.1007/s13534-018-0080-5.

[48] M. V. J. Braham *et al.*, “Endosteal and Perivascular Subniches in a 3D Bone Marrow Model for Multiple Myeloma,” *Tissue Eng. - Part C Methods*, vol. 24, no. 5, pp. 300–312, 2018, doi: 10.1089/ten.tec.2017.0467.

[49] H. Fairfield *et al.*, “Development of a 3D bone marrow adipose tissue model,” *Bone*, vol. 118, pp. 77–88, 2019, doi: 10.1016/j.bone.2018.01.023.

[50] H. J. Kim, U. J. Kim, G. Vunjak-Novakovic, B. H. Min, and D. L. Kaplan, “Influence of macroporous protein scaffolds on bone tissue engineering from bone marrow stem cells,” *Biomaterials*, vol. 26, no. 21, pp. 4442–4452, 2005, doi: 10.1016/j.biomaterials.2004.11.013.

[51] S. Kazemnejad *et al.*, “Biochemical and molecular characterization of hepatocyte-like cells derived from human bone marrow mesenchymal stem cells on a novel three-dimensional biocompatible nanofibrous scaffold,” *J.*

Gastroenterol. Hepatol., vol. 24, no. 2, pp. 278–287, 2009, doi: 10.1111/j.1440-1746.2008.05530.x.

[52] W. Tutak *et al.*, “The support of bone marrow stromal cell differentiation by airbrushed nanofiber scaffolds,” *Biomaterials*, vol. 34, no. 10, pp. 2389–2398, 2013, doi: 10.1016/j.biomaterials.2012.12.020.

[53] N. Thi Hiep, H. Chan Khon, N. Dai Hai, L. Byong-Taek, V. Van Toi, and L. Thanh Hung, “Biocompatibility of PCL/PLGA-BCP porous scaffold for bone tissue engineering applications,” *J. Biomater. Sci. Polym. Ed.*, vol. 28, no. 9, pp. 864–878, Jun. 2017, doi: 10.1080/09205063.2017.1311821.

[54] A. Sola *et al.*, “Development of solvent-casting particulate leaching (SCPL) polymer scaffolds as improved three-dimensional supports to mimic the bone marrow niche,” *Mater. Sci. Eng. C*, vol. 96, pp. 153–165, 2019, doi: 10.1016/j.msec.2018.10.086.

[55] Y. Liu, S. Wang, J. W. Lee, and N. A. Kotov, “A floating self-assembly route to colloidal crystal templates for 3D cell scaffolds,” *Chem. Mater.*, vol. 17, no. 20, pp. 4918–4924, Oct. 2005, doi: 10.1021/cm048050g.

[56] G. Kumar *et al.*, “The determination of stem cell fate by 3D scaffold structures through the control of cell shape,” *Biomaterials*, vol. 32, no. 35, pp. 9188–9196, Dec. 2011, doi: 10.1016/j.biomaterials.2011.08.054.

[57] V. M. Weaver *et al.*, “β4 integrin-dependent formation of polarized three-dimensional architecture confers resistance to apoptosis in normal and malignant mammary epithelium,” *Cancer Cell*, vol. 2, no. 3, pp. 205–216, Sep. 2002, doi: 10.1016/S1535-6108(02)00125-3.

[58] F. Wang *et al.*, “Reciprocal interactions between β1-integrin and epidermal growth factor receptor in three-dimensional basement membrane breast cultures: A different perspective in epithelial biology,” *Proc. Natl. Acad. Sci. U. S. A.*, vol. 95, no. 25, pp. 14821–14826, Dec. 1998, doi: 10.1073/pnas.95.25.14821.

[59] R. McBeath, D. M. Pirone, C. M. Nelson, K. Bhadriraju, and C. S. Chen, “Cell shape, cytoskeletal tension, and RhoA regulate stem cell lineage commitment,” *Dev. Cell*, vol. 6, no. 4, pp. 483–495, Apr. 2004, doi: 10.1016/S1534-5807(04)00075-9.

[60] R. Singhvi *et al.*, “Engineering cell shape and function,” *Science (80-.).*, vol. 264, no. 5159, pp. 696–698, Apr. 1994, doi: 10.1126/science.8171320.

[61] C. S. Chen, M. Mrksich, S. Huang, G. M. Whitesides, and D. E. Ingber, “Geometric control of cell life and death,” *Science (80-.).*, vol. 276, no. 5317, pp. 1425–1428, May 1997, doi: 10.1126/science.276.5317.1425.

[62] K. A. Kilian, B. Bugarija, B. T. Lahn, and M. Mrksich, “Geometric cues for directing the differentiation of mesenchymal stem cells,” *Proc. Natl. Acad. Sci. U. S. A.*, vol. 107, no. 11, pp. 4872–4877, Mar. 2010, doi: 10.1073/pnas.0903269107.

[63] H. Zhang and S. Hollister, “Comparison of bone marrow stromal cell behaviors on poly(caprolactone) with or without surface modification: Studies on cell adhesion, survival and proliferation,” *J. Biomater. Sci. Polym. Ed.*, vol. 20, no. 14, pp. 1975–1993, Oct. 2009, doi: 10.1163/156856208X396074.

[64] O. Chaudhuri, J. Cooper-White, P. A. Janmey, D. J. Mooney, and V. B. Shenoy, “Effects of extracellular matrix viscoelasticity on cellular behaviour,” *Nature*, vol. 584, no. 7822. Nature Research, pp. 535–546, Aug. 27, 2020, doi: 10.1038/s41586-020-2612-2.

[65] D. T. Butcher, T. Alliston, and V. M. Weaver, “A tense situation: Forcing tumour progression,” *Nature Reviews Cancer*, vol. 9, no. 2. Nat Rev Cancer, pp. 108–122, Feb. 2009, doi: 10.1038/nrc2544.

[66] C. Hahn and M. A. Schwartz, “Mechanotransduction in vascular physiology and atherogenesis,” *Nature Reviews Molecular Cell Biology*, vol. 10, no. 1. Nat Rev Mol Cell Biol, pp. 53–62, Jan. 2009, doi: 10.1038/nrm2596.

[67] D. E. Ingber, “Mechanobiology and diseases of mechanotransduction,” *Annals of Medicine*, vol. 35, no. 8. Donald Ingber, pp. 564–577, 2003, doi: 10.1080/07853890310016333.

[68] D. E. Discher, D. J. Mooney, and P. W. Zandstra, “Growth factors, matrices, and forces combine and control stem cells,” *Science*, vol. 324, no. 5935. Science, pp. 1673–1677, Jun. 26, 2009, doi: 10.1126/science.1171643.

[69] A. J. Engler, S. Sen, H. L. Sweeney, and D. E. Discher, “Matrix Elasticity Directs Stem Cell Lineage Specification,” *Cell*, vol. 126, no. 4, pp. 677–689, Aug. 2006, doi: 10.1016/j.cell.2006.06.044.

[70] K. Saha *et al.*, “Substrate modulus directs neural stem cell behavior,” *Biophys. J.*, vol. 95, no. 9, pp. 4426–4438, Nov. 2008, doi: 10.1529/biophysj.108.132217.

[71] B. Venugopal, P. Mogha, J. Dhawan, and A. Majumder, “Cell density overrides the effect of substrate stiffness on human mesenchymal stem cells’ morphology and proliferation,” *Biomater. Sci.*, vol. 6, no. 5, pp. 1109–1119, May 2018, doi: 10.1039/c7bm00853h.

[72] J. P. Winer, S. Oake, and P. A. Janmey, “Non-Linear Elasticity of Extracellular Matrices Enables Contractile Cells to Communicate Local Position and Orientation,” *PLoS One*, vol. 4, no. 7, p. e6382, Jul. 2009, doi: 10.1371/journal.pone.0006382.

[73] F. R. Maia, A. H. Lourenço, P. L. Granja, R. M. Gonçalves, and C. C. Barrias, “Effect of Cell Density on Mesenchymal Stem Cells Aggregation in RGD-Alginate 3D Matrices under Osteoinductive Conditions,” *Macromol. Biosci.*, vol. 14, no. 6, pp. 759–771, Jun. 2014, doi: 10.1002/mabi.201300567.

[74] M. J. Dalby *et al.*, “The control of human mesenchymal cell differentiation using nanoscale symmetry and disorder,” *Nat. Mater.*, vol. 6, no. 12, pp. 997–1003, Sep. 2007, doi: 10.1038/nmat2013.

[75] D. B. Burr, A. G. Robling, and C. H. Turner, “Effects of biomechanical stress on

bones in animals," in *Bone*, 2002, vol. 30, no. 5, pp. 781–786, doi: 10.1016/S8756-3282(02)00707-X.

[76] J. Wolff, *The Law of Bone Remodelling*. Springer Berlin Heidelberg, 1986.

[77] M. Hassanshahi, A. Hassanshahi, S. Khabbazi, Y. W. Su, and C. J. Xian, "Bone marrow sinusoidal endothelium: damage and potential regeneration following cancer radiotherapy or chemotherapy," *Angiogenesis*, vol. 20, no. 4. Springer Netherlands, pp. 427–442, Nov. 01, 2017, doi: 10.1007/s10456-017-9577-2.

[78] C. H. Wilkes and M. B. Visscher, "Some physiological aspects of bone marrow pressure," *J. Bone Jt. Surg. - Ser. A*, vol. 57, no. 1, pp. 49–57, Jan. 1975, doi: 10.2106/00004623-197557010-00009.

[79] M. V. Hillsley and J. A. Frangos, "Review: Bone tissue engineering: The role of interstitial fluid flow," *Biotechnol. Bioeng.*, vol. 43, no. 7, pp. 573–581, 1994, doi: 10.1002/bit.260430706.

[80] S. C. Cowin and L. Cardoso, "Blood and interstitial flow in the hierarchical pore space architecture of bone tissue," *J. Biomech.*, vol. 48, no. 5, pp. 842–854, Mar. 2015, doi: 10.1016/j.jbiomech.2014.12.013.

[81] I. Martin, D. Wendt, and M. Heberer, "The role of bioreactors in tissue engineering," *Trends in Biotechnology*, vol. 22, no. 2. Elsevier Ltd, pp. 80–86, 2004, doi: 10.1016/j.tibtech.2003.12.001.

[82] W. Mueller-Klieser, J. P. Freyer, and R. M. Sutherland, "Influence of glucose and oxygen supply conditions on the oxygenation of multicellular spheroids," *Br. J. Cancer*, vol. 53, no. 3, pp. 345–353, 1986, doi: 10.1038/bjc.1986.58.

[83] G. N. Bancroft *et al.*, "Fluid flow increases mineralized matrix deposition in 3D perfusion culture of marrow stromal osteoblasts in a dose-dependent manner," *Proc. Natl. Acad. Sci. U. S. A.*, vol. 99, no. 20, pp. 12600–12605, Oct. 2002, doi: 10.1073/pnas.202296599.

[84] A. S. Goldstein, T. M. Juarez, C. D. Helmke, M. C. Gustin, and A. G. Mikos, "Effect of convection on osteoblastic cell growth and function in biodegradable polymer foam scaffolds," *Biomaterials*, vol. 22, no. 11, pp. 1279–1288, Jun. 2001, doi: 10.1016/S0142-9612(00)00280-5.

[85] S. Weinbaum, S. C. Cowin, and Y. Zeng, "A model for the excitation of osteocytes by mechanical loading-induced bone fluid shear stresses," *J. Biomech.*, vol. 27, no. 3, pp. 339–360, Mar. 1994, doi: 10.1016/0021-9290(94)90010-8.

[86] T. A. Metzger, S. A. Schwaner, A. J. LaNeve, T. C. Kreipke, and G. L. Niebur, "Pressure and shear stress in trabecular bone marrow during whole bone loading," *J. Biomech.*, vol. 48, no. 12, pp. 3035–3043, Sep. 2015, doi: 10.1016/j.jbiomech.2015.07.028.

[87] P. Ole Iversen, E. Berggreen, G. Nicolaysen, and K. Heyeraas, "Regulation of extracellular volume and interstitial fluid pressure in rat bone marrow," 2001. Accessed: Mar. 26, 2021. [Online]. Available: http://www.ajpheart.org.

[88] R. J. McCoy and F. J. O'Brien, "Influence of shear stress in perfusion bioreactor cultures for the development of three-dimensional bone tissue constructs: A review," *Tissue Eng. - Part B Rev.*, vol. 16, no. 6, pp. 587–601, 2010, doi: 10.1089/ten.teb.2010.0370.

[89] E. J. Arnsdorf, P. Tummala, R. Y. Kwon, and C. R. Jacobs, "Mechanically induced osteogenic differentiation - The role of RhoA, ROCKII and cytoskeletal dynamics," *J. Cell Sci.*, vol. 122, no. 4, pp. 546–553, Feb. 2009, doi: 10.1242/jcs.036293.

[90] M. R. Kreke, W. R. Huckle, and A. S. Goldstein, "Fluid flow stimulates expression of osteopontin and bone sialoprotein by bone marrow stromal cells in a temporally dependent manner," *Bone*, vol. 36, no. 6, pp. 1047–1055, Jun. 2005, doi: 10.1016/j.bone.2005.03.008.

[91] N. N. Batra *et al.*, "Effects of short-term recovery periods on fluid-induced signaling in osteoblastic cells," *J. Biomech.*, vol. 38, no. 9, pp. 1909–1917, Sep. 2005, doi: 10.1016/j.jbiomech.2004.08.009.

[92] R. C. Riddle, A. F. Taylor, D. C. Genetos, and H. J. Donahue, "MAP kinase and calcium signaling mediate fluid flow-induced human mesenchymal stem cell proliferation," *Am. J. Physiol. Physiol.*, vol. 290, no. 3, pp. C776–C784, Mar. 2006, doi: 10.1152/ajpcell.00082.2005.

[93] M. Knippenberg, M. N. Helder, B. Zandieh Doulabi, C. M. Semeins, P. I. J. M. Wuisman, and J. Klein-Nulend, "Adipose Tissue-Derived Mesenchymal Stem Cells Acquire Bone Cell-Like Responsiveness to Fluid Shear Stress on Osteogenic Stimulation," *Tissue Eng.*, vol. 11, no. 11–12, pp. 1780–1788, Nov. 2005, doi: 10.1089/ten.2005.11.1780.

[94] G. M. Shivaram, C. H. Kim, N. N. Batra, W. Yang, S. E. Harris, and C. R. Jacobs, "Novel early response genes in osteoblasts exposed to dynamic fluid flow," *Philos. Trans. R. Soc. A Math. Phys. Eng. Sci.*, vol. 368, no. 1912, pp. 605–616, Feb. 2010, doi: 10.1098/rsta.2009.0231.

[95] Y. J. Li *et al.*, "Oscillatory fluid flow affects human marrow stromal cell proliferation and differentiation," *J. Orthop. Res.*, vol. 22, no. 6, pp. 1283–1289, Nov. 2004, doi: 10.1016/j.orthres.2004.04.002.

[96] L. A. McMahon, "The effect of cyclic tensile loading and growth factors on the chondrogenic differentiation of bone-marrow derived mesenchymal stem cells in a collagen-glycosaminoglycan scaffold," 2007.

[97] S. H. Park, W. Y. Sim, B. H. Min, S. S. Yang, A. Khademhosseini, and D. L. Kaplan, "Chip-Based Comparison of the Osteogenesis of Human Bone Marrow- and Adipose Tissue-Derived Mesenchymal Stem Cells under Mechanical Stimulation," *PLoS One*, vol. 7, no. 9, p. e46689, Sep. 2012, doi: 10.1371/journal.pone.0046689.

[98] J. Kim, H. Lee, Š. Selimović, R. Gauvin, and H. Bae, "Organ-On-A-Chip: Development and Clinical Prospects Toward Toxicity Assessment with an Emphasis on Bone Marrow," *Drug Saf.*, vol. 38, no. 5, pp. 409–418, May 2015,

doi: 10.1007/s40264-015-0284-x.

[99] G. S. Rosalem, L. A. G. Torres, E. B. de Las Casas, F. A. S. Mathias, J. C. Ruiz, and M. G. R. Carvalho, “Microfluidics and organ-on-a-chip technologies: A systematic review of the methods used to mimic bone marrow,” *PLoS ONE*, vol. 15, no. 12 December. Public Library of Science, p. e0243840, Dec. 01, 2020, doi: 10.1371/journal.pone.0243840.

[100] B. Carrion *et al.*, “Recreating the perivascular niche ex vivo using a microfluidic approach,” *Biotechnol. Bioeng.*, vol. 107, no. 6, pp. 1020–1028, 2010, doi: 10.1002/bit.22891.

[101] S. S. Kotha *et al.*, “Engineering a multicellular vascular niche to model hematopoietic cell trafficking,” *Stem Cell Res. Ther.*, vol. 9, no. 1, Mar. 2018, doi: 10.1186/s13287-018-0808-2.

[102] A. Marturano-Kruik *et al.*, “Human bone perivascular niche-on-a-chip for studying metastatic colonization,” *Proc. Natl. Acad. Sci. U. S. A.*, vol. 115, no. 6, pp. 1256–1261, Feb. 2018, doi: 10.1073/pnas.1714282115.

[103] D. B. Chou *et al.*, “On-chip recapitulation of clinical bone marrow toxicities and patient-specific pathophysiology,” *Nat. Biomed. Eng.*, vol. 4, no. 4, pp. 394–406, 2020, doi: 10.1038/s41551-019-0495-z.

[104] S. Sieber *et al.*, “Bone marrow-on-a-chip: Long-term culture of human haematopoietic stem cells in a three-dimensional microfluidic environment,” *J. Tissue Eng. Regen. Med.*, vol. 12, no. 2, pp. 479–489, Feb. 2018, doi: 10.1002/term.2507.

[105] J. Aleman *et al.*, “Deconstructed Microfluidic Bone Marrow On-A-Chip to Study Normal and Malignant Hemopoietic Cell–Niche Interactions,” *Small*, vol. 15, no. 43, pp. 1–13, 2019, doi: 10.1002/smll.201902971.

[106] Y. S. Torisawa *et al.*, “Bone marrow-on-a-chip replicates hematopoietic niche physiology in vitro,” *Nat. Methods*, vol. 11, no. 6, pp. 663–669, 2014, doi: 10.1038/nmeth.2938.

[107] Y. Torisawa *et al.*, “Modeling Hematopoiesis and Responses to Radiation Countermeasures in a Bone Marrow-on-a-Chip,” *Tissue Eng. Part C Methods*, vol. 22, no. 5, pp. 509–515, May 2016, doi: 10.1089/ten.tec.2015.0507.

[108] S. Sieber *et al.*, “Bone marrow-on-a-chip: Long-term culture of human haematopoietic stem cells in a three-dimensional microfluidic environment,” *J. Tissue Eng. Regen. Med.*, vol. 12, no. 2, pp. 479–489, 2018, doi: 10.1002/term.2507.

[109] M. R. Nelson, D. Ghoshal, J. C. Mejías, D. F. Rubio, E. Keith, and K. Roy, “A multi-niche microvascularized human bone marrow (hBM) on-a-chip elucidates key roles of the endosteal niche in hBM physiology,” *Biomaterials*, p. 120683, Jan. 2021, doi: 10.1016/j.biomaterials.2021.120683.

[110] A. Bruce *et al.*, “Three-Dimensional Microfluidic Tri-Culture Model of the Bone Marrow Microenvironment for Study of Acute Lymphoblastic Leukemia,” *PLoS*

One, vol. 10, no. 10, p. e0140506, Oct. 2015, doi: 10.1371/journal.pone.0140506.

[111] Y. Zheng *et al.*, “Angiogenesis in Liquid Tumors: An In Vitro Assay for Leukemic-Cell-Induced Bone Marrow Angiogenesis,” *Adv. Healthc. Mater.*, vol. 5, no. 9, pp. 1014–1024, May 2016, doi: 10.1002/adhm.201501007.

[112] W. Zhang, W. Y. Lee, D. S. Siegel, P. Tolias, and J. Zilberberg, “Patient-specific 3D microfluidic tissue model for multiple myeloma,” *Tissue Eng. - Part C Methods*, vol. 20, no. 8, pp. 663–670, Aug. 2014, doi: 10.1089/ten.tec.2013.0490.

II. Fabrication of 3D porous microenvironments

In this chapter, we will discuss the technological developments that have been performed for the design of in-*vitro* models. We will focus on the different combinations of material and methods used to fabricate 3D porous architectures.

First, we will provide a brief overview of the latest developments in the field of 3D fabrication, including the blooming of additive manufacturing and discuss the advantages and disadvantages of this technology for the construction of 3D architectures. Consequently, we will discuss the difficulties arising in the selection of materials, whose properties should be adapted to the fabrication method to achieve the resolution and complexity of 3D architecture while offering a sufficient biocompatibility to support cell culture. Then, we will present our developments using stereolithography fabrication techniques to generate designed 3D architectures and the characterization methods employed.

We will further analyze fabrication alternatives to additive manufacturing, such as the gas foaming or the use of emulsions. Despite a limited control of the 3D architecture and a poor control of the dimensional aspects, these free-form fabrication methods offer a practical alternative. Their simplicity, low-cost and versatility to create of porous scaffolds open the route towards soft and deformable materials that are not accessible through additive manufacturing. In particular, we will introduce a novel fabrication technique using a silicone-based biomaterial[e] non-compatible with additive manufacturing that will unlock the capacities of this material to achieve 3D cellular microenvironment [1].

---

[e] Biomaterial : *Material* exploited in contact with living tissues, organisms, or microorganisms [1].

Both routes, additive manufacturing or free-form fabrication, can provide similar topologies from the point of view of the cellular microenvironment yet differences in many other aspects such as adhesion and mechanical properties. Here, we will present the main differences between the additive manufacturing that offers an accurate control of the topography but restricted material choice versus a free-form fabrication that provides a larger material catalogue compatibility and that is more cost-effective.

1. Designed vs free-form architectures

In **Chapter 1**, we proposed an overview of the different aspects of the cellular microenvironment and their potential impact on the cellular behavior. One of the main cues to modify to obtain advanced *in-vitro* models is the topography, changing 2D cell culture supports into 3D architectures. Generating structures with overhanging architectures constitutes a challenge in terms of technological development and materials. In particular, suspended features weaken the structure and can potentially provoke the structural failure of the porous scaffold. In the last two decades, material scientists have strongly promoted the investigation of techniques and methods to generate complex architectures, opening a catalogue of alternative methods for different applications. These technologies are usually categorized by the material source or the kind of physicochemical processes carried out within them. This point of view presents the fabrication of 3D structures as a technological problem, which is useful when developing such techniques. In this work, we aim to go one step further and deal with the fundamental impact of the topological transitions happening when inducing these changes and we have decided to investigate two different approaches to fabricate the structures: designed architectures or free-form architectures.

a. Designed architecture: additive manufacturing

In the first category, we discuss most of technologies developed in the latest decades: additive manufacturing technologies[f]. These techniques involve the use of 3D digital models conceived by computer-aid design (CAD) to generate designed architectures which will be further exploited by an additive manufacturing system. For the purpose,

---

[f] Peter Zelinski, editor-in-chief of Additive Manufacturing pointed out in 2017 that the terms *additive manufacturing* and *3D printing* are used as synonyms in casual usage.

digital models are sliced to form layers of 2D patterns, and subsequently the 3D object is fabricated by piling one layer on top of the other, following the design.

This process presents the advantages of speeding up the development pace, reducing the time and cost of the process and unlocking certain shapes and structures that are often difficult to fabricate. This approach is thus well adapted to rapid prototyping. With the blooming of these manufacturing processes, a vast catalogue of fabrication technologies became available for the fabrication of 3D structures. **Figure 2.1** presents the main additive manufacturing technologies to this date. The large variety of 3D printing technologies with specific performances and associated materials has blurred the limits from one technology to another, overlapping certain systems and making a classification of those unclear.

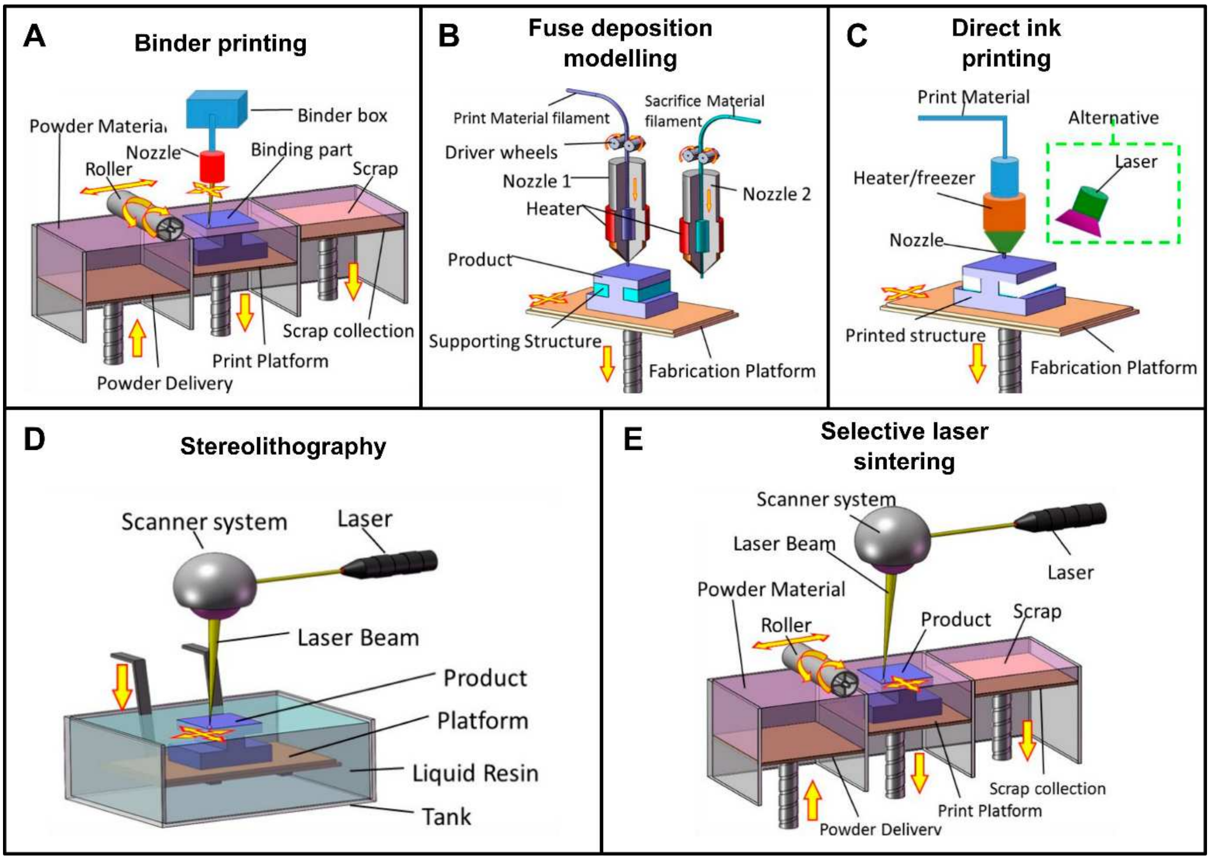

Figure 2.1. *Presentation of various additive manufacturing techniques.* ***(a)*** *Binder printing.* ***(b)*** *Fused deposition modelling.* ***(c)*** *Direct ink printing.* ***(d)*** *Stereolithography.* ***(e)*** *Selective laser sintering. Adapted from [1].*

As mentioned before, the additive manufacturing industry moves at high speed and it tends to combine different approaches to try to cope with the specific limitation of each technology. Here, we present the 5 main categories based on their approach to deposit material and form porous structures. There are several existing classifications depending on the purpose of the categorization such as material employed or applications targeted. In this manuscript, we are interested in comparing how technologies shape materials into 3D architecture, therefore this classification seems pertinent for this project.

- Binder jetting (BJ) is a powder-based technology in combination with an extruder binder [2], [3]. A roller lays down a powder layer that is solidified in a 2D pattern by extruding a liquid binder. Then, another layer of powder is added into the powder bed. The process is repeated sequentially until the 3D architecture is completed. Once concluded, the pieces are freed from the unsolidified powder [4]. Although, this technology is not as popular as other options, it allows large versatility in terms of materials. Ceramic [5] or sand [6] are the most common materials used with this technology, though it is also possible to use metals [7] or polymers [8]. The resolution of this technique will largely depend on the grain-size of the powder, ratio powder/binder and the capillary forces ruling the infiltration of the liquid in the powder. Though it is possible to fabricate porous architectures and suspended features, the typical resolution of these technologies is limited to ~200 µm [5], [9].
- Fused deposition modelling (FDM) consists in the controlled continuous deposition of a melted material, usually a thermoplastic. The material, presented as a thin filament rolled in a spool, passes through a heated printed extruder head. This brings the material temperature to a value above its glass transition temperature (T_g). The temperature, velocity, extrusion rate can be adjusted to regulate the width and height of the deposited material [10]. This is a popular technology among the 3D printer hobbyists with a large penetration in the home-market due to the low cost of the equipment available. In academia, extrusion printers have shined in versatility, allowing scientist to produce multiple home-made materials with less constraints than other technologies [11]. From the wide variety of materials available, we would like to highlight the value of acrylonitrile

butadiene styrene (ABS) [12], polylactic acid (PLA) [13], thermoplastic polyurethane (TPU) [14] and aliphatic polyamides (Nylon) [15]. FDM is one of the most extended technologies for macroscopic manufacturing and material catalogue. However, it presents resolution issues when engaging at sub-millimetric scale (>300 µm) and producing overhanging features [16].

- Direct ink writing (DIW) uses nozzles that directly extrude viscous materials over a fabrication platform to form the pattern defined by each sliced layer [17], that is then solidified by heat or light exposure [18]. A controlled deposition of the material imposes the need of a high viscosity to retain the shape after deposition. The main advantage of this technique is the wide catalogue of materials that are compatible with these techniques, ranging from composite materials [19], [20], to hydrogels [21] or even living cells [22]. Depending on those, a post-fabrication process might be needed to harden the material and improve the mechanical properties of the object. Generating porous architecture with this technology represents a technical issue that limits the inks to highly viscous materials [19], [20]. However, the loss of shape after deposition is notable and it commonly requires the use of supporting viscous liquids to host the architectures [23]. In terms of resolution, it has been possible to achieve high resolutions (~ 10 µm) when sacrificing the fabrication of suspended architectures [24].
- Selective sintering laser (SLS) is a powder-based additive manufacturing technique that uses a laser as a power source to selectively heat and sinter the powdered material [25]. The set-up of SLS is similar to the binder printer. A layer of powder is deposited on a platform and a laser sinters the powder into a solid pattern. Then, the platform moves down and another layer of powder is applied in order to repeat the process. When the object is finished, the powder left is removed from the piece. This technology allows the use of a wide range of materials as polymeric powders such as polyamides (PA) [26], polystyrenes (PS) [27] or thermoplastic elastomers (TPE) [28], or different ceramics [29], [30]. A sister technology, selective laser melting (SLM), was developed to be used with metal alloys by fully melting the metallic layer. The applications of SLS are mostly devoted to the

manufacturing of macroscopic and low-resolution structures (> 0.2 mm). The surfaces produced by SLS tend to display a high roughness related to the grain-size of the powder used and the sintering process.

- 3D Laser-assisted lithography techniques are additive manufacturing processes based on the photopolymerization, i.e., the solidification of a liquid polymer using a laser to bind together the polymeric chains. This sort of technologies is commonly grouped under the term stereolithography (SLA), yet they display certain technical differences between them (i.e., linear optics vs second-harmonic excitation). Typically, the liquid material is placed in a transparent vat, and a platform goes down to the bottom of the vat, until leaving a small gap that will corresponds to the thickness of the slice to print. Then, a laser in the UV spectrum draws the pattern within that slice and solidifies the layer. To conclude the iteration, the head will move vertically to a distance of a layer and the gap left behind will be refilled with the liquid polymer. The previous steps are then repeated to fabricate an additional layer. Once the process is completed, the parts are washed in a solvent to remove the excess of resin from the object. A post-treatment under UV light or controlled temperature is required to complete the polymerization of the material to reach its final properties. This additive manufacturing technique requires a higher investment than other systems. However, the resolution of such systems enables the realization of small features. Nowadays, a standard system can achieve < 5 μm features [31] and two-photon polymerization equipment are able to resolve submicrometric details [32], [33]. With the purpose of reducing the cost of these systems to target the hobbyist market, the industry has developed systems based on LCD masking or DLP projectors. In terms of materials, there is a large catalogue of resins available with different properties, that can be tuned by the addition of supplementary materials in form of powder to generate composites. However, the requirements in terms of viscosity sensitivity to UV/blue light largely limit the application of these materials, especially in the field of biomedicine [34]. This can be explained by the modifications in formulation required for classic materials to be photopolymerizable and sensitive to light dosing. Typically, additives potentially remain in the final structure and may have an adverse impact on the cellular physiology, requiring a finer development or post-treatment attempting to rinse harmful by-products. Laser-assisted technologies display the highest overall resolution to produce porous architectures with micrometric resolution (< 5 µm) [31] and achieving sub-micrometric resolutions in two-photon configurations [35].

b. Free-form structures

Although additive manufacturing technologies have provided a revolution in microfabrication and rapid prototyping, they present important drawbacks. Most of additive manufacturing approaches allow fabricating at millimetric or sub-millimetric scales down to submicrometric scale. This goes usually with a compromise in terms of time required to complete a structure with high level of detail. Furthermore, those systems tend to present limitations in the overall size of the object to fabricate. And, even if the large penetration of the 3D printers in the home-market has largely reduced the price of those equipment, the cost of high-resolution systems can be still elevated for certain applications.

The biological ambition of this project highlighted another challenge when working with additive manufacturing technologies: scarcity of cell culture validation in the literature of materials for biomedical applications. Even though much has been done to develop a catalogue of new materials for additive manufacturing, cell culture applications raise specific material requirements, not just in term of biocompatibility but also in term of biophysical properties discussed in **Chapter 1**. To cope with this limitation, alternatives technologies to produce porous architectures, even at industrial scale, have been used for few decades before additive manufacturing became a reality. These techniques are usually based on the use of a physicochemical property to generate cavities within a bulk material. In **Figure 2.2**, we gather the main free-form fabrication techniques used to produce porous architectures.

Here, we introduce some of these techniques than can be easily adapted to well-established biocompatible materials and can bypass the incertitude generated by chemically modifying the materials to adapt them to additive manufacturing.

- Gas foaming is an important technique widely used in the industry to produce foamed polymers [36], [37]. This process can be divided in three stages: first, the cavity formation results from the introduction of a gas into a molten or liquid polymer under specific conditions to produce a polymer/gas solution. When the amount of gas is large enough and overpass the supersaturation limit, the gas escapes from the solution and starts to generate cell nucleus within the polymer. Second, the cavity grows to balance the pressure of the gas inside the cell. Third, cells are stabilized by adding surfactants, cooling or solidifying the foam. Gas can be introduced in the liquid polymer mechanically, by stirring, or chemically, by chemical reactions happening within the polymer. This technique is compatible many different material, especially polymers such as poly(L-lactic acid) (PLLA) [38], poly(propylene carbonate) (PPC) [39] or polyurethane (PU) [40]. Between the most common uses of these porous structures is the fabrication of high-performance capacitors [41] or gas trapping [42].

- Sacrificial templating is an alternative widely used as a method to generate porous architectures and monoliths for several applications [43]–[45]. The method consists in using a specific material to generate a 3D structure in combination with a liquid material that can be solidified afterwards. This can mean a liquid polymer to be reticulated or a molten material that will resolidify. Another option is the use of solid composites with different sintering temperatures [46], [47]. This liquid material is cast over the structure, penetrating the cavities and then solidifies. Once this is achieved, the supporting structure must be dissolved, melted or burnt according to the nature of such material. Conventionally, it has been extended to the use of granular materials such as sugars or salts [48], [49], or the used of particles of targeted sizes [50]. These sacrificial templates can be fused together or left as isolated grains, giving rise to open-cells or closed-cells depending on the needs. With the arrival of cost-effective additive manufacturing techniques, industries have developed materials that are compatible with this 3D sacrificial templating [51]. The main inconvenient with this method is the potential residues that are left in the interface between both materials, from the sacrificial material or the solvent used for the leaching [45][52]. The main applications for such techniques are energy storage [43], [53], filtration [54] or chemical reaction enhancing [55].

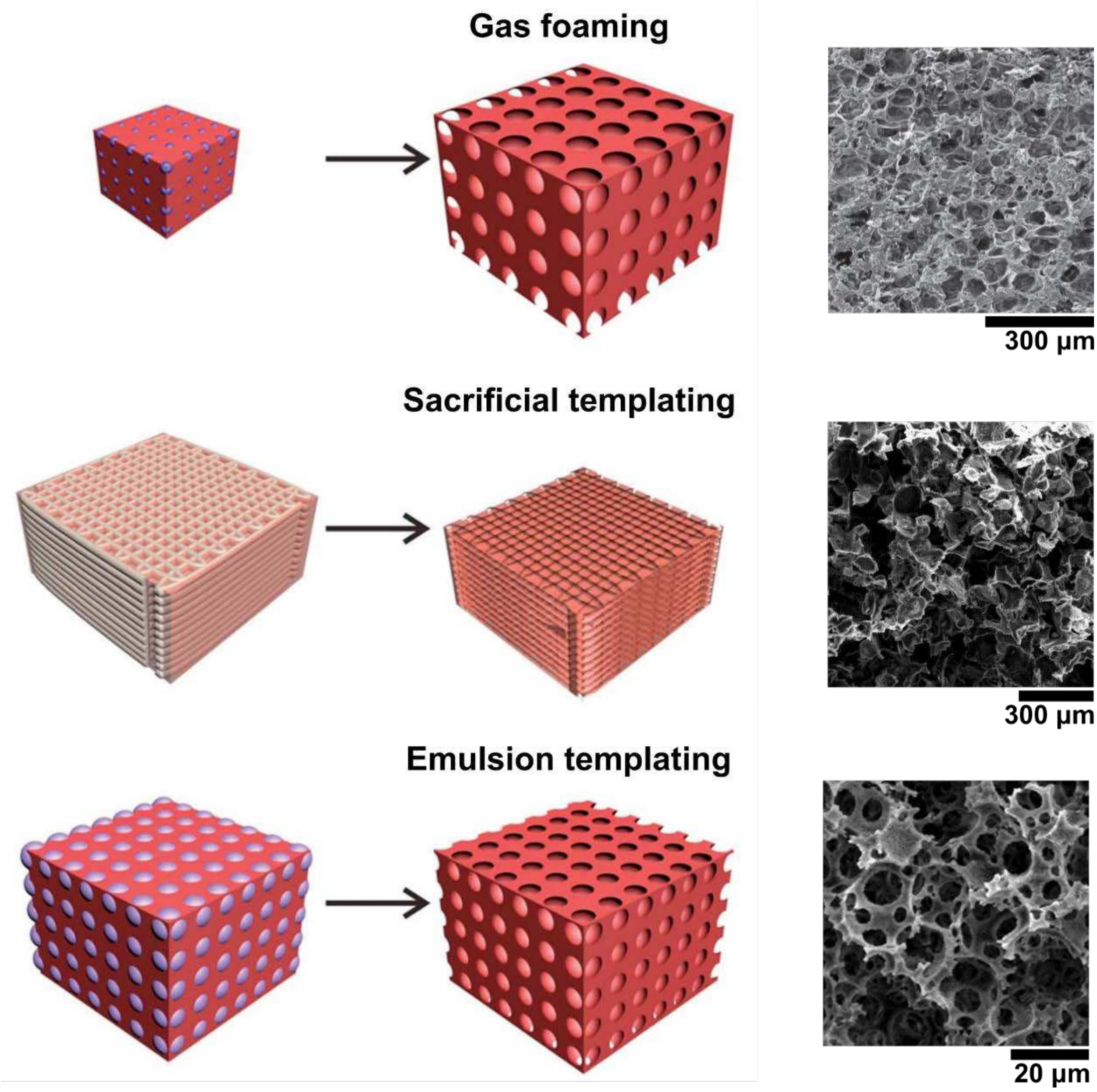

Figure 2.2. *Presentation of the main techniques to produce free-form 3D architectures.* ***(a)*** *Gas foaming.* ***Right.*** *SEM image of gas foaming monolith of poly(propylene carbonate).* ***(b)*** *Sacrificial templating.* ***Right.*** *SEM image of salt leaching PLA monolith.* ***(c)*** *Emulsion templating.* ***Right.*** *SEM image generated by polyHIPE in polystyrene. Adapted from* [39], [48], [56], [57].

- PolyHIPEs are porous emulsion-templated polymers synthesized within high internal phase emulsions (HIPEs). HIPEs are highly viscous emulsions, similar to pastes with an internal phase emulsion over 74% of the total volume. Once the continuous phase is polymerized, the left structure receive the name of polyHIPE [58], [59]. Emulsions with internal phases between 30% and 74% are denominated MIPEs, for medium internal phase emulsions, and lower than 30% are called LIPEs, for low internal phase emulsions. Nevertheless, the term HIPE is commonly used to refer to all emulsion-templated systems. There are often differences between the structure of the original HIPE and the resulting polyHIPE due to the process occurring during polymerization that alters the distribution and size of the droplets of the emulsion due to coalescence and/or ripping of the droplets. This is usually enhanced by the elevated temperatures or conditions of the polymerization. Depending on the conditions of the initial emulsions, interconnections or windows can appear in the thinnest points of the continuous phase, transforming discreate close-cell cavities into interconnected porous networks, open-cell pores. There is a myriad of applications where polyHIPEs show their values and versatility, especially when using biodegradable, thermo-responsive or pH-responsive materials. One of the most prolific applications is the used of polyHIPEs for membranes for chemical reactions [60], [61] and phase separations [62], [63], though the productions of composite polyHIPEs have opened the possibility of conductive foams to be use as pressure-sensor [64], [65].

c. Our approaches

In the last pages, we have analyzed the current situation of the technological scene regarding the fabrication of 3D architectures. We recognized the material selection as the largest constraint. Then, we have classified the different methods to fabricate 3D structures according the kind of architecture produced. Beyond of the topological characteristics of the structures lies the compatibility of the fabrication techniques with specific materials. Well-established and well-known materials usually require reformulations to achieve compatibility with additive manufacturing techniques. These reformulations of the material do not represent a major issue for the vast majority of applications, yet biocompatibility assays must be conducted when targeting biological applications. Cellular behavior is ruled by the delicate balance of the biophysical and biochemical cues found in the cellular microenvironment and minor modifications in the formulation of a material can drive large impacts on the physiology or the phenotype of cells.

In this chapter, we now present the technological developments that we have conducted to fabricate 3D architectures following the two previously described scientific approaches: additive manufacturing using a novel material, and the development of a novel free-form technique with a well-known material.

First, we focus on the additive manufacturing approach. Employing high-resolution stereolithography systems, we develop a 3D scaffold based on bone architecture obtained by X-ray micro-computed tomography (µCT) and fabricated with a photosensitive resin. Second, we present an alternative to stereolithography for 3D fabrication: a physical method that uses a well-known cell culture compatible material, polydimethylsiloxane (PDMS), to create a 3D porous architecture without chemical modification. This novel technique is based on emulsion templating. We produce a water-in-PDMS emulsion, with water droplets. The water in the emulsion acts as a porogen in a process in which PDMS is reticulated in two steps at low and high temperatures, compared to the boiling point of the water. The key feature of this process lies in the pressure-heat controlled environment that dictates the evaporation of the water droplets and the expansion of the steam with in the cavities of the PDMS monolith. This porous architecture was characterized by SEM and µCT and then biologically validated with SaOS-2 and MSCs spheroids. The results of this work were published in 2019 [66].

Biological results corresponding to the 3D architectures presented here, additive manufactured or free-form fabricated, will be discussed in **Chapter 3.**

2. Stereolithography: designed architecture

a. Digital trabecular microarchitecture

The starting point of this thesis is to produce a 3D structure to mimic the trabecular bone where bone marrow is located. Then, use this architecture to culture cells in a 3D microenvironment and observe the viability of the culture. In this section, we discuss the fabrication of this structure by stereolithography techniques using digital models. We were able to build on the group past experience reproducing the trabecular bone porous morphology for instrumentation purposes (**Figure 2.3**) [67]. Previous work of our team studied the structural characteristics and mechanical properties of the spongy bone by ultrasound propagation, in order to establish a better protocol to diagnose osteoporosis[g].

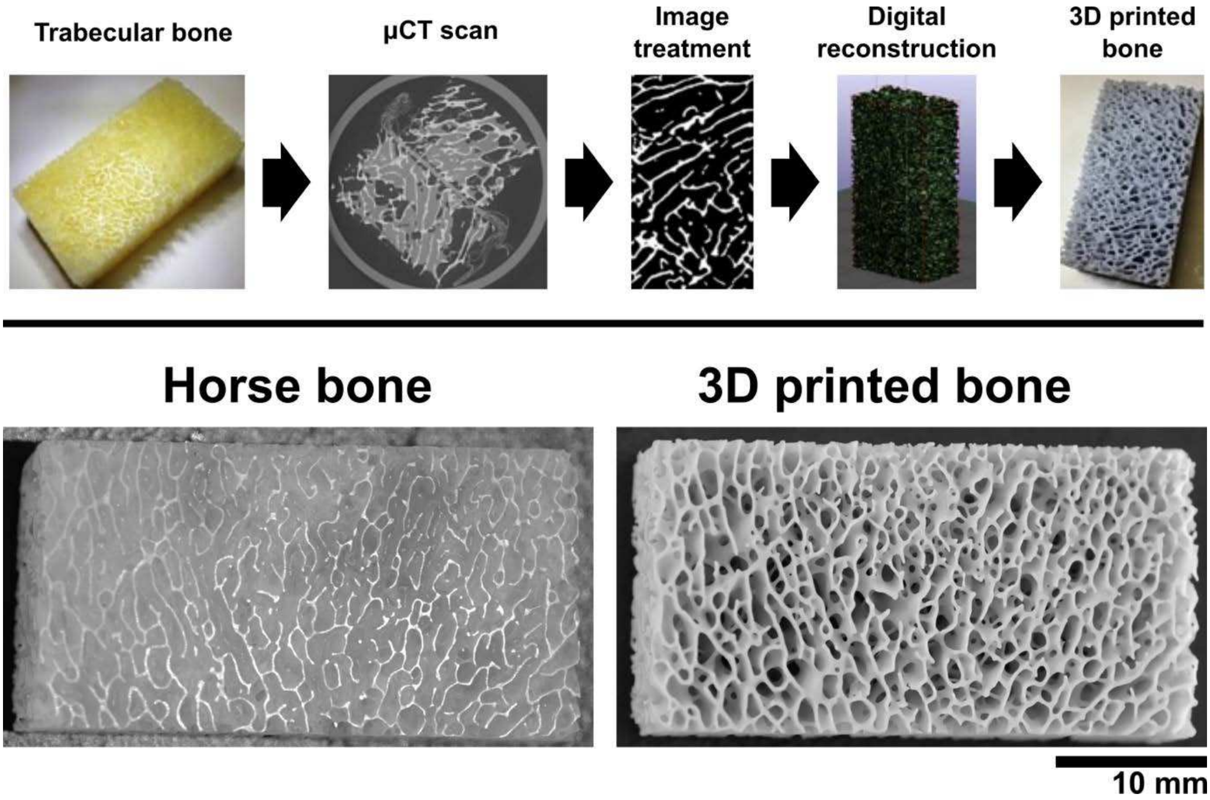

Figure 2.3. *3D printing of a spongy bone replica. A trabecular bone portion from a horse knee cap was sectioned into a tetrahedron volume of* $20 \times 25 \times 30\ mm^3$ *and characterized by μCT.* ***Up.*** *Sequence of steps followed to fabricate the bone replica: from the biological decellularized sample to the 3D printed object.* ***Down.*** *Optical imaging comparison of the biological sample and the resulted 3D printed trabecular bone architecture.*

The authors employed X-ray micro-computed tomography (μCT) in order to precisely reproduce the complex topology of the spongy bone sample of $38.0 \times 33.3 \times 13.9$ mm in a 3D digital model. Then, a realistic replica of the trabecular bone monolith was fabricated using a commercial resin, DL260. The trabecular structure was obtained by propagation phase contrast synchrotron microtomography (PPC-SR-μ-CT) from the ID19 beamline of the European Synchrotron Radiation Facility (ESRF, Grenoble, France) using a filtered-pink beam[h] with a total integrated energy of 110 keV. The distance sample-detector was 14 m and 1200 radiographs were acquired over 360º

---

[g] Osteoporosis is a bone disease occurring by the excess loss of mineralized bone, which thin the architecture that turns and fragile, leading to frequent fractures with minor bumps.

[h] Pink mode refers to an alternative monochromatic beam which substitute the monochromator by a grazing incidence mirror that reflects energies below a certain threshold.

with 0.15 s between them. Radiographs were recorded with a 1x optical setup and a FReLoN 2K camera with an isotropic voxel dimension of 12.64 µm. In order to obtain a 3D reconstruction from the angular projection radiographs, a modified Paganin algorithm was applied using the software PyHST2 and then the obtained images in the *XYZ* axis were binarized to isolate the mineralized bone from the bone marrow or air gaps and converted into the standard STL file for 3D printing. The 3D printed bone was fabricated with a stereolithography system DWS 028J+ from DWS Systems (Italy) using the PRECISA DL260 photosensitive ceramic composite material, which exhibits similar mechanical properties to bone (**Table 2.1**).

Table 2.1. *Density ρ, longitudinal (c_L), and transverse (c_T) speeds of sound. Trabecular bone values from* [67], [68].

	ρ (g cm^{-3})	**c_L (mm µs^{-1})**	**c_T (mm µs^{-1})**
Bone	2.05	4	1.8
DL260	1.338 ± 0.004	2.49 ± 0.05	1.21 ± 0.02

Ultrasound measurements were performed in the real bone and the replica in order to study their propagation and evaluate the accuracy of the 3D printed reproduction. These results show 3D printed architectures displaying a similar behavior than natural bone. This presents additive manufacturing as a robust and accurate technique to reproduce the complex porous microarchitecture of the trabecular bone 1:1 and replicate similar sound propagation properties. The authors concluded that this technology is mature enough to manufacture controlled architecture with bone-like realistic features for diverse applications. In our case, we are able to mimic the structure of the trabecular bone. This architecture will provide us insights of how cells interact in a 3D microenvironment closer to the *in-vivo configuration* of the bone tissue.

b. Fabrication of the trabecular bone structure by stereolithography

For the reproduction of the 3D cellular microenvironment of a trabecular bone, the use of smaller template is preferable in order to reduce the quantities of cells and reagents used during the experiments. We subtracted a portion of the digital model obtained by µCT into a cylinder of 10-mm diameter and 4.5-mm height, a size compatible with the use of commercial bioreactors.

In **Chapter 1**, we provided an overview of the tissue architecture and impact of the topology on the cellular system. One of the key parameters regarding 3D structures is the surface available, where cells can adhere. The modification of the topography of a structure increases the surface available for cells to attach, which it is an important parameter to evaluate for architectures destinated to host cell colonies. We analyzed the cropped structure with the software Meshmixer, obtaining a porosity $\phi \sim 73.39\ \%$ and a surface available $S \sim 1238.56\ mm^2$. This is approximately the half of the surface of a standard petri dish of 55 mm in diameter.

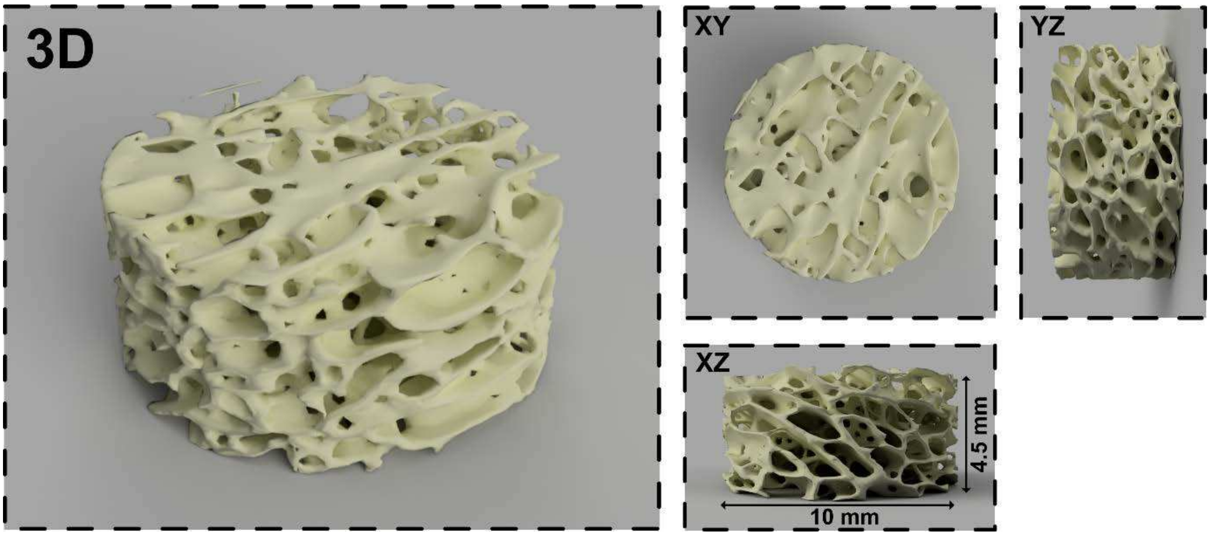

Figure 2.4. *3D digital model of the segmented portion of trabecular bone model. The dimensions of the cylinder are 10 mm diameter and 4.5 mm height, in order to be compatible with commercial bioreactor systems. Structural values: porosity, Φ ~ 73.39% and surface available, S ~1238.56 mm^2.*

The bone scaffold was fabricated in a stereolithography system DWS 029J+ using a biocompatible commercial resist, DS3000 (DWS Italy), which displays similar mechanical properties to trabecular bone. The laser-assisted stereolithography DWS 029J+ is a high-speed and high-precision system that combines a large printing volume $15 \times 15 \times 10$ cm^3, and employs a 405-nm laser at 6000 mm/s. The laser spot displays a diameter of 17 µm, which leads to an effective XY-resolution ~ 30-40 µm. The Z-resolution is determined by the movement of the vertical platform, giving a range of layer thickness ~ 10-100 µm. On the other hand, DS3000 is a Class I biocompatible resin also commercialized by DWS [69]. This material is devoted to the fabrication of implants for dental applications and displays mechanical properties similar to the mineralized bone such as tensile modulus ~ 2.0 – 4.0 GPa [31], [69]. The general protocol to fabricate digital models using a DWS 029J+ system is detailed in **Protocol 1**.

In order to reproduce accurately the features of complex structures, it is fundamental to control the printing parameters and to take certain precautions. The first layers of the fabrication process are key to secure the adhesion of the polymer to the printer

Protocol 1. Standard 3D Fabrication with DWS 029J+

General protocol and recommendation for the fabrication of 3D object by stereolithography with DWS 029J+ system. We assume the head platform and the resin tank have been previously z-calibrated. **Information remark:** *XY*-resolution = 30-40 µm, z-resolution = 10-100 µm.

1. Open NAUTA software and load the STL design
2. Select the XYZ-tilting orientation and the place of the object in the platform. Centered position is recommended. XYZ-tilting orientation will compromise the resolution of certain smooth surfaces due to the resolution anisotropy yet help to relax potential strain between parallel surfaces for same reason.
3. Set the support based to ensure the adhesion of the object in the platform. Usually 2-mm height pillars and a homogeneous base of 0.5-mm thick are enough. The diameter of the pillars, and the breaking point and strength will depend largely on the mechanical properties of the resins employed.
4. Save project and process into a FICTOR file
5. Open FICTOR and load the FICTOR file
6. Select the resin chosen for the work and place the parameters selected. Commonly, first layers of the based are overexposed at low speed and large thickness. The following layers containing the pillars will be partially overexposed at medium speed. Run the printing
7. Once finish, remove the platform head and with a spatula/blade detach the piece from the surface. Breaking the pillars to remove the piece and then detach the base would simplify the process.
8. Rinse the piece with Ethanol/Isopropanol for about 30 min. If the piece present cavities/porosity, 15-min ultrasound bath is encouraged.
9. Air-dry the sample and post-treat it with 15-min UV.

head. Therefore, they are typically overexposed, losing all trace of detailed elements in XY-plane and the possibility of fabricating overhanging features. To avoid the overexposure of the first layers of the structure which results in the clogging of one of the sides of the porous structure, it is required to add an overexposed base of a few hundred microns thick (in our case, $h = 500\ \mu m$). On the surface of the base, and supporting the structure, we locate several straight pillars ($d = 0.7\ mm$, $h = 1\ mm$) that will create a gap between base and structure and assure the correct porosity of the structure. These precautions will ensure the reproducibility of the printing process while the fragility of the pillars will allow us to remove the base and release the integral bone scaffold.

The fabrication of overhanging structures can be a challenge in terms of resolution and resin residue removal. The distribution of dose[i] is thus critical as it affects the *xy*-resolution (overexposing the structure induces an increase of the lateral dimensions of a given structure). The intensity of the laser may also affect the thickness of overhanging structures which is strongly dependent to the penetration of the laser beam and thus to the transparency of the material. It is common then, to increase the laser speed or vary the laser power in order to modify the dose received by the resin and therefore, to reduce the effect of overexposure. Another option is to modify the indentation (xy-offset) or the z-compensation (z-offset) in order to digitally compensate for the laser penetration and the over exposure of hollow cavities, in *xy*-plane or *z*. The reduction of the number of contours decreases as well the overexposure, leading to a better resolution with a slightly rougher surface. Clogged features are also common when distance between them is reduced, due to the capillary forces. This is one of the largest limitations regarding the use of stereolithography for the fabrication of microfluidics chips.

In **Figure 2.5**, we can observe a characterization of the DS3000 printed bone structure, with the detailed protocol presented in **Protocol 2**. An optical image of the printed scaffold can be observed in **Figure 2.5A**. Although the material is translucid yellow color under visible light, we used UV light to better observe the features of the structure benefiting of the photoluminescence of the DS3000. The apparent opacity that we can

---

[i] Dose: common for *Exposure energy,* it is equal to the light intensity times the exposure time.

observe in the structure is due to the rugosity of the surfaces of the structure typical of 3D printed object, caused by the slicing process and the repeated laser paths. In **Figure 2.5B**, there is a 30-degree tilted SEM image of the structure (Hitachi S-3700), where we can observe the complexity of the bone microarchitecture fabricated over the pillars and the base. **Figure 2.5C-D** shows a XY-view and close-up of the 3D printed bone replica. Using a high-resolution S-4800 Hitachi SEM, we show the large magnification and higher resolved images of the structure. In these images, we observe the overhanging struts produced in the bone microarchitecture and the higher heterogeneity of the scaffold.

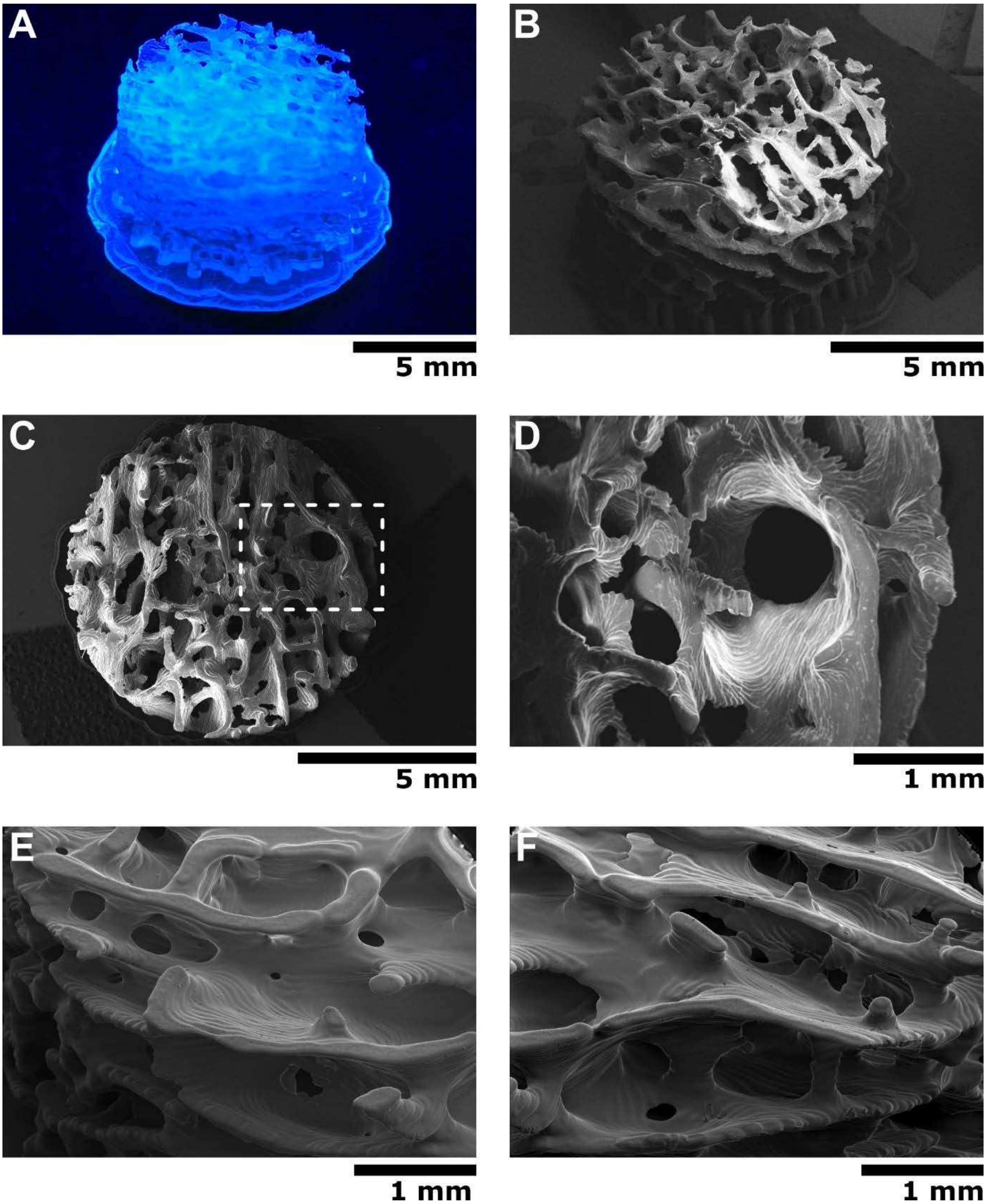

Figure 2.5. *3D printed trabecular bone microarchitecture reproducing the bone structures.* ***(a)*** *Optical micrograph of the 3D printed scaffold. SEM images taken with low vacuum system Hitachi S-3700:* ***(b)*** *30-degrees tilted image showing the porous structure of the bone replica.* ***(c)*** *Upper XY plane of the printed replica.* ***(d)*** *close-up view of the white dashed squared region in (c). High-resolution SEM images taken with a high-vacuum system Hitachi S-4800N:* ***(e)*** *and* ***(f)*** *30-degrees titled images depicting the overhang struts and the different pore sizes of the 3D printed trabecular bone microarchitecture.*

Protocol 2. Fabrication of 3D printed Trabecular bone microarchitecture

We will assume previous knowledge described in **Protocol 1** around the system. This protocol focuses on the fabrication of the 10-mm diameter and 4.5-mm thickness bone scaffold DS3000 resin.

1. Once placed the bone microarchitecture STL in NAUTA, manually add pillars in the down-plane XY. Fix the pillar diameter at 0.6-mm and 2-mm height, the number of pillars should be around 20. Add a base of 0.5-mm
2. Save the project and create the FICTOR file
3. In FICTOR software, add the FICTOR file and fix the material in DS3000. Modify the appeared default configuration:

Blocks:	✓ 1	✓ 2	✓ 3
To Z	0.200	1.500	0.000
Layers	4	25	∞
Slice	0.050	0.050	0.020
Contours Number	3	3	1
Indentation	0.020	0.020	0.020
Hatching	0.070	0.070	0.030
Ops	↑ ↓	✓ ↑ ✓ ↓	✓ ↑ ✓ ↓
TTT	✓	✓	✓
Z Compensation	0.120	0.120	0.120
Laser Speed	200	2800	5800

4. Once the fabrication process is finish, detach the sample using a razor blade and remove the pillars and base
5. Deep the scaffolds in a 10-mL falcon with ethanol and sonicate for 15 min. Then air-dry the sample
6. Post-process the samples for 15 min under UV light

c. Summary

- We have used the previous knowledge on trabecular bone characterization developed within the team to obtain a digital model of the spongy bone architecture.
- The digital model was prepared and adapted to our experimental needs, reducing the structure to a total cylindrical volume of 10-mm diameter by 4.5-mm height.
- The scaffold was printed and structurally analyzed, showing a porosity of Φ ~ 73.39% and a surface available for cell attachment of S ~ 1238.56 mm.
- We characterized in detail the resulting scaffold with electron microscopy and optical imaging, showing the photoluminescence of the material in the process.

3. Porous PDMS: Water-in-PDMS emulsion

a. An introduction to PDMS

As mentioned at the beginning of the chapter, the search of a suitable material for tissue engineering is mainly defined by both technological aspects and biocompatibility constraints imposed by the cellular models. Most of the actual research in the field is carried out by looking new formulations of brand-new materials with capacities to generate 3D architectures and then, testing their capabilities as biocompatible material. Here, we address the issue by taking a long-established renown biomaterial and modifying the standard reticulation protocol to structure it into a 3D architecture.

Polydimethylsiloxane (PDMS) is widely known silicone-based material with multiple applications. Discovered by Wacker Chemie in the 1950s, this organic elastomer has proved its capabilities in large range of applications such as isolation and protection of electronic circuits [70], [71], flexible electronics [72], [73], energy storage [74] or piezoelectrical actuators [75], [76].

Polydimethylsiloxane belongs to the class of inert semi-organic polymers called polysiloxanes, being the simplest silicone chain possible with a $-[Si(CH_3)_2O]-$ as the monomeric base. This formulation is the common structure of a siloxane macromolecule, with a chain composed of alternating Si and O atoms and two $-CH_3$ methyl groups linked to the silicon atoms. Due to their low reactivity, methyl groups are replaced to enable the crosslink by more reactive functions such as $–CH=CH_2$ vinyl groups or hydrogen atoms. Both terminations react with one another under the presence of a catalyst such as platinum and crosslink into a reticulated network (**Figure 2.6**).

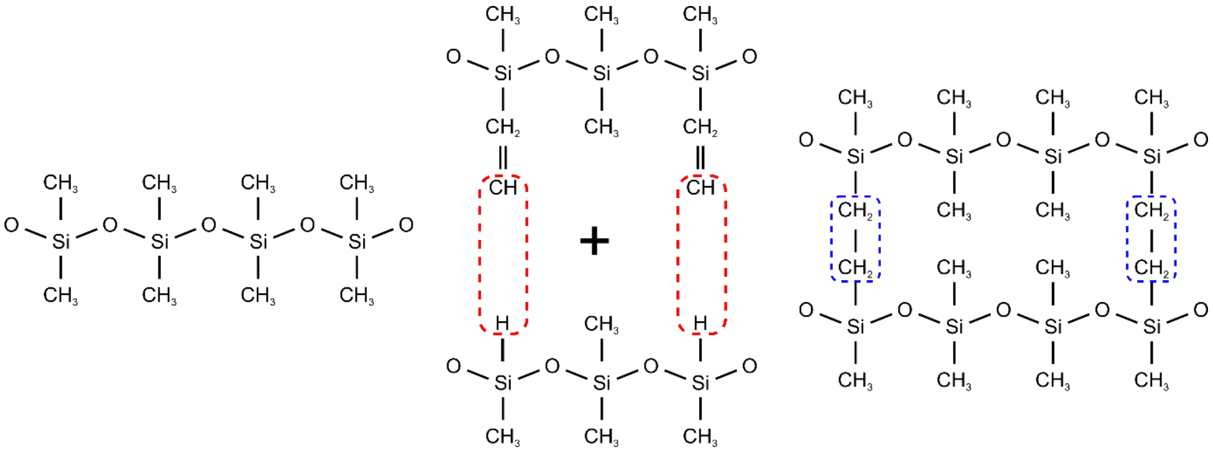

Figure 2.6. *Simplified chemical diagram of the silicone chains and their modifications to give rise to a reticulated network.*

PDMS has shined due to its medical grade formulations as a transparent biocompatible material in medical devices or contact lenses. In 1998, George M. Whitesides demonstrated the capabilities of PDMS to reproduce micropatterns from master molds [77], proving its adequacy for rapid prototyping. Nowadays, it is broadly used in academic research and industries despite its limitations [78]. PDMS has become notably popular due to its capabilities of patterning molecules down to the nanoscale by microcontact printing.

Microfluidics is possibly one of the fields where PDMS is more dominant as main benchtop technique for the fabrication of cost-effective disposable devices. Microfluidics consists in the precise control and manipulation of fluids in spatially constrained environments, often in the micrometric scale. It presents large practical applications in engineering, chemistry, biology or nanotechnology due to the reduced volumes of fluids, the multiplexing and automation capabilities, and possibility of using high-throughput screening techniques.

PDMS is optically clear and in general chemically inert and non-toxic [79]. Furthermore, it is permeable to gases which is a key feature for cell culture applications due to the need of oxygenating the cell culture medium [80]. Though it is a hydrophobic material, its surface properties can be tuned by oxidizing the surface via plasma or chemical treatment, to introduce hydroxyl groups on the surface. The surface activation allows the grafting of proteins and diverse functional groups, improving cell adhesion [56]. For those reasons, it has become a popular material broadly use in many biological applications, especially in microfluidic devices [81], [82].

b. Generating porous structures with liquid polymers: polyHIPEs

The goal of this work is to structure PDMS to obtain a 3D porous architecture that can mimic the trabecular bone microarchitecture with a certain degree of control. Conventional PDMS can only be used in stereolithography after chemical modification [83]. As previously described at the beginning of this chapter, a large community of chemists and material scientists have worked for years and found solutions to create porous structures from the vast majority of polymer using emulsions [59], [84], gas foaming [36], [37] or the use of sacrificial materials [43]–[45].

The technique developed in this work is based in the so-called polymeric High Internal Phase Emulsions (polyHIPE) [85]. As a reminder from the introduction, those are emulsions that contain an internal phase with a volume greater than 74% of the total volume of the mixture which is the volume represented by the maximum occupancy of packed regular spheres. For most of the systems, the phase reversion occurs close to this value. Of course, this view is just a model and presents its limitations, as the size of the droplets in a real emulsion tends not to be monodisperse, yet it helps to illustrate the concept behind it.

Most porous structures generated using porogens tend to use sacrificial materials to generate cavities. In order to obtain a connected network pores, the sacrificial forms a continuous structure generated by additive manufacturing, crystallization or melting. Once the casted material is solidified, the porogen is dissolved or burnt to obtain the porous structure. Casting and molding polyHIPE to obtain porous structures is possible by interpretating the use of the internal phase as a porogen[j], as shown in **Figure 2.7**.

---

[j] Porogen: any material, solid or not, used to generate pores in molded structures when removed afterwards, usually by dissolution.

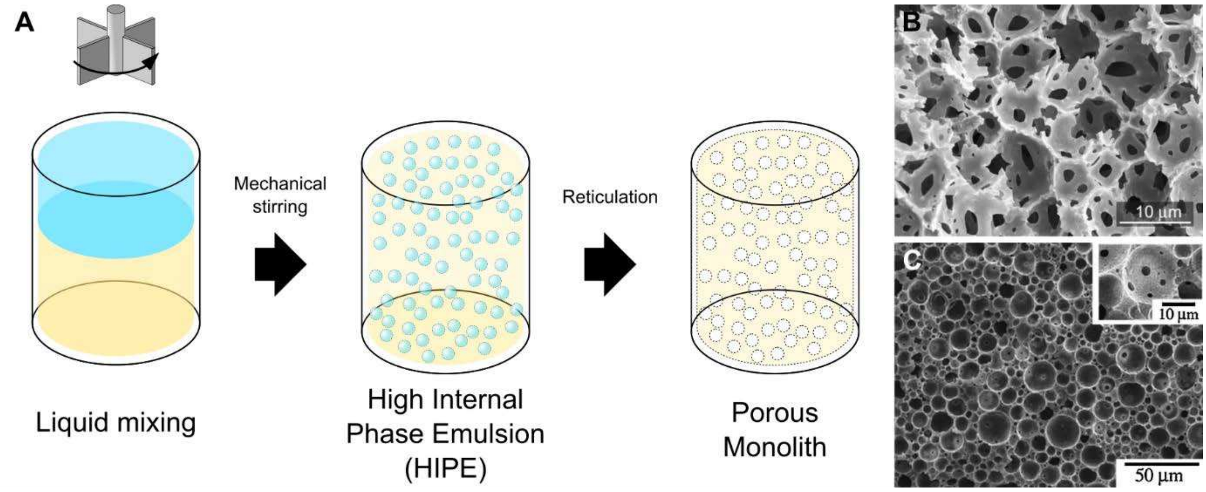

Figure 2.7. (a) *Schematic illustration of the formation of a polyHIPE.* ***(b-c).*** *SEM images depicting a typical porous polyHIPE structure generated by HIPE. Adapted from* [86] *and* [87].

This consists in the removal of the internal phase once the polymer which consititudes the continuous phase has became solid. The removal of the internal phase is linked to the nature of the porogen, for sacrificial material is mainly disolution or burning [52], [88]. For most of polyHIPEs the exchange of chemical species and a drying step are required to extract the internal phase and then to remove potential residues [89], [90]. The sort polyHIPEs porous architectures depends on the chemical properties of the phases and their interactions at the interfaces.

The main challenge to overcome while using polyHIPE to generate a porous monolith is to create open-cells or porous networks. By definition, a polyHIPE requires isolated droplets of internal liquid phase which that lead to isolated cavities as pores, i.e., close-cell porous architecture. The consequence of overpassing the limit of internal phase is the phase separation due to the coalescence of the liquid droplets. Considering such definition, most of the polyHIPEs result in close-cell porous architectures. The chemical properties of the emulsion, or more specific, the surfactant concentration at the inteface plays a major role when determining the obtained structure. For instance, Williams et al. proved that in water-in-oil emulsions of styrene/divinylbenzene/water could be used to tune the interconnectivity of the porous network by changing the concentration of sorbitan monooleate [91]. Concentrations under 5% would give rise to close-cells while a mild variation to 7% would interconnect the entire structure. This is due to a decrease in the quantity of material needed to isolate the droplet as results of the changes on the inferace of the phases. This leads to a reduction of the distance droplets tend to connect during the solidification of the polymer.

For a deeper explanation on HIPEs, the author recommends to read the chapter of N. R. Cameron and D. C. Sherrington, *High internal phase emulsions (HIPEs) — Structure, properties and use in polymer preparation*, in the book *Biopolymers Liquid Crystalline Polymers Phase Emulsion* [85].

c. Porous PDMS via Water-in-PDMS emulsion

In the coming pages, we will show an innovative alternative to perform this transition from closed-cell to open-cell architecture without the need of any additional surfactants. Our contribution constitudes a novel disruptive approach which erase one of the main concern for the application of polyHIPEs for tissue engineering, which is the chemical residues. Our proposal is the use of the thermodynamical properties of water steam during evaporation in combination with a thermo-curable polymer to generate our polyHIPEs. The silicone formulation used for this work as the continuous phase in our polyHIPEs is the popular kit *Sylgard 184* commercialized by *DOW Corning*. This is a bi-component pack with a silicone-base and a hardener that starts a thermal reaction when combined. The standard protocol to fabricate bulk PDMS is collected in the **Protocol 3**.

In our porous PDMS fabrication protocol, water acts as the internal phase of the emulsion, generating the porosity of the monoliths. The idea behind using water as porogen resides in the simplicity of removing water without any residues. As commented at the beginning of this chapter, one of the major challenges when talking about novel biomaterials, is achieving biocompatibility levels. When using a porogen to generate such architectures, there is always a risk of leaving residues at the interface between both phases/materials. These unwanted residues could compromise the proven convenience of PDMS for cell culture.

Protocol 3. Manufacturer recommendation for Sylgard 184 fabrication

Manufacturer instructions for the fabrication bulk PDMS from the bi-component kit Sylgard 184 provided by DOW Corning.

1. Calculate the volume of bulk PDMS required, $\boldsymbol{V_{PDMS}}$
2. In a disposable container, weight the volume of silicon-base need for the final amount ($\rho_{PDMS} = 0.996 \sim 1$, therefore $V \sim m$)

$$\boldsymbol{V_{base} = \frac{10}{11} \times V_{PDMS}}$$

3. Add the needed proportion of hardener to the container, recommended used of a pipette

$$\boldsymbol{V_{had} = \frac{1}{11} \times V_{PDMS}}$$

4. Mix thoroughly the viscous solution, between 30 s and 2 min depending on the quantities
5. De-gas the mixture until no visible bubbles
6. Cast the silicone by pouring it in the selected mold. If bubbles can be observed after the casting, de-gas again
7. Follow the manufacturer recommendations to obtain fully reticulated bulk PDMS:

T (ºC)	Time recommended
25 (RT)	48h
100	35 min
125	20 min
150	10 min

The curing mechanism of Sylgard 184 is a thermal process triggered by the mixture of a pre-polymer with a crosslinker in an established ratio (10:1 w/w). The variation of this ratio has been reported to impact the Young's modulus of the obtained silicone material [86], [87]. In our case we, performed all the experiments with the recommended stoichiometry. The kinetics of this thermal-reticulation reaction is schematically illustrated in **Figure 2.8.**

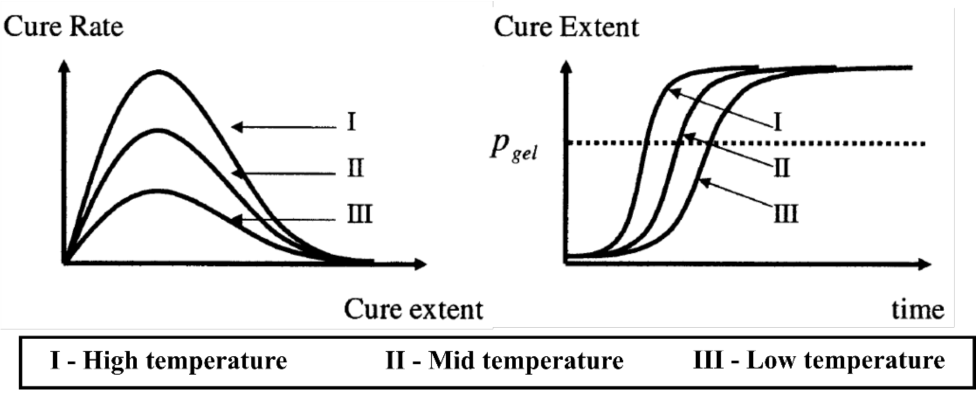

Figure 2.8. *Schematic illustration of the curing kinetics at (I) High, (II) Mid and (III) Low temperature regime. The increment of the temperature induces a gelation sooner and a faster transition to solid state. Adapted from* [94].

In **Figure 2.9**, we can observe a sketch of the fabrication process and crosslinking happening in the prepolymer. We can see how the transition from liquid to solid happens in a time window that it is controlled by the temperature of the baking process, that tunes the curing rate in which this is process take place.

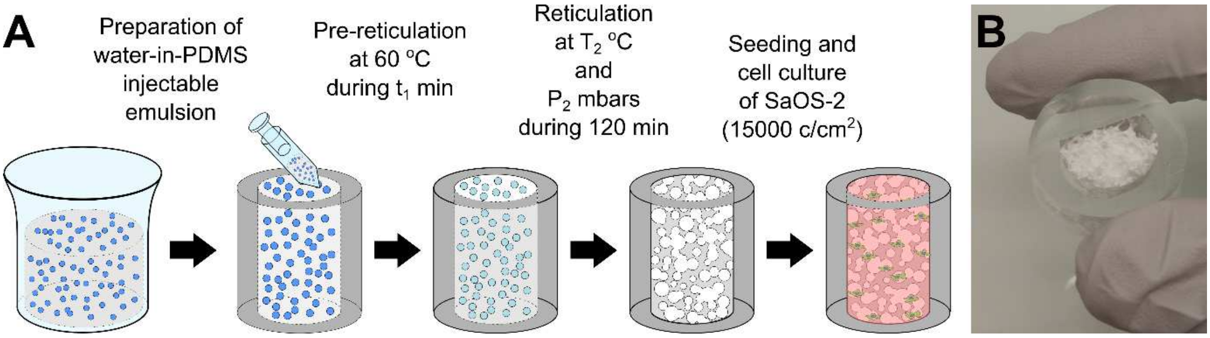

***Figure 2.9**. **(a)** Schematic illustration of the fabrication process of biological samples with a porous PDMS structure embedded in the center. It consists in a double baking using a standard oven and a pressure-controlled oven. The main parameters that will determine the final porosity are: **t_1**, duration of the first baking, fixed at **60 ºC** and **1 atm**; and for the second baking: **t_2**, duration; **T_2**, temperature and **P_2**, pressure. **(b)** Optical micrograph of the resulting sample.*

To overcome the limitations caused by the close-cell porous architecture typically generated with polyHIPEs without additional surfactants, we propose to use the thermodynamical properties of gas expansion during evaporation of a liquid. Water presents a boiling point at lower temperature compared to the temperature that PDMS can hold during reticulation (< 200 ºC) [95]. This allows us to use a temperature superior to the boiling point of water and to control the cure kinetics of the silicone at the same time. When the temperature overpasses 100 ºC during the curing process of the polyHIPE, water of the emulsion starts to boil and the generated steam increases the pressure in the former droplet cavity that starts to expand. This process competes with the crosslinking of the continuous phase, composed of pre-reticulated PDMS. By varying the state of gelation of the PDMS when water boils, we can control the steam expansion and hold this deformation of the droplet cavity. In order to have a better control on the gelation state of the PDMS, we introduce a previous curing step to trigger the crosslinking at 60 ºC, while the water remains in liquid state. This temperature permits a slow PDMS reticulation, proving a larger margin to select the reticulation point for the expansion step.

Therefore, we have indentified a double-step process in order to control the parameters of the fabrication of the porous monolith from a water-in-PDMS emulsion. We have fabricated porous samples, using a bulk hollow PDMS cylinder following **Protocol 4**. It consisted in using a 12-well multiplate with a 3D printed solid semi-cylinder to generate a semi-cylindrical cavity. The water-in-PDMS emulsion was cast into the cylindrical sample before reticulation and steam expansion. This format helped us to standardize the sample by respecting constant dimensions on the samples in order to characterize the obtained porosities during the optimization of the fabrication. Our ultimate target would be defining a set of conditions in which the porous monolith fabricated mimic the spongy bone architecture.

Protocol 4. Fabrication of Multi-well plate compatible sample

Designing the samples to make it compatible with standard cell culture consumable simplify certain aspect of the experimental manipulation and the sterilization steps. To obtain a cylinder with the dimensions of a 12-multiwell plate with an empty cavity in the center, we designed and 3D printed an object to be place in the holes of the plate once the PDMS has been cast in them.

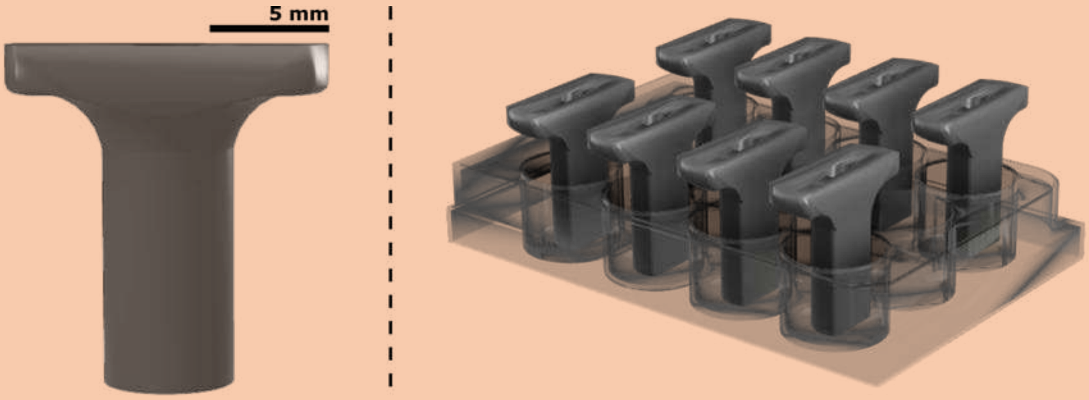

Protocol Figure 2.1. *3D view of the fabricated "puncher" object used to obtain a regular cavity in the 12-well cylindrical samples.*

1. Following the manufacturer indications for Sylgard 184 (10:1), weigh and mix the silicone-base and the hardener using a balance and degas the PDMS until no bubble is visible
2. Pour the liquid solution into the holes of the multiwell plate until half of their volume
3. Place the cylindrical piece in the center of each hole. Be sure to touch the bottom of the hole. If bubbles were generated during the process, remove them using a Pasteur pipette
4. Put the multi-well plate in the tray of the oven at 60 ºC
5. Add few drops of isopropanol/ethanol on the top of the reticulated PDMS cylinder. With the help of a flat spatula, detach the PDMS from the multi-well plate by pushing the spatula in between the surfaces. This will introduce the solvent which will act as lubricant and will allow you to remove the sample
6. Repeat the process with the spatula and the solvent to remove the 3D printed cylinder from the sample

d. Understanding the physico-chemical process of generating porous PDMS

In the **Figure 2.10**, we illustrate the physico-chemical process happening during this two-step fabrication procedure. The step-by-step protocol for the fabrication of the porous PDMS is described in **Protocol 5.**

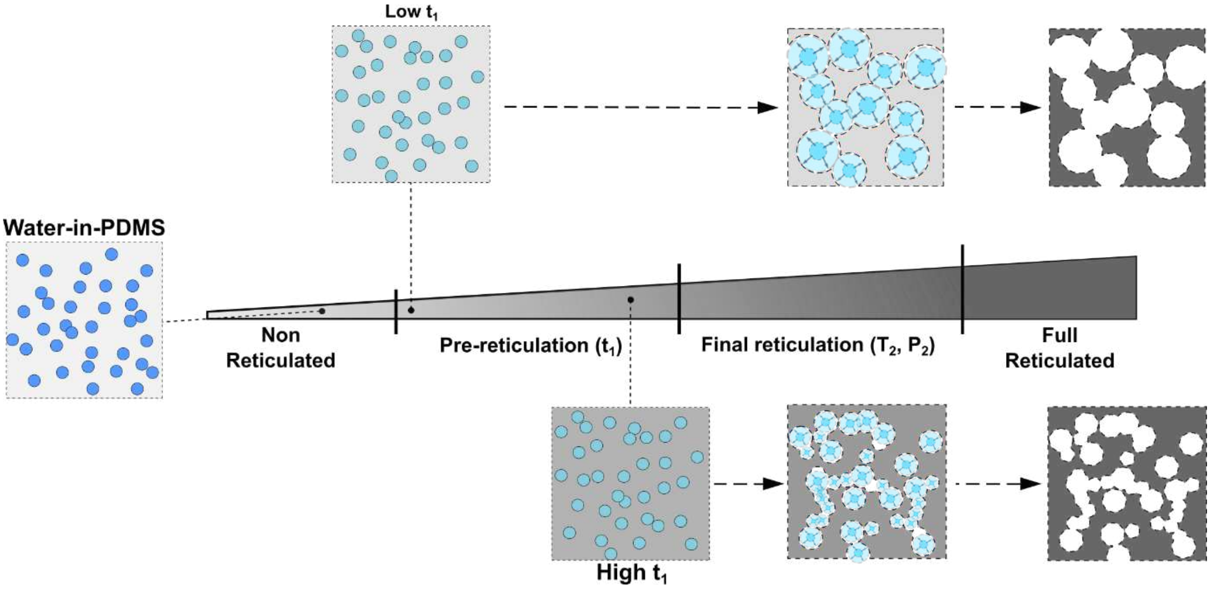

Figure 2.10. *Sketch of the impact of the physical parameters of the double-step process of crosslinking into the polyHIPE. The parameters for the first reticulation are* $\boldsymbol{t_1}$, $\boldsymbol{T_1}$ *and* $\boldsymbol{P_1}$. *For reasons of simplicity, we have chosen to fix* $\boldsymbol{T_1}$ = 60 ºC *and* $\boldsymbol{P_1}$ = 1 *atm. And for the second reticulation,* $\boldsymbol{t_2}$, $\boldsymbol{T_2}$ *and* $\boldsymbol{P_2}$. *Since the final result will be a fully reticulated PDMS and the water evaporated, we define* $\boldsymbol{t_2} = \infty$. *The resulting parameters to fix the kinetic of the process are:* $\boldsymbol{t_1}$, $\boldsymbol{T_2}$ *and* $\boldsymbol{P_2}$.

We describe this process as a competition between a resistance to deformation exerted by the internal phase of PDMS while reticulating, and an expansive force exerted by the water steam trying to escape the droplet cavities. The duration of the pre-reticulation (**t_1**) of the PDMS serves to modulate of the constraining force. This step, happening at a temperature lower than the boiling point of the porogen liquid, is used to fix the gelation point desired before the steam expansion happens.

The gelation process of the PDMS can be analysed via the *Complex modulus,* $\boldsymbol{E^*}$:

$$\boldsymbol{E^* = E' + iE''}$$

Where $\boldsymbol{E'}$ represents the storage modulus and $\boldsymbol{E''}$ represents the viscous modulus (or loss modulus). Conceptually speaking, the former contributes to the elastic resistance

Protocol 5. Water-in-PDMS Emulsion

The essence of this protocol resides in the general protocols of casting High Internal Phase Emulsions (HIPE), adapted to water as internal phase into a PDMS solution. Therefore, it is important to **respect the ratio** of the emulsion. In this case, **70 wt%** of water-in-PDMS. As PDMS solutions, we will be using the bi-component pack, 10:1 base-hardener, of **Sylgard 184 (DOW Corning)**.

***Protocol Figure 2.2**. Optical image of the final state of the emulsion after following the protocol.*

1. Calculate the volumes of PDMS and de-ionize water (DIW) needed from a targeted final volume (V_T). $\boldsymbol{V_{DIW} = 0.7 \times V_T}$ $\boldsymbol{V_{PDMS} = 0.3 \times V_T}$
    - *Alternative: Calculating from a volume of PDMS (V_{PDMS})*
      $\boldsymbol{V_T = \frac{1}{0.3} \times V_{PDMS}}$ $\boldsymbol{V_{DIW} = \frac{0.7}{0.3} \times V_T}$
2. Weight the volume of silicon-base ($\boldsymbol{V_{base} = \frac{10}{11} \times V_{PDMS}}$) using a disposable plastic container ($\rho_{PDMS} = 0.996 \sim 1$, therefore $V \sim m$)
3. Weight the volume of hardener ($\boldsymbol{V_{had} = \frac{1}{11} \times V_{PDMS}}$)
4. Mix the solution, then degas in a vacuum chamber until no bubble are visible. Depending on the quantities and the power of the vacuum pump times ranges from 10 to 30 minutes usually
5. Prepare the volume of DIW in a clean container.
6. Once finalized the degasification, proceed to add 1-2 mL of DIW into the PDMS container and hand-stir using a rigid plastic bar (such as a serological pipette) until the water is not visible anymore
7. Continue until finishing the volume of DIW, the mixture must be a white thick paste that holds its shape

and the latter contribute to the inelastic resistance. A purely elastic solid will present a real number as $\boldsymbol{E^*}$ and a purely viscous material will present an pure imaginary as ***E****. If we consider un-crosslinked PDMS as a viscous liquid ($\boldsymbol{E^* = iE''}$), the crosslinking process of PDMS consists in increasing the contribution of the storage modulus, turning it into a viscoelastic solid (a solid with an complex value as complex modulus, i.e., a number with real and imaginary contributions). The higher the degree of crosslinking before the evaporation of the water, the higher will be the elastic contribution of the resistance opposing the expansion force and therefore, the less deformed pores will be (in relation with the original droplet shape). Hence, we can correlate the parameter $\mathbf{t_1}$ to ***E****. The other experimental parameters would be $\mathbf{T_1}$, the temperature of this step and $\mathbf{P_1}$, and the applied pressure. We have fixed the former at $\mathbf{T_1}$ = 60 ºC. This is a temperature below the boiling point of the water and it allows a kinetic speed in the reticulation process slow enough to experience changes when modifying $\mathbf{t_1}$. At this temperature, liquid PDMS turns into bulk PDMS within 60-90 minutes. The pressure during this step does not have any impact since the water remains in liquid state, therefore $\mathbf{P_1}$ was kept at 1 atm.

Once the first step of the reticulation has pre-conditioned the starting complex modulus E^*, we proceeded with the next step of the fabrication process that consists in the final PDMS reticulation while water transits to gas state and expands the pores. This step is carried out in a pressure-controlled oven. The temperature $\mathbf{T_2}$ and pressure $\mathbf{P_2}$ of the final reticulation step act as driven forces of the expansion of the pores forming the interconnected network, as opposing to the elastic forces exerted by the PDMS. By varying both parameters, we can modify the kinetics of the water evaporation and modulate the forces that we want to exert within the pores. Since we target to have a solid porous monolith, the parameter corresponding to $\mathbf{t_2}$, the time of the reticulation, loose relevance since PDMS will not present large differences once the reticulated network is formed. Accordingly, we set $\mathbf{t_2} > 2$ hours. Summarizing, we have determined 3 main parameters that allow us to modify the physicochemical process of fabricating the porous PDMS by water-in-PDMS emulsion. The variation of $\mathbf{t_1}$, $\mathbf{T_2}$ and $\mathbf{P_2}$ permits us to obtain different porosities according to the commented process.

e. Characterizing our Porous PDMS monolith

In **Figure 2.11**, we present a table of SEM images with porous PDMS monolith of different porosities induced by changing the parameters $\mathbf{t_1}$, $\mathbf{T_2}$ and $\mathbf{P_2}$. These architectures were obtaining following the combination of **Protocol 4, 5** and **6**. Upon, the variation of $\mathbf{t_1}$ we expect to impact the complex modulus E^* during the steam expansion. When comparing the samples obtained for different $\mathbf{t_1}$, we indeed can observe that the longer times correspond to smaller pores generated during the process. This result seems to agree with our hypothesis in which the reticulation state can determine the pore size. Secondly, at the same temperature $\mathbf{T_2}$, we can observe striking variations when changing the pressure. There are two main reasons for such an impact. A lower pressure decreases the boiling point of the water and triggers the evaporation earlier during the process. Furthermore, the pressure drop causes a change in the balance of forces during the steam expansion and enhances the impact of the deformation caused by the steam. Thirdly, for a given pressure, we can see a minor variation in the porosity when modifying the temperature. In the columns 1-3 and 2-4, we compare results obtained with equal $\mathbf{P_2}$ pressure but with a variation in $\mathbf{T_2}$ temperature from 110 ºC to 130 ºC. The modification of the temperature impacts the reticulation kinetics and the phase transition of the water at the same time, though this impact is limited by the thermal conduction of the PDMS. Then, for an experimentalist point of view, the simplest way to change the porosity of the porous monolith is to modify the time $\mathbf{t_1}$ to change the pre-reticulation state. The reason for this choice is that we are just modifying one single kinetics (the pre-reticulation) when changing the parameters, while the variation during the second step would change the kinetics of the phase transition and the reticulation at the same time.

Protocol 6. Reticulation of a polyHIPE to obtain Porous PDMS

The tuning of certain parameters during the reticulation process of our *water-in-PDMS emulsion* permits us to modify the morphology of the porous structures obtained from the process. This method consists in two baking steps using a convection oven and a vacuum oven and takes advantage of the low boiling point of water compared to the reticulation time-temperature of the PDMS.

Protocol Figure 2.3. *Optical image of the fabrication of the porous PDMS inside the vacuum oven.*

1. Place the emulsion in the syringe from the piston side
2. Cast the emulsion into the mold/sample by injecting directly the emulsion on it. In our case, we inject the emulsion in the empty cavity of the multi-well plate until filled
3. Bake for t_1 minutes at T_1 = 60 ºC in a conventional oven (P_1 = atmospheric/1 bar; Universal Oven UF30plus, Memmert)
4. Transfer the samples to a vacuum oven (Vacuum Oven VO29L, Memmert) set at T_2 ºC and P_2 bar for at least 2 hours.
5. Using a surgical blade slide a superficial cut of the edges of the structure to remove the excess of foam coming out of the cylinder (in one single move if possible, for a clean surface).

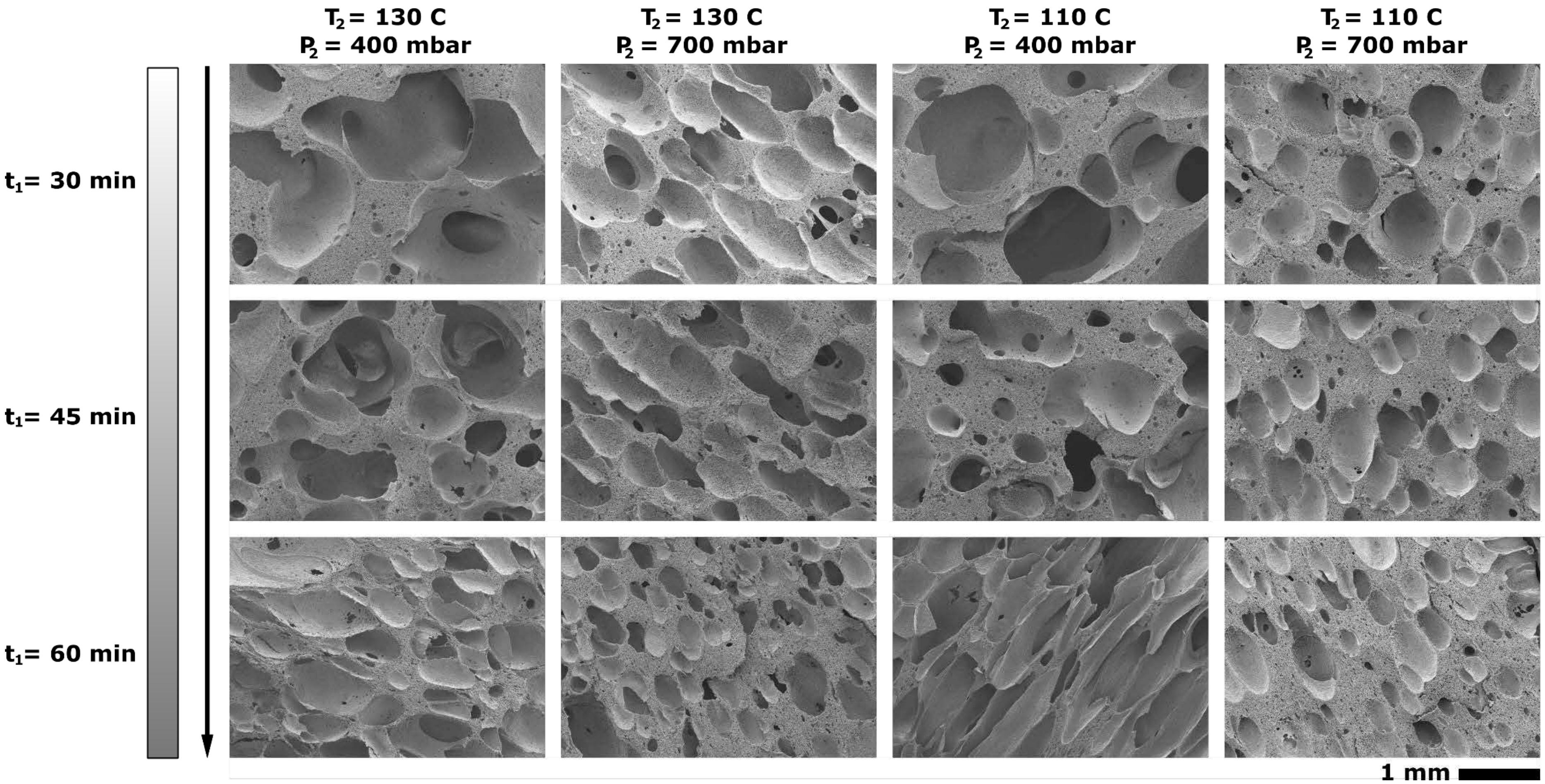

Figure 2.11. *SEM characterization of cross-cut of the porous PDMS scaffold generated at different curing parameters. Along the vertical axis, we vary the time of pre-reticulation* $\boldsymbol{t_1}$ *in a conventional oven at 60 ºC. In the horizontal axis, we vary the temperature* $\boldsymbol{T_2}$ *and the pressure* $\boldsymbol{P_2}$ *of the second step in the vacuum oven. SEM images were taken with a scanning electron microscopy Hitachi S-4800 system with an accelerating voltage of 5 kV and 10 µA current. Samples were metallized with a 15 nm layer of sputtered of gold using a PECS I from Gatan Systems. The scalebar is 1 mm for all the images.*

After having optimized the protocol and analyzed the types of morphologies resulting from the control of parameters **t_1**, **T_2** and **P_2**, we have selected the best suited morphology to reproduce the trabecular bone in terms of porosity, as described in **Chapter 1**. The sample produced by (**t_1** = 30 min, **T_2** = 130 ºC, **P_2** = 400 mbar) presents an apparent porosity ranging from $0.5 - 2\,mm$, giving a similar porosity that can be found in a trabecular bone.

To provide a more quantitative analysis of the pore size and the spatial distribution, we performed a X-ray microcomputed tomography over the porous PDMS scaffold. As previously commented, this technique consists in the acquisition of several radiographs with a slight angle variation and then a computed reconstruction taking into account the constrast difference between these radiographs. In this case, we employed a X-ray microtomography machine EasyTom XL 150 (manufactured by RX Solutions) from the Institute de Mechanique de Fluids de Toulouse. The X-ray source energy was adjusted to the resolution of the scan: the source voltage was fixed at 66 kV and source current at 268 µA. Before the acquisition, standard black and gain calibrations were performed. A complete scan was acquired by recording 1440 projections of the sample at different angles, equally distributed on a 360° rotation angle, with a flat panel of 1920 × 1536 pixels. Each projection had average exposure times of 0.11 and 5 s. The 3D volume and corresponding slices were reconstructed with the RX Solutions software, X-Act, using a filtered back-projection algorithm. Reconstructed slices had an isotropic resolution of 18 µm. Post-processing of images was performed with Avizo 9.7.0, a software dedicated to data visualization, segmentation, and quantification.

Figure 2.12A depicts a crosscut of the reconstructed structure obtained from the µCT characterization. The raw data was then segmentated with a threshold to obtain a neat structure to analyze the porosity as we can see in **Figure 2.12B**. The reconstructed structure from the porous PDMS scaffold is presentend in the **Figure 2.13A**, showing the porosity of the 3D architecture obtained under the defined parameters. Crosscuts of the planes XY and XZ are shown as well to illustrate the highly interconnected porosity found in the inner core of the structure. The binarized structure was analyzed and the porosity of the monolith equals around 57%. A second validation was carried out over the reconstructured structure, segmenting the porosity with a watershed segmentation algorithm[k] to obtain a porosity of 58.7%. The connectivity of the porosity was studied using the Axis Connectivity module available in Avizo Software. **Figure 2.13B** shows the porous network, where the white pores are connected and thus participate to the effective porosity and the red pores are isolated. The total volume of the pores is equal to 406.2 mm^3 in the samples, while the nonconnected pores represent only 4.3 mm^3, which equals to the 1% of the total volume of pores. Finally, pore size distribution was analyzed and shown as an histrogram in **Figure 2.13E**. In this graph we can observe the distribution by size of the colorimetric 3D visualization in **Figure 2.13D**. The diameter of the majority of reported pores varies between 0.02 and 0.10 mm, although the resolution limit for this configuration is set to a voxel of 18 µm Most of those small pores represent a limited contribution to the total volume of the pore network. This technique allowed to verify the porosity obtained with this parameter set to produce a similar porous architecture than what we could expect from a trabecular bone.

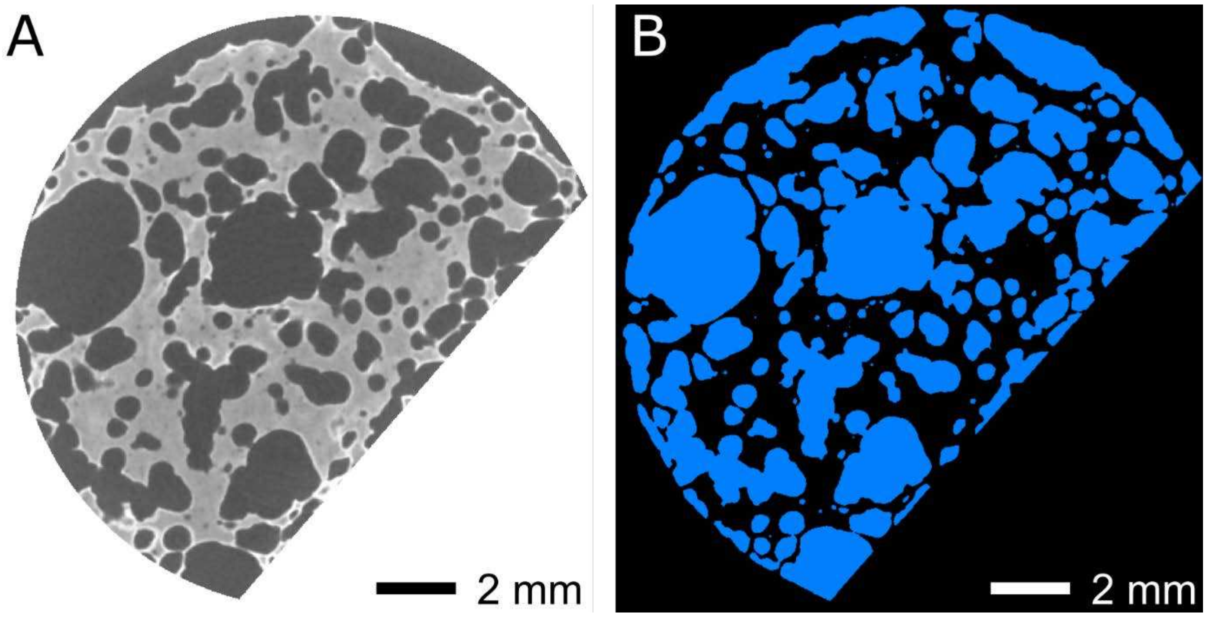

***Figure 2.12. (a)** Reconstructed slice of the porous PDMS biological standard sample after denoising. (**b)** Same slice after segmentation with a used defined threshold.*

---

[k] Watershed-based segmentation consists of transforming the gray-level image as a topographic map, where high intensity represents peaks and hills while low intensity represents valleys. The obtained topographic image is then flooded, starting from user-defined seeds, using an automatic gradient magnitude algorithm. Dams are built to avoid merging water from two different catchment basins. The segmentation result is defined by the locations of the dams, i.e., the watershed lines.

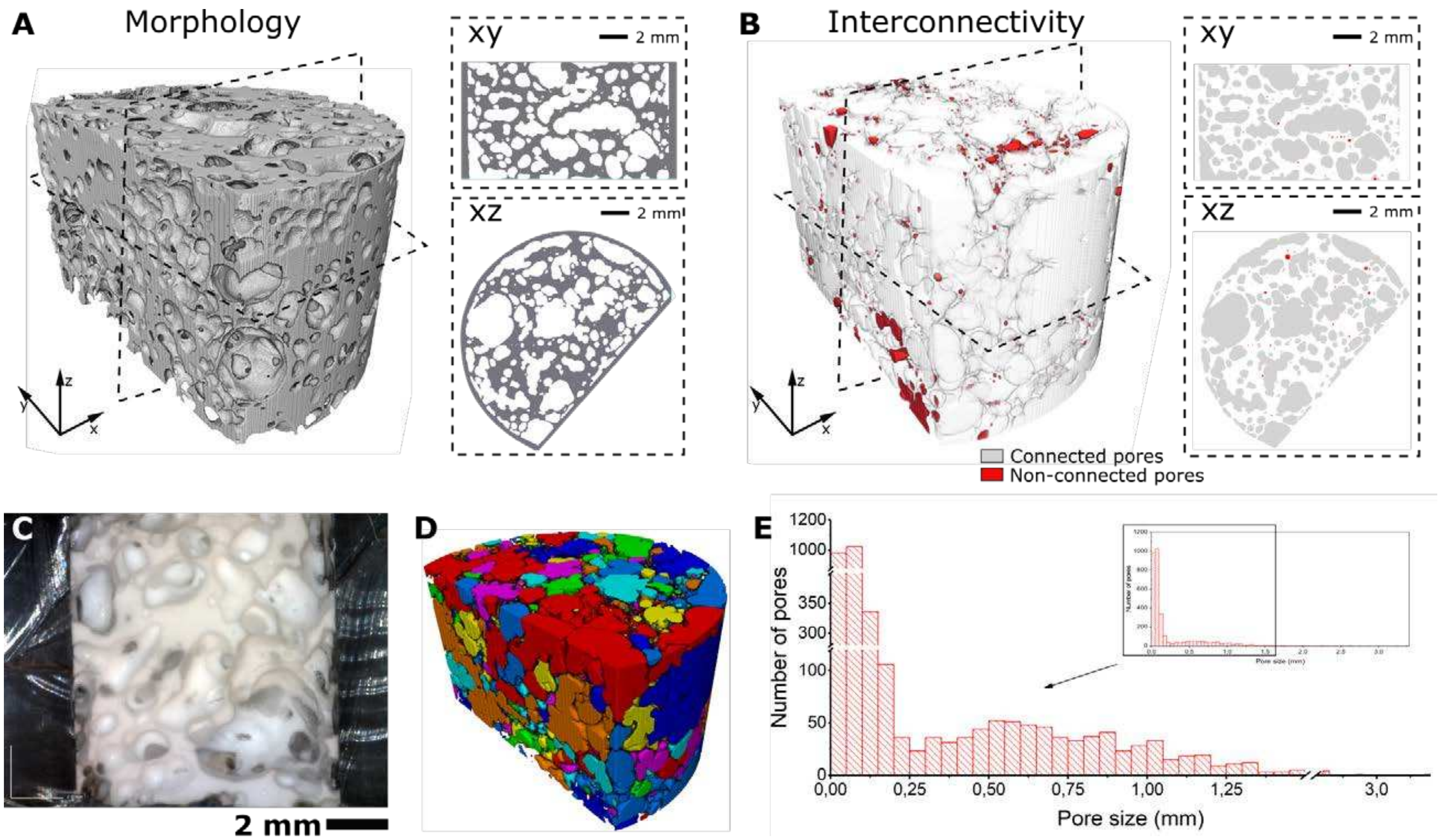

Figure 2.13. ***(a)*** *3D view of the PDMS scaffold after segmentation process. On the right, crosscuts of the reconstruction along the xy and xz planes.* ***(b)*** *3D view of the pores: nonconnected pores (red), connected pores (white). On the right, crosscuts of the reconstruction along the xy and xz planes.* ***(c)*** *Optical micrograph of the inner core of a PDMS porous scaffold.* ***(d)*** *3D colorimetric view of the pores size distribution with a watershed-based algorithm.* ***(e)*** *Distribution of the number of pores according to the pore size depicted in* ***(d).***

To complete the characterization, we performed an experiment to provide information about the water absorbance within the 3D architecture. The porous PDMS samples were dried in a vacum oven at 60 ºC overnight and then weighed, obtaining the value W_{dry}. A plasma-activation treatment was used to change wettability of the samples: 5 sccm oxygen flow, 0.5 mbar, 5 min, 50 W. Samples were immediately soaked in PBS for several hours. Samples were weighed again for different periods of time in order to retrieve W_{wet}. Liquid retention was calculated following the next equation:

$$Liquid\ retention\ (\%) = \frac{(W_{wet} - W_{dry})}{W_{dry}} \times 100$$

The results for this concluding experiment are presented in **Figure 2.14**. We can observe that the full of wetting process (i.e., when the liquid access to the complete structure) lasts about 12 hours before reaching the maximum water absorbed close to ~ 300% w/w. This values triplicate the weight of the dry sample, approaching the empirical porosity of the sample to about 75% (3:1, water/PDMS). Though, these values share the same order of magnitude as compared to the porosity obtained with µCT (around 58%), there is a non-negligeable deviation in the values. This difference can be explained by several hypotheses. First, there are multiple pores that cannot be measured due to the voxel size of 18 µm which could impact to the total volume and the interconnectivity of the overall porosity. Second, the water retention method is a manual technique to estimate experimental values and posses a large experimental error and a large dependance on the experimenter. In the later case, underestimation of the potential volume infravalued would hardly represent more than a ~ 1-3% of the total volume. Then, the former seems more realistic from the experimental point of view and we will accept this measure as an estimation of the order of maginitude.

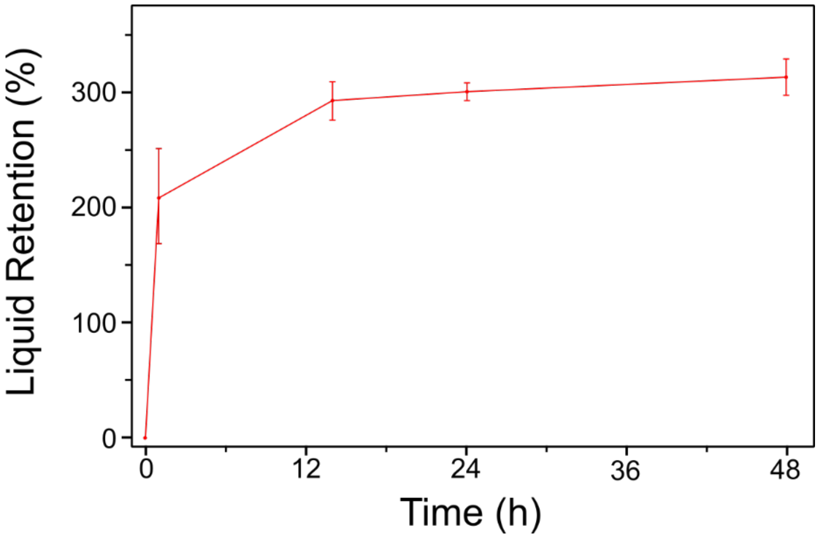

Figure 2.14. *Percent of liquid retained within the PDMS scaffold after different hours soaking in PBS.*

f. Summary

- We have presented the properties of polydimethylsiloxane, a well-established material for the cell culture applications.
- We have develop a novel technique to structure it in 3D architectures based on the principles of polyHIPES and emulsion templating.
- This method consists in producing an emulsion, water-in-PDMS, where the water acts as a porogen. We achieve the expansion of the water steam in the pores by performing a two-step thermal reticulation process at low and high temperature, regarding the boiling point of water.
- There are 3 main process parameters used to control the generated porosity via the control of the kinetics of gelation of the PDMS and the water evaporation.
- We have characterized the resulting porous monolith using SEM to select a mimicking topography for the bone marrow. This configuration was characterized by X-ray tomography with a porosity of Φ ~ 58.7% and a pore connectivity of 99%.

4. Conclusions

In this chapter, we presented an overview of the main techniques found in the literature to produce 3D porous architectures. We differenciated two types of fabrication techniques: designed architectures, such as additive manufacturing or 3D printing, and free-form architectures, such as polyHIPES or foaming. The main difference between them are the possibility to accurately define the topographies or not, and the material available for each technique.

This chapter has pointed out the link between the types of materials and the techniques used to fabricate porous architectures for biological applications. The fabrication of on-design architectures, often carried out by additive manufacturing techniques, limits the catalogue of proven materials available to those compatible with this technologies. This is more specifically the case of stereolithography that requires photo sensitive materials. Generally, these materials are presented in the literature with uncertain cell culture compatibilities due to their composition and may demand considerable efforts in terms of chemical modifications or post processing to meet biocompatibility standards [96]. On the other hand, free-form techniques sacrifice the control over the structure for a more versatile fabrication route, usually compatible with well-established materials for the cell culture community.

In the first section, dedicated to the use of stereolithography, we have shown the capabilities of this technique for 3D fabrication. We have demonstred that this technique is suitable to reproduce trabecular bone microarchitectures unsing a digial reproduction of real bones. The structures were fabricated and characterized used SEM imaging.

In the second section, we have introduced a novel 3D free-form fabrication technique using a well-known cell culture compatible material using physicochemical method without modification of the chemical composition of the material. This technique represents a fast and costless method to produce porous architectures for biological applications. Moreover, we have explained the physical characteristic of the process and demonstrated the control of the porosity generated using 3 key process parameters. A large set of samples have been produced in order to study the effect of each of these parameters using SEM characterization and we have been able to obtain a porous architecture similar to the trabecular bone. This architecture configuration was intensely characterized using µCT to obtain a quantification of the porosity and the interconectivity of the porous network. This process was published in ACS Applied Materials & Interfaces [66] and it can be found in the Appendix of this manuscript.

References

[1] M. Vert *et al.*, “Terminology for biorelated polymers and applications (IUPAC recommendations 2012),” *Pure Appl. Chem.*, vol. 84, no. 2, pp. 377–410, 2012, doi: 10.1351/pac-rec-10-12-04.

[2] F. Dini, S. A. Ghaffari, J. Jafar, R. Hamidreza, and S. Marjan, “A review of binder jet process parameters; powder, binder, printing and sintering condition,” *Met. Powder Rep.*, vol. 75, no. 2, pp. 95–100, Mar. 2020, doi: 10.1016/j.mprp.2019.05.001.

[3] A. Mostafaei *et al.*, “Binder jet 3D printing – Process parameters, materials, properties, and challenges,” *Progress in Materials Science*. Elsevier Ltd, p. 100707, Jun. 15, 2020, doi: 10.1016/j.pmatsci.2020.100707.

[4] M. Vaezi, H. Seitz, and S. Yang, “A review on 3D micro-additive manufacturing technologies,” *Int. J. Adv. Manuf. Technol.*, vol. 67, no. 5–8, pp. 1721–1754, 2013, doi: 10.1007/s00170-012-4605-2.

[5] P. Kunchala and K. Kappagantula, “3D printing high density ceramics using binder jetting with nanoparticle densifiers,” *Mater. Des.*, vol. 155, pp. 443–450, Oct. 2018, doi: 10.1016/j.matdes.2018.06.009.

[6] T. Sivarupan *et al.*, “A review on the progress and challenges of binder jet 3D printing of sand moulds for advanced casting,” *Addit. Manuf.*, vol. 40, p. 101889, Feb. 2021, doi: 10.1016/j.addma.2021.101889.

[7] L. Ren *et al.*, “Process parameter optimization of extrusion-based 3D metal printing utilizing PW-LDPE-SA binder system,” *Materials (Basel).*, vol. 10, no. 3, 2017, doi: 10.3390/ma10030305.

[8] Y. Wang, Z. Xu, D. Wu, and J. Bai, “Current status and prospects of polymer powder 3D printing technologies,” *Materials (Basel).*, vol. 13, no. 10, p. 2406, May 2020, doi: 10.3390/ma13102406.

[9] M. Lanzetta and E. Sachs, “Improved surface finish in 3D printing using bimodal powder distribution,” *Rapid Prototyp. J.*, vol. 9, no. 3, pp. 157–166, 2003, doi: 10.1108/13552540310477463.

[10] O. A. Mohamed, S. H. Masood, and J. L. Bhowmik, “Optimization of fused deposition modeling process parameters: a review of current research and future prospects,” *Adv. Manuf.*, vol. 3, no. 1, pp. 42–53, Mar. 2015, doi: 10.1007/s40436-014-0097-7.

[11] A. Bellini, L. Shor, and S. I. Guceri, “New developments in fused deposition modeling of ceramics,” *Rapid Prototyp. J.*, vol. 11, no. 4, pp. 214–220, 2005, doi: 10.1108/13552540510612901.

[12] M. Montero, D. Odell, S. Roundy, J. M. Brock, S. H. Ahn, and P. K. Wright, “Material Characterization of Fused Deposition Modeling (FDM) Process,” *Rapid Prototyp. Manuf. Conf.*, p. 1650, 2001.

[13] R. A. Wach, P. Wolszczak, and A. Adamus-Wlodarczyk, “Enhancement of Mechanical Properties of FDM-PLA Parts via Thermal Annealing,” *Macromol. Mater. Eng.*, vol. 303, no. 9, p. 1800169, Sep. 2018, doi: 10.1002/mame.201800169.

[14] J. Xiao and Y. Gao, “The manufacture of 3D printing of medical grade TPU,” *Prog. Addit. Manuf.*, vol. 2, no. 3, pp. 117–123, Sep. 2017, doi: 10.1007/s40964-017-0023-1.

[15] R. Singh and S. Singh, “Development of Nylon Based FDM Filament for Rapid Tooling Application,” *J. Inst. Eng. Ser. C*, vol. 95, no. 2, pp. 103–108, Apr. 2014, doi: 10.1007/s40032-014-0108-2.

[16] Z. Liu, Y. Wang, B. Wu, C. Cui, Y. Guo, and C. Yan, “A critical review of fused deposition modeling 3D printing technology in manufacturing polylactic acid parts,” *International Journal of Advanced Manufacturing Technology*, vol. 102, no. 9–12. Springer London, pp. 2877–2889, Jun. 19, 2019, doi: 10.1007/s00170-019-03332-x.

[17] L. Friedrich and M. Begley, “Corner accuracy in direct ink writing with support material,” *Bioprinting*, vol. 19, p. e00086, Sep. 2020, doi: 10.1016/j.bprint.2020.e00086.

[18] D. A. Rau, J. Herzberger, T. E. Long, and C. B. Williams, “Ultraviolet-Assisted

Direct Ink Write to Additively Manufacture All-Aromatic Polyimides," *ACS Appl. Mater. Interfaces*, vol. 10, no. 41, pp. 34828–34833, Oct. 2018, doi: 10.1021/acsami.8b14584.

[19] J. A. Lewis, J. E. Smay, J. Stuecker, and J. Cesarano, "Direct Ink Writing of Three-Dimensional Ceramic Structures," *J. Am. Ceram. Soc.*, vol. 89, no. 12, pp. 3599–3609, Dec. 2006, doi: 10.1111/j.1551-2916.2006.01382.x.

[20] J. A. Lewis, "Direct Ink Writing of 3D Functional Materials," *Adv. Funct. Mater.*, vol. 16, no. 17, pp. 2193–2204, Nov. 2006, doi: 10.1002/adfm.200600434.

[21] R. A. Barry, R. F. Shepherd, J. N. Hanson, R. G. Nuzzo, P. Wiltzius, and J. A. Lewis, "Direct-Write Assembly of 3D Hydrogel Scaffolds for Guided Cell Growth," *Adv. Mater.*, vol. 21, no. 23, pp. 2407–2410, Jun. 2009, doi: 10.1002/adma.200803702.

[22] J. Kim *et al.*, "Direct-write patterning of bacterial cells by dip-pen nanolithography," *J. Am. Chem. Soc.*, vol. 134, no. 40, pp. 16500–16503, Oct. 2012, doi: 10.1021/ja3073808.

[23] G. M. Gratson, M. Xu, and J. A. Lewis, "Direct writing of three-dimensional webs," *Nature*, vol. 428, no. 6981, p. 386, Mar. 2004, doi: 10.1038/428386a.

[24] H. Sirringhaus *et al.*, "High-resolution inkjet printing of all-polymer transistor circuits," *Science (80-.).*, vol. 290, no. 5499, pp. 2123–2126, Dec. 2000, doi: 10.1126/science.290.5499.2123.

[25] J. P. Kruth, P. Mercelis, J. Van Vaerenbergh, L. Froyen, and M. Rombouts, "Binding mechanisms in selective laser sintering and selective laser melting," *Rapid Prototyping Journal*, vol. 11, no. 1. Emerald Group Publishing Limited, pp. 26–36, 2005, doi: 10.1108/13552540510573365.

[26] A. Franco, M. Lanzetta, and L. Romoli, "Experimental analysis of selective laser sintering of polyamide powders: An energy perspective," *J. Clean. Prod.*, vol. 18, no. 16–17, pp. 1722–1730, Nov. 2010, doi: 10.1016/j.jclepro.2010.07.018.

[27] Y. Shi, Y. Wang, J. Chen, and S. Huang, "Experimental investigation into the selective laser sintering of high-impact polystyrene," *J. Appl. Polym. Sci.*, vol.

108, no. 1, pp. 535–540, Apr. 2008, doi: 10.1002/app.27686.

[28] A. Ronca *et al.*, “Selective Laser Sintering Fabricated Thermoplastic Polyurethane/Graphene Cellular Structures with Tailorable Properties and High Strain Sensitivity,” *Appl. Sci.*, vol. 9, no. 5, p. 864, Feb. 2019, doi: 10.3390/app9050864.

[29] I. Gibson and D. Shi, “Material properties and fabrication parameters in selective laser sintering process,” *Rapid Prototyp. J.*, vol. 3, no. 4, pp. 129–136, 1997, doi: 10.1108/13552549710191836.

[30] J. P. Kruth, X. Wang, T. Laoui, and L. Froyen, “Lasers and materials in selective laser sintering,” *Assem. Autom.*, vol. 23, no. 4, pp. 357–371, 2003, doi: 10.1108/01445150310698652.

[31] A. Accardo, R. Courson, R. Riesco, V. Raimbault, and L. Malaquin, “Direct laser fabrication of meso-scale 2D and 3D architectures with micrometric feature resolution,” *Addit. Manuf.*, vol. 22, pp. 440–446, Aug. 2018, doi: 10.1016/J.ADDMA.2018.04.027.

[32] A. Accardo, M.-C. Blatché, R. Courson, I. Loubinoux, C. Vieu, and L. Malaquin, “Direct laser fabrication of free-standing PEGDA-hydrogel scaffolds for neuronal cell growth: Engineering 3D biocompatible microenvironments,” *Mater. Today*, vol. 21, no. 3, pp. 315–316, Apr. 2018, doi: 10.1016/J.MATTOD.2018.02.004.

[33] N. Buch-Månson, A. Spangenberg, L. P. C. Gomez, J. P. Malval, O. Soppera, and K. L. Martinez, “Rapid prototyping of polymeric nanopillars by 3D direct laser writing for controlling cell behavior,” *Sci. Rep.*, vol. 7, no. 1, pp. 1–9, Dec. 2017, doi: 10.1038/s41598-017-09208-y.

[34] F. P. W. Melchels, J. Feijen, and D. W. Grijpma, “A review on stereolithography and its applications in biomedical engineering,” *Biomaterials*, vol. 31, no. 24. Elsevier, pp. 6121–6130, Aug. 01, 2010, doi: 10.1016/j.biomaterials.2010.04.050.

[35] A. Accardo, M. C. Blatché, R. Courson, I. Loubinoux, C. Vieu, and L. Malaquin,

"Two-photon lithography and microscopy of 3D hydrogel scaffolds for neuronal cell growth," *Biomed. Phys. Eng. Express*, vol. 4, no. 2, 2018, doi: 10.1088/2057-1976/aaab93.

[36] F.-L. Jin, M. Zhao, M. Park, and S.-J. Park, "Recent Trends of Foaming in Polymer Processing: A Review," *Polymers (Basel).*, vol. 11, no. 6, p. 953, Jun. 2019, doi: 10.3390/polym11060953.

[37] F. Dehghani and N. Annabi, "Engineering porous scaffolds using gas-based techniques," *Curr. Opin. Biotechnol.*, vol. 22, no. 5, pp. 661–666, Oct. 2011, doi: 10.1016/j.copbio.2011.04.005.

[38] Y. S. Nam, J. J. Yoon, and T. G. Park, "A novel fabrication method of macroporous biodegradable polymer scaffolds using gas foaming salt as a porogen additive," *J. Biomed. Mater. Res.*, vol. 53, no. 1, pp. 1–7, 2000, doi: 10.1002/(SICI)1097-4636(2000)53:1<1::AID-JBM1>3.0.CO;2-R.

[39] I. Manavitehrani *et al.*, "Formation of porous biodegradable scaffolds based on poly(propylene carbonate) using gas foaming technology," *Mater. Sci. Eng. C*, vol. 96, no. November 2018, pp. 824–830, 2019, doi: 10.1016/j.msec.2018.11.088.

[40] K. Gorna and S. Gogolewski, "Preparation, degradation, and calcification of biodegradable polyurethane foams for bone graft substitutes," *J. Biomed. Mater. Res. - Part A*, vol. 67, no. 3, pp. 813–827, Dec. 2003, doi: 10.1002/jbm.a.10148.

[41] T. Ouyang *et al.*, "High-throughput fabrication of porous carbon by chemical foaming strategy for high performance supercapacitor," *Chem. Eng. J.*, vol. 352, pp. 459–468, Nov. 2018, doi: 10.1016/j.cej.2018.06.184.

[42] X. Liu, S. C. Qi, A. Z. Peng, D. M. Xue, X. Q. Liu, and L. B. Sun, "Foaming Effect of a Polymer Precursor with a Low N Content on Fabrication of N-Doped Porous Carbons for CO2 Capture," *Ind. Eng. Chem. Res.*, vol. 58, no. 25, pp. 11013–11021, Jun. 2019, doi: 10.1021/acs.iecr.9b02063.

[43] N. Hedayat, Y. Du, and H. Ilkhani, "Review on fabrication techniques for porous

electrodes of solid oxide fuel cells by sacrificial template methods," *Renewable and Sustainable Energy Reviews*, vol. 77. Elsevier Ltd, pp. 1221–1239, Sep. 01, 2017, doi: 10.1016/j.rser.2017.03.095.

[44] R. C. Thomas *et al.*, "Sacrificial Crystal Templated Hyaluronic Acid Hydrogels As Biomimetic 3D Tissue Scaffolds for Nerve Tissue Regeneration," *ACS Biomater. Sci. Eng.*, vol. 3, no. 7, pp. 1451–1459, Jul. 2017, doi: 10.1021/acsbiomaterials.7b00002.

[45] P. Yin *et al.*, "Engineering of removing sacrificial materials in 3D-printed microfluidics," *Micromachines*, vol. 9, no. 7, pp. 1–12, 2018, doi: 10.3390/mi9070327.

[46] A. R. Studart, U. T. Gonzenbach, E. Tervoort, and L. J. Gauckler, "Processing routes to macroporous ceramics: A review," in *Journal of the American Ceramic Society*, Jun. 2006, vol. 89, no. 6, pp. 1771–1789, doi: 10.1111/j.1551-2916.2006.01044.x.

[47] I. Hölken *et al.*, "Sacrificial Template Synthesis and Properties of 3D Hollow-Silicon Nano- and Microstructures," *ACS Appl. Mater. Interfaces*, vol. 8, no. 31, pp. 20491–20498, Aug. 2016, doi: 10.1021/acsami.6b06387.

[48] Q. Hou, D. W. Grijpma, and J. Feijen, "Porous polymeric structures for tissue engineering prepared by a coagulation, compression moulding and salt leaching technique," *Biomaterials*, vol. 24, no. 11, pp. 1937–1947, 2003, doi: 10.1016/S0142-9612(02)00562-8.

[49] Y. Xie *et al.*, "High-performance porous polylactide stereocomplex crystallite scaffolds prepared by solution blending and salt leaching," *Mater. Sci. Eng. C*, vol. 90, no. 2017, pp. 602–609, 2018, doi: 10.1016/j.msec.2018.05.023.

[50] Q. Li, T. Duan, J. Shao, and H. Yu, "Fabrication method for structured porous polydimethylsiloxane (PDMS)," *J. Mater. Sci.*, vol. 53, no. 16, pp. 11873–11882, Aug. 2018, doi: 10.1007/s10853-018-2396-z.

[51] L. Alison *et al.*, "3D printing of sacrificial templates into hierarchical porous materials," *Sci. Rep.*, vol. 9, no. 1, pp. 1–9, 2019, doi: 10.1038/s41598-018-

36789-z.

[52] J. González-Rivera *et al.*, “Structural and Thermoanalytical Characterization of 3D Porous PDMS Foam Materials: The Effect of Impurities Derived from a Sugar Templating Process,” *Polymers (Basel).*, vol. 10, no. 6, p. 616, Jun. 2018, doi: 10.3390/polym10060616.

[53] Y. Zhao *et al.*, “Fine-regulating ultramicropores in porous carbon: Via a self-sacrificial template route for high-performance supercapacitors,” *Nanoscale*, vol. 13, no. 3, pp. 1961–1969, Jan. 2021, doi: 10.1039/d0nr07480b.

[54] C. Yu *et al.*, “Facile Preparation of the Porous PDMS Oil-Absorbent for Oil/Water Separation,” *Adv. Mater. Interfaces*, vol. 4, no. 3, p. 1600862, Feb. 2017, doi: 10.1002/admi.201600862.

[55] J. Miao, X. J. Zhao, Y. T. Li, and Z. H. Liu, “Facial preparation of hierarchical porous Ba(B2Si2O8) microsphere by sacrificial-template method and its highly efficient selective adsorption of triphenylmethane dyes,” *Colloids Surfaces A Physicochem. Eng. Asp.*, vol. 602, p. 124883, Oct. 2020, doi: 10.1016/j.colsurfa.2020.124883.

[56] J. Zhou, A. V. Ellis, and N. H. Voelcker, “Recent developments in PDMS surface modification for microfluidic devices,” *Electrophoresis*, vol. 31, no. 1. pp. 2–16, 2010, doi: 10.1002/elps.200900475.

[57] X. Yang, L. Tan, L. Xia, C. D. Wood, and B. Tan, “Hierarchical porous polystyrene monoliths from PolyHIPE,” *Macromol. Rapid Commun.*, vol. 36, no. 17, pp. 1553–1558, Sep. 2015, doi: 10.1002/marc.201500235.

[58] M. S. Silverstein, “PolyHIPEs: Recent advances in emulsion-templated porous polymers,” *Prog. Polym. Sci.*, vol. 39, no. 1, pp. 199–234, 2014, doi: 10.1016/j.progpolymsci.2013.07.003.

[59] M. S. Silverstein, “PolyHIPEs: Recent advances in emulsion-templated porous polymers,” *Progress in Polymer Science*, vol. 39, no. 1. Pergamon, pp. 199–234, Jan. 01, 2014, doi: 10.1016/j.progpolymsci.2013.07.003.

[60] R. J. Wakeman, Z. G. Bhumgara, and G. Akay, “Ion exchange modules formed

from polyhipe foam precursors,” *Chem. Eng. J.*, vol. 70, no. 2, pp. 133–141, Jun. 1998, doi: 10.1016/s0923-0467(98)00088-8.

[61] M. T. Grosse, M. Lamotte, M. Birot, and H. Deleuze, “Preparation of microcellular polysiloxane monoliths,” *J. Polym. Sci. Part A Polym. Chem.*, vol. 46, no. 1, pp. 21–32, Jan. 2008, doi: 10.1002/pola.22351.

[62] K. M. L. Taylor-Pashow and J. G. Pribyl, “PolyHIPEs for Separations and Chemical Transformations: A Review,” *Solvent Extr. Ion Exch.*, vol. 37, no. 1, pp. 1–26, 2019, doi: 10.1080/07366299.2019.1592924.

[63] Z. Bhumgara, “Polyhipe foam materials as filtration media,” *Filtr. Sep.*, vol. 32, no. 3, pp. 245–251, Mar. 1995, doi: 10.1016/S0015-1882(97)84048-7.

[64] H. H. Mert, “PolyHIPE composite based-form stable phase change material for thermal energy storage,” *Int. J. Energy Res.*, vol. 44, no. 8, pp. 6583–6594, Jun. 2020, doi: 10.1002/er.5390.

[65] L. Yang *et al.*, “Development of a Highly Sensitive, Broad-Range Hierarchically Structured Reduced Graphene Oxide/PolyHIPE Foam for Pressure Sensing,” *ACS Appl. Mater. Interfaces*, vol. 11, no. 4, pp. 4318–4327, Jan. 2019, doi: 10.1021/acsami.8b17020.

[66] R. Riesco *et al.*, “Water-in-PDMS Emulsion Templating of Highly Interconnected Porous Architectures for 3D Cell Culture,” *ACS Appl. Mater. Interfaces*, 2019, doi: 10.1021/acsami.9b07564.

[67] F. Mézière *et al.*, “Experimental observation of ultrasound fast and slow waves through three-dimensional printed trabecular bone phantoms,” *J. Acoust. Soc. Am.*, vol. 139, no. 2, pp. EL13–EL18, Feb. 2016, doi: 10.1121/1.4939297.

[68] R. N. McCarthy, L. B. Jeffcott, and R. N. McCartney, “Ultrasound speed in equine cortical bone: Effects of orientation, density, porosity and temperature,” *J. Biomech.*, vol. 23, no. 11, pp. 1139–1143, Jan. 1990, doi: 10.1016/0021-9290(90)90006-O.

[69] DWS Systems, “DS3000 Technical Data Sheet,” 2010. [Online]. Available: https://www.dwssystems.com/en/configurator/D/13/ds3000-en.

[70] D. H. Han, D. J. Kang, D. P. Kang, and K. E. Min, “Characteristics of electrical insulation in PDMS-ATH composite for high voltage insulators,” *Polym. Bull.*, vol. 61, no. 5, pp. 611–617, Nov. 2008, doi: 10.1007/s00289-008-0980-0.

[71] J. Park, H. S. Kim, and A. Han, “Micropatterning of poly(dimethylsiloxane) using a photoresist lift-off technique for selective electrical insulation of microelectrode arrays,” *J. Micromechanics Microengineering*, vol. 19, no. 6, p. 065016, May 2009, doi: 10.1088/0960-1317/19/6/065016.

[72] S. Saem, D. Fong, A. Adronov, and J. Moran-Mirabal, “Stretchable and Resilient Conductive Films on Polydimethylsiloxane from Reactive Polymer-Single-Walled Carbon Nanotube Complexes for Wearable Electronics,” *ACS Appl. Nano Mater.*, vol. 2, no. 8, pp. 4968–4973, Aug. 2019, doi: 10.1021/acsanm.9b00912.

[73] J. C. Agar, K. J. Lin, R. Zhang, J. Durden, K. S. Moon, and C. P. Wong, “Novel PDMS(silicone)-in-PDMS(silicone): Low cost flexible electronics without metallization,” in *Proceedings - Electronic Components and Technology Conference*, 2010, pp. 1226–1230, doi: 10.1109/ECTC.2010.5490654.

[74] V. L. Trinh and C. K. Chung, “Harvesting mechanical energy, storage, and lighting using a novel PDMS based triboelectric generator with inclined wall arrays and micro-topping structure,” *Appl. Energy*, vol. 213, pp. 353–365, Mar. 2018, doi: 10.1016/j.apenergy.2018.01.039.

[75] Y. Ye, J. Chen, Y. J. Ren, and Z. H. Feng, “Valve improvement for high flow rate piezoelectric pump with PDMS film valves,” *Sensors Actuators, A Phys.*, vol. 283, pp. 245–253, Nov. 2018, doi: 10.1016/j.sna.2018.09.064.

[76] A. Kachroudi, S. Basrour, L. Rufer, A. Sylvestre, and F. Jomni, “Micro-structured PDMS piezoelectric enhancement through charging conditions,” *Smart Mater. Struct.*, vol. 25, no. 10, p. 105027, Sep. 2016, doi: 10.1088/0964-1726/25/10/105027.

[77] D. C. Duffy, J. C. McDonald, O. J. A. Schueller, and G. M. Whitesides, “Rapid prototyping of microfluidic systems in poly(dimethylsiloxane),” *Anal. Chem.*,

vol. 70, no. 23, pp. 4974–4984, Dec. 1998, doi: 10.1021/ac980656z.

[78] R. Mukhopadhyay, “When PDMS isn’t the best,” *Analytical Chemistry*, vol. 79, no. 9. American Chemical Society , pp. 3249–3253, May 01, 2007, doi: 10.1021/ac071903e.

[79] N. J. Fendinger, “Polydimethylsiloxane (PDMS): Environmental Fate and Effects,” in *Organosilicon Chemistry Set*, Weinheim, Germany: Wiley-VCH Verlag GmbH, 2005, pp. 626–638.

[80] S. Halldorsson, E. Lucumi, R. Gómez-Sjöberg, and R. M. T. Fleming, “Advantages and challenges of microfluidic cell culture in polydimethylsiloxane devices,” *Biosens. Bioelectron.*, vol. 63, pp. 218–231, 2015, doi: 10.1016/j.bios.2014.07.029.

[81] K. J. Regehr *et al.*, “Biological implications of polydimethylsiloxane-based microfluidic cell culture,” *Lab on a Chip*, vol. 9, no. 15. Royal Society of Chemistry, pp. 2132–2139, Aug. 07, 2009, doi: 10.1039/b903043c.

[82] S. Torino, B. Corrado, M. Iodice, and G. Coppola, “PDMS-Based Microfluidic Devices for Cell Culture,” *Inventions*, vol. 3, no. 3, p. 65, Sep. 2018, doi: 10.3390/inventions3030065.

[83] N. Bhattacharjee, C. Parra-Cabrera, Y. T. Kim, A. P. Kuo, and A. Folch, “Desktop-Stereolithography 3D-Printing of a Poly(dimethylsiloxane)-Based Material with Sylgard-184 Properties,” *Adv. Mater.*, vol. 30, no. 22, May 2018, doi: 10.1002/adma.201800001.

[84] M. S. Silverstein, “Emulsion-templated porous polymers: A retrospective perspective,” *Polymer (Guildf).*, vol. 55, no. 1, pp. 304–320, 2014, doi: 10.1016/j.polymer.2013.08.068.

[85] N. R. Cameron and D. C. Sherrington, *High Internal Phase Emulsions (HIPEs) - Structure, Properties and Use in Polymer Preparation*, vol. 126. Springer New York, 1996.

[86] A. Y. Sergienko, H. Tai, M. Narkis, and M. S. Silverstein, “Polymerized high internal-phase emulsions: Properties and interaction with water,” *J. Appl.*

Polym. Sci., vol. 84, no. 11, pp. 2018–2027, Jun. 2002, doi: 10.1002/app.10555.

[87] Y. Zhu, S. Zhang, Y. Hua, J. Chen, and C. P. Hu, “Hydrophilic porous polymers based on high internal phase emulsions solely stabilized by poly(urethane urea) nanoparticles,” *Polymer (Guildf).*, vol. 51, no. 16, pp. 3612–3617, Jul. 2010, doi: 10.1016/j.polymer.2010.06.008.

[88] T. Dahlberg *et al.*, “3D printed water-soluble scaffolds for rapid production of PDMS micro-fluidic flow chambers,” *Sci. Rep.*, vol. 8, no. 1, p. 3372, Dec. 2018, doi: 10.1038/s41598-018-21638-w.

[89] A. Giustiniani, P. Guégan, M. Marchand, C. Poulard, and W. Drenckhan, “Generation of Silicone Poly-HIPEs with Controlled Pore Sizes via Reactive Emulsion Stabilization,” *Macromol. Rapid Commun.*, vol. 37, no. 18, pp. 1527–1532, Sep. 2016, doi: 10.1002/marc.201600281.

[90] I. Gurevitch and M. S. Silverstein, “Nanoparticle-based and organic-phase-based AGET ATRP polyHIPE synthesis within pickering HIPEs and surfactant-stabilized HIPEs,” *Macromolecules*, vol. 44, no. 9, pp. 3398–3409, May 2011, doi: 10.1021/ma200362u.

[91] J. M. Williams and D. A. Wrobleski, “Spatial distribution of the phases in water-in-oil emulsions. open and closed microcellular foams from cross-linked polystyrene,” *Langmuir*, vol. 4, no. 3, pp. 656–662, 1988, doi: 10.1021/la00081a027.

[92] A. Mata, A. J. Fleischman, and S. Roy, “Characterization of Polydimethylsiloxane (PDMS) Properties for Biomedical Micro/Nanosystems,” *Biomed. Microdevices*, vol. 7, no. 4, pp. 281–293, Dec. 2005, doi: 10.1007/s10544-005-6070-2.

[93] Z. Wang, A. A. Volinsky, and N. D. Gallant, “Crosslinking effect on polydimethylsiloxane elastic modulus measured by custom-built compression instrument,” *J. Appl. Polym. Sci.*, vol. 131, no. 22, p. n/a-n/a, Nov. 2014, doi: 10.1002/app.41050.

[94] E. J. Wong, “Modeling and Control of Rapid Cure in Polydimethylsiloxane

(PDMS) for Microfluidic Device Applications in Partial Fulfillment of the Requirements for the Degree of Doctor of Philosophy in Mechanical Engineering," 2010.

[95] I. D. Johnston, D. K. McCluskey, C. K. L. Tan, and M. C. Tracey, "Mechanical characterization of bulk Sylgard 184 for microfluidics and microengineering," *J. Micromechanics Microengineering*, vol. 24, no. 3, 2014, doi: 10.1088/0960-1317/24/3/035017.

[96] F. Alifui-Segbaya, S. Varma, G. J. Lieschke, and R. George, "Biocompatibility of Photopolymers in 3D Printing," *3D Print. Addit. Manuf.*, vol. 4, no. 4, pp. 185–191, Dec. 2017, doi: 10.1089/3dp.2017.0064.

III. 3D porous scaffolds as cell culture microenvironments

In this chapter, we will present the results obtained from the culture of cells in the developed 3D architecture presented in **Chapter 2**. We will address a recurrent concern highlighted in the literature regarding the use of new materials for biological applications, the study of the biocompatibility [1], [2]. We will study the different conditions needed to ensure the viability of the cell culture on a new material from the perspective of additive manufacturing. These cell culture studies will be carried out using an osteosarcoma cell line, SaOS-2, and primary human bone marrow mesenchymal stromal cells, BMSCs. SaOS-2 is a cell line derived from human osteosarcoma cells, which possess different osteoblastic features (such as phenotype or alkaline phosphatase activity) and is a classical cell line for bone-related applications [1]-[3]. We will continue the developments of two potential material candidates, DS3000 and porous PDMS, for the creation of systems to reproduce the bone marrow microenvironment in an *in-vitro* model.

Here, we will introduce certain notions regarding cell viability and the potential issues occurring when using new materials for cell culture. This will require designed experiments to understand the nature of the cell culture requirements and we will supply specific solutions to achieve cell viability. Then we will move to the 3D cell culture and the optimization of the culture in such conditions. We will also describe the techniques employed to characterize the 3D cell culture, with their technical challenge and limitations.

1. Material compatibility

To ensure the viability of the cell culture in 3D, first, we must ensure the welfare of the cells in a 2D cellular environment composed of the material of choice [2]. The use of non-standardize materials for cell culture always bring questions regarding its suitability in the context of the cellular microenvironment and the potential alterations caused by its chemical nature. It is common to use methods of sequential washing/rinsing of, in order to remove/extract the potential harmful byproduct from the substrates, such as free radicals produced during the photopolymerization process [6]–[8]. Moreover, the role of the chemical nature of a new substrate for cell culture is not limited to cytotoxicity. The differences in surface chemistry can as well alter the cell adhesion, varying and modulating how cells attach to the substrate. The results of both issues can lead to similar measures when evaluating the viability of the material for biological applications, though the solution for each is essentially different.

It is possible to decrease the effect of a cytotoxic materials by the implementing post-treatments such as different rinsing with solvent/water solutions, UV curing or thermal treatment, committed to decrease the specific physicochemical properties of the material related with the cellular damage [9], [10]. To ensure cell adhesion, it is common to modify the surface properties of the material. For this, the use of protein coating or plasma treatment are common and aim to enhance the adhesion of cells to the substrates [11]–[13]. Here, we present the work we have conducted to ensure that the materials we have used to create new 3D cellular environment are suited for cell culture.

a. DS3000 substrates

In order to prove the DS3000 compatibility with cell culture, we have conducted two types of studies: first, we have identified potential sources of byproducts and we have established a sample treatment to reduce their harmful impact; and second, we have implemented ways to enhance, if needed, the cell adhesion. Thanks to prior knowledge within our group and information found in the literature [14]–[16], we have assumed the need of a protein coating in order to enhance the adhesion of the cells, where proteins are known to play an important role in cell adhesion. Particularly, we have used the results of a prior study conducted by our collaborator from the RESTORE unit, on the most favorable protein coating for the adherence of MSCs on biomaterials, where fibronectin was demonstrated to be efficient.

The ISO standard rule 10993-5:2009 establishes a protocol for the biological evaluation of medical devices, regarding the cytotoxicity for *in-vitro* test [17]. This rule defines three types of tests to evaluate the cytotoxicity:

- Test by liquid extract: incubation of the material in cell culture medium for different periods of time in the denominated extraction conditions. Then expose the cell culture to the incubated medium for a period of time.
- Test by indirect contact: incubation of the material in the culture medium during culture while preventing direct contact of cells with the sample.
- Test by direct contact: incubation of the cell in close contact with the material.

In our project, we conducted a liquid extracts test, followed by the evaluation of the best protocol for protein coating on the material. Then, we proved the viability of the cell culture with a direct contact test to conclude with the study of different enhancing adhesion protocols.

i. Liquid extract test

In **Figure 3.1**, we present the data collected from the liquid extracts test using a culture of SaOS-2 cells. Our test consisted in the incubation of DS3000 slabs in culture medium, changing the medium every 24h, and using the solutions obtained in Day 1, 2 and 3 for the cell culture. Besides providing us information regarding the cytotoxicity of the material. The sequential exchanges of medium aim to determine the release of material extracts and its impact on the cells, proving a specific number of steps to achieve reliable use. We used a glass coverslip as negative control, reproducing a non-toxic material. A solution of 3mM of chloroquine was added to a culture on glass coverslip as positive control, simulating a toxic condition. The detailed process is described in **Protocol 7**. **Figure 3.1A** illustrate the protocol in a schematic fashion. The cell cultures using the extracts were analyzed by a MTT assay (**Protocol 8**) and a Live/Dead assay (**Protocol 9**), as shows **Figure 3.1B**. Cell culture exhibit viability higher than 70% for the glass control and the DS3000 in both viability test from Day 1. There are minor differences regarding the DS3000 and glass control during MTT test, yet these are not significant. These results show the lack of harmful extracts diluted in the culture medium via the incubation of the DS3000 in the solution.

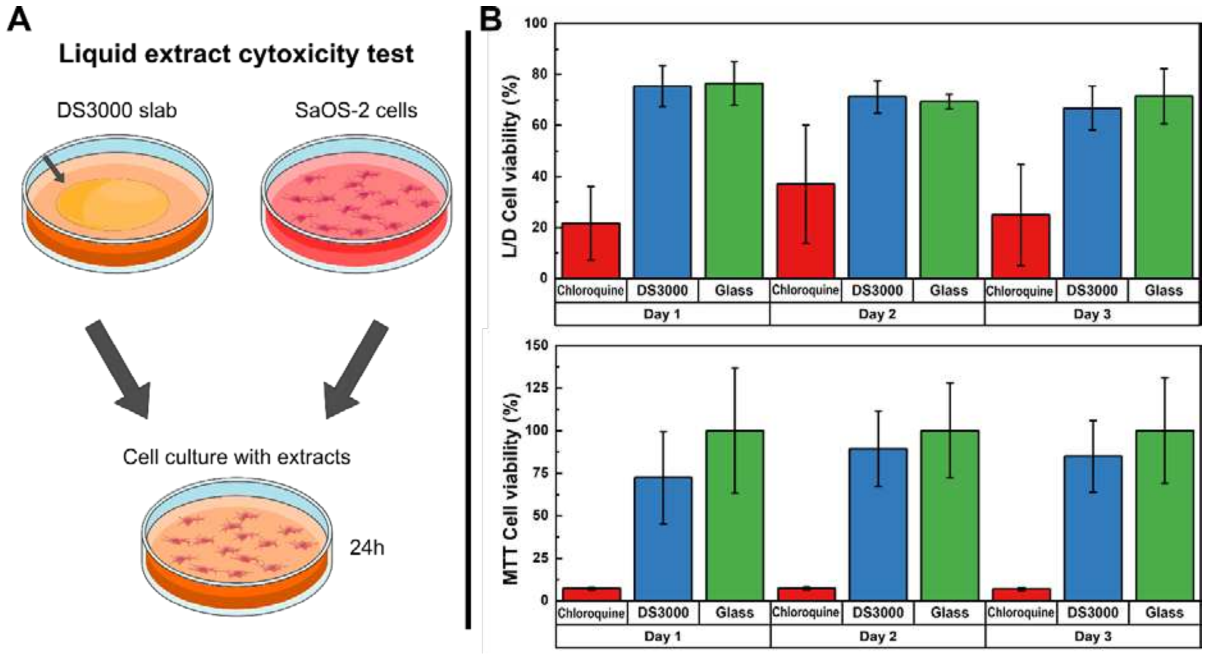

Figure 3.1. *Liquid extracts cytotoxicity test.* ***(a)*** *Schematic illustration of the protocol followed for the test.* ***(b)*** *Analysis of the cell viability of the SaOS-2 culture for the liquid extracts test by Live/Dead assay and MTT assay.* ***Death:*** *positive control obtained by diluting 3mM of chloroquine.* ***DS3000:*** *DS3000 slab.* ***Glass:*** *negative control on an 18-mm glass coverslip.*

Protocol 7. Liquid extracts cytotoxicity test

This protocol details the test by liquid extracts to evaluate the cytotoxicity of a material.

1. Prepare the samples to test. In our case, we used 18-mm coverslip MAPTMS-coated:
    a. Prepare a 2% MAPTMS water-solution
    b. Dip-clean the coverslips with sequential baths in acetone, ethanol then water and air-dry them
    c. Plasma-activate the glass surface using an Air-plasma at 0.2 mbar and 30W for 5 min
    d. Deposit a MAPTMS 150-200 µL droplet on the surface of the coverslip and incubate at RT for 2h
    e. In PDMS surface, deposit 30-35 µL droplet of DS3000 and cover with the MAPTMS-coated face of the glass coverslip. Then polymerize for 3 min and rinse in ethanol
2. Using a multi-well plate, incubate culture medium, changing it every 24h. Reserve culture medium for Day 1, 2 and 3
3. Incubate a subconfluent culture of SaOS-2 cells with the extracts obtained in point 2

Protocol 8. MTT assay

This protocol details the MTT assay used to evaluate the cell viability of a cell culture

1. MTT solution is diluted at 1 mg/mL in DMEM without phenol red nor SVF
2. Cell medium from the culture is replaced by 250 µL of MTT solution and incubate for 2h at 37 ºC
3. Solution is aspirated and the samples are left to dry for 30 min, then 250 µL of pure DMSO is added to each well to homogenise the solution
4. A control well (blank) is kept as background control
5. Absorbance is characterized using a Varioskan microplate reader at 570 nm (excitation at 650 nm). The percent of viability is calculated as:

$$\boldsymbol{Viability}\ (\%) = \frac{\boldsymbol{OD}_{\mathbf{570}\ \boldsymbol{Samp}} - \boldsymbol{OD}_{\mathbf{570}\ \boldsymbol{blank}}}{\boldsymbol{OD}_{\mathbf{570}\ \boldsymbol{Glass}}} \times \mathbf{100}$$

Protocol 9. Live/Dead assay

This protocol details the Live/Dead assay used to evaluate the cell viability of a cell culture

1. Prepare a solution of 2 µM of calcein and 4 µM of ethidium, diluted in DMEM without phenol red nor SVF
2. Aspirate the medium of the culture and replace it with the described solution. Then incubate for 30 min at 37 ºC
3. Re-aspirate the medium and change it with fresh DMEM without phenol red nor SVF
4. Image in green live cells (calcein) and red dead cells (ethidium), then count the cells

$$\boldsymbol{Viability}\ (\%) = \frac{\boldsymbol{n}_{\boldsymbol{LIVE}}}{\boldsymbol{n}_{\boldsymbol{LIVE}} + \boldsymbol{n}_{\boldsymbol{DEAD}}} \times \mathbf{100}$$

ii. Enhancing adhesion-coatings

To continue with the evaluation of the direct contact test, first, we need to ensure the adhesion of cells on the DS3000 substrates. As mentioned, we aim to use fibronectin to enhance the cell attachment to the surface of the DS3000. Due to the complexity of the final 3D architecture, we have first investigated the homogeneity of the coating directly on the 3D architectures. The structures were coated with a fibronectin solution at 10 µg/mL and then stained with anti-fibronectin fluorescence antibodies (AF594) in order to characterize the coating layer. The detailed protocol can be found in **Protocol 10**.

Protocol 10. Fibronectin coating and staining

This protocol details the fibronectin coating of samples and the staining with a fluorescence dye of such protein.

1. Place the samples in a multi-well plate and sterilize the samples with EtOH 70% (2 mL) for 1h. Then rinse with PBS (2 mL) and dry the samples for at least a day
2. **(Optional)** Activate the surface with a O_2-plasma treatment at 0.5 mbar and 50 W for 90 s
3. Deposit a droplet (300-400 µL) of a fibronectin solution (10 µg/mL) and incubate for 2 h at RT. Then rinse in PBS (2 mL) at least twice
4. Saturate nonspecific binding sites by incubating the samples in a solution of BSA (3% in PBS, 2 mL) for 45 min at RT. Then rinse in PBS (2 mL) 3 times
5. Deposit antibody anti fibronectin (rabbit) diluted 1/500 in PBS and incubate for 1 h at RT. Then rinse in PBS (2 mL) 3 times
6. Deposit secondary antibody anti rabbit-red AF594 diluted 1/500 in PBS and incubate 30 min at RT. Then rinse in PBS (2 mL) 3 times

In **Figure 3.2**, we show the resulting images obtained with a fluorescence confocal microscope at several z-planes. Images were compiled in a z-stack for better visualization of the 3D architectures. In the different columns we show the different conditions tested for this experiment: pristine[12], plasma-activated, fibronectin adsorption, and fibronectin adhesion by plasma-activation. The plasma-activated condition was carried out by using a O_2-plasma at 0.50 mbar of pressure and 50 W power for 90 s. We used the DAPI filter to observer the DS3000 architecture due to its photoluminescence properties in the UV-blue wavelength band. We can observe the two fluorescence channels imaged and the merged images.

---

[12] Pristine condition is considered as original state without any further modification after fabrication.

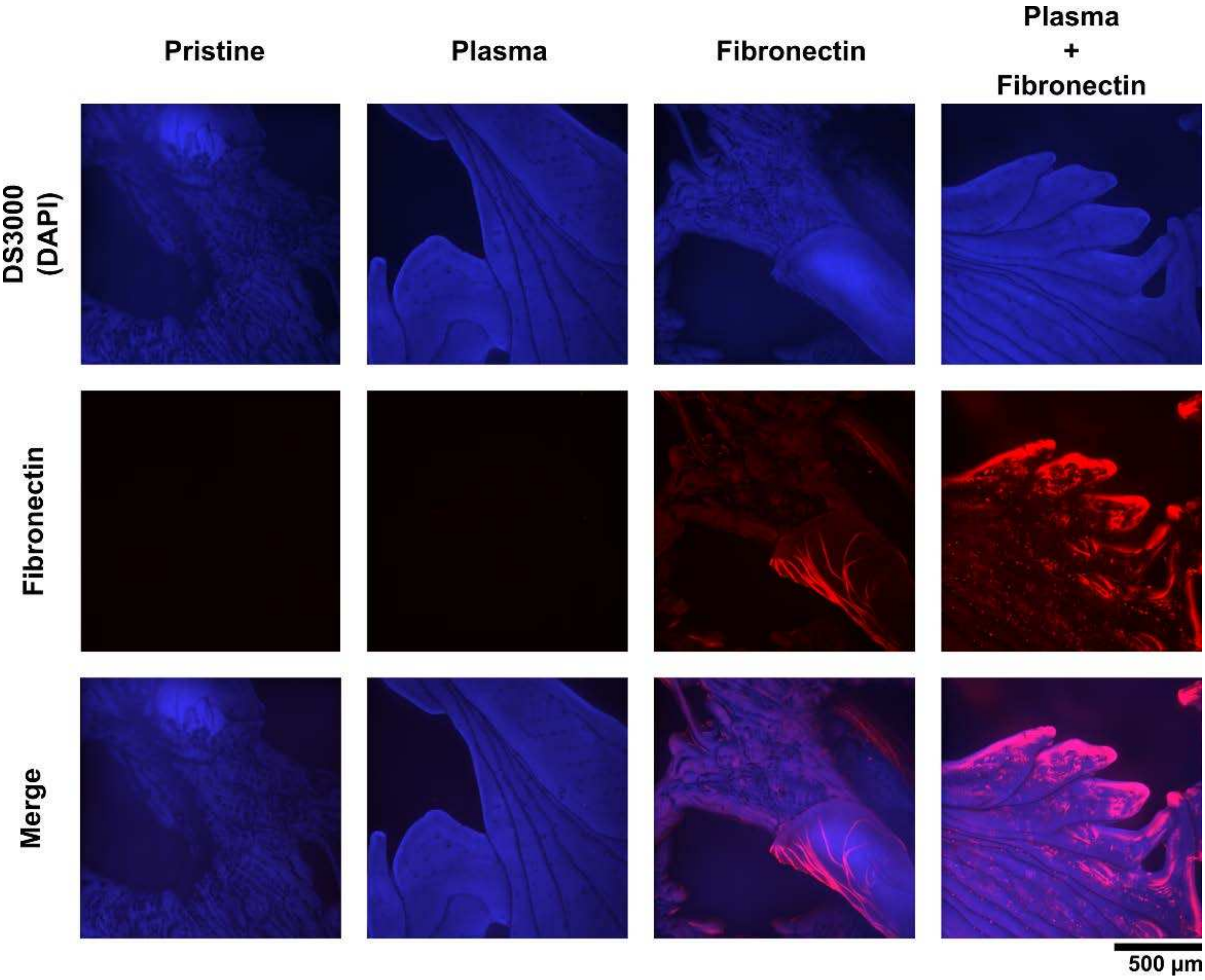

Figure 3.2. Fluorescence images characterizing the fibronectin coating on a 3D printed bone architecture (DS3000). First row depicts the sample structure using a 405-nm laser/DAPI filter. Second row presents the fluorescence data obtained by the anti-fibronectin dye AF594. Third row shows the merged channels overlapping the features of the DS3000 structures and the fibronectin coating.

This undesirable effect for the imaging of the cells, turned as a useful feature when characterizing the printed structures. Here, we can observe the different layers of the printed object along the z-axis which thickness was defined during the fabrication as 20 µm. Beneath these images, we can observe the corresponding images with the red dye AF594. For the pristine and the plasma conditions, we did not add any fibronectin solution. Hence, the anti-fibronectin antibodies did not interact to the surface which is consistent with the lack of fluorescence for these conditions. In the other two conditions, we can see the fluorescence signal due to the fibronectin absorbed on the surface. There are no visible differences due to the plasma-activation of the surfaces. Some granularity in the coating was observed with plasma-activation but we could not clearly correlate this effect to the plasma-activation. The last row corresponds to the merged channels, where we can see the overlapping of the fluorescence dye with the DS3000 structure. These images demonstrate the absorption of the fibronectin to the surface of the trabecular scaffold. For reasons of simplicity and due to the lack of differences in the process, we will disregard the use of the plasma activation for the coatings of DS3000 structures in the following experiments.

iii. Direct contact cell culture

After adequately coating the printed template, we proceeded to study the cytotoxicity of the material regarding the cell culture in direct contact with the material. In order to carry out these experiments we had to ensure the attachment of cells to the substrate and we used a fibronectin coating by adsorption as described at the beginning of **Protocol 10**. **Figure 3.3** presents images of the direct contact cell culture test. For this experiment, the 3D printed samples were previously rinsed. Samples sterilized with an 70% ethanol solution then incubated for different durations, changing washing liquid every 24h. The times selected for this evaluation were 0h, 24h and 48h. Once the washing step was completed, cells were seeded on the samples at 15000 c/cm^2 in droplet form and cultured in direct contact with the DS3000 for 48h in all the conditions, following **Protocol 11.** This period of time is enough to conclude on the harmful impact of the material (ISO 10993-5 recommends at least 24h). Then, cells were fixed and stained for fluorescence characterization as described in **Protocol 12.** Glass coverslips were used as negative controls.

Protocol 11. Cell seeding and cell culture

This protocol details the cell seeding of coated supports, 2D or 3D.

1. Once supports were coated and rinsed, cells were seeded at specified number according to the surface available for each support in a droplet form. Then incubate at 37 ºC for 1h
2. Fill the support with extra medium until complete 2 mL and incubate at 37 ºC
3. Change culture medium every 48-72h

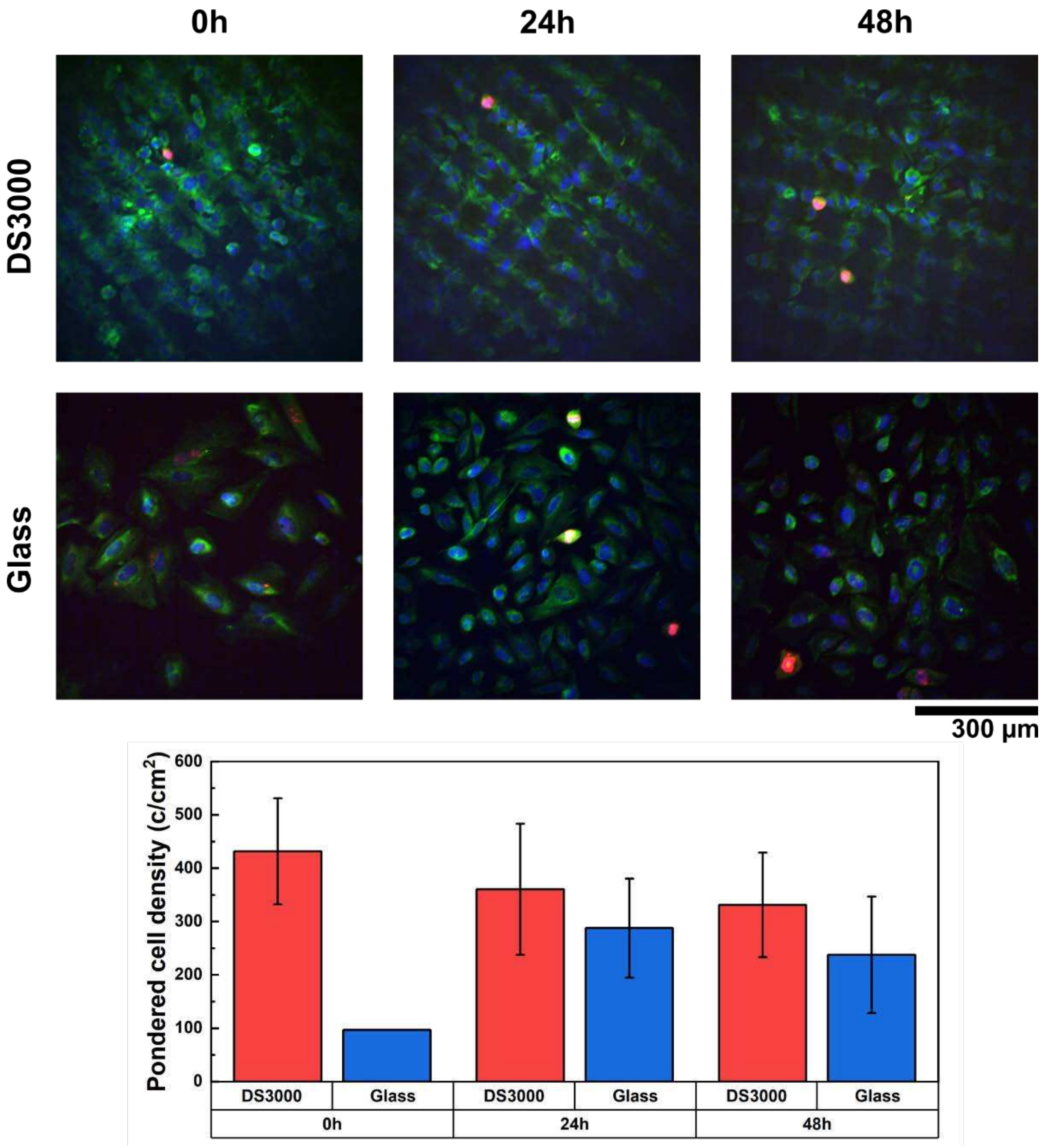

Figure 3.3. *Direct contact cytotoxicity evaluation of SaOS-2 on DS3000. A quantity of 15000 c/cm^2 was seeded in a droplet form on the substrate and culture for 48h. The study was carried out by immunofluorescence characterization of the welfare of the cells on DS3000 for different washing time: 0h, 24h and 48h.* ***Staining****: DNA-nuclei (blue), β-tubulin (green), Ki67 (red). Beneath, we present a cell counting per cm^2 for this experiment for the DS3000 substrates and the glass controls.*

Protocol 12. Cell fixation and staining

This protocol details the cell fixation and staining used along this work. In our case, we use DRAQ5 to stain DNA in the nuclei, anti-β-tubulin to stain the cytoskeleton and anti-Ki67 as proliferation tracker. These dyes can be changed by adapting concentrations and timings following manufacturer recommendations.

1. Remove culture medium and rinse with PBS. Then fix the cells with formalin for 30 min at RT and rinse 3 times with PBS
2. Permeabilize the membrane and saturate non-specific binding locations using BSA 3% and triton X100 0.2% for 50 min. Then rinse 3 times with PBS
3. Incubate primary antibodies for 1h15 at RT: anti-Ki67 (rabbit) 1/250 and anti-β-tubulin (mouse) 1/250. Then rinse 3 times with PBS
4. Incubate secondary antibodies for 45 min at RT: anti-rabbit-Cy3 1/250 and anti-mouse-AF488 1/250. Then rinse 3 times with PBS
5. Incubate DRAQ5 at 1/1000 for 15 min at RT. Then rinse 3 times with PBS

We first analyzed the evolution of the cell density on printed DS300 substrates according to the washing time. The data shows no significant difference in the evolution of the cell density according to the incubation conditions. We could observe certain differences in cell density when comparing the DS3000 substrate and the glass coverslip. We believe that this phenomenon can be related to the typical rugosity induced by the hatching of the printed process, which favors the adhesion and slightly higher surface available (due to the effect of the topography) and increases the apparent cell density. The organization of the cells over the DS3000 substrate, follows a grid pattern corresponding to the polymerization pattern created by the laser in the stereolithography process. We can conclude from the figure that DS3000 offers a good compatibility for cell culture, including a negligeable cytotoxicity by cell contact. Furthermore, in both our cytocompatibility assays, we did not found evidence of the need of a washing step to rinse the liquid extract from the material. Consequently, we will neglect this step for the rest of the project.

iv. Investigating cell adhesion

To conclude our investigation regarding the use of DS3000 as a cell culture support, we investigated cell adhesion using different surface treatments on DS3000 substrates, using glass coverslips as control substrates. As previously, samples were sterilized with 70% ethanol then surface activated or fibronectin coated. Cells were seeded at 15000 c/cm^2 in the form of droplet deposited and kept at 37 ºC for 1h before complete filling the wells with extra α-MEM medium. The cells were kept in culture for 48h and then fixed and stained following the steps described in **Protocol 11** and **12**.

Figure 3.4 shows the immunofluorescence images obtained for the described adhesion experiment. In the first row, we can observe the growth of cells over the DS3000 substrate, while in the second, we observe the data obtained for the cells growing on the glass coverslip controls. The different rows correspond to the different adhesion enhancing conditions: pristine, plasma activation and fibronectin adsorption. In all the images presented, we observe a dense layer of cells growing over the 6 conditions evaluated with no significant difference in the apparent cell density. We thus cannot conclude on the potential impact of the investigated conditions on cell adhesion. Pristine DS3000 shows as well adequate conditions for cell adhesion on 2D configuration. We can note the limitations presented in the imaging when using the UV-blue band (350-450 nm) due to the photoluminescence of the DS3000 that makes the quantification of the cells more difficult. This might be an issue when observing cells on 3D complex structures, such as trabecular bone microarchitectures. Yet, it can be turned into a useful feature under certain circumstances to image the 3D fabricated structure.

Despite these conclusions that suggest a weak influence of the surface treatment conditions, we use the fibronectin coating as a standard condition for the rest of the project. Fibronectin allows to both enhance the adhesion and favor hydrophilic behavior of the materials surfaces. However, it is interesting to notice that cell adhesion is highly cell-type dependent. The results obtained on SaOS-2 cell lines may not be generalized to other cell types or primary cells [3], [18], [19].

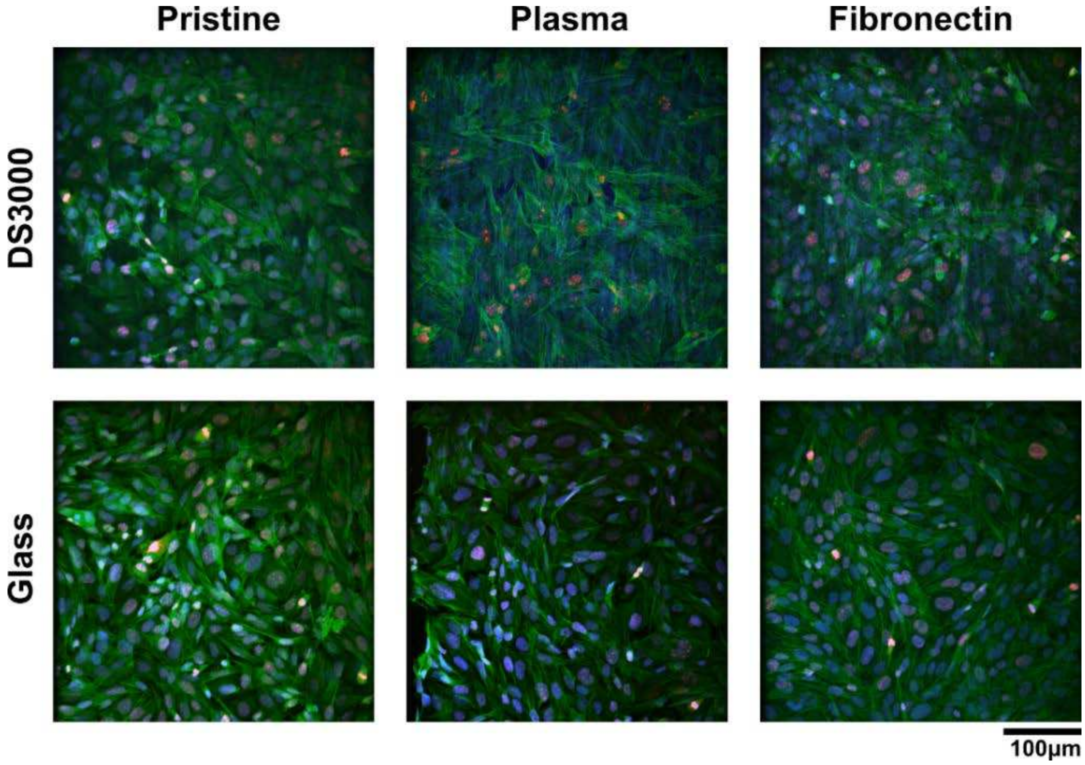

Figure 3.4. *SaOS-2 culture to evaluate the cell adhesion on DS3000 and glass with different adhesion enhancement protocols: pristine, surface plasma-activation and fibronectin adsorption. A droplet containing 15000 cells/cm^2 was deposited and culture for 48h prior fixation and staining.* ***Staining:*** *nuclei (blue), β-tubulin (green), Ki67 (red).*

b. PDMS substrates

Polydimethylsiloxane is a well-known biocompatible material, described in the **Chapter 2.** There is an extensive literature regarding the cell culture compatibility with PDMS [20]–[23]. This is the main reason why we selected PDMS as an alternative to additive manufacturing materials, trying to adapt free-form manufacturing technique to this silicone material. From here, as many others before us, we will assume that PDMS (in particular, Sylgard 184 from Dow Corning) is a cell culture compatible material and we will obviate the need of washing step and experiments to clarify this. In order to verify the viable conditions for cell culture and the state of the cells regarding adhesion on this hydrophobic material, we performed an experiment based on prior knowledge acquired within our team and guided by the literature [11], [14], [24], [25]. **Figure 3.5** shows the data obtained by seeding SaOS-2 cells at 15000 c/cm^2 on PDMS slabs of 2.5 cm^2 fabricated by the standard processes detailed in **Protocol 3**, from **Chapter 2.** Due to the inherent hydrophobicity of pristine PDMS surface [24], the deposition of cells and consequently cell culture on such substrate has been obviated due to the difficulties of depositing the cell solution droplet and incubate it in the surface for 1h. The surface conditions analyzed for these experiments were plasma-activation and fibronectin-coating after plasma activation (O_2-plasma at 0.5 mbar, 90 s, 50 W, Diener Electronic). Cells were characterized using immunofluorescence staining to identify the cell density and the cytoskeleton. As shown in **Figure 3.5**, cells seeded on the plasma-activated surface present a clumpier organization and globular shape. We can observe the cells on the fibronectin-coated surfaces present a more spread morphology with a stronger red signal coming from the actin fibers.

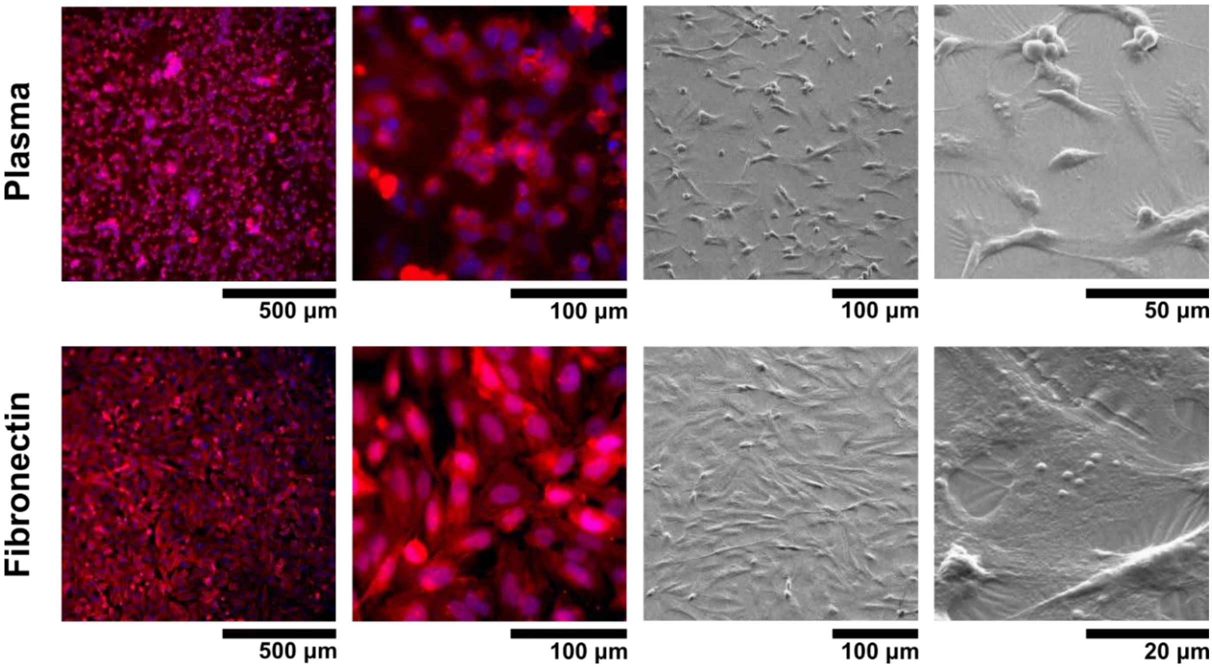

Figure 3.5. *SaOS-2 growing in PDMS with different adhesion treatment: plasma-activated surface and plasma activated surface + fibronectin coating. A cell suspension with 15000 cells/cm^2 was seeded and cultured for 48h prior fixation and staining.* ***Left.*** *Immunofluorescence images at different magnification shows the welfare and attachment of the cells.* ***Staining:*** *nuclei (blue), F-actin (red).* ***Right.*** *SEM characterization was performed in order to obtain a better view of the cell morphology over the treated substrates.*

To observe with more details the cell morphology, we also investigated SEM characterization. Samples dedicated for the purpose were fixed with a specific protocol dedicated for SEM with the intent of maintaining the cell morphology during dehydration, this fixation process is detailed in **Protocol 13**. Afterwards, cells were metallized and imaged (**Figure 3.5**). There is a clear difference in term of morphology and adhesion regarding both surface treatments. SaOS-2 cells seeded on the fibronectin-coated PDMS display a much more flatten morphology while in the plasma activated PDMS, they present the globular morphology commented before which is typical of poorly attached cells [26]. We can conclude then that fibronectin promotes the cell adhesion and provides a healthier microenvironment for the welfare of cell culture.

Protocol 13. Cell fixation and staining for SEM characterization

This protocol details the cell fixation and preparation prior a SEM characterization

1. Remove culture medium and rinse with PBS
2. Incubate the cells in 4% glutaraldehyde solution for 4h at RT. Then rinse 3 times with PBS
3. Dehydrate the sample by incubating it sequentially in 50, 70, 90 and 100 % ethanol solutions for 4 min each step
4. Remove the ethanol and let evaporate at room temperature
5. **(Optional)** Metallize the sample using a 15-nm thickness layer of Au

c. Summary

- We have presented a full protocol to validate a new material for cell culture applications, adapting a standardization rule for our experiments [17].
- We carried out the protocol on DS3000 in order to prove the viability of cells during culture, using viability test as MTT or L/D assays and fluorescence microscopy for the 4-steps validation process:
    - Cytotoxicity test by liquid extract
    - Protein-coating characterization of the surfaces
    - Cytotoxicity test by direct contact cell culture
    - Investigation of the promotion of cell adhesion
- The previous protocol was simplified to be used with PDMS, a well-known biocompatible material and to only investigate the cell adhesion conditions.

- These two sets of experiments allowed to confirm the viability of DS3000 and PDMS as candidate to fabricate *in-vitro* models.

2. Investigating cell culture in 3D scaffolds

Next, we performed a validation of cell culture in the 3D microenvironments created with both materials, focusing on the topology and its impact on the cellular behavior, cell morphology and proliferation. Therefore, in this section, we will focus on the analysis of the 3D cell culture performance in a trabecular bone microarchitecture fabricated in DS3000 resin, and the culture in a porous PDMS monolith. In both cases, the structures will be coated with fibronectin to enhance the adhesion of cells and try to provide the environment with a similar surface chemistry.

a. DS3000 trabecular bone microarchitecture

The main goal of these experiments is to prove the viability of cell culture in a 3D architecture fabricated by additive manufacturing using the commercial resin DS3000. We already proved in the past section the compatibility of the material in terms of cytotoxicity, yet remains the challenge of imaging a 3D architecture.

There are several delicate points to face when characterizing a 3D structure. First, the already mentioned photoluminescence of the DS3000 may induce a strong background light in the UV-blue band of the visible spectrum and should limits the use of certain fluorescence markers. Second, the scattering of the light when passing through the material. Though DS3000 is not fully transparent, it allows light to pass across the material, scattering the light especially on the edges of the slicing artefact created by the fabrication method. Third, the liquid retention typical for these porous architectures that remains trapped even in dry conditions and further create additional optical interfaces with different refraction indexes. Drying the sample is a partial solution that could harm the state of the fixated cells if they remain a long time in such condition. Performing the immersion imaging it is another potential solution that will compromise the depth of field and generate other potential distortions. Both solutions have been explored along this work using the different microscopes available. Upright epifluorescence microscopy and confocal fluorescence microscopy have yielded the best results regarding imaging these structures.

In **Figure 3.6**, we show immunofluorescence images obtained by upright epifluorescence microscopy of SaOS-2 seeded on a 3D trabecular bone structure (10-mm diameter and 4.5-mm height). A cell solution of 15000 c/cm^2 was deposited in a droplet and incubated for 72h prior fixation and staining. Blue color channel presented a strong background light thus RGB images were composed with green and red channels only, depicting the cytoskeleton and the proliferating cells respectively. In the right image, we can observe a low magnification image of the structure covered by cells at different depths. We see how cells have reached the different levels of porosity and covered rather homogeneously the architecture. Certain distortions can be observed in the images due to the liquid retained in the porosity and air bubbles. In the left image, we can observe a higher magnification image of the cells in the scaffold. There, we can also observe cells adapting to the edges of the structure and displaying a spread shape on the structure. We note as well a rather high cell density on the surface, with most of the cells exhibiting red staining marker of proliferation, Ki67. This marker is expressed during DNA replication and is typically located at the of chromosomes vicinity. It is typically displayed as small red dots located in the nuclei. In our case, the complexity of the trabecular architecture induces light scattering and optical distortions that affects the image resolution and induce blurring of the image. As a result, Ki67 provides a homogeneous staining of the nucleus that appears with a rounded homogeneous shape.

The samples were then analyzed using upright confocal fluorescence microscopy in an immersion configuration. Several z-stacks were taken in order to perform the 3D reconstruction of the structure. One of these 3D reconstructions is shown in **Figure 3.7A**, representing a 250 µm-depth z-scan. **Figure 3.7B** shows a schematic illustration of the image acquisition along the z-axis and presented in **Figure 3.7C-F**. In these images we highlighted how cells adapt their shape to the topology of the structure. In **Figure 3.7C-D**, we observe cells bounded in packed configuration in a planar organization parallel to the image plane. While **Figure 3.7E-F** displayed cells along the vertical walls of the pores.

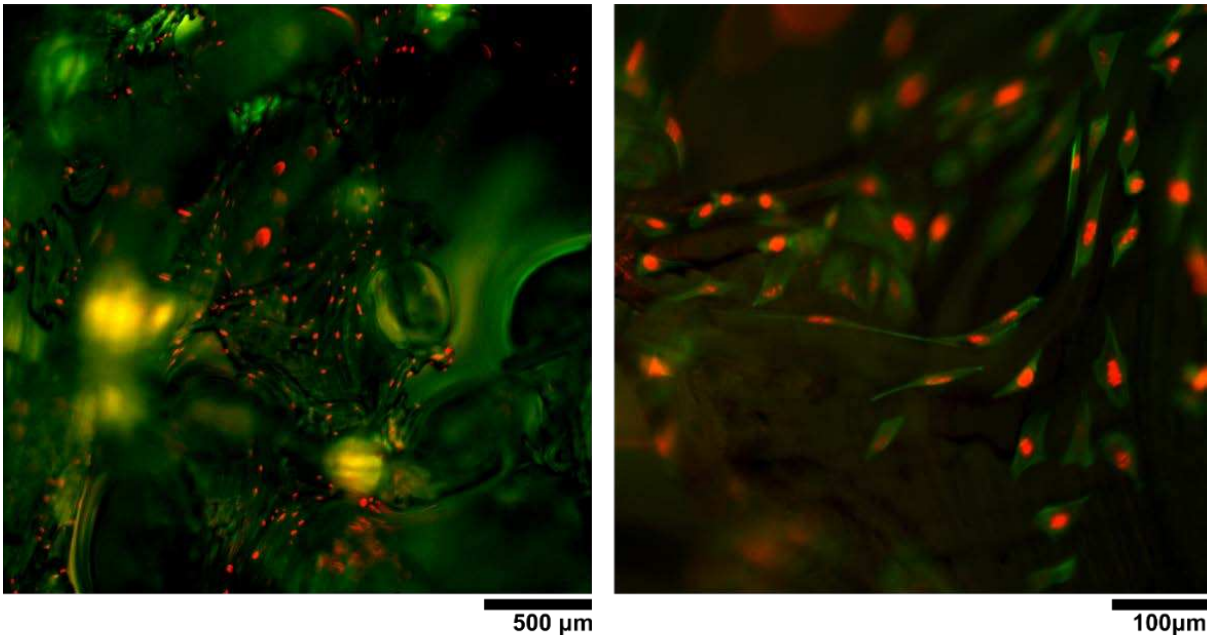

Figure 3.6. *Immunofluorescence images of 3D cell culture of SaOS-2 proliferating in a trabecular bone microarchitecture 3D printed in DS3000 using stereolithography. Bone scaffold was fibronectin-coated following the protocol described in* ***Protocol 10****. Cell solution was deposited at 15000 c/cm^2 and kept in culture for 72h prior fixation and staining, following* ***Protocol 11*** *and* ***12****.* ***Staining:*** *DAPI-architecture (blue, not shown), F-actin (green), Ki-67 (red). Distortions in the pictures are caused by the scattering of the light passing through the PBS retain in the porous architecture.*

These results have been reproduced at different points of this project with culture length ranging from 72h to 1 week of *in-vitro* culture. In these scaffolds, we have achieved diverse spatial configuration with cells attached to the surface of the architecture from diverse orientations, displaying a strong expression of proliferation markers. Finally, we can conclude that DS3000 3D architectures are adapted to host a cell colony in 3D organization without any harm for the cells. The subsequent works will lead to the culture of primary bone marrow mesenchymal stromal cells and the inclusion of the fluid movement within the systems. This will provide another cue to the cellular microenvironment of the bone marrow. From there, we will start to study the impact of the porosity on cellular behavior. We have prioritized the development of the perfusion system due to the impact that the porosity will have on the fluid mechanics, which could potentially invalid the static culture outcomes. Moreover, to avoid the overlap between the photoluminescence signal and the DAPI-labeling, we will use when possible alternative nuclei staining such as DRAQ5 in the far-red band.

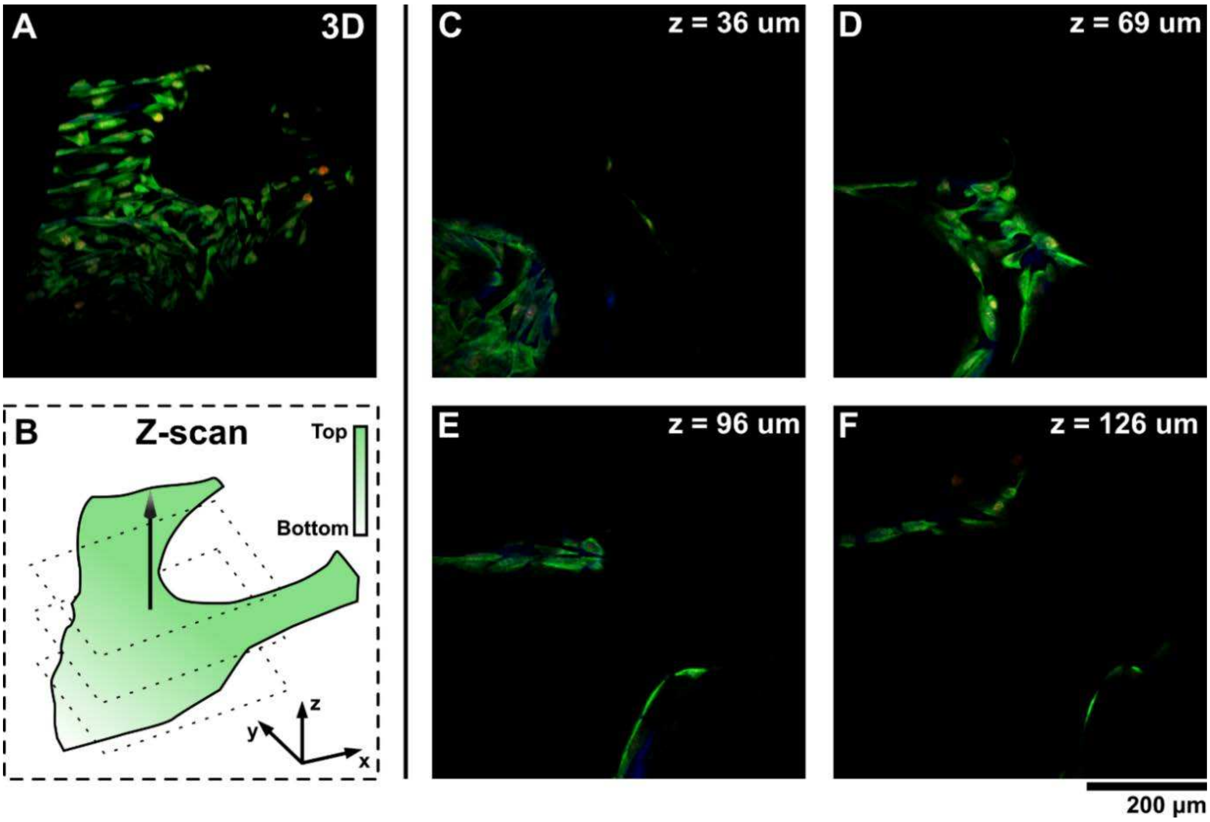

***Figure 3.7.** 3D Confocal microscope imaging of the experiment show in Figure 3.6. **(a)** 3D reconstruction from a 250 µm depth z-stack. **(b)** 3D schematic illustration representing the 3D reconstruction and the subsequently z-planes displayed in (c-f). **(c-f)** Fluorescence images showing the 3D structure and the cell distribution at different z: 36, 69, 96 and 126 µm.*

b. Free-form fabricated Porous PDMS

In **Chapter 2**, we introduced a novel technique to structure PDMS into a porous monolith. This technique is based on a water-in-PDMS emulsion that does not involve any further reactant nor surfactant; thus, we could assume that the resulting structure will be uniquely composed of PDMS displaying a specific morphology, without additional modification in terms of physico-chemical properties. In order to validate this hypothesis, we implemented cell culture into the porous architecture as a tool for the 3D cell culture. The scaffolds were coated with fibronectin following the indications in **Protocol 10**. Because the hydrophobic nature of the PDMS makes difficult the penetration of water-based solutions into the structure, plasma-activation is recommended. Cells were deposited in the form of a droplet on top of the architecture with a concentration of 15000 c/cm^2. Then, the cells were left to infiltrate the core of the scaffold and adhere to the PDMS surfaces for 1h at 37 ºC. Additional α-MEM was added into the samples and cells were cultured for 72h prior fixation and staining.

In terms of imaging, porous PDMS raises other challenges compared to the previous DS3000 architecture. Porous PDMS displays negligeable photoluminescence effect at any band of the visible spectrum. However, PDMS is prone to non-specific binding of proteins or staining reactants that can lead to fluorescence background, yet less intense than specific binding. Furthermore, as we could notice, porous PDMS displays an opaque white color along the whole structure. We relate this effect to the dense rugosity and numerous microcavities that can scatter light at any wavelength. Nevertheless, intense fluorescence activity can pass though some points of the architecture if the cavity membranes are thin enough. Moreover, the possibility of cutting the structure without risk of material fracturing gives us direct access to the inner porous in the structure without having to image through the material.

Figure 3.8 presents the epifluorescence characterization performed over a porous PDMS monolith (semi-cylindrical shape of 14-mm diameter and 15-mm height). The sample was cut at its center and shows the distribution and welfare of cells within the porous scaffold. In **Figure 3.8A**, we can observe the cell spreading and colonization along the different pores of the interconnected structure. We can distinguish several cells colonizing the full structure at different out-focus planes and inside the cavities. In **Figure 3.8B**, we present a close-up view of a single pore (enclosed by the blue square in the **Figure 3.8A**). It depicts how the elongated cytoskeleton of the cells adapts to the surrounding environment following the geometrical profile of the pore and displays a rounded shape. Finally, **Figure 3.8C** shows a fluorescence image of another region of the scaffold where we can easily identify the cell nuclei and observe a homogeneous coverage of the whole PDMS architecture.

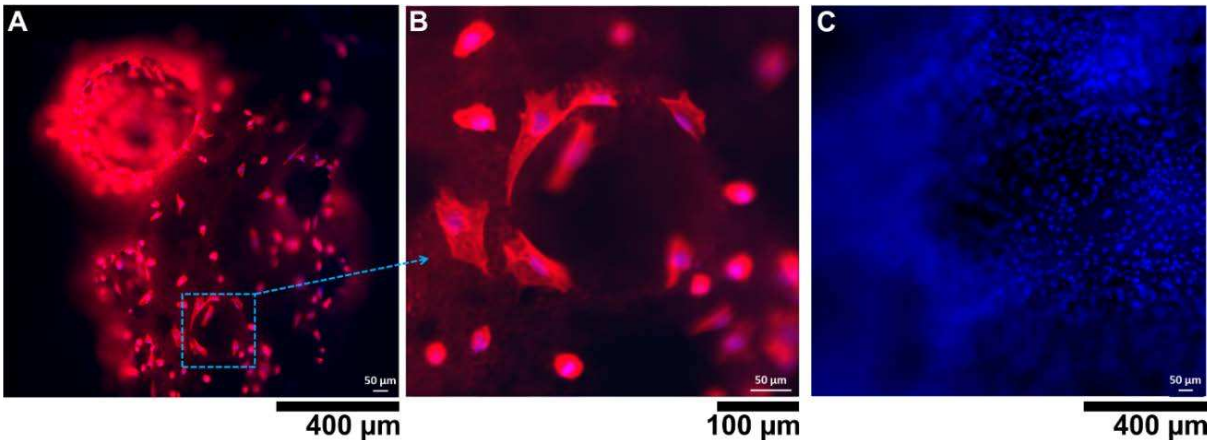

Figure 3.8. *Immunofluorescence imaging of SaOS-2 growing inside a porous PDMS monolith.* ***(a)*** *Cells colonizing the pores of the porous PDMS scaffold and reaching the different cavities of the structure.* ***(b)*** *Close-up view on the region enclosed in the blue dotted square, depicting cells adapting to the curvature of the different pores.* ***(c)*** *Dense layer of SaOS-2 observed on the PDMS porous scaffold surface.* ***Staining:*** *nuclei (blue) F-actin (red).*

To better visualize the morphological features of the SaOS-2 cell cultured on the 3D scaffold, we employed SEM characterization. In **Figure 3.9**, we report false-colored SEM close-up images highlighting the typical cell morphology observed in the different regions of the inner-core of the scaffold. Cells tend to develop cytoskeletal extensions anchoring at several points of the side walls of the micropores. This induces a tridimensional spatial configuration that can be observed in **Figure 3.9A-B.** Clusters of cells with a more flattened and elongated morphology can be found as well in different sites of the PDMS meshes (**Figure 3.9C).** Furthermore, we can discriminate several round protuberances within the cytoskeleton and around the SaOS-2. Similar features have been already reported in literature and are associated with mineralized buds and calcopherulites related to the mineralization process characteristic of this cell line [16], [17].

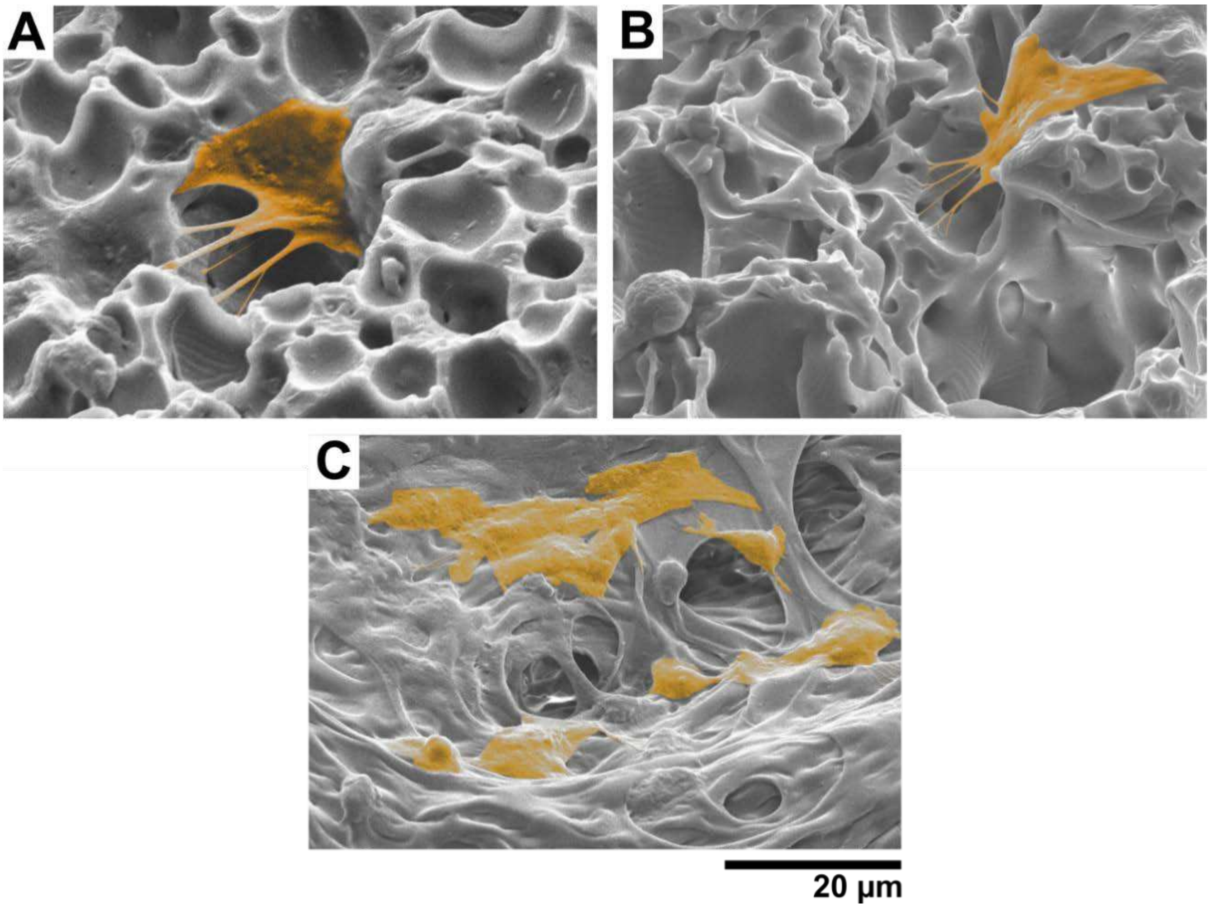

Figure 3.9. *SEM characterization images of the cells over the rough porous PDMS surface. Cells have been false-colored to highlight the typical morphology of the cells with several anchoring points over the walls of the cavities in a 3D spatial configuration.*

Furthermore, an extra viability test was performed over the porous PDMS to confirm the similar performance between the 3D architecture and the bulk PDMS. **Figure 3.10** shows a Live/Dead assay with bulk PDMS and glass as positive controls to confirm the cell viability. Live cells were stained with calcein (green), while dead cells were stained with ethidium (red). Both populations were counted and normalized, and the results of the viability test reached values of ~ 99% with a homogeneous cell distribution.

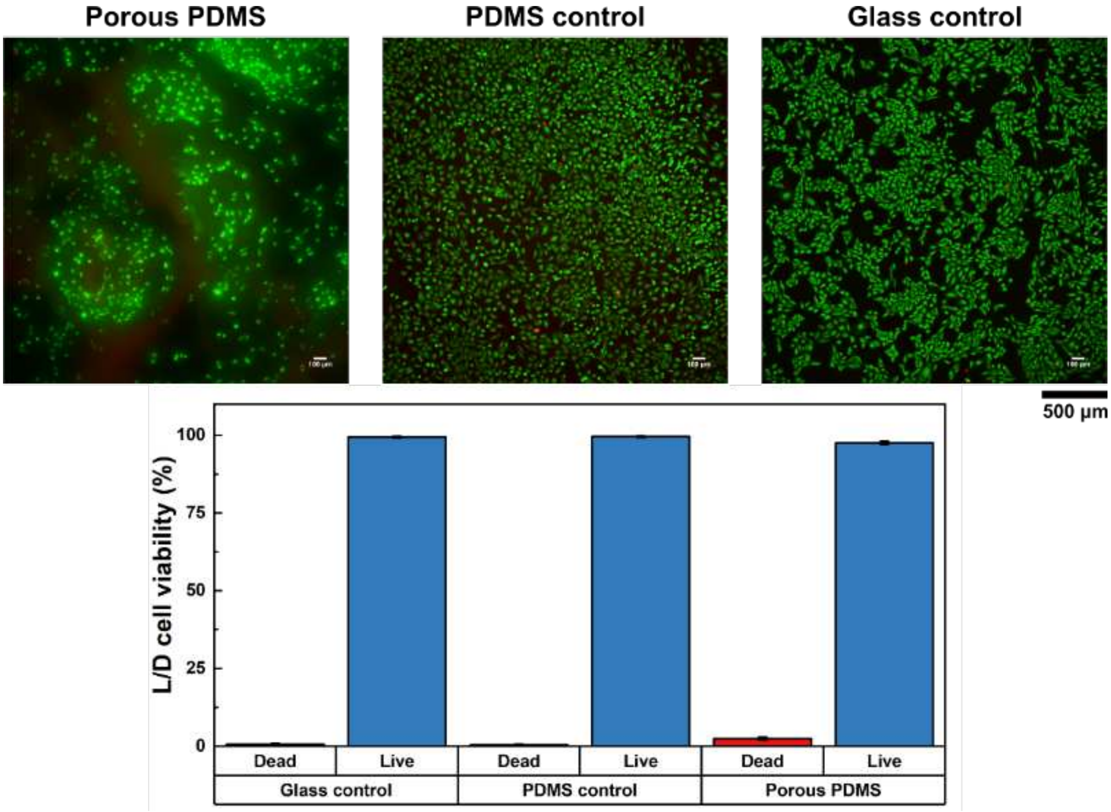

Figure 3.10. (a-c) *Live/Dead assay results of SaOS-2 cell culture after 72h on porous PDMS scaffold and positive controls of bulk PDMS and glass.* ***(d)*** *Analysis of the cell viability test.*

A 3D characterization was carried out via two-photon confocal imaging, a widely used technique for unveiling cell features in the inner core of 3D architecture that otherwise would not be accessible by a more conventional morphological imaging approaches, such as SEM or AFM. In this case, living cells were labeled using CMFDA (green), staining the cytoplasm and Hoechst (blue), staining the DNA. In **Figure 3.11**, we report several 3D reconstructions to study the 3D cell colonization scenario of the PDMS porous scaffold. In **Figure 3.11A-B**, we present the characterization of the upper part of the 3D scaffold where the cell solution was deposited. The configuration of the laser beam regarding the scaffold orientation is depicted in the inset of the **Figure 3.11A**. The overall field of view of the acquisition is $1.96 \times 1.30 \times 0.49\ mm^3$, obtained by stitching several smaller areas with the mosaic modality of the system. **Figure 3.11A** shows a quite homogeneous cell cover on the porous PDMS surface, while **Figure 3.11B** highlights how cells are able to colonize the inner part of the architecture by infiltrating the pore necks into new cavities. We can attribute the absence of cells in the central part of the 3D reconstruction to the empty space of the cavity where there is no surface for cells to adhere, or low accessibility regions in the porous PDMS due to small or non-connected pores. **Figure 3.11C-D** presents a further insight into the cellular distribution within the 3D architecture by characterizing the inner core access by a cross-cut using a surgical blade. This internal view depicts a region of $1.30 \times 1.96 \times 2.19\, mm^3$ of the inner surface, employing the mosaic featured mentioned. In these images, we can clearly observe the penetration of the cells within the scaffold and the presence of cell clusters few millimeters deep into the structure.

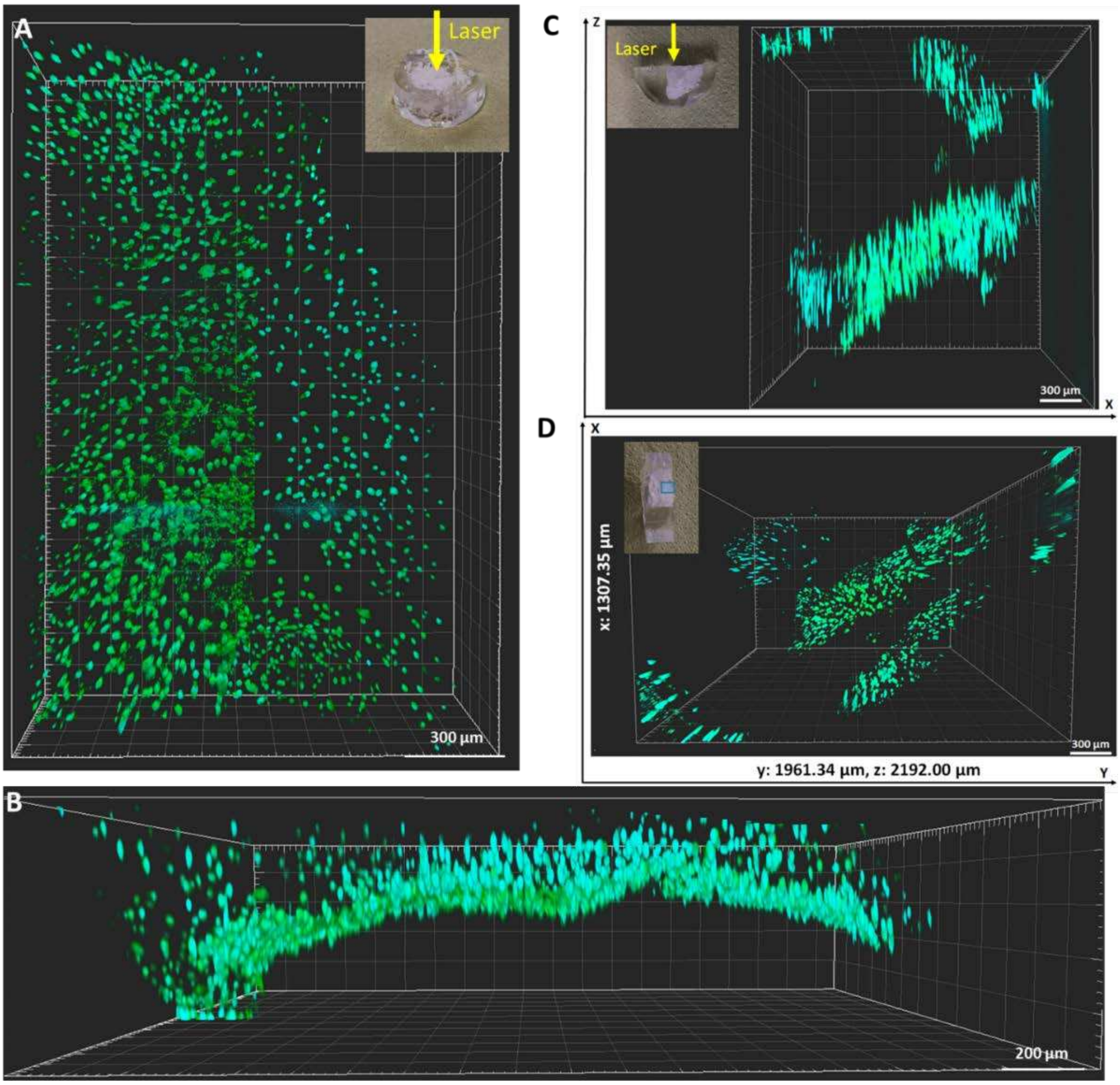

***Figure 3.11**. Two-photon confocal imaging of the PDMS porous scaffold colonized by SaOS-2 cells. **(a)** XY-view of the 3D reconstruction of the scaffold imaged with the laser beam impinging the sample as shown in the inset. **(b)** XZ-view of the 3D reconstruction in (a). **(c)** XZ-view of the 3D reconstruction of a cross-cut of the scaffold imaged with the laser beam impinging the sample as shown in the inset. **(d)** XY-view of the 3D reconstruction in (c). The inset shows the sample orientation and the region depicted in the 3D reconstruction. **Staining**: cytoplasm (green, CMFDA), DNA (cyan)*

c. Summary

- We have performed the first validation of 3D cell culture in trabecular bone microarchitectures fabricated in DS3000 and coated with fibronectin.
- Cell culture was characterized using epifluorescence microscopy to observe the cells on the scaffold and then confocal microscopy to obtain 3D visualization of the cells at different z-planes.
- An alternative staining for the cell nuclei, DRAQ5 instead of DAPI, has been proposed to avoid the overlap between the photoluminescence of DS3000 and blue-band dyes.
- Regarding porous PDMS, a first 3D cell culture was carried out for 72h on the structure after fibronectin coating.
- Cell culture was characterized by epifluorescence microscopy and two-photons confocal microscopy to investigate the 3D coverage of the material.
- Despite the difficulties to quantify populations in 3D, a Live/Dead assay was performed over the porous PDMS to confirm the viability of the material to host 3D cell colonies.

3. Conclusions

In this chapter, we explore a recurrent question expressed in the literature regarding the need for experimental evaluation of the cytotoxicity of the new materials. The main considerations are related to the capacity of the materials to provide an adherent substrate where cells can attach, and to display a chemical activity non-harmful for the cells to the cellular microenvironment. The main challenge when considering these two points is the fact that both are entangled. Hence, it might be difficult to discern the origin of this result from a negative outcome. To evaluate these two parameters, it is required to carefully design a set of experiments to isolate cytotoxicity from adhesion. Here, we proposed: first, to study the impact of potential liquid extracts from the material on the cells; second, to homogenize the chemical surface of the tested materials using fibronectin coating as common adhesion promoter; third, to perform subsequential washing step with direct contact cell culture in order to verify the impact of extracting by-products from the material; and finally, to evaluate the adhesion performance of the materials by seeding cells in different conditions. This back-and-forth experimental investigation between adhesion and cytotoxicity ensures the compatibility of the material with the selected cell culture. DS3000 provided an excellent cell viability in our 2D assays in terms of adhesion and cytotoxicity. PDMS was obviated from cytotoxicity test and protein coatings evaluation due to the wide literature confirming the biocompatibility of PDMS, yet it was confronted to the cell adhesion experiments where we proved the need of a fibronectin coating.

After concluding on the viability test and proving the capacities of DS3000 and PDMS to host cell culture, we implemented the 3D cell culture in static conditions. Here, a major challenge when working with 3D architectures is the imaging of the cells within the structures. In the case of DS3000, we have a photoluminescent material that impedes the use the UV-blue band in immunofluorescence staining due to the large background light. Cells were seeded by droplet deposition on top of the bone scaffold and successfully infiltrated the porous structure with a homogeneous cover. They displayed flatten and elongated shapes and a strong expression of proliferation markers, sign of the welfare of the cells. In the case of porous PDMS scaffolds, a similar outcome was shown. Cells colonized the structure and presented strong expression of proliferation markers. The SEM images showed that cells adapted to the surface of the cavities, displaying prolongation to adhere in a three-dimension spatial organization within the scaffold. The possibility of cutting the scaffold with a surgical blade allowed us to better characterize the inner core of the structure, which presents a major advantage compare to other 3D architectures.

The coming pages will take us to the last step to consider to reproduce the *in-vivo* biophysical conditions of the bone marrow cellular microenvironment, the fluid movement. The integration of the 3D scaffolds into perfusion systems will allow us to control the flow within the structures and thus to tune the supply of nourishment and to mechanically stimulate the cells by shear stress. We consider this to be a key element to achieve a tissue-like organization in *in-vitro* systems.

References

[1] Z. Li *et al.*, “Initiation efficiency and cytotoxicity of novel water-soluble two-photon photoinitiators for direct 3D microfabrication of hydrogels,” *RSC Adv.*, vol. 3, no. 36, pp. 15939–15946, Sep. 2013, doi: 10.1039/c3ra42918k.

[2] S. Kreß, R. Schaller-Ammann, J. Feiel, J. Priedl, C. Kasper, and D. Egger, “3D Printing of Cell Culture Devices: Assessment and Prevention of the Cytotoxicity of Photopolymers for Stereolithography,” *Materials (Basel).*, vol. 13, no. 13, p. 3011, Jul. 2020, doi: 10.3390/ma13133011.

[3] S. Vohra, K. M. Hennessy, A. A. Sawyer, Y. Zhuo, and S. L. Bellis, “Comparison of mesenchymal stem cell and osteosarcoma cell adhesion to hydroxyapatite,” *J. Mater. Sci. Mater. Med.*, vol. 19, no. 12, pp. 3567–3574, Dec. 2008, doi: 10.1007/s10856-008-3525-z.

[4] S. B. Rodan *et al.*, “Characterization of a Human Osteosarcoma Cell Line (Saos-2) with Osteoblastic Properties,” *Cancer Res.*, vol. 47, no. 18, pp. 4961–4966, 1987, doi: 10.1016/j.smallrumres.2012.09.013.

[5] H. J. Hausser and R. E. Brenner, “Phenotypic instability of Saos-2 cells in long-term culture,” *Biochem. Biophys. Res. Commun.*, vol. 333, no. 1, pp. 216–222, Jul. 2005, doi: 10.1016/j.bbrc.2005.05.097.

[6] K. J. Lampe, R. M. Namba, T. R. Silverman, K. B. Bjugstad, and M. J. Mahoney, “Impact of lactic acid on cell proliferation and free radical-induced cell death in monolayer cultures of neural precursor cells,” *Biotechnol. Bioeng.*, vol. 103, no. 6, pp. 1214–1223, Aug. 2009, doi: 10.1002/bit.22352.

[7] Y. Xu, A. B. Xepapadeas, B. Koos, J. Geis-Gerstorfer, P. Li, and S. Spintzyk, “Effect of post-rinsing time on the mechanical strength and cytotoxicity of a 3D printed orthodontic splint material,” *Dent. Mater.*, Feb. 2021, doi: 10.1016/j.dental.2021.01.016.

[8] K. H. Reinert, “Aquatic toxicity of acrylates and methacrylates: Quantitative structure-activity relationships based on Kow and LC50,” *Regul. Toxicol. Pharmacol.*, vol. 7, no. 4, pp. 384–389, Dec. 1987, doi: 10.1016/0273-

2300(87)90059-6.

[9] F. Alifui-Segbaya, S. Varma, G. J. Lieschke, and R. George, “Biocompatibility of Photopolymers in 3D Printing,” *3D Print. Addit. Manuf.*, vol. 4, no. 4, pp. 185–191, Dec. 2017, doi: 10.1089/3dp.2017.0064.

[10] N. P. MacDonald *et al.*, “Assessment of biocompatibility of 3D printed photopolymers using zebrafish embryo toxicity assays,” *Lab Chip*, vol. 16, no. 2, pp. 291–297, Jan. 2016, doi: 10.1039/c5lc01374g.

[11] J. H. Seo, K. Sakai, and N. Yui, “Adsorption state of fibronectin on poly(dimethylsiloxane) surfaces with varied stiffness can dominate adhesion density of fibroblasts,” *Acta Biomater.*, vol. 9, no. 3, pp. 5493–5501, Mar. 2013, doi: 10.1016/j.actbio.2012.10.015.

[12] Y. Gustafsson *et al.*, “Viability and proliferation of rat MSCs on adhesion protein-modified PET and PU scaffolds,” *Biomaterials*, vol. 33, no. 32, pp. 8094–8103, Nov. 2012, doi: 10.1016/j.biomaterials.2012.07.060.

[13] B. Richter *et al.*, “Guiding Cell Attachment in 3D Microscaffolds Selectively Functionalized with Two Distinct Adhesion Proteins,” *Adv. Mater.*, vol. 29, no. 5, p. 1604342, Feb. 2017, doi: 10.1002/adma.201604342.

[14] A. Béduer, C. Vieu, F. Arnauduc, J. C. Sol, I. Loubinoux, and L. Vaysse, “Engineering of adult human neural stem cells differentiation through surface micropatterning,” *Biomaterials*, vol. 33, no. 2, pp. 504–514, Jan. 2012, doi: 10.1016/j.biomaterials.2011.09.073.

[15] V. Onesto, A. Accardo, C. Vieu, and F. Gentile, “Small-world networks of neuroblastoma cells cultured in three-dimensional polymeric scaffolds featuring multi-scale roughness,” *Neural Regen. Res.*, vol. 15, no. 4, pp. 759–768, Apr. 2020, doi: 10.4103/1673-5374.266923.

[16] A. Accardo, M. C. Blatché, R. Courson, I. Loubinoux, C. Vieu, and L. Malaquin, “Two-photon lithography and microscopy of 3D hydrogel scaffolds for neuronal cell growth,” *Biomed. Phys. Eng. Express*, vol. 4, no. 2, 2018, doi: 10.1088/2057-1976/aaab93.

[17] I. INTERNATIONAL STANDARD, “ISO 10993-5:2009 - Biological evaluation of medical devices- Part 5: Tests for in vitro cytotoxicity,” 2009, Accessed: Mar. 18, 2021. [Online]. Available: https://www.iso.org/standard/36406.html.

[18] H. Özçelik, C. Padeste, and V. Hasirci, “Systematically organized nanopillar arrays reveal differences in adhesion and alignment properties of BMSC and Saos-2 cells,” *Colloids Surfaces B Biointerfaces*, vol. 119, pp. 71–81, Jul. 2014, doi: 10.1016/j.colsurfb.2014.03.019.

[19] K. L. Kilpadi, A. A. Sawyer, C. W. Prince, P. L. Chang, and S. L. Bellis, “Primary human marrow stromal cells and Saos-2 osteosarcoma cells use different mechanisms to adhere to hydroxylapatite,” *J. Biomed. Mater. Res. - Part A*, vol. 68, no. 2, pp. 273–285, Feb. 2004, doi: 10.1002/jbm.a.20043.

[20] M. Tehranirokh, A. Z. Kouzani, P. S. Francis, and J. R. Kanwar, “Microfluidic devices for cell cultivation and proliferation,” *Biomicrofluidics*, vol. 7, no. 5, p. 51502, Sep. 2013, doi: 10.1063/1.4826935.

[21] M. Tanyeri and S. Tay, “Viable cell culture in PDMS-based microfluidic devices,” in *Methods in Cell Biology*, vol. 148, Academic Press Inc., 2018, pp. 3–33.

[22] S. Halldorsson, E. Lucumi, R. Gómez-Sjöberg, and R. M. T. Fleming, “Advantages and challenges of microfluidic cell culture in polydimethylsiloxane devices,” *Biosens. Bioelectron.*, vol. 63, pp. 218–231, 2015, doi: 10.1016/j.bios.2014.07.029.

[23] M. C. Bélanger and Y. Marois, “Hemocompatibility, biocompatibility, inflammatory and in vivo studies of primary reference materials low-density polyethylene and polydimethylsiloxane: A review,” *J. Biomed. Mater. Res.*, vol. 58, no. 5, pp. 467–477, 2001, doi: 10.1002/jbm.1043.

[24] J. Zhou, A. V. Ellis, and N. H. Voelcker, “Recent developments in PDMS surface modification for microfluidic devices,” *Electrophoresis*, vol. 31, no. 1. pp. 2–16, 2010, doi: 10.1002/elps.200900475.

[25] T. Bhuvanesh *et al.*, “Langmuir–Schaefer films of fibronectin as designed

biointerfaces for culturing stem cells," *Polym. Adv. Technol.*, vol. 28, no. 10, pp. 1305–1311, Oct. 2017, doi: 10.1002/pat.3910.

[26] M. Yamaguchi *et al.*, "Surface modification of poly(L-lactic acid) affects initial cell attachment, cell morphology, and cell growth," *J. Artif. Organs*, vol. 7, no. 4, pp. 187–193, Dec. 2004, doi: 10.1007/s10047-004-0267-7.

[27] H. C. Schröder, O. Boreiko, A. Krasko, A. Reiber, H. Schwertner, and W. E. G. Müller, "Mineralization of SaOS-2 cells on enzymatically (silicatein) modified bioactive osteoblast-stimulating surfaces," *J. Biomed. Mater. Res. - Part B Appl. Biomater.*, vol. 75, no. 2, pp. 387–392, 2005, doi: 10.1002/jbm.b.30322.

[28] C. Barreau *et al.*, "Regionalization of browning revealed by whole subcutaneous adipose tissue imaging," *Obesity*, vol. 24, no. 5, pp. 1081–1089, 2016, doi: 10.1002/oby.21455.

IV. Dynamic cell culture

In this chapter, we will present of the integration of the 3D architectures shown in **Chapter 3**, into microfluidic devices. The objective is to incorporate the last cue to complete the bone marrow microenvironment introduced in the **Chapter 1**. In particular, we will focus on the need of the models to include perfusion aspects to control the biochemical cellular micro-environment and the fluid movement to better mimic the real shear conditions of the bone marrow. To achieve this point, we will describe different devices that permit the perfusion of liquid through 3D architectures and we will present the steps taken in order to integrate the free-form and 3D design as described in **Chapter 2** and **3.** In addition to confocal fluorescence microscopy and electron microscopy observations, we will discuss how metabolic follow-ups can be used to monitor the glucose consumption and the lactate secretions in order to control the welfare of the cells during the culture. The use of additive manufacturing allows us to precisely control the shape and dimensions of the designed architecture and thus to integrated it within commercial systems. In order to use the porous PDMS in a microbioreactor, a fabrication technique based on injection molding was developed to fabricate the porous PDMS directly inside a microfluidic device. This resulting device permits the dynamic cells culture within porous PDMS structures.

1. Dynamic cells culture on DS3000 designed architecture

This section will be centered on the study of the 3D architectures in combination with dynamic cell culture. For such purpose and as explained in **Chapter 3**, we have segmented and fabricated our 3D architectures to fit the specific dimensions of a commercial bioreactor, U-Cup from Cellec Biotek, currently used as a reference system by our collaborators in the Restore Laboratory. This system allowed to perfuse liquid at a define flow rates and generate shear stress within the scaffold. Here, we will present the culture of primary bone marrow mesenchymal stromal cells (BMSCs) in dynamic seeding for 2 weeks. We have investigated the evolution and behavior of the cells in the bioreactor using periodical metabolic sampling. This technique allows one to trace the consumption of glucose and its conversion into lactate, monitoring the welfare and the proliferation of a cell culture. Human bone marrow tissue was provided from our collaborators in the RESTORE laboratory and EFS, obtained from surgical removed femoral heads. Patients were provided prior written informed consent according to the ethics committees of Toulouse University Hospitals. Cells were then multiplied in EGM2 culture medium for 14 days, prior detachment and re-seeding in the cell culture supports. Due to the nature of the cells, mostly hips implant surgery from elder patients, cells can display a wide range of behavior related with the age and health conditions of the patients.

a. Integration in a commercial bioreactor

The scaffolds were fabricated using stereolithography in DS3000 resins, designed with the purpose to be compatible with the U-Cup bioreactor from Cellec Biotek (Switzerland). This is a commercial solution devoted to the cell culture of cells in 3D architectures in perfusion conditions using a multi-syringe pump solution (**Figure 4.1A**). The system is a biocompatible U-shaped plastic tube with a compartment to host the 3D architecture in one of the vertical sides of the system, as presented in **Figure 4.1B-C**. The disposable bioreactors are held in a 10-multirack with dimensions to fit it into an incubator. The system is usually operated using commercial ceramic or collagen scaffolds of standardized dimensions (10-mm diameter and 4-mm height). The 3D printed structures were then fabricated in cylindrical shapes of 10-mm diameter and 4-mm thickness, suitable to the compartment of the bioreactor. Moreover, the systems possess two valves over and beneath the scaffold compartment to permit to load cells and to change the medium.

The system works by sequentially injecting air in one side of the bioreactor to increase the pressure, which will be leveled until reaching hydrostatic stability by moving liquid through the scaffold to the opposite side of the bioreactor. The back-and-forth movement of the syringes generates the variation of pressure that keep the medium flowing. It is important to notice that the flow depends on the height difference between the liquid on both side of the bioreactor and it might present variations. The typical flow used during this project will be 0.5 mL/min for 6 min, in each direction. The technical specifications of the system can be found in **Table 4.1.**

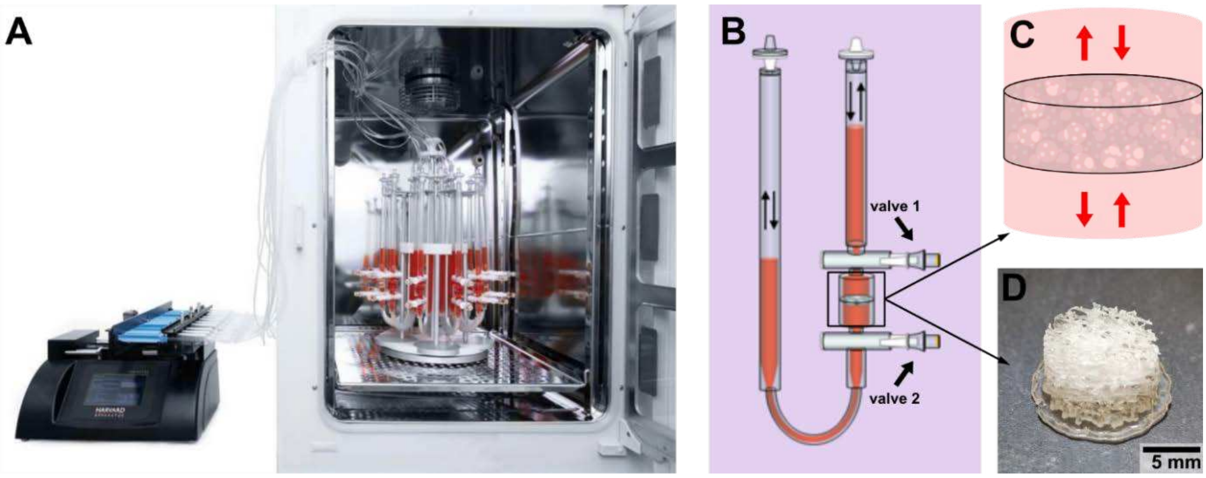

Figure 4.1. *Experimental set-up employed for the use of 3D printed designed architectures.* ***(a)*** *Complete U-Cup bioreactor set-up, showing a multi-syringe pump supplying culture medium to the rack of U-Cup bioreactors installed in an incubator.* ***(b)*** *Schematic illustration of an individual U-Cup bioreactor.* ***(c)*** *Close-up illustration of the compartment dedicated to host the 3D architecture in the bioreactor.* ***(d)*** *Optical micrograph of 3D printed bone microarchitecture. Adapted from* [1], [2].

This bioreactor is classified as a perfusion bioreactor. It provides a quasi-homogenous flow to the system, where the shear stress and the mass transport depends on the distribution of the porosity within the scaffold placed in the compartment. Furthermore, the system operates using a determined amount of medium placed in the bioreactor, 12 mL in our case, and it is renewed every 72h. This constitutes a closed system regarding nutriments and secretions, while the oxygen is provided by a 200-nm filtered air opening on the top of the U tube. The renewal of the culture medium is carried out using the valves placed over and beneath the scaffold compartment, which remains untouched during the process. This implied that there will be a volume of liquid remaining in the compartment that is not renewed during the culture media exchanges.

Table 4.1. *U-cup technical specifications [1].*

System size	**Scaffold type**	**Scaffold size**	**Working volume**	**Perfusion speed**	**Cell density**
Rack can host 10 independent bioreactors and it fits into an incubator	Rigid or soft; ceramic, synthetic or polymeric	Thickness: 2-4 mm Diameter: 6-8-10 mm	6 mL to 14 mL per bioreactor	1 µm/s to 10000 µm/s	> 10 millions cells per bioreactor

b. Dynamic cell culture: bone marrow mesenchymal stromal cells (BMSCs)

To evaluate the performance of 3D printed structures under perfusion, we investigated 6 fibronectin-coated bone scaffolds fabricated in DS3000 as 3D architecture to host BMSCs: 3 scaffolds were studied in dynamic conditions in the U-Cup system while 3 samples were placed in static conditions in multi-well plates (see **Chapter 2** and **3**). For the dynamic cell culture, 250000 cells suspended in EGM2 culture medium were placed in the bioreactors and dynamic seeded process was started. The detailed protocol of the cell seeding is described in **Protocol 14**. The solutions move back-and-forth with a periodicity of 2 min at 1.5 mL/min for 48h to maximize the number of travels that cells make across the scaffold. Static conditions were obtained by seeding cells in a droplet, with the same number of cells, as described in **Protocol 11**, in **Chapter 3**. Then cells were incubated for 1h and filled with extra cell culture medium until reaching 2 mL in the wells. Metabolic follow-ups were carried out at day 2, 6,12 and 15 during the change of medium, in order to control the evolution of the culture. After 15 days in culture, samples were removed, fixed and coated following the protocols presented in **Chapter 3** regarding fixation and fluoresce staining.

i. Confocal immunofluorescence observations

In **Figure 4.2**, we show a 3D reconstruction of BMSCs on porous region in the bone scaffold after 15 days of dynamic cell culture. The inset describes the direction of the z-scan images that were acquired with a spinning-disk inverted Leica confocal

Protocol 14. U-cup cell seeding and culture

This protocol details the seeding and culture of BMSCs under dynamic conditions using the commercial bioreactor U-Cup from Cellec Biotek. The culture media used for this experiment was EGM2 (2% SVF).

1. Place the scaffolds in the silicone tube suited for the scaffold compartment of the U
2. Remove the 200-nm air filter from the opposite side of the scaffold
3. Inject the 6 mL of the cell suspension in each side of the U tube, using the respective valve
4. Place 5 mL of air in the external syringe and plug the tubes to the U tubes
5. Connect 200-nm air filter in the free entrance of the U tube
6. Move the U-rack into an incubator, placing the air-syringes in the multi-syringe pump
7. Run the seeding program: 1.5 mL/min for 3mL in each direction for 720 repetitions (48h)
8. Change the mode to dynamic cell culture after 48h: 0.5 mL/min for 3 mL in each direction, repeat until medium changed.

microscope. Cells were fixed and stained following the protocol detailed in **Protocol 12,** in **Chapter 3**. The immunofluorescence dyes chosen in this experiment correspond to: DRAQ5 in blue, β-tubulin in green and Ki67 in red. In this case, we changed the DAPI for the DRAQ5 to stain the nuclei in order to improve the characterization of the biological features and avoid the overlap of the staining with the photoluminescence of the DS3000 scaffold. However, the UV-blue band was still imaged to obtain information on the structure, exploiting the photoluminescence of the material. This procedure was used to study the location and the organization of the cells regarding the 3D architecture. In the 3D reconstruction shown in **Figure 4.2A**, we observe how the cells have densely covered a three-dimensional surface of the architecture. Cells penetrated the pores and covered the walls of the cavity. **Figure 4.2B** presents a z-projection obtained from the z-scan described previously. In this image, we identify the elongated morphology of the cytoskeleton of the BMSCs, densely packed in the 3D structure. In the right quadrant of the image, we can see a cavity highlighted with a white dash line. Here, we observe the cells aligned around the edge of the pore. Within the pore, we recognize fibular structures crossing the cavity. When compared with the 3D reconstruction, we detect these structures overhanging on different z-images and just anchored in two points at opposing sides of the cavity.

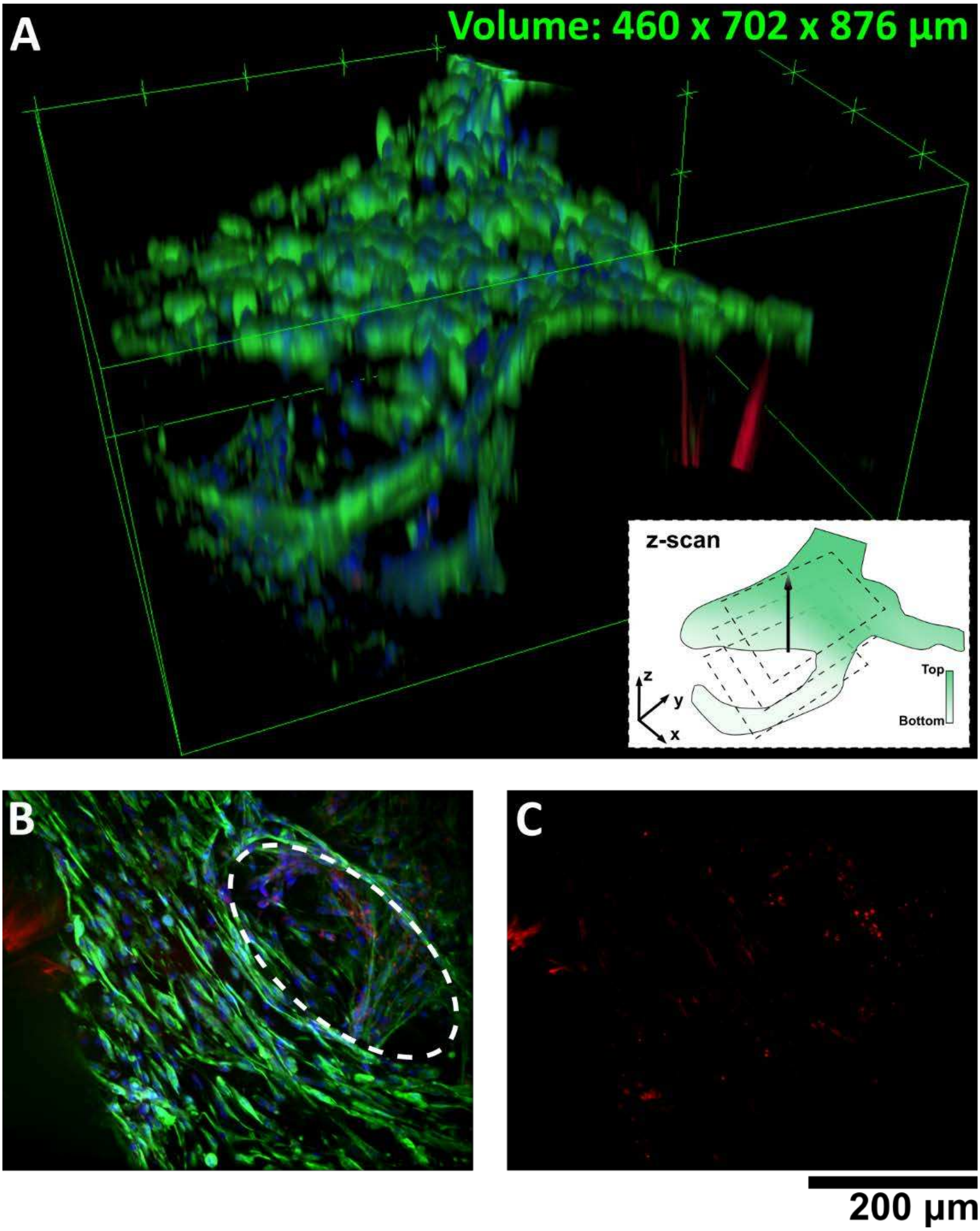

Figure 4.2. ***(a)*** *3D confocal fluoresce microscope reconstruction of MSCs over the bone scaffold after 15 days of perfusion on the U-Cup bioreactor. The imaged volume corresponds to 460 x 702 x 876* μm^3*. The z-scan is described in the illustration on the inset.* ***(b)*** *Fluorescence confocal z-projection of the volume showed in (a).* ***(c)*** *Proliferation staining Ki-67 of the cell coverage over the bone scaffold.* ***Colors:*** *DRAQ5-nuclei (blue), β-tubulin (green) and Ki67 (red).*

We believe that the architectures of ~ 150-200 μm in length are composed of secreted ECM and several cells. To investigate the cell proliferation, Ki67 stained is shown in **Figure 4.2C**, where we observe part of the population in a proliferation state.

The confocal z-scan is presented as a mosaic at different z in **Figure 4.3**. This permits a better understanding of the three-dimensional cell organization displayed on the DS3000 bone scaffold. The images correspond to the 3D reconstruction presented in **Figure 4.2**. Images are presented in two rows, showing first the immunofluorescence staining of the BMSCs and secondly the photoluminescence emission from the DS3000 scaffold. To highlight the overhanging structures described in **Figure 4.3**, we have used numbered pairs of arrows pointing at such features. The solid arrows evidence the overhanging structures described previously, while the hollow arrows point the same location at a different z-plane. Furthermore, the locations of these three--dimensional cell organizations are displayed as well in the DS3000 architecture, highlighting the lack of solid materials for cells to adhere on it. The comparison between both rows of images at different z-planes demonstrates that BMSCs were able to organize in suspended fibular structure along the pores of the material. For instance, in between the planes z = 90 μm and z = 135 μm, the arrows numbered 2 point the same fibular cell organization described in **Figure 4.3**. We note that this cellular structure, which has appeared already at z = 75 μm, disappeared from the same location at z = 135 μm. Moreover, these regions do not display any solid material in the equivalent photoluminescence images. Another example is shown by the arrow pair 3, at z = 135 μm and z = 270 μm. In the z-plane 135 μm, we observe a fibular thin organization of cells suspended over 300 μm. The careful observation of the complete z-scan and the 3D reconstruction demonstrate that this overhanging structure is anchored in two points, to fibular construct located at z ~ 90 μm and to the wall of the pore at z ~ 250 μm.

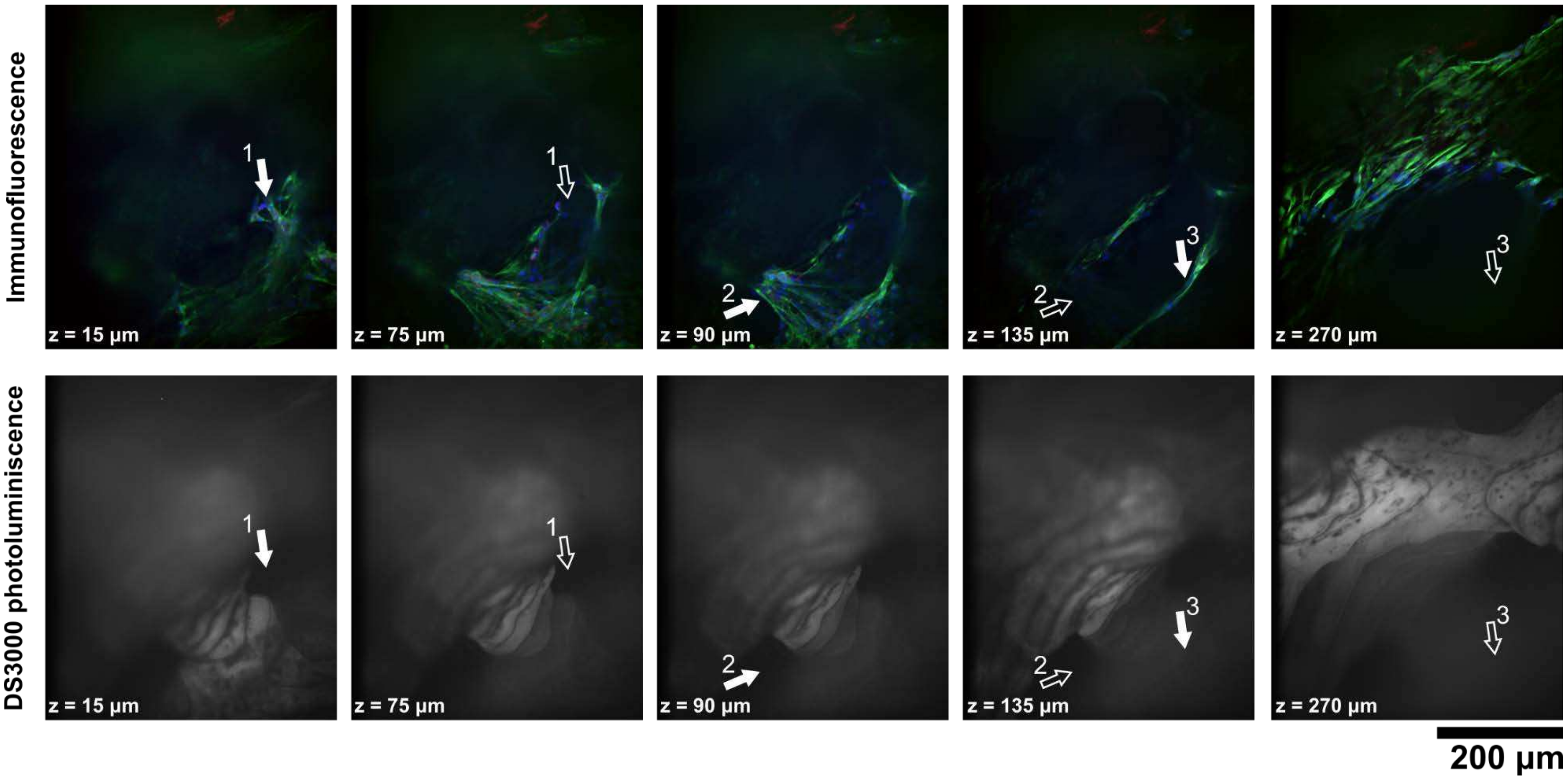

Figure 4.3. Fluorescence confocal images mosaic corresponding to the z-scan used to produce **Figure 4.2**, showing the 3D structure and the cells at different z: 15, 75, 90, 135 and 270 µm. Images are presented by pairs, with the upper picture presenting the cells stained with DRAQ5-nuclei (blue), β-tubulin (green) and Ki67 (red), and the low image depicting the DS3000 photoluminescent structure. The numbered paired arrows highlight specific three-dimensional features of the BMSCs culture. The solid arrows point the location of the organized group of cells and the hollow arrow, the same empty location at a different z-plane. **Colors:** DRAQ5-nuclei (blue), β-tubulin (green), Ki67 (red) and DS3000 photoluminescence (white).

In **Figure 4.4**, we compare static versus dynamic cell culture conditions by confronting confocal fluorescence images. There is a striking difference in terms of cell population and organization. Cells cultured in static conditions seem healthy and elongated, developing protrusions reaching other cells. However, cells in dynamic conditions exhibit a much denser population and richer profile in terms of biological material covering the scaffold. They are much more developed, present a packed three-dimensional organization and display overhanging structures. The quantification of cell population is extremely difficult in such 3D configuration for several reasons. First, the difference in z-plane causes a gradient of intensity in the acquired z-stack images, which required implementing specific technical solution as the modulation of the laser power along the z-axis. Second, the three-dimensional organization of cells constitutes a great challenge to perform a reliable counting of individual cells.

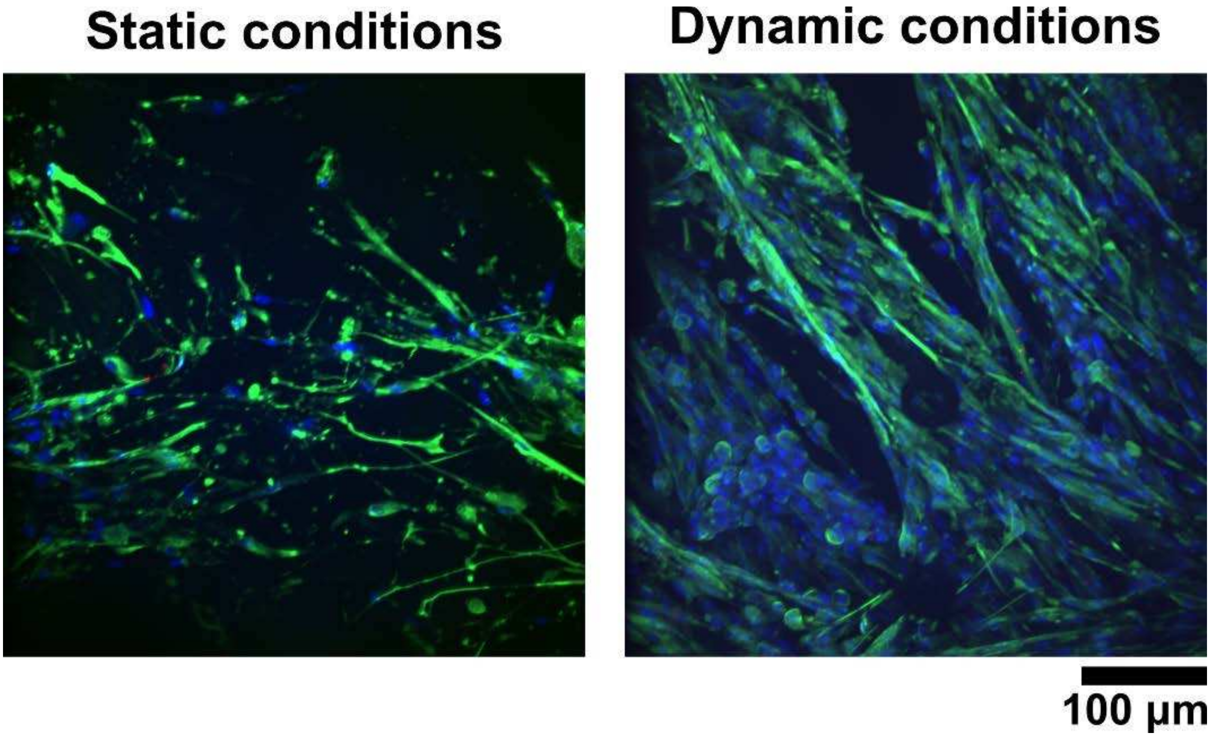

Figure 4.4. *Confocal fluorescence microscopy images for the same patient BMSCs after 15 days in culture under static and dynamic conditions.* ***Colors:*** *DRAQ5-nuclei (blue), β-tubulin (green) and Ki67 (red).*

ii. Electronic microscopy

In **Figure 4.5** and **Figure 4.6**, we present electron microscopy characterizations of the samples presented in the previous section. Due to the limitations in cell supply and availability of samples for imaging, these images were obtained by dehydrating the prior samples fixed with 10% formaldehyde solution for the fluoresce microscopy and not the standard SEM fixation with 4% glutaraldehyde. Though both aldehydes work similarly, the formaldehyde presents a longer molecule that provides a more rigid and tight fixation, which is better suited to dehydrate the histological samples. However, we can still obtain remarkable information from the use of electron microscopy in these conditions. Samples were dehydrated following the **Protocol 13** presented in **Chapter 3**. Due to the capabilities of the electron microscope employed, Hitachi S-4800N, images are separated in two figures according to the magnification used.

In **Figure 4.5**, we show low magnification pictures of the DS3000 bone scaffold colonized by BMSCs. **Figure 4.5A** presents the typical view of a pristine DS3000 bone scaffold. **Figure 4.5B-D** shows the scaffold covered by BMSCs after 14 days in dynamic culture. Here, we observe most of the pore cavities filled by suspended architecture where the original features of the stereolithography are barely recognizable under the cellular layer. These cellular assemblies, pointed by the arrows, are similar to three-dimensional membranes, recognizable in the previous confocal images, and attached at several points on the pore walls. Due to the large density of material, it seems difficult to identify divisions or individual structures.

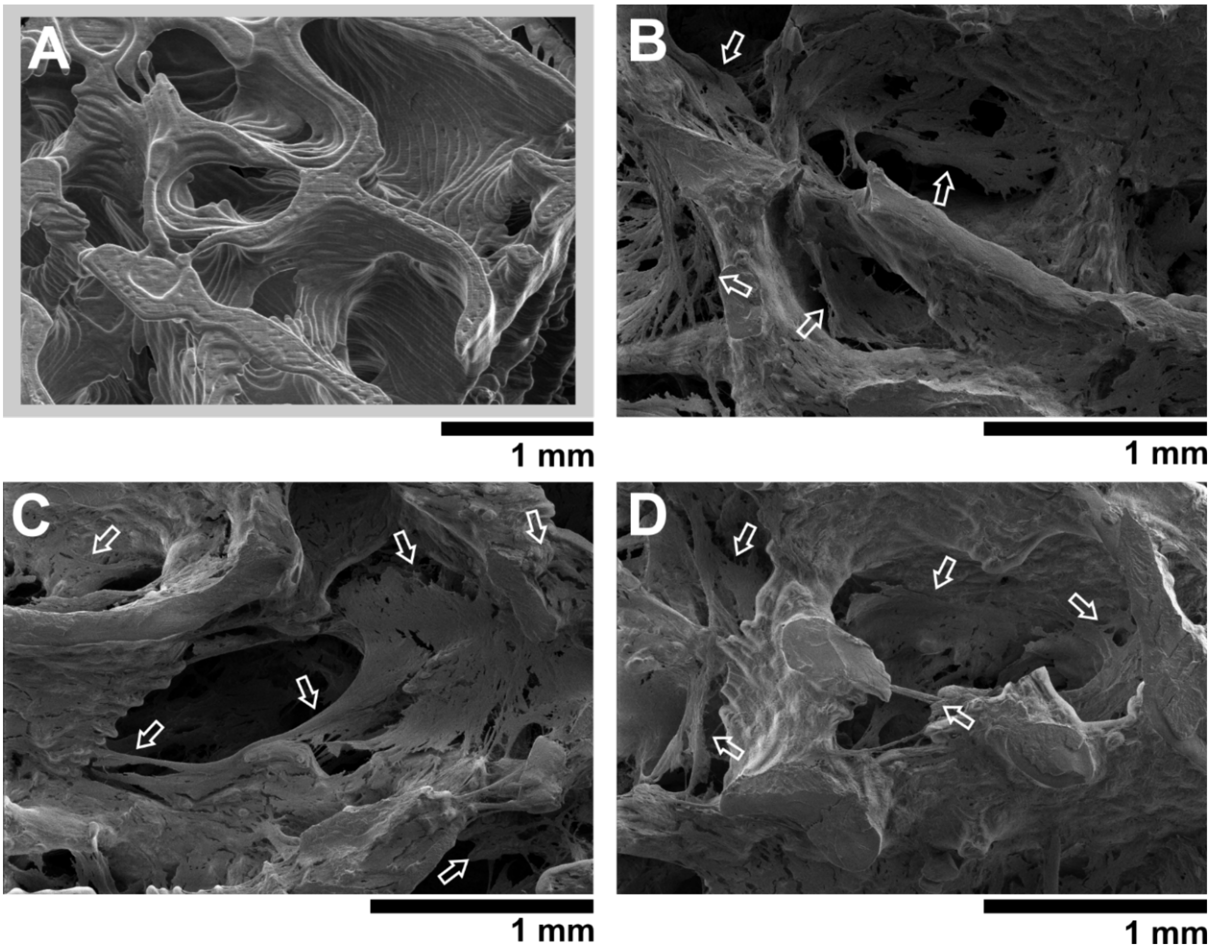

Figure 4.5. *SEM low magnification images presenting the BMSCs culture under perfusion conditions for 14 days over a DS3000 bone microarchitecture replica.* ***(a)*** *SEM image of a pristine DS3000 bone scaffold.* ***(b-d)*** *SEM images of the BMSCs culture on the DS3000 bone scaffold. The dense proliferation of the cells has led to biological overhanging constructs within the cavities of the porous structure, pointed by the white hollow arrows.*

Figure 4.6 presents high magnification SEM images from the cavities of the bone architectures. In the gaps between the cell constructs, we detect meshes of thin fibular structures in the border of the cellular constructs, which have been false-colored. Due to the typical dimension of a cell (10-30 μm diameter), the struts of the web-like architecture it is unlikely to be formed by cells. However, this kind of organization is similar to the formations of decellularized ECM or collagen hydrogels imaged with SEM shown in **Figure 4.6** [3], [4]. Thus, these features could be a sort of ECM pre-scaffolding that cells segregates prior to migration allowing them to form 3D constructs in the pores. This could explain the capacity of cells to reach large distances as few millimeters. The characterized structures show an organization which is consistent with tissue-like morphologies, though further investigation regarding the phenotype and functionality of the cells is required to conclude on this hypothesis.

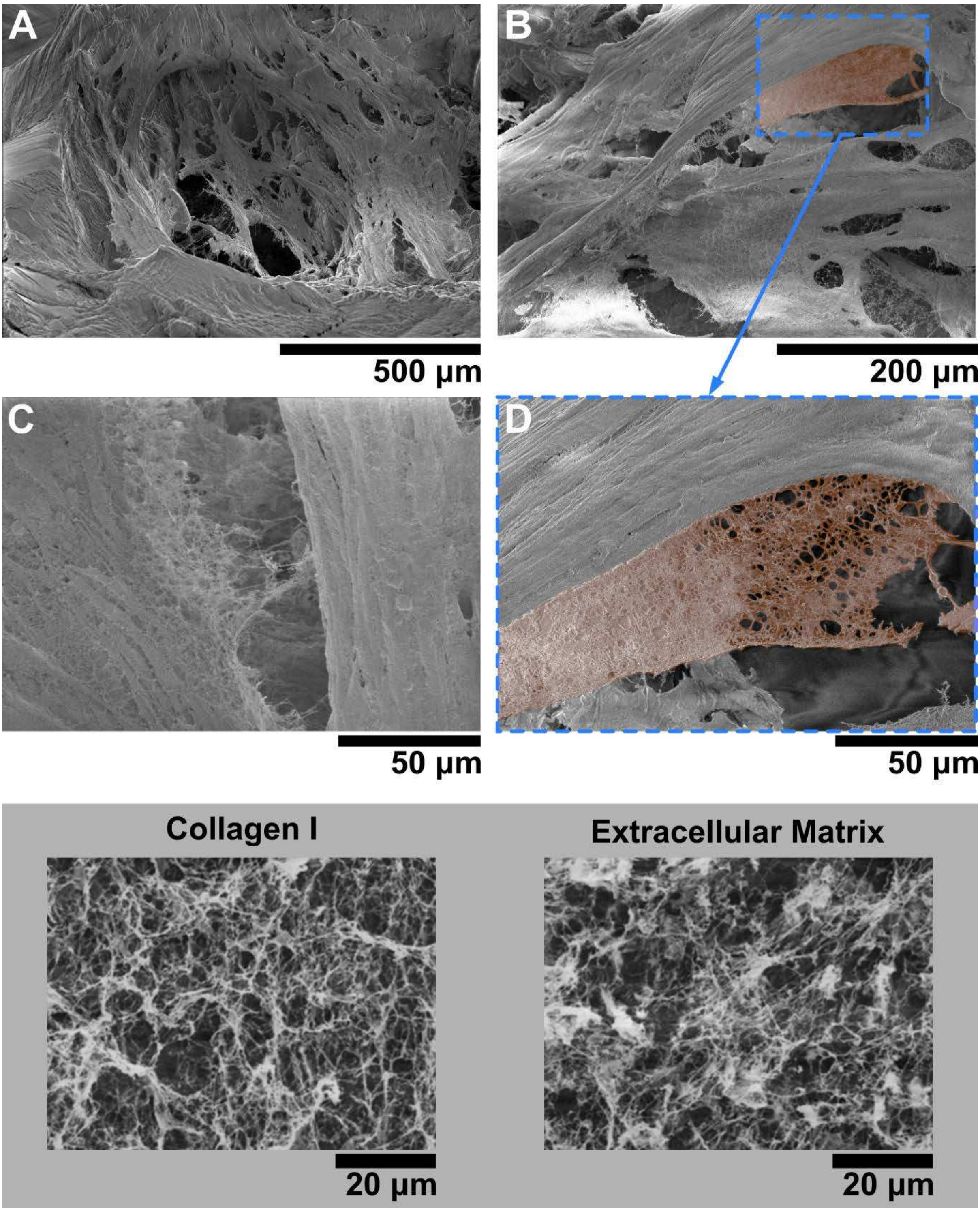

Figure 4.6. *SEM high-magnification characterization of BMSCs culture under perfusion conditions for 14 days over a DS3000 bone microarchitecture replica. The close-up views show the details of the biological architectures with false-colored web-like architectures.* ***Down.*** *Decellularized collagen and ECM dried gels characterized by SEM adapted from* [3].

iii. Multi-scale characterization

Figure 4.7 displays a multi-scale comparison between a pristine DS3000 scaffold characterized by electron microscopy (as shown in **Chapter 2**) and the results obtained by immunofluorescence for the dynamic culture previously shown. In the SEM images we observed the 3D printed scaffold exhibiting the typical features caused by the digital slicing of the model. A close-up to the center region shows a pore with few suspended struts of DS3000 crossing the pore. In the middle, we observe the images obtained by confocal fluorescence microscopy displaying on the right, the fluorescence immunostaining images and, on the left, the DS3000 photoluminescence already discussed. The numbered arrows highlight the recognizable features visible on the SEM and photoluminescence images. On the bottom, we show the merge of the photoluminescence and the immunofluorescence overlaying in transparency. Here, we can recognize the organization of the cells to align along the suspended struts. Furthermore, a large amount of biological material, probably secreted ECM can be found densely populated by cells in the spaces between the struts. This cell formation covering several hundreds of micron square of empty space on the pore is distinguishable as overhanging over the cavity.

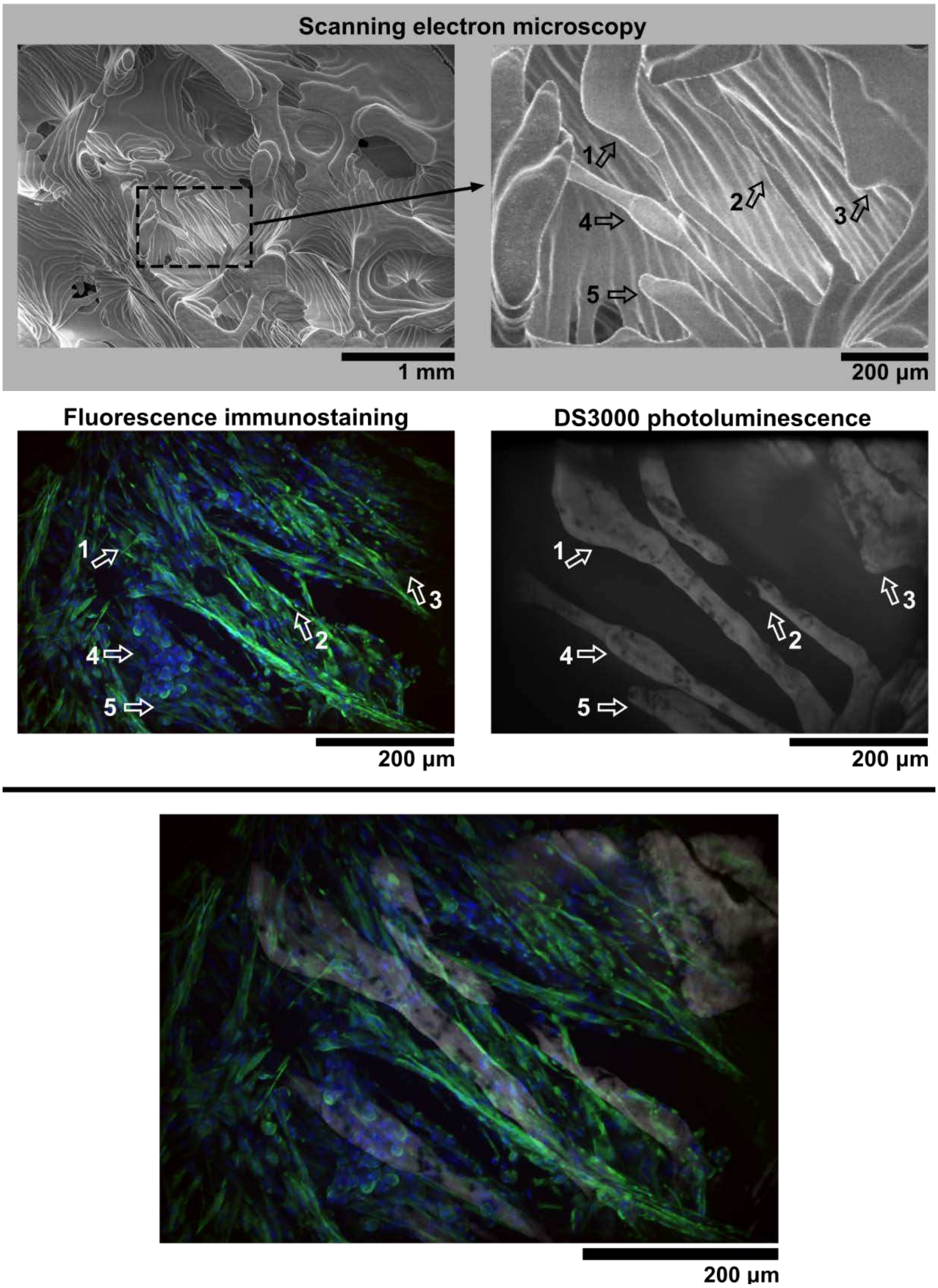

Figure 4.7. *Comparison between a pristine DS3000 scaffold and the immunofluorescence characterization carried out on a dynamic cell culture of BMSCs for 14 days. The hollow arrows highlight distinguishable features of the 3D printed structure in both characterization techniques.* ***Down.*** *Overlay of the DS3000 architecture with the immunofluorescence image of the corresponding region.*

iv. Metabolic analysis

To complement the microscopy images, presented in **Figure 4.8**, we have obtained data from the periodical metabolic analysis of the culture media of the samples during the change of culture media. The glucose consumption is calculated by taking the difference in glucose concentration between the extracted sample and the fresh culture medium (5.8 mM of glucose). This medium was analyzed using a glucose meter system Contour XT (Ascencia Diabetes Care) and a lactate analyzer Lactate Pro2 LT-173 (Arkray), by depositing few microliters in the test strips and reading them. In the case of dynamic cell culture, we can observe a steady decrease of glucose concentration for the whole duration of the experiment for the patients 1 and 3, decreasing from 5.8 mM to 3.5 mM. The culture of patient 2 cells showed a much lower consumption level (5.8 mM to 5.3 mM of glucose drop). This result agrees with the microscopy characterization with low cell concentration compared to the other patients (as shown in the inset). For the static cell culture condition, the measurements started at day 6 due to technical issues. The measurement of the static conditions described a much lower concentration of glucose during the whole experiment (0.5 – 3.0 mM).

For the lactate concentration measurements, we observe a large increase in concentration of the samples that stabilizes around the second week, with lower values for the patient 2 as well. The static samples present similar steady values of lactate production much higher than the dynamic case. The metabolic experiment carried out during the cell culture of the BMSCs presents a good opportunity to monitor the development of the cell colonies without interrupting the experiment. The data obtained in the dynamic conditions is similar to the values found in the literature for MSCs seeded at similar concentrations [5], [6].

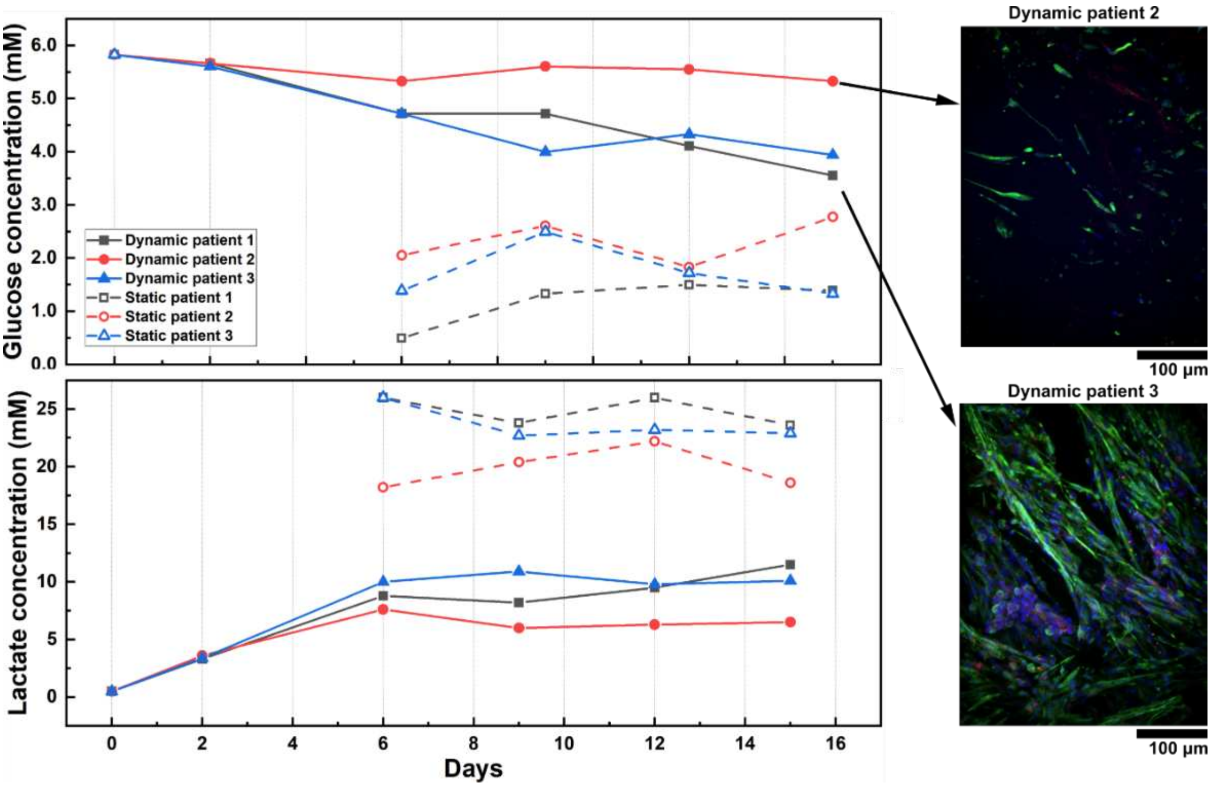

Figure 4.8. *Metabolic tracing of the glucose consumption and the lactate production of the BMSCs dynamic culture in the DS3000 trabecular bone microarchitecture for 14 days of culture. Microscopy z-stack images are shown as inset depicting the state of cultures in agreement with the metabolic results.*

It is difficult to compare dynamic to static conditions because of the large difference in volumes between both supports and the trapped volume of culture media remaining in the bioreactor after the medium exchanges. In general, static conditions present a much lower concentration of glucose which can be a limiting factor for the proliferation of the cultures. The larger volume of medium of the bioreactor provides more nutriments available for the cells. With the same argument, the secreted lactate was diluted to lower concentrations in the bioreactor. To complete the analysis, we calculated the total amount of glucose consumed for each culture from the obtained data (pondering the dead volumes of the bioreactor), that is presented in **Figure 4.9**. These results confirm that the limit of nutrients is a critical factor for the proliferation on static conditions, since the initial nutriment is lower than in the bioreactor. Furthermore, the liquid movement may provide more favorable conditions for the cell proliferation which could explain the vastly more developed ECM of the cells in the dynamic conditions. The anomalies found in patient 2 could be explained by the cellular discrepancies proper to the biological differences between patients. In general, this data agrees with the microscopy characterization presented previously and it consolidates the use of metabolic follow-ups as a tool to monitor the state of a cell culture without interrupting the experiment.

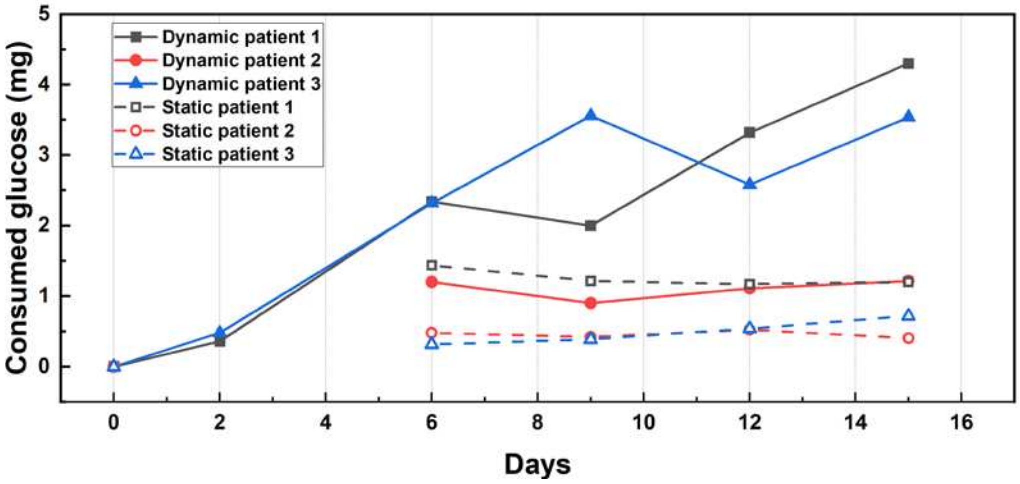

Figure 4.9. *Consumed glucose obtained by pondering the dead volumes of the bioreactor and the total amount of glucose available for each condition.*

c. Summary

- We have integrated a 3D printed bone scaffold into a commercial perfusion bioreactor, completing the last cue of the bone marrow model described in **Chapter 1**. Flow control permits a better mass transport which affect the distribution of nutriments and cellular secretions in the culture.
- BMSCs were seeded in the bioreactor and in static conditions to investigate the impact of the liquid movement on the cultures.
- We monitored the cultures using metabolic measurement of glucose and lactate and further characterized the experiments using confocal fluorescence and electron microscopy.
- Comparison between static and dynamic conditions showed a larger complexity in the organization of cells under perfusion.
- In dynamic conditions, cells built dense overhanging architectures of hundreds of micrometers to few millimeters in length, filling the pores of the scaffold.

- Moreover, we detected web-like micro-meshes similar to decellularized ECM that we identified as a sort of ECM pre-scaffolding to form 3D complex organization.

2. Dynamic cell culture on porous PDMS free-form micro-bioreactor

Regarding the porous PDMS, we have developed a molding technique that permits to inject the emulsion into a microfluidic device and to carry out the porous reticulation directly on-chip. This has allowed us to fabricate PDMS microfluidic chips with a 3D porous architecture made exclusively of silicone. The fabricated chips offer an important advantage regarding other 3D microfluidic approaches due to their simplicity, cost and mass-fabrication potential. In the following pages, we will be introducing the experimental protocol developed to fabricate the microfluidic devices and integrate the porous PDMS monolith. Morphological characterizations were carried out using electron microscopy of a sliced device and non-destructive X-ray microcomputed tomography (μCT) over the whole system. Then, we characterized the hydrodynamic capabilities of the device by fluorescence solution injection and X-ray contrast-agent video-radiography. In order to study the flow inside the porous PDMS and the shear stress produced by the liquid movement, fluid mechanic simulation was carried with our collaborators at the Institut de Mécanique des Fluides de Toulouse (IMFT), Omar Mokhtari and Yohan Davit. Systems were as well tested using SaOS-2 cell line and BMSCs and by monitoring the metabolic evolution of the devices. Afterwards, the devices were sliced and imaged to characterize the core of the structures using confocal fluoresce imaging and electron microscopy.

a. Microfluidic device and porous PDMS integration

Our motivation for the production of porous PDMS microdevice relies on the advantage of the injectability of our water-in-PDMS emulsion. This point permits to induce the expansion of the water droplets *in-situ* via the two-step curing process described in **Chapter 2** to generate the porous network within a PDMS microfluidic device. Under this premise, we developed a microfluidic chip with a large volume central chamber (2.12 mL) connected to inlet and outlet channels. The microfluidic devices were fabricated using soft lithography in combination with 3D printed molds fabricated using CAD designs. The upper half of the device was produced with a mold designed by combining 2 removable pieces, featuring the positive replica of the microfluidic chamber and a containing wall around it. Those pieces were fabricated with a laser-assisted 3D printer DWS 29J+ using DL260 resins from DWS Systems. The device featured a 37 mm long, 17 mm wide and 4 mm high hexagonal central chamber shown in **Figure 4.10**.

The microfluidic substrate (about 4 mm thick) was produced by casting PDMS into a 55 mm diameter polystyrene Petri dish and by reticulating it at 60 °C overnight. In order to bind both parts of the microfluidic device, a thin layer of PDMS was spin-coated over the PDMS substrate and the chamber was put in contact, then baked for 60 minutes at 60 °C.

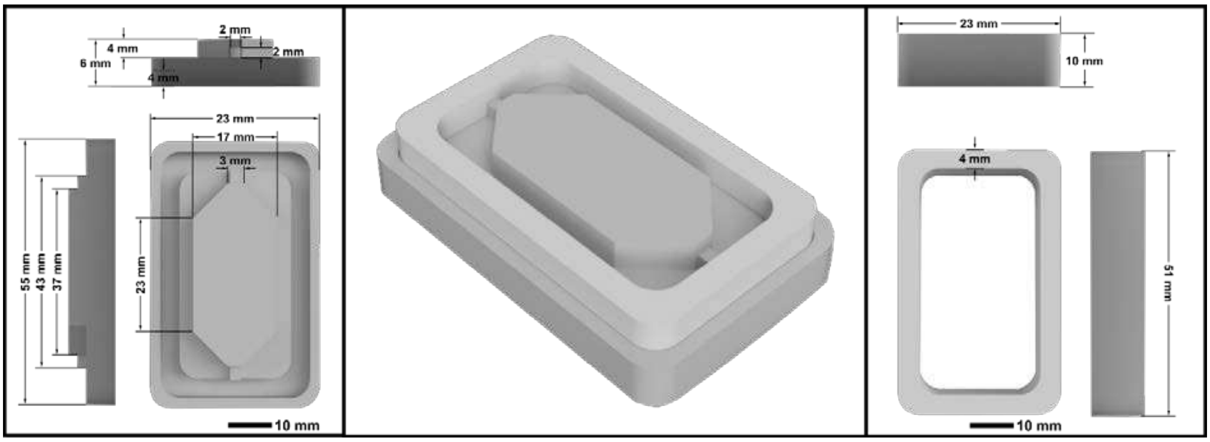

Figure 4.10. *3D digital model of the 3D printed mold used to fabricate the microfluidic device to host the porous PDMS architecture in the central chamber. The hexagonal central chamber displays a maximum length of 37 mm with a width of 17 mm and a height of 4 mm. A containing wall completes the mold.*

Figure 4.11 presents the fabrication of the porous fluidic chip following the **Protocol 15** used produce the water-in-PDMS emulsion to fabricate porous PDMS. Once the emulsion is produced, it is placed in a syringe and injected into the PDMS fluidic device until filling ~50% of the chamber volume in order to leave free-space for the foam to expand. A lower quantity of emulsion will lead to large gaps in the scaffold and trapped air-bubbles, a larger quantity will lead to the swelling and deformation of the chip due to the excess of foam in the chamber. The microfluidic chips were then baked in a two-step reticulation process detailed in **Protocol 6**, in **Chapter 2.** The first bake took place in a conventional oven at 60 °C for 15 minutes, then in a vacuum oven at 130 °C and 400 mbar for at least 2h. Both inlet/outlet edges of the microfluidic device were cut with a surgical blade to have a clean surface in the channels, where commercial conical connectors were plugged. To ensure the sealing of the fluid connections, the edge of the microfluidic connector was covered with PDMS and reticulated again at 60 °C for 1h.

Protocol 15. Fabrication of porous PDMS microfluidic device

This protocol details the process of fabrication of porous PDMS microfluidic devices

1. Following the manufacturer indications for Sylgard 184 (10:1), weight and mix the silicone-base and the hardener using a balance and degas the PDMS until no bubbles are visible
2. Cast the liquid mixture into the 3D printed mold and the 55 mm petri dish and reticulate them at 60 ºC for at least 2h
3. Extract the PDMS pieces from the mold using a thin spatula and few droplets of solvent as lubricant
4. In the spin-coater, place the 55-mm diameter PDMS substrate and cover 1/3 of the surface with liquid PDMS. Then spincoat at 500 rpm for 1 min
5. Carefully, place the upper piece in contact with the PDMS. Reticulate them at 60 ºC for at least 2h
6. Prepare the water-in-PDMS emulsion as described in the **Protocol 5** and place it in a disposable syringe
7. Inject from both side of the microfluidic device the emulsion until filling ½ of the volume of the central chamber
8. Reticulate following the two-step process described in **Protocol 6** with the following parameters: t_1 = 15 min, T_1 = 60 ºC, P_1 = 1 bar; t_2 > 2h, T_2 =130 ºC, P_2 = 400 mbar
9. Cut off the excess of porous PDMS from the channels with a surgical blade and plug the commercial microfluidic connectors. Cover with PDMS the connection point and reticulate at 60 ºC for at least 2h

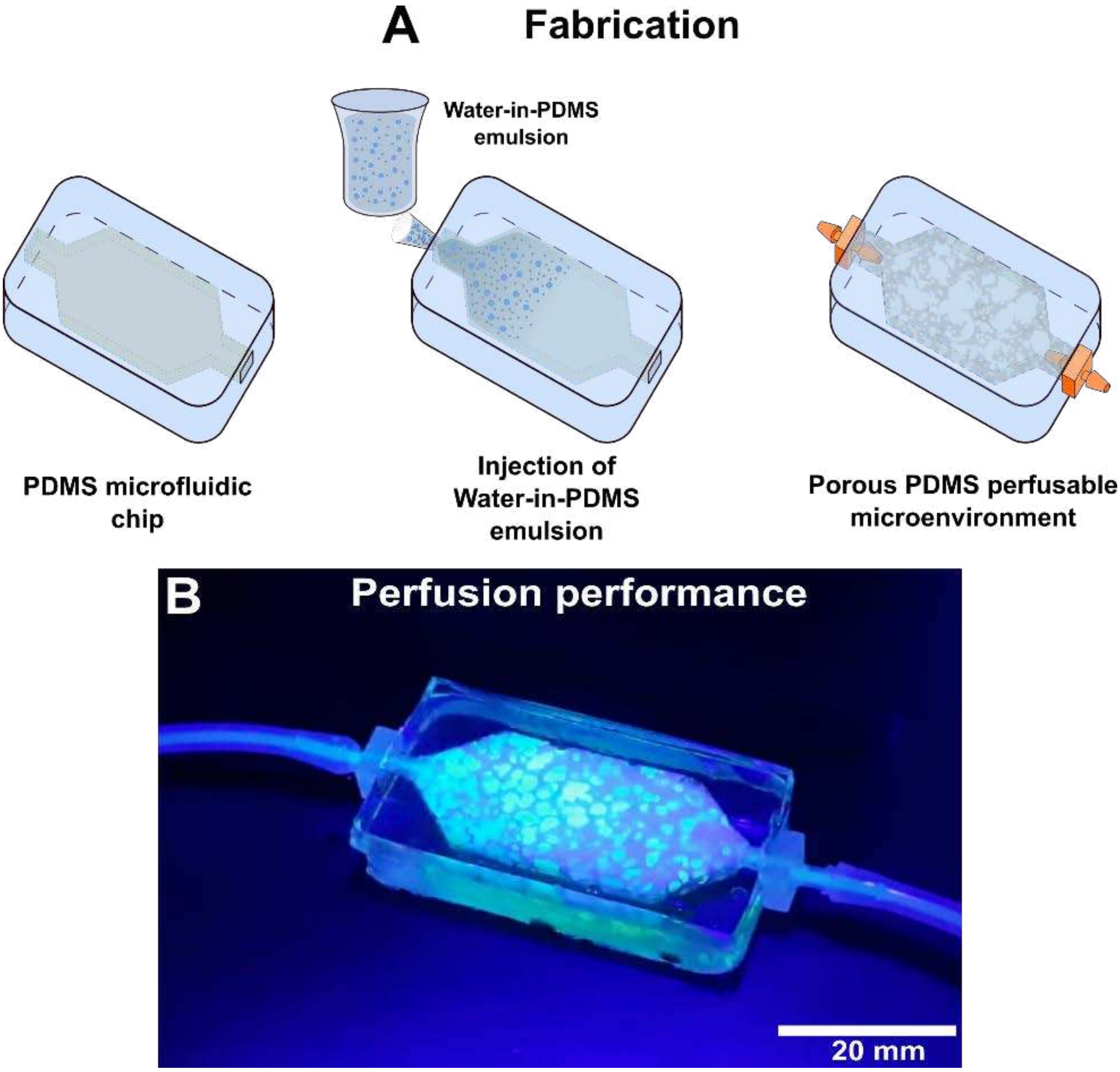

Figure 4.11. (a) *Illustration of the integration of the porous PDMS into the chip.* ***(b)*** *Optical image showing the perfusion of the microfluidic device with a suspension 500-nm diameter green fluorescent microbeads.*

The reticulation parameters to generate the porous PDMS were adapted for the *in-situ* fabrication of the architecture. The time of the first baking step was reduced in order to maintain similar pores size to the cylindrical configuration. There are different reasons to explain the need for this modification. First, the flat configuration of the device could potentially increase the heat transfer of the whole device since the emulsion is exposed to a larger surface. This could accelerate the temperature increase of the emulsion, accelerating the reticulation of the PDMS. Second, the reduce apertures (2×2 mm^2 vs 14-mm diameter) may have implications regarding foam expansion and the gas exchange inside the microfluidic device, altering the reticulation due to the local variations of the pressure and steam concentration in the gas phase (i.e., humidity). The relative humidity reached inside the chip during the reticulation impacts the evaporation rate of the water due to the vapor pressure, which can potentially lead to modifications in the process of reticulation and reduce the expansion of the droplet cavities that generate the porosity. To counter this effect, we have reduced the first baking step duration in order to decrease the rigidity of the PDMS, thus facilitating the expansion of the steam during the second baking step.

b. Device characterization

To confirm the generation of free-form porous PDMS architectures in the fluidic PDMS device, we have morphologically characterized the porous PDMS microfluidic device. Furthermore, since the main purpose of this device is to operate under perfusion conditions, we have characterized the dynamic capacity of the systems by perfusion fluorescence nanoparticles and X-ray contrast agents. Finally, we conducted fluidic mechanics simulations in order to prove the interconnection of the pores.

i. Morphological characterization

In order to characterize the morphology of the structure formed inside the microfluidic chip, the porous PDMS foam was accessed through a cross-cut segment. This is one of the main advantages of using PDMS as fabrication material, it is easily processed and cut to access to the inner core of the scaffold. This constitutes an advantage compared to harder materials such as DS3000 or ceramic scaffolds, which tend to be brittle and crack upon cutting due to the fragility of the 3D porous architectures. In order to do this, the microfluidic device was sliced in segments of 3-4 mm in thickness. In **Figure 4.12**, we present the images obtained by optical characterization and electron microscopy of a cross-cut segment of the fluidic device. We can observe a highly interconnected porous network with a typical pore dimensionality of 1-3 mm and interconnection opening ranging from 50 µm to 500 µm. The comparison between the optical and the SEM observations (**Figure 4.12A** and **Figure 4.12B**) provides a closer inspection of the features of the structure. We observe cavities (delimited in orange dotted lines) displaying interconnections to other pores (pointed by the arrows). In the optical micrograph, the pore is formed by a transparent thin membrane of PDMS. These membranes display a few apertures visible in the corresponding SEM image.

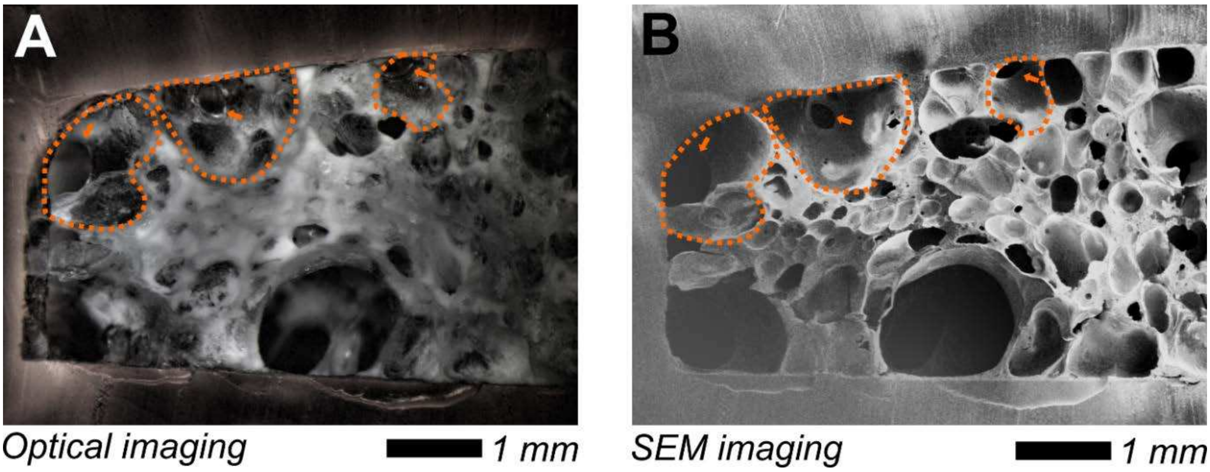

Figure 4.12. *Microscopy characterization of the cross-cut segment of a porous PDMS microfluidic device by:* ***(a)*** *optical micrograph of a cross-section of the inner core of porous PDMS within the 3D microbioreactor;* ***(b)*** *SEM characterization of the previous crosscut depicting the surface of the 3D porous PDMS scaffold. The orange dotted lines delimit few cavities on the graph and the arrows point the apertures of these pores.*

SEM close-up views of the surfaces are shown in **Figure 4.13**. We can observe the cavities of the porous architecture displaying multiple microcavities ranging from 5 to 10 µm allocated along the surface. These microcavities, generated probably by the smaller micro-droplets of the water-in-PDMS emulsion, have a large impact on the surface topography, generating micro-roughness non-negligible at the cellular scale.

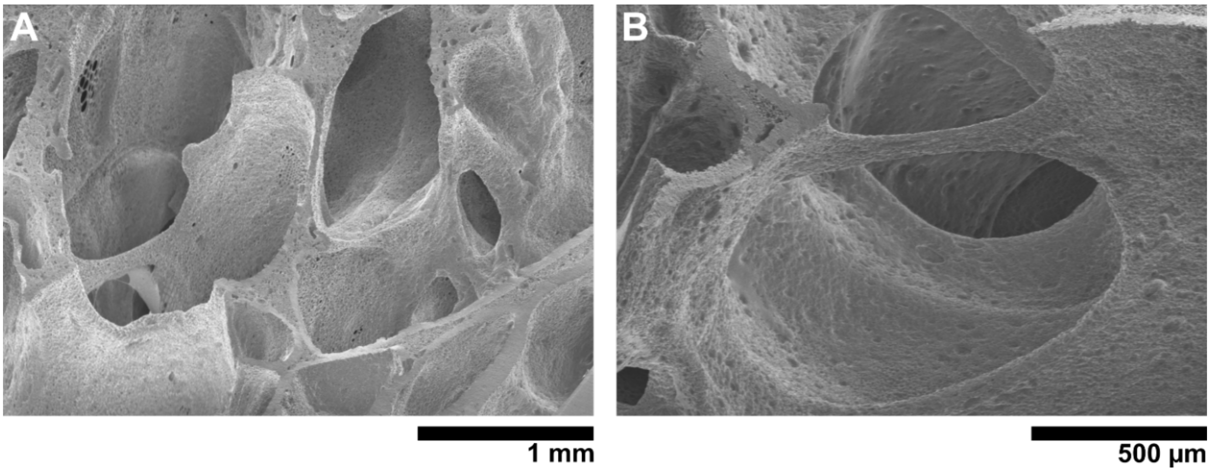

Figure 4.13. *SEM close-up on the surface of the porosity displaying the typical porous micro-cavities that induce a rough surface on the porous PDMS architecture.*

ii. X-ray tomography: 3D digital model

To provide a further analysis of the 3D architecture characteristics of our device and a whole vision of the porous microdevice, we employed X-ray Computed microtomography (μCT) with the help of our collaborations, Paul Duru and Sarah Blosse from the Institut de Mécanique des Fluides de Toulouse (IMFT). For this study, we used again the EasyTom XL 150 (RX Solutions) equipped with an X-ray source of beryllium target. The energy of the beam was adjusted to the sample and the resolution of the scan, resulting in a source voltage fixed at 85 kV with a source current at 180 μA. A complete scan was acquired, recording 1440 angular projections equally spaced along 360º. **Figure 4.14** shows a 3D representation of the central chamber obtained after denoising and binarizing the raw data. The crosscut views in the *XY* and *YZ* planes illustrate the highly interconnected structure of the internal core of the architecture, where a wide range of pore sizes can be observed.

The analysis of this structure shows a mean porosity of 63.5% and an available surface for cell culture close to 38.45 cm^2. This porosity value matches with the typical BV/TV[13] value of $26-31\ \pm\ 7\ \%$. We can observe as well a wide range of pore size, similar to the ones observed in **Chapter 2.** These cavities typically range from $500\ \mu m$ to $4\ mm$, in agreement with the images of the sliced segments. In the longitudinal edges of the device, we can observe a larger density of bulk PDMS. We associate this to regions of lower porosity caused by the closure of the fluidic chamber into the channel, which can lead to the accumulation of bulk material during the expansion of the cavities of our porous PDMS generation process. Another possible explanation is the compression of the PDMS foam when introducing the microfluidic connectors in the channels.

---

[13] *Bone volume fraction (BV/TV) is the volume of mineralized bone over total volume. We can understand it as the inversed value of the porosity.*

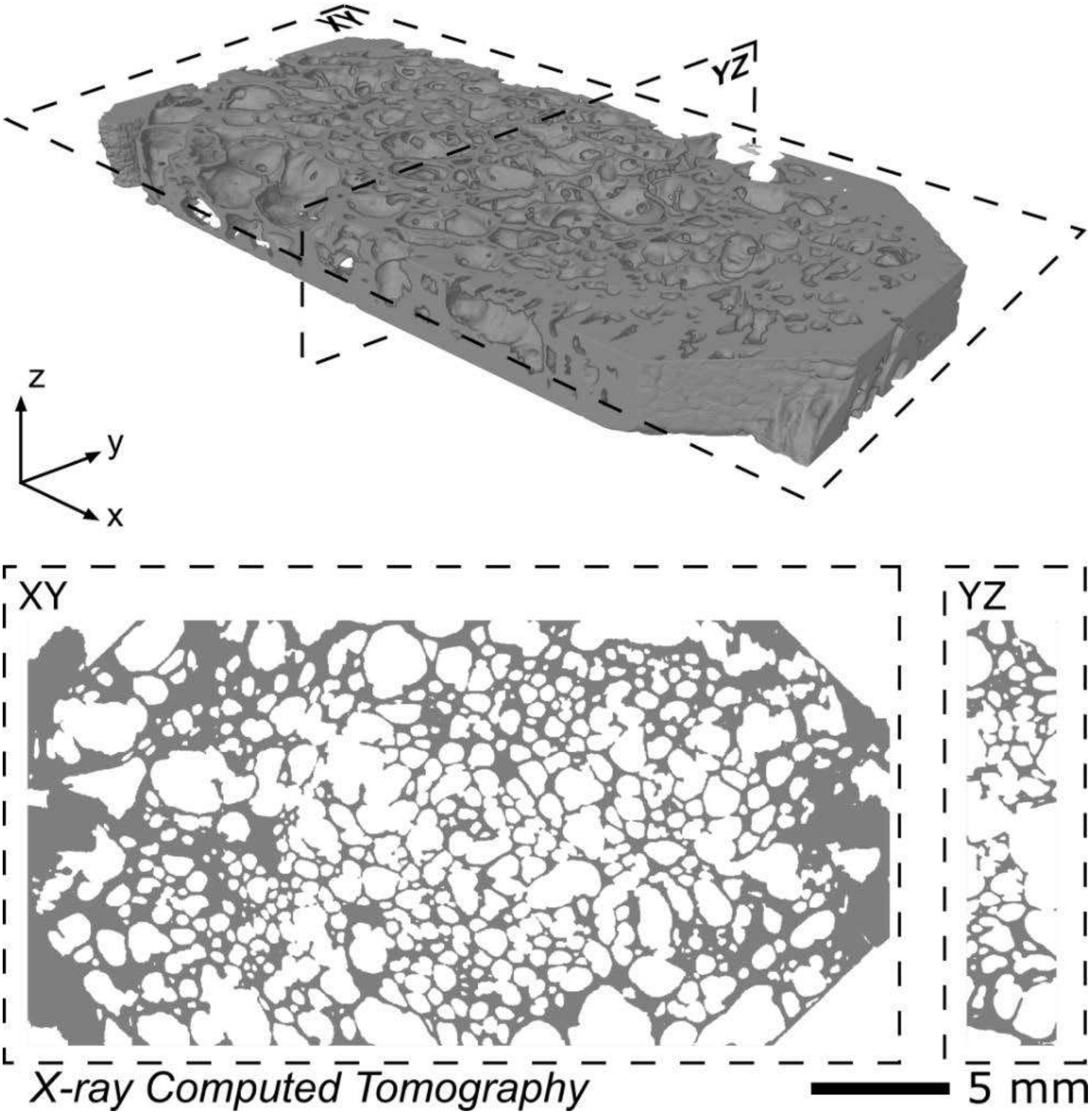

Figure 4.14. *X-ray µCT 3D view of the porous PDMS architecture of the PDMS bioreactor after segmentation. Beneath, crosscut of the 3D reconstruction along the planes xy and yz.*

iii. Hydrodynamic characterization

In order to characterize the hydrodynamics of the devices, we used fluorescence and X-ray imaging of tracers through the structure. This set of experiments conducted on different chips provides information on the liquid movement within the porous architecture and helps us to understand the fluid behavior in dynamic cell culture conditions.

In **Figure 4.15**, we present the results of injecting a solution 0.1% of 500 nm carboxylated-modified fluorescence particles (FluoSphere 505/515 nm) at 400 µL/min. This device was previously filled with water to extract as much air as possible from the structure. Since the size of the particle used is much smaller than the typical pore dimension, this experiment provides a relevant cartography of the advective flows in the whole architecture. A mosaic of different frames shows the penetration of the fluorescence solution into the inner porous core of the microfluidic device, with the fluorescent signal being proportional to the average concentration of spheres over the depth of the device. In the mosaic, we observe how the inferior half of this device permits an easier path of the fluorescence solution than the other half, which takes longer time to fill. This behavior can be induced by a lower porosity or interconnectivity of the discussed region or air-bubbles trapped in the device.

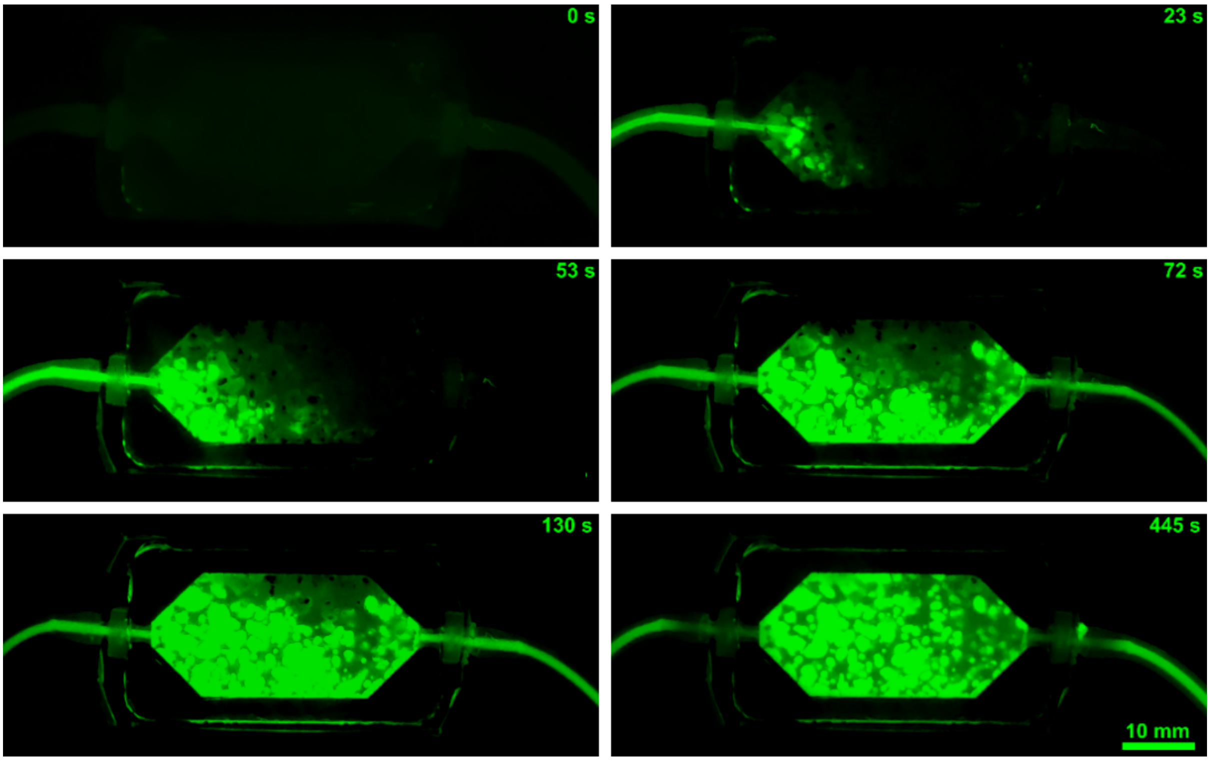

Figure 4.15. *Optical images of the perfusion of fluorescent microbeads (green) perfusion through a pre-filler porous PDMS microfluidic device at 400 µL/min at different times: 0, 23, 53, 72, 130 and 445 s.*

Quantitative characterization of the injection was also performed using X-ray radiographic imaging while perfusing a radiopaque KI solution. KI solution blocks the transmission of the X-ray passing across the device and reduces the intensity captured by the X-ray sensor. For reasons of representativity and concordance with the rest of the fluorescence images, we display the X-ray radiographies with radiopaque solutions in inverted intensity. Therefore, the images that follows represent high concentration of KI with high intensity and the analysis of these images is carried out accordingly.

In **Figure 4.16**, we show the perfusion of KI solution 10% w/w and the contrast analysis performed over time in a radiography mode on a different device. Again, the device was filled with water before the experiment. The central image depicts the perfusion at t = 200 s. The solution was injected using a computer-controlled syringe pump CETONI neMESYS 290N featuring a constant flow of 0.2 mL/min. And the acquisition was performed at 5 frames per second, with a noise reduction of the data by averaging 5 images. The horizontal and vertical dashed lines in **Figure 4.16** illustrate the location of the intensity analysis shown in the graphs of the figure. The analysis was performed averaging the inverted intensity on a 50-pixel band centered on the dashed lines. This process allows to smooth the noise of the acquisition and average the specific porous features of the region to better observe the solution advancing. These results are presented in the plot on the left and beneath the image, where we can observe the evolution of the intensity of the contrast while the solution penetrates the structure at different times of the experiment.

When the cavities of the device are fully filled with the KI solution, we have access to the intrinsic shape of the structure. A region with high porosity will accumulate more KI content which is reflected as a peak on the graph; while a region of low porosity or reduced connectivity, will possess less radiopaque agent leading to a valley region on the data. In the vertical graph, we can identify two regions, at the top and the bottom of the device which present low porosity close to the inlet and outlet of the device. This is in agreement with the presented X-ray tomography cross-cuts presented in **Figure 4.14**.

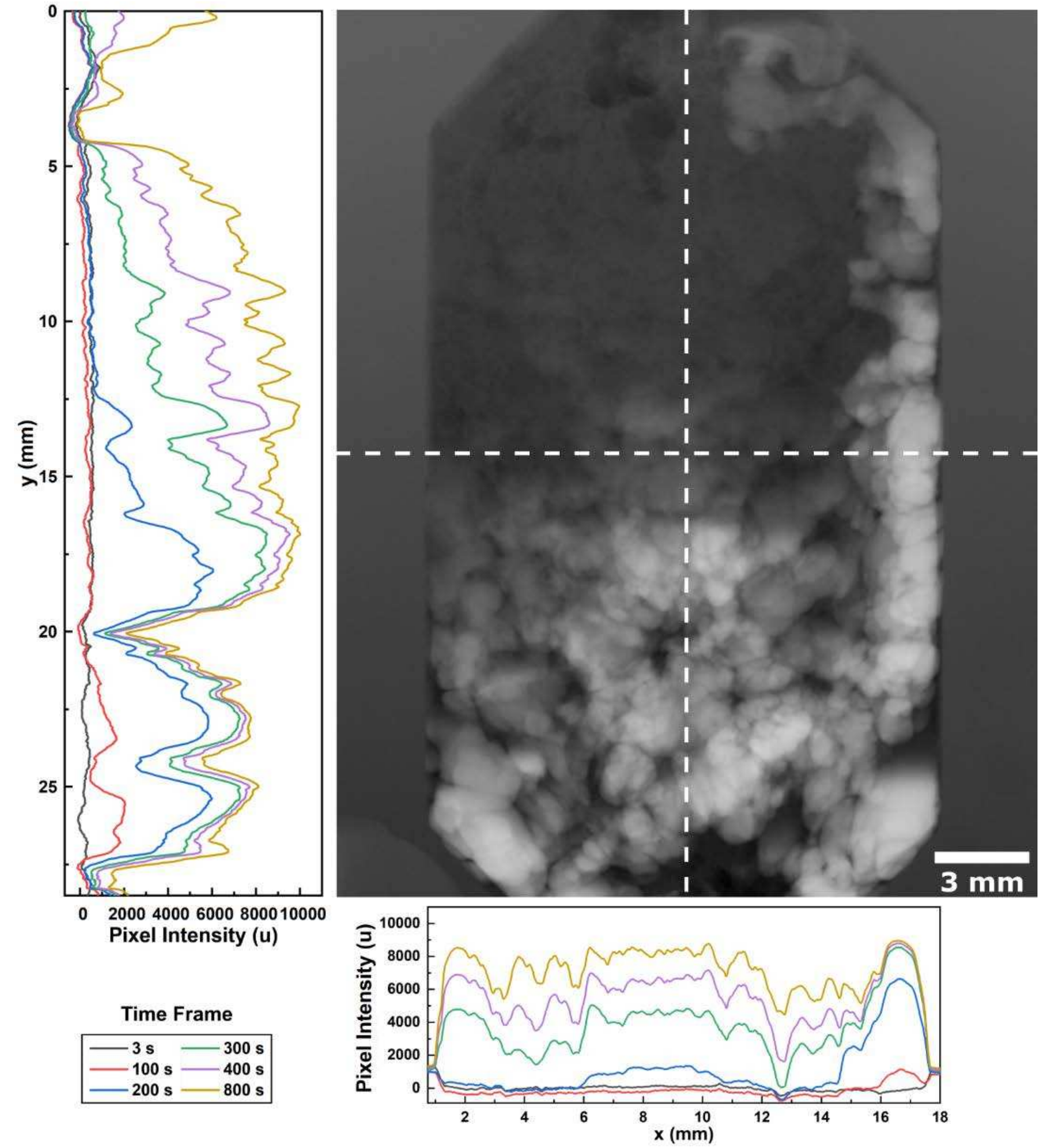

Figure 4.16. *Perfusion of X-ray radiopaque KI solution in the porous PDMS microfluidic device. The image corresponds to the frontal view of the microfluidic device while perfusing a KI enhancing contrast solution at 200 µL/min at t = 200 s, which represents a transient-state of the liquid progression across the structure. Inverted intensity profiles, 50-pixel width averaged, linked to the increase of KI concentration are presented on the left and beneath the depicted view at different temporal times.*

Figure 4.17 displays a set of frames corresponding to the time evolution of the intensity shown in the graphs of the **Figure 4.16**. These images feature again the inverted intensity of the X-ray acquisition to correlate it to the KI concentration, using a heat colormap. This figure represents six images at different time points and allows us to observe the preferential flow paths due to the heterogeneities of the porosity within the chip. This free-formed architecture exhibits anisotropies in the distribution of the fluidic resistance within the structure which leads to an inhomogeneous flow path along the porous network. In the images, we can see how the KI solution progresses faster in the left half-segment of the device than in the other side. This difference in flow distribution observed between two devices with the fluorescence beads and KI solution is representative from the variability of the free-formed porosity generated with our technique.

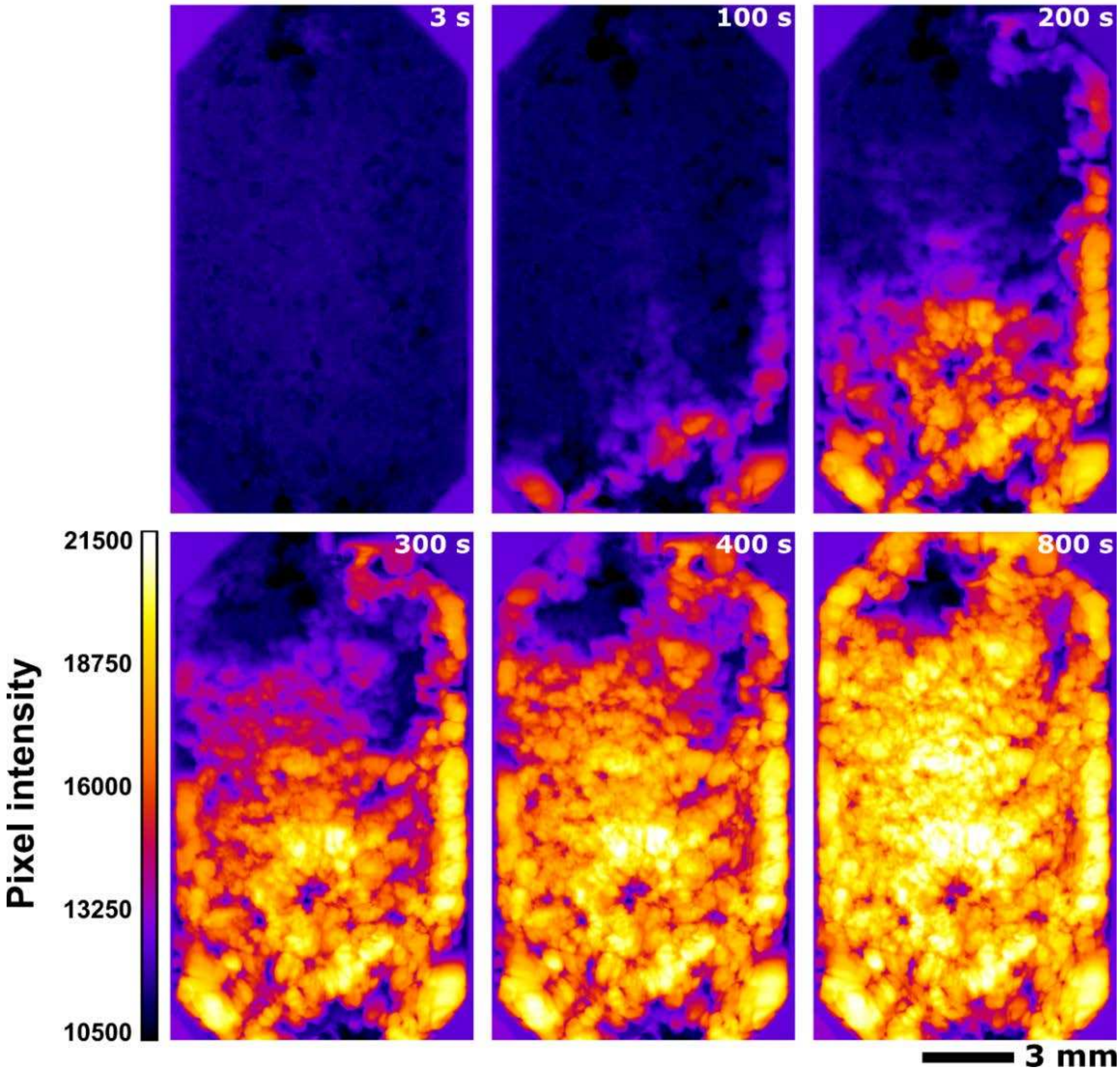

Figure 4.17. *X-ray radiographs displayed as a heat colormap of the inverted intensity to show the perfusion of a KI solution at different times.*

With these two characterization methods, we have studied the progression the liquid within the device. This flow showed a similar behavior in both cases, featuring preferential paths for the liquid to flow through the porosity that could be due to the inhomogeneous organization of the porosity or by air-bubbles trapped in the structure of the device.

iv. Hydrodynamic simulation in cell culture conditions

The flow distribution, flow velocity and the shear stress impact the behavior adherent cells. In collaboration with Omar Mokhtari and Yohan Davit (IMFT), we locally quantified these parameters and their distribution along the microfluidic device by solving the incompressible Navier-Stokes equations using the digital model obtained by X-ray tomography (presented in **Figure 4.14**). For this calculation, we selected a low flowrate similar to the one used for cell culture conditions. This value was defined so as to change the volume of medium inside the chip within a day ($100\ \mu L/h$). At low flowrates, the Reynolds number is much smaller than one and the flow equations degenerate to incompressible Stokes equations. In this limit of creeping flows, i.e., when the viscous forces are dominant over the inertial forces, the equations are linear and can be rescaled by the inlet flowrate. Computations are run in parallel with the open-source CALIF^{3}S software developed at IRSN [7]. A detailed explanation of the process is described in the appendix. In **Figure 4.18A**, we present the solution for a 3D representation of the flow velocity corresponding to an inlet flowrate of 100 µL/h, with cross-views along the planes *xy* and *yz* beneath. The data is presented in form of a 3D crosscut colormap with a logarithmic scale to visualize the wide range of velocity magnitudes found within the pores. The largest values $\sim 2 \cdot 10^2\ \mu m/s$ correspond to the inlet-outlet connectors of the device where the whole quantity of liquid is imposed to pass through. The lowest values of flowrate, i.e., $\sim 5\ \cdot 10^{-2}\ \mu m/s$, correspond to smallest pores of the structure. The cross-cut along the plane *xy* shows that the high velocity regions are related with large pores and the interconnections between those and low velocity regions appear in regions with small pores as expected considering a Poiseuille-like flow. The cross-cut along the plane *yz* shows the diameter of the pores along the pores in the plane perpendicular to the flow. In both cross-cuts, we clearly observe how locally, the flow velocity increases with the distance to the pore walls, which is consistent with the expected creeping flow.

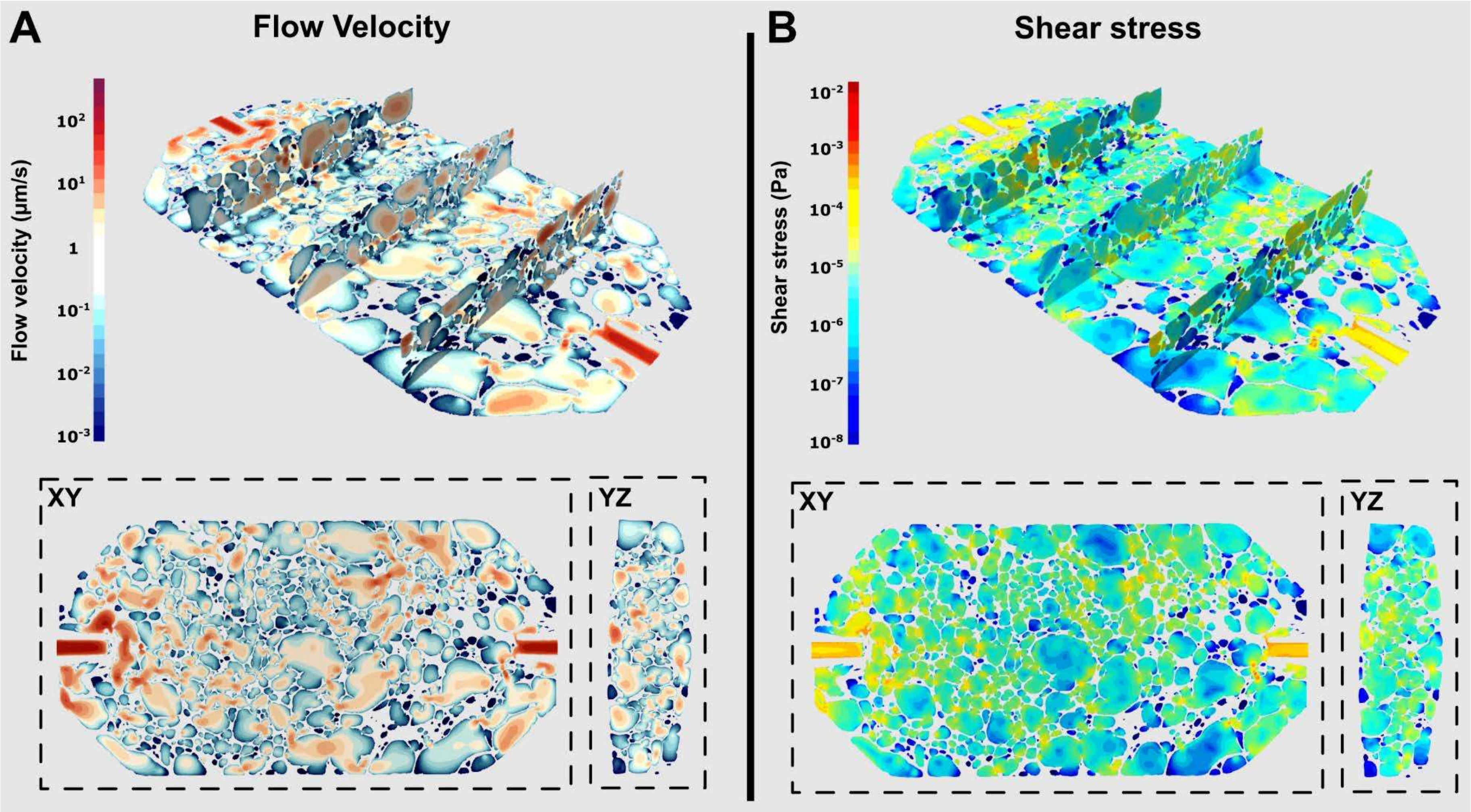

Figure 4.18. *Solutions of the incompressible Navier-Stokes equations within the microfluidic device for a flow rate at 100 μL/h.* ***(a)*** *3D crosscut colormap of the flow velocity within the device. Beneath a cross-sectional representation along the planes xy and yz. Colormap scale is logarithmic.* ***(b)*** *3D colormap of the shear stress within the device. Beneath a cross-sectional representation along the planes xy and yz. Colormap is in logarithmic scale.*

The shear stress solution is as well presented as a 3D transparency colormap in the **Figure 4.18B** with cross-views of the planes *xy* and *yz* underneath. The largest values for the shear stress $\sim 5 \cdot 10^{-2}\ Pa$ can be found inside the connectors of the chip, where the total flow of the sample is condensed in a of 1 mm diameter channel. Regions of high shear stress, ranging from $2 \cdot 10^{-2} - 5 \cdot 10^{-3}\ Pa$ are generally located in the immediacies of interconnections of large pores that involve a spatial confinement of the flow.

For a better quantitative visualization of the results obtained, the values calculated were condensed in the so-called probability distribution functions (PDF). This mathematical construct depicts all the values obtained and normalizes them, an provides a relative frequency of these values in the system. For a more illustrative representation, we have removed the values corresponding to the inlet/outlet connections for this analysis. **Figure 4.19** represents the PDF for the flow velocity (v_x) normalized by their averaged values ($0.203\ \mu m/s$) and the shear stress were calculated and normalized by $1\ Pa$ for the shear stress : this value was found in the literature and taken as a reference value to trigger the osteogenesis in BMSCs culture [8]. The data is presented with a logarithmic scale to cover the wide range of values. For the flow velocity data, we observe a segment of the data displaying a low or even a negative velocity. We can associate this data with zones of stagnation or reflow linked to the tortuosity of the flow trajectories in the heterogeneous structure. For positive velocities, the PDF decays close to an exponential behavior. This emphasizes the rarity that represent high velocities in the distribution.

In the shear stress data, we can observe a peak in low values with a decay for the larger values. This data shows that the shear stress induced by the liquid movement remains withing the biological limits for cell culture. Indeed the $100\ \mu L/h$ selected flow induces a shear stress ranging from 0.1-30% of the reference value from the literature, a range of stress that has shown no detrimental impact on the cell behavior [8], [9].

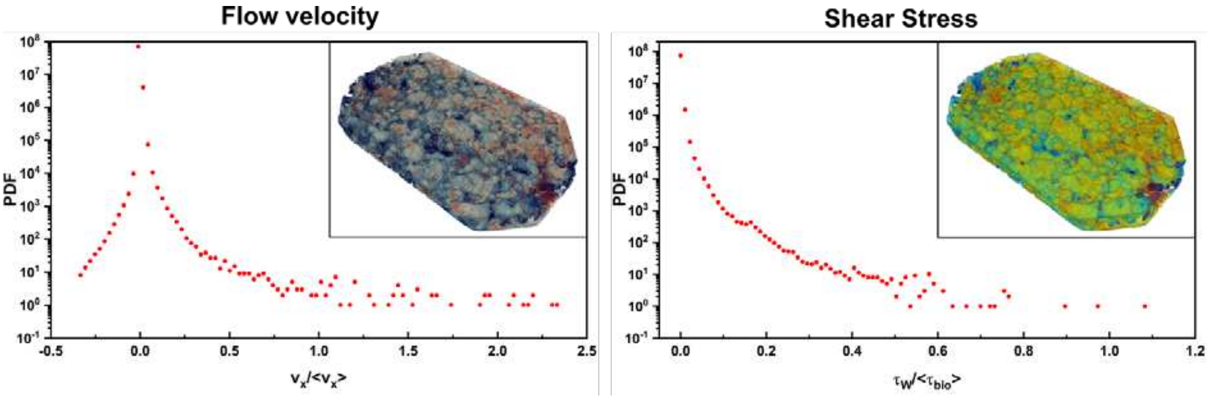

Figure 4.19. *Profile density function of flow velocity V_x along the x-axis and shear stress presented with the corresponding inserts showing the 3D fields in transparency. The y-axis is represented in logarithmic scale.*

In addition to advection, it is important to take into account the contribution of diffusion of species to the total mass transfer balance since it impacts the distribution of nourishment and cell secretions within the scaffold. To study the distribution of the concentration in the device, we solved an advection-diffusion equation for a concentration C of species in the perfused liquid. **Figure 4.20** presents a mosaic of images at different point of times showing the progression of the concentration through the porous architecture of the device at two flowrates: 100 µL/h to simulate the chosen dynamic cell culture conditions and 12000 µL/h, equivalent to 200 µL/min as used during the perfusion of KI solution for X-ray characterization. The frames selected represent the equivalent injected volume at both flowrates. At the start of the simulation, the liquid with maximum concentration penetrates through the scaffold. We can see how the liquid advances at this point maintaining a defined concentration profile. As the liquid advances through the structure, we can observe how the gradient of concentration becomes less steep and a diffusion front appears more prominent in the images. The simulation proves that the selected flow permits a full renewal of the culture medium within the device within 24-30h, which represents a valid interval for the welfare of the cells. We do not observe large differences between both experiments, concluding that the advection is more dominant than the diffusion at both flowrates.

Furthermore, we can calculate the Peclet number to verify the relation between the advective transport and the diffusive transport:

$$Pe = \frac{advective\ transport}{diffusive\ transport} = \frac{L \cdot u}{D}$$

Where ***L*** is the typical distance of the system, ***u*** es the local flow velocity and ***D*** the mass diffusion coefficient. For the typical length, we considered the value from the morphological characterization of porous PDMS, L ~ 0.5 - 1.0 mm. The flow velocity was calculated for a Q = 100 μL/h, as 0.203 μm/s. As mentioned previously, we can scale the flow velocity fields in an incompressible Stokes flow, obtaining 24.36 μm/s for Q = 12000 μL/h. The typical diffusion coefficient for biological molecules ranges about ~ 10^{-10}-10^{-11} m^2/s. The number of Peclet in each situation is $Pe_{100} = 20$ and $Pe_{12000} = 2400$. This proves the dominant contribution of the advective transport on the distribution of species over the diffusion phenomenon.

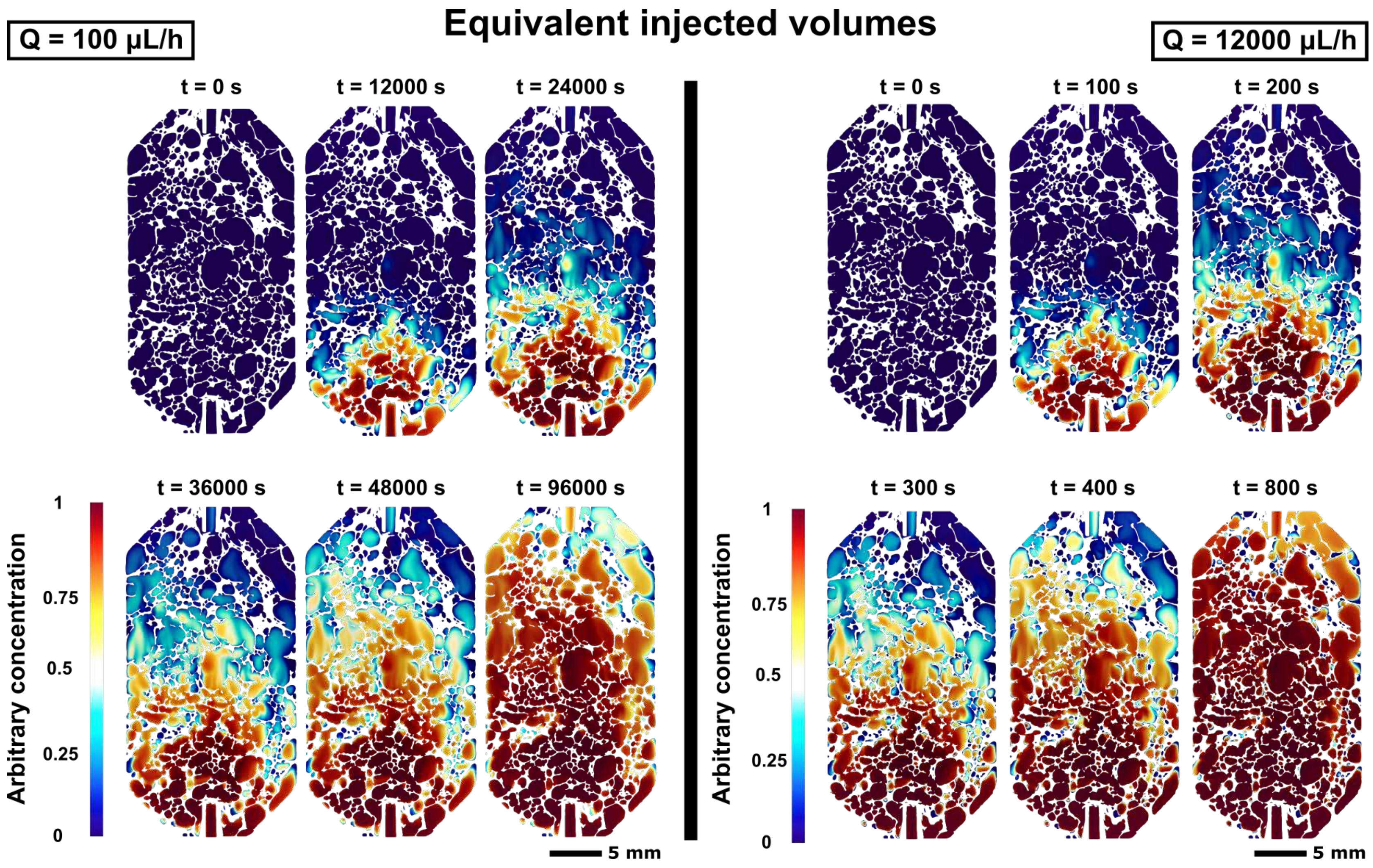

Figure 4.20. *Colormap solutions of the advection-diffusion equations to calculate an arbitrary concentration gradient evolution with time for two flow rates: 100 µL/h and 12000 µL/h. The time frames display equivalent injected volumes for both flowrates.*

c. Dynamic cell culture in porous PDMS

In the previous sections, we have presented the integration of our novel water-in-PDMS emulsion templating into a microfluidic device. The system was topologically and hydrodynamically characterized using SEM, fluorescence microscopy and microcomputed X-ray tomography. The resulting porous PDMS bioreactor was tested in the context of bone marrow cellular microenvironment. The dynamic cell culture was studied using SaOS-2 and BMSCs. For these experiments, we included a computer-assisted syringe pump and we placed the device inside an incubator. This configuration allows us to collect medium from the outlet of the chip and measure the metabolic tracers. The set-up is presented in **Figure 4.21**.

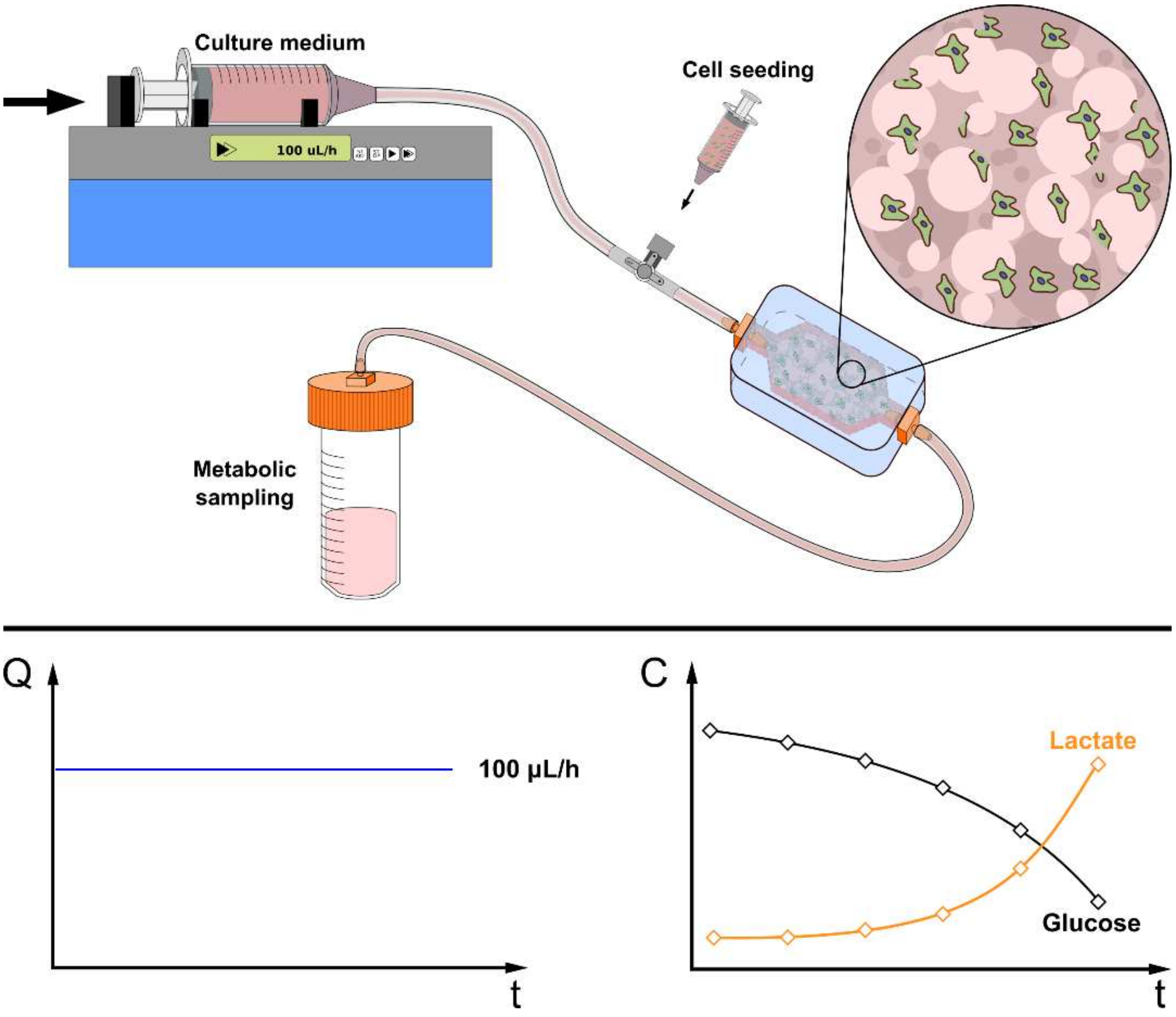

Figure 4.21. *Schematics of the experimental set-up developed for the direct seeding of cells; the subsequent constant flow dynamic cell culture and the metabolic analysis which are illustrated on the associated graphs.*

In **Protocol 16**, we present the main steps of the protocol employed in the microbioreactor to validate its performance for cell culture applications. To enhance the adhesion of cells to the porous PDMS, we applied a fibronectin coating by injecting the solution in the scaffold and incubating it for 4h. Then, we seeded 3,85 x 10^5 cells suspended in 2 mL in each chip and they were incubated overnight to ensure their attachment to the surface prior the start the dynamic cell culture conditions. Culture medium was perfused using a syringe pump at $100\ \mu L/h$. During the experiment time, cell culture medium was collected every day from the bioreactor outlet and analyzed to obtain metabolic data from the cell culture. Once the experiment ended, the common protocols of fixation, permeabilization and staining were carried out directly by injecting the solutions into the chip. This is an important feature as it permits an automatization of the protocols and allows a significant reduction of wasted solutions during the experiments. The samples were sliced with a surgical blade and cell were observed directly over the inner core of the porous PDMS architecture.

Protocol 16. Cell seeding and dynamic cell culture on porous PDMS devices

This protocol details the process of seeding and culture of cells in dynamic culture conditions in the porous PDMS microfluidic devices.

7. Samples were sterilized using autoclave
8. In sterile conditions, fluidic circuit was plugged and samples were wetted injecting PBS and incubated for 4h at RT
9. Then, samples were coated with a fibronectin solution 10µg/mL over night at RT
10. Samples were rinsed with PBS and the culture medium was injected
11. A quantity of 2 mL cell suspension of 4000 c/cm^2 was injected then were incubated overnight at 37 °C
12. Dynamic conditions were initiated by perfusion culture medium at 100 µL/h

i. SaOS-2 cell culture

The dynamic cell culture validation was performed first with the cell line SaOS-2 for 14 days, and then with human BM-derived MSC for 21 days. In both cases, daily metabolic follow-ups were performed in order to follow the cell behavior during the assay. In **Figure 4.22**, we present the imaging of the cross-cuts of the porous PDMS devices cultured with SaOS-2 for 14 days. Samples were stained with DAPI (blue), β-tubuline (green) and Ki67 (red) and characterized with confocal fluorescence microscopy. **Figure 4.22A** displays a z-stack of a typical inner pore in the core of the scaffold (Δz = 351 µm). These images show a dense layer of cells covering the bottom of a pore. In white dash line, we can notice an interconnection between both adjacent pores and the cytoskeletons of the cells aligning with the border of the cavity. The diversity in topographies generated in this free-formed porous architecture helps cells to display elaborated 3D morphologies absent in standard cell culture conditions, as seen in **Chapter 3**. In **Figure 4.22B**, we show the image projection corresponding to a z-stack over Δz = 1008 µm. The displayed morphology is an entangled porous PDMS membrane fully covered with SaOS-2 cells. In this configuration, we can observe some regions of the structure where cells formed clusters, similar to the ones reported in the literature [10]. In **Figure 4.22C**, we present a pore-throat between two large cavities. In this image, we can observe a significant background signal in the porous PDMS. We believe that in addition to a potentially weak fluorescence signal from the PDMS, it is also probably due to the non-specific adsorption of β-tubulin at the surface of PDMS. This effect, as the photoluminescence of the DS3000, can be exploited to determine the scaffold architecture using florescence imaging while not impeding the analysis of the cells and its distribution on the scaffold. In **Figure 4.22D**, we report an overhanging structure over several hundred microns, formed purely by cells and attached to the pore walls. This is clearly visible due to the lack of green background light associated to the porous PDMS. A close-up view of this self-organized cellular arrangement is presented in the **Figure 4.22E**. Here, we can observe the large quantity of cells that conform the structure, which presents a higher density than the rest of the pore. Furthermore, we can observe an elongated extension formed by individual cells in the upper side of the image. We believe that this type of structure, that would not be possible to obtain in 2D culture conditions, is very encouraging in the perspective of the creation of large-scale cellular assemblies and further tissue regeneration.

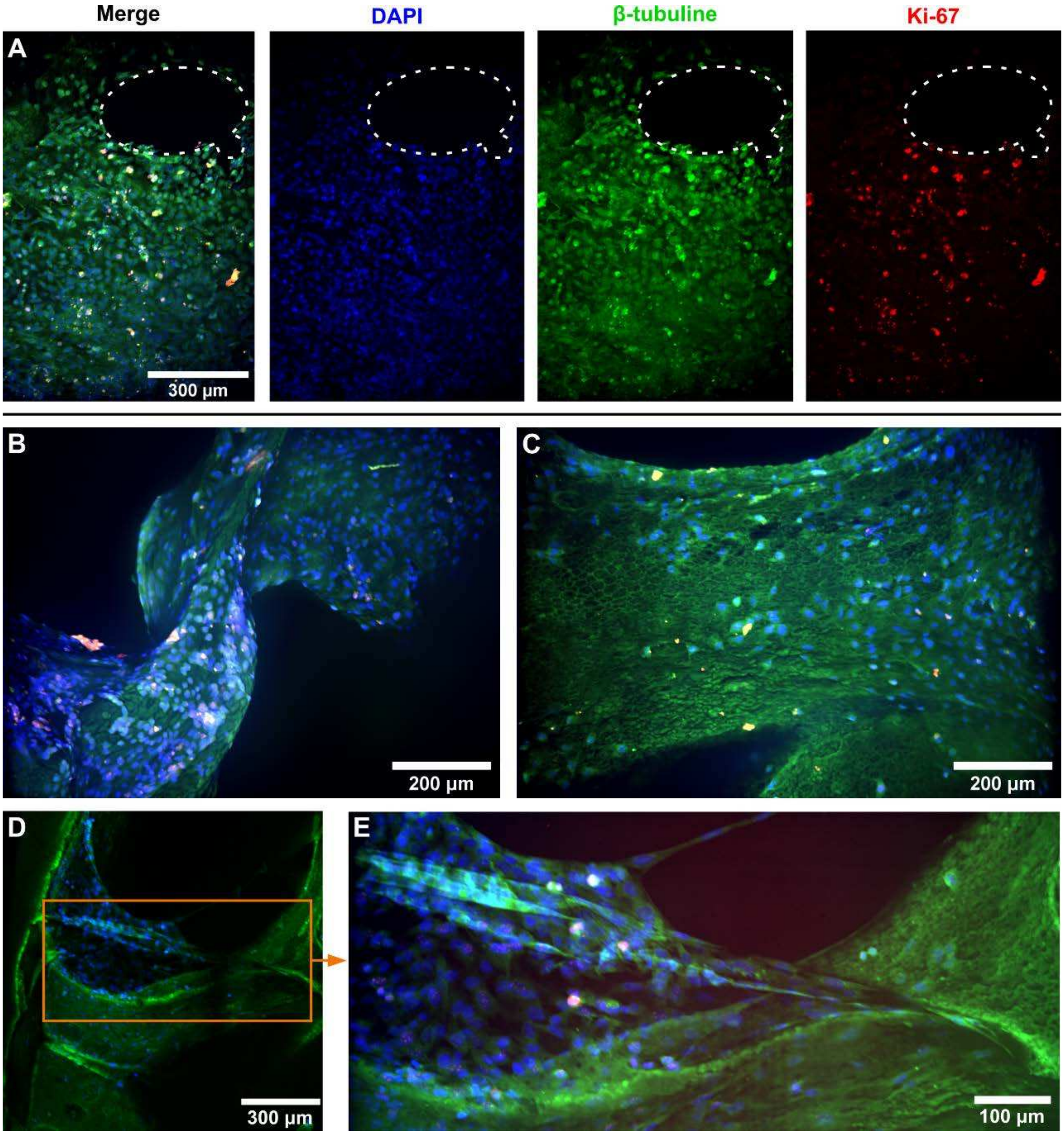

Figure 4.22. *Immunofluorescence confocal imaging z-projection of SaOS-2 cells colonizing the pores of the porous PDMS inner core (blue: Hoeschst; green: β-tubulin; red: Ki-67).* ***(a)*** *A cell layer in the architecture, dashed line delimits the pore interconnection.* ***(b)*** *3D cell construct over an entangled PDMS membrane between pores.* ***(c)*** *Cells organized along the microstructured surface present on the scaffold at the intersection of two pores.* ***(d)*** *Suspended cell construct over a macro-pore formed by tens of cells adhering to each other.* ***(e)*** *Close-up view of the suspended cell formation depicted in (d).*

To monitor the proper development and the viability of the cells inside the bioreactor, we performed a daily metabolic follow-up, presented in **Figure 4.23.** This consists in a daily collection of a minor quantity of medium and in measuring the glucose and the lactate concentration. This gave us daily information of the state of the colony and the cellular activity in the bioreactor. The glucose concentration, which is directly related with the glucose consumption of the cells, shows a continuous decay with time. The values dropped from $\sim 5.2 - 5.0\ mM$ for day 2 to $\sim 3.6 - 3.2\ mM$ at day 13. As result of the glucose consumption and the metabolic cellular activity, lactate is secreted by the cells as byproduct. The concentrations of lactate increased gradually from $\sim 10 - 5\ mM$ at day 2 to $\sim 18 - 15\ mM$ at day 13. The coordination between both cellular activity tracers shows a normal evolution expected from cells under these conditions. Therefore, we can infer an increase of the metabolic activity, mostly likely related to the proliferation of cells in the bioreactor. This hypothesis is supported by the Ki-67 immunostaining characterization performed over the devices shown in **Figure 4.22A**.

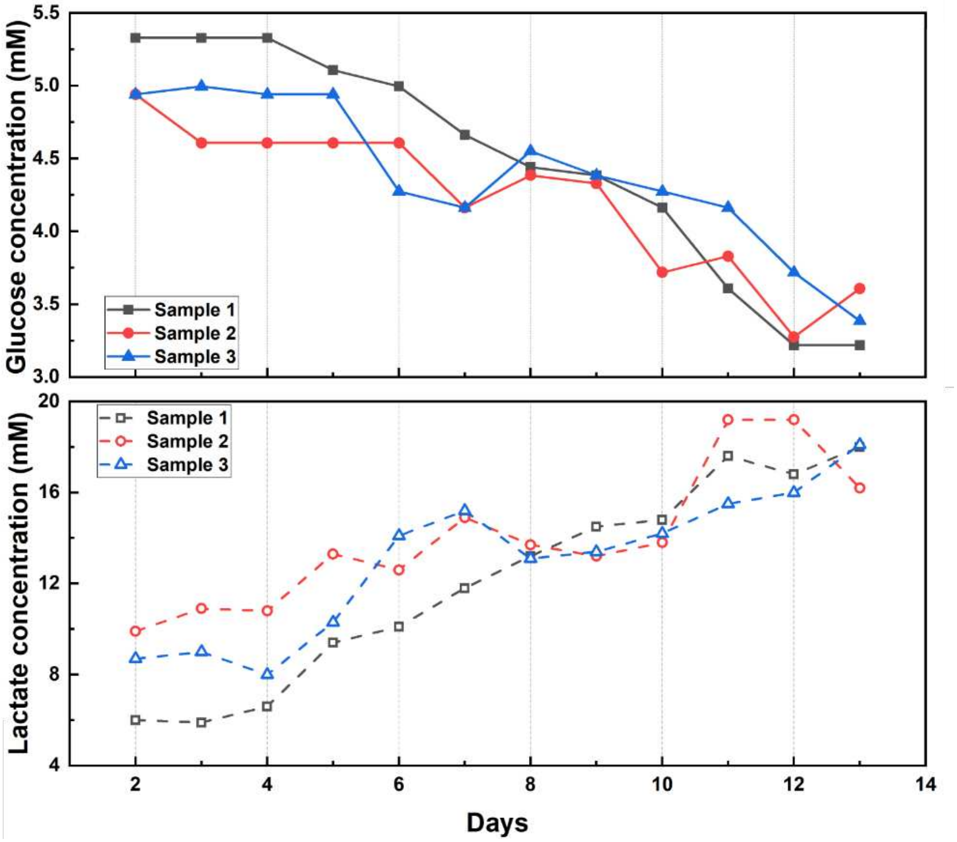

Figure 4.23. *Glucose and lactate concentrations: metabolic tracing of SaOS-2 dynamic culture for 14 days.*

For comparison, we present in **Figure 4.24** the data collected in parallel on a 2D culture carried out under standard conditions, i.e., 2D flat slabs of fibronectin-coated PDMS. In the immunofluorescence images we can observe a dense layer of cells covering the surface and expressing the proliferation marker Ki-67. The concentrations of the metabolic species for those 2D controls strongly oscillate during the 14 days (glucose concentration $\sim 4.7 - 0.6\ mM$ and lactate concentration $\sim 10.1 - 25.0\ mM$), due to the changes of culture medium. This shows a large instability of nutrients supply for the cell colony in the bioreactor related to the culture medium changes. The same trend, i.e., these abrupt variations, can be identified for the lactate secretions. These steep variations in the metabolic concentrations could lead to alteration of the cellular behavior induced by metabolic stress. By comparison, the continuous perfusion of culture medium within our bioreactor seems better for cell culture. The stable supply of nutriment and the continuous flush of metabolic by product both lead to a stable system favoring continuous cellular development and avoiding the abrupt variation of the biochemical microenvironment.

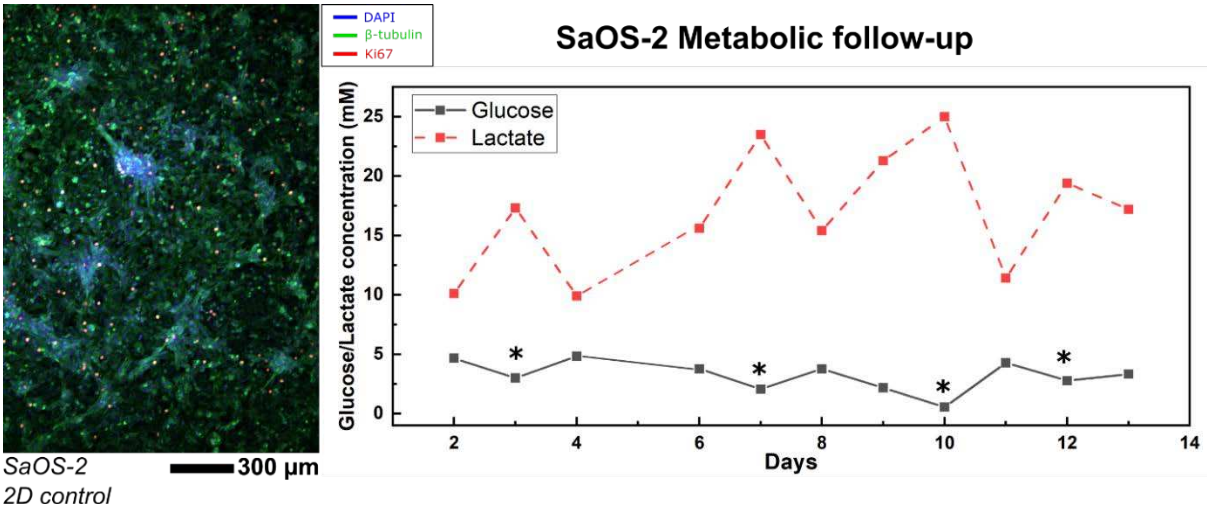

Figure 4.24. *Immunofluorescence characterization and metabolic follow-up of the 2D PDMS slabs, fibronectin-coated, used as static cell culture control for SaOS-2. "*"-symbol indicates the change of medium in the cell culture multi-well plate.*

ii. BMSCs cell culture

Finally, we tested the performance of the porous PDMS microfluidic device in the presence of primary human MSCs using EGM2 medium. Cells were seeded as described in **Protocol 16** and kept under dynamic conditions for 21 days prior fixation and staining. To investigate the proliferation of MSCs we adapted a live-staining protocol using a click reaction fluorescence stain (Click-iT EdU imaging kit Alexa Fluor 594, Invitrogen) [11]. Our protocol consisted in diluting the EdU marker in the culture medium and supplying it to the bioreactor under dynamic conditions for 72h. The full protocol is detailed in **Protocol 17.** This staining marker is added to the culture medium and cells incorporate it to their nuclei during the active DNA synthesis, hence the requirement of continuing the culture. Though it represents a higher degree of complexity, as informed by the manufacturer, it also depicts a more accurate information of the cell cycle.

Protocol 17. Dynamic live-staining with EdU Click-it Kit for 3 days

This protocol details the process of live-staining using the click-it kit in dynamic conditions in the porous PDMS microfluidic devices.

1. Add the EdU solution 1X to culture media. Prepare 15 mL/chip: initial volume + 2.5 mL/day + dead volumes
2. Inject 3 mL at 1 mL/min, then change to 100 µL/h
3. After 72h, proceed with fixation and permeabilization as usual (**Protocol 12**)
4. Prepare the EdU click-it buffer diluting it at 1/10 in DIW
5. Prepare the reaction cocktail respecting the quantities recommended by the manufacturer and the following order:
    a. Click-it reaction buffer
    b. Copper protectant
    c. AF picolyl azide
    d. Mix with the EdU click-it buffer
6. Rinse the cells with PBS BSA 3% then inject the EdU cocktail in the chip and incubate for 30 min at RT, in the dark. Then rinse cells at PBS BSA 3%

Figure 4.25 shows the images obtained from the immunostaining and confocal imaging with the associated metabolic activity. Cells were stained with Hoescht-DNA (blue), β-tubulin (green) and the mentioned EdU (red) for proliferation tracking. **Figure 4.25A** shows a mosaic of images along the z-axis in 2 different channels. The first column displays the red channel corresponding the EdU staining overexposed in order to have a background light to observe the porous architecture. The second column corresponds to the merged images showing the stained cells. This z-stack images represent a scanning depth of 530 µm, where we can observe a uniform distribution of proliferating cells. The metabolic activity, shown in **Figure 4.25B**, was monitored during the experiment and is in good agreement with the EdU proliferation staining. It presents a notorious increase in the lactate concentration coupled with the continuous decrease of glucose concentration associated with the incremental metabolic activity suggesting a significant level of proliferation during the culture as observed previously. As mentioned in the previous section regarding dynamic cell culture on DS3000 scaffolds, these metabolic rates are in agreement with the literature, yet the lactate concentration reached values close to the inhibition lactate concentration in MSCs [5], [6]. This could explain the stabilization of the glucose consumption after the first week of experiment. The close control of the flow, combined with the daily monitoring of the metabolism of the cells, opens the possibility to vary the flow during the experiment to flush faster the cellular byproducts. This would decrease the lactate levels to proliferation levels and restart the development of the cells, we will investigate this via future experiments. **Figure 4.25C** shows a z-projection of a pore and a close-up view of the interconnection between to cavities. BMSCs display flatten morphologies with multiple protrusions forming a network connecting close-neighbors. This sort of organization in MSCs has been previously reported in *ex-vivo* bone marrow tissue at 3D multiscale characterization [12]. We highlight in particular the ability of cells to adhere to the surface adapting their cytoskeleton to the interconnecting pores thus following the morphology of the geometrical features of the PDMS structure.

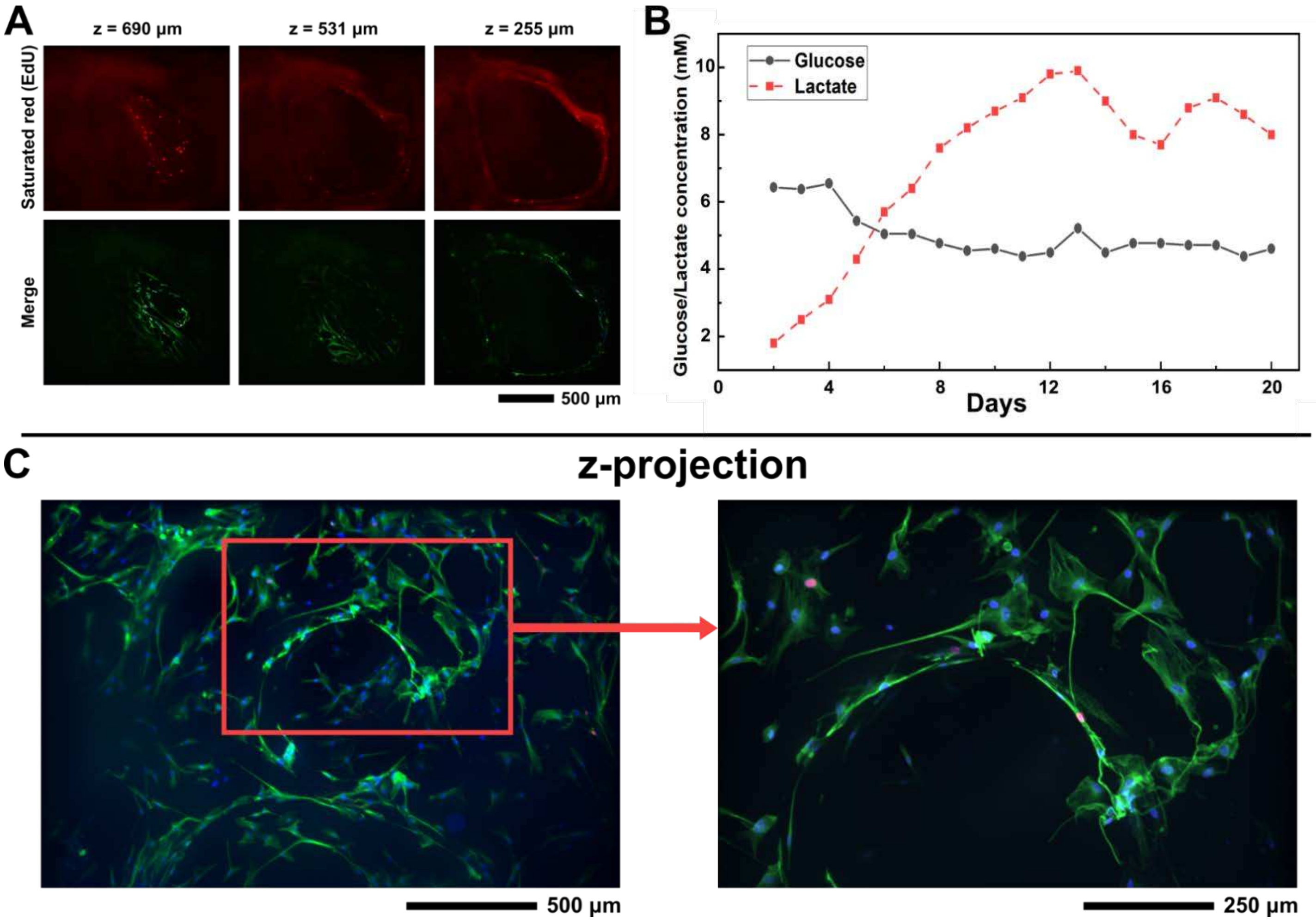

Figure 4.25. *Immunofluorescence confocal imaging and metabolic activity of human derived BMSC for 21D in dynamic cell culture conditions at 100 µL/h perfusion.* ***(a)*** *Mosaic red, and merged images at different depth to provide information of the 3D architecture. Red channel was contrast-modified over the saturation point in order to observe background light from the porous PDMS architecture;* ***(b)*** *metabolic analysis of the MSC dynamic cell culture;* ***(c)*** *Z-projection of a pore presenting the cell colonization; close-up view of the region enclosed in the orange square in (b). (red: EdU; green: β-tubulin; blue: Hoechst).*

In **Figure 4.26**, we present the 2D controls carried out in a similar manner on fibronectin-coated PDMS slabs, where the seeded BMSCs are kept in standard cell culture conditions for 21 days. In the fluorescence image, we can observe a dense cover of cells displaying flat elongated morphologies. EdU live-staining was carried out as well, in static conditions for 72 h. The metabolic analysis displays a similar behavior than the previously reported SaOS-2 2D static controls, with large abrupt variations due to the pile-up of cellular activity byproduct and the changes in cell culture medium.

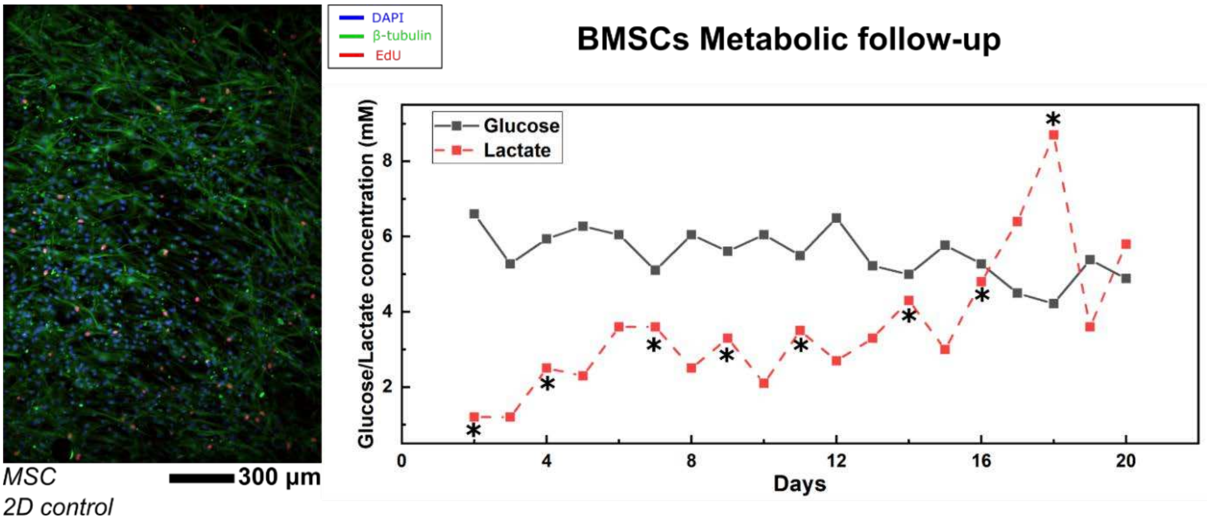

Figure 4.26. *Immunofluorescence characterization and metabolic follow-up of the 2D PDMS slabs, fibronectin-coated, used as static cell culture control for human bone marrow derived MSCs. "*"-symbol represent the change of medium in the cell culture multi-well plate.*

d. Summary

- We have integrated our porous PDMS into the fluidic chamber of a PDMS microfluidic device, obtaining a functional bioreactor.
- The devices were characterized using optical and electron microscopy and X-ray tomography, confirming the similar porous morphology than the PDMS architectures presented in **Chapter 2.**
- We studied the hydrodynamics characteristic of the devices by perfusion fluorescence nanoparticles or radiopaque solutions, observing the hydrodynamic flow distributions in each chip.

- Fluidic simulations were used with our collaborators from IMFT to locally study the properties of the flow. Flow and shear rates were spatially calculated using the digital model obtained by X-ray tomography, showing that the characteristics of the device under cell culture condition do not have any negative impact on the cells.
- We studied the advection-diffusion of the medium in the porous structure to simulate the refreshment of culture media through the device, showing a total renewal within 24h.
- Dynamic cell culture was engaged using SaOS-2 and BMSCs in dynamic conditions (100 µL/h) for 14 and 21 days respectively. The cells, characterized by confocal microscopy, displayed 3D architectures and overhanging features.
- Glucose and lactate were measured during the experiment to monitor the state of the cultures.

3. Conclusions

In this chapter, we have presented the integration of both technical approaches - the designed architectures obtained in DS3000 by stereolithography into a bioreactor and the free-formed structures produced *in-situ* in a PDMS microfluidic device - to enable cell culture in dynamic conditions.

Along the previous pages, we have provided experimental data concluding on the operativity of both techniques for their use as micro-bioreactors to host a 3D cellular microenvironment for the bone marrow. This represents a promising path for the tissue engineering and the micro-physiological systems communities in terms of access to 3D microbioreactors.

The integration of both sorts of 3D architecture with perfusion systems have been validated and the dynamic cell culture was performed, providing interesting insight regarding the cellular microenvironment. The continuous movement of culture media represents a stable supply of nutriment for the hosted cells in the structures, and it helps to dilute and spread the metabolic byproducts and biochemical signals secreted by the cells. Moreover, we have observed overhanging structures generated by cells within the pores of the structures in both scaffolds that were not found in static conditions. Furthermore, we could characterize a sort of suspended architecture similar to the structures obtained by dehydrated ECM or collagen in the pores of the DS3000 scaffold. We believe that this architectural arrangement could be a premise of the scaffold secreted by the cells in order to be used as a supporting structure for their migration and the development of three-dimensional complex architectures. The shear stress produced by the liquid movement could contribute to increase the ECM secretions, stimulating cells to establish complex structures within the architectures. The used of metabolic measurement allows us to monitor the development of the colonies. Unfortunately, the different nature of the bioreactors: close-circuit vs open-circuits impedes the comparison between both systems.

To conclude, we would like to point out the robustness and readiness of these microenvironments as interesting tools to continue the exploration of fundamental questions regarding the development of cell microenvironments. We have fabricated by two different scientific approaches tools that gather the biological cues of the bone marrow microenvironment discussed in **Chapter 1**. In the following chapter, we will conclude the manuscript and we will provide some perspectives and future works that were initiated during these last 3 years.

References

[1] "U-Cup bioreactor technical specifications." [Online]. Available: http://www.cellecbiotek.com.

[2] "U-CUP - a perfusion bioreactor for 3D cell and tissue culture." http://www.cellecbiotek.com.

[3] H. Ijima, S. Nakamura, R. Bual, N. Shirakigawa, and S. Tanoue, "Physical Properties of the Extracellular Matrix of Decellularized Porcine Liver," *Gels*, vol. 4, no. 2, p. 39, May 2018, doi: 10.3390/gels4020039.

[4] A. Thale and B. Tillmann, "The collagen architecture of the sciera — SEM and immunohistochemical studies," *Ann. Anat.*, vol. 175, no. 3, pp. 215–220, Jun. 1993, doi: 10.1016/S0940-9602(11)80004-X.

[5] D. Schop *et al.*, "Growth, metabolism, and growth inhibitors of mesenchymal stem cells," *Tissue Eng. - Part A*, vol. 15, no. 8, pp. 1877–1886, Aug. 2009, doi: 10.1089/ten.tea.2008.0345.

[6] F. dos Santos *et al.*, "A xenogeneic-free bioreactor system for the clinical-scale expansion of human mesenchymal stem/stromal cells," *Biotechnol. Bioeng.*, vol. 111, no. 6, pp. 1116–1127, Jun. 2014, doi: 10.1002/bit.25187.

[7] "CALIF3S. A software components library for the computation of reactive turbulent flows." https://gforge.irsn.fr/gf/project/isis.

[8] M. V. Hillsley and J. A. Frangos, "Review: Bone tissue engineering: The role of interstitial fluid flow," *Biotechnol. Bioeng.*, vol. 43, no. 7, pp. 573–581, 1994, doi: 10.1002/bit.260430706.

[9] A. Bissoyi, A. Bit, B. K. Singh, A. K. Singh, and P. K. Patra, "Enhanced cryopreservation of MSCs in microfluidic bioreactor by regulated shear flow," *Sci. Rep.*, vol. 6, no. 1, pp. 1–13, Oct. 2016, doi: 10.1038/srep35416.

[10] M. Rimann *et al.*, "An in vitro osteosarcoma 3D microtissue model for drug development," *J. Biotechnol.*, vol. 189, pp. 129–135, 2014, doi: 10.1016/j.jbiotec.2014.09.005.

[11] N. Espagnolle, F. Guilloton, F. Deschaseaux, M. Gadelorge, L. Sensébé, and P. Bourin, “CD146 expression on mesenchymal stem cells is associated with their vascular smooth muscle commitment,” *J. Cell. Mol. Med.*, vol. 18, no. 1, pp. 104–114, Jan. 2014, doi: 10.1111/jcmm.12168.

[12] A. Gomariz *et al.*, “Quantitative spatial analysis of haematopoiesis-regulating stromal cells in the bone marrow microenvironment by 3D microscopy,” *Nat. Commun.*, vol. 9, no. 1, pp. 1–15, Dec. 2018, doi: 10.1038/s41467-018-04770-z.

V. Perspectives and conclusions

This is a peculiar final chapter to conclude this PhD manuscript. Here, we will introduce to you the work in progress impacted by the COVID-19 situation and that could not be concluded on time. As with many scientific projects, the work can go on indefinitely while ideas and results keep flowing. In the coming pages, we will try to sketch the future of this project and what it could have been if it had unrolled under normal circumstances.

The major motivation for this project was to obtain an operative technology to reproduce the complexity of the bone marrow microenvironment *in-vitro*. We used a tandem of technologies that generate 3D architectures from two different scientific approaches – stereolithography and template emulsion - aiming to exploit the advantages of each one of them.

We integrated our scaffolds into bioreactors, and we were planning to study means to use topology, mass transport and shear stress to induce differentiation in the bone marrow mesenchymal stromal cells. In the coming pages, we will present you future directions and studies that are of interest for this project and we will discuss the partial results obtained, before concluding on the work.

1. Perspectives regarding the designed DS3000 architectures as a cellular microenvironment

As described along the chapters of this manuscript, the largest advantage of using additive manufacturing techniques is its versatility and the tight control of the geometries and dimensions of the generated architectures. Here, we will summarize perspective research studies that take advantage of these features.

a. Designed periodic architectures for the investigation of topological aspects

In **Chapter 2**, we presented the fabrication of a bone replica that reproduces the complex and irregular topography of the natural niche of the bone marrow. This heterogenous structure constitutes a 3D cellular microenvironment where the biophysical cues are hard to decipher. Our goal here would be to isolate the impact of the porosity and pore size on the cellular behavior from other cues using the capability to design architectures with stereolithography. We propose to simplify the architecture using a periodic structure that homogenizes the porosity. This structure would be devoted to suppress the highly variable porosity that can potentially cause local biases during cell culture. From this model we could study the impact of cell-cell distance on their ability to communicate and to generate overhanging constructs.

Respecting the dimensions to be used with the U-Cup bioreactor discussed in **Chapter 4**, we designed periodic porosity scaffolds to generate an isotropic architecture with defined pore size. To do so, we have designed the porogen architecture that would be subtracted from the 10-mm diameter and 4.5-mm high cylinder to fit in the bioreactor. The porogen was generated by piling periodically spheres of identical size in the 3 directions of the space as we can observe in **Figure 5.1A**. The key point of this design lies in the symmetry between the architecture and the direction of the flow. We have already discussed the importance of the preferential path within the structures and how the resistance of the structures can induce such anisotropies. When the diameter of the all the channels in a porous structure are identical, the preferential path is the shortest path from inlet to outlet. In that case, the flow and shear stress are determined by the orientation of the porous structure and the interconnections between the cavities, regarding the direction of the incoming flow. To avoid the generation of preferential path and obtain a homogeneous flow pattern within the porous structure, a rotation of the porogen can break this anisotropy as shown in **Figure 5.1B**. This will modify the flow distribution within the structure, generating a homogeneous distribution through the structure, as described in **Figure 5.1C**.

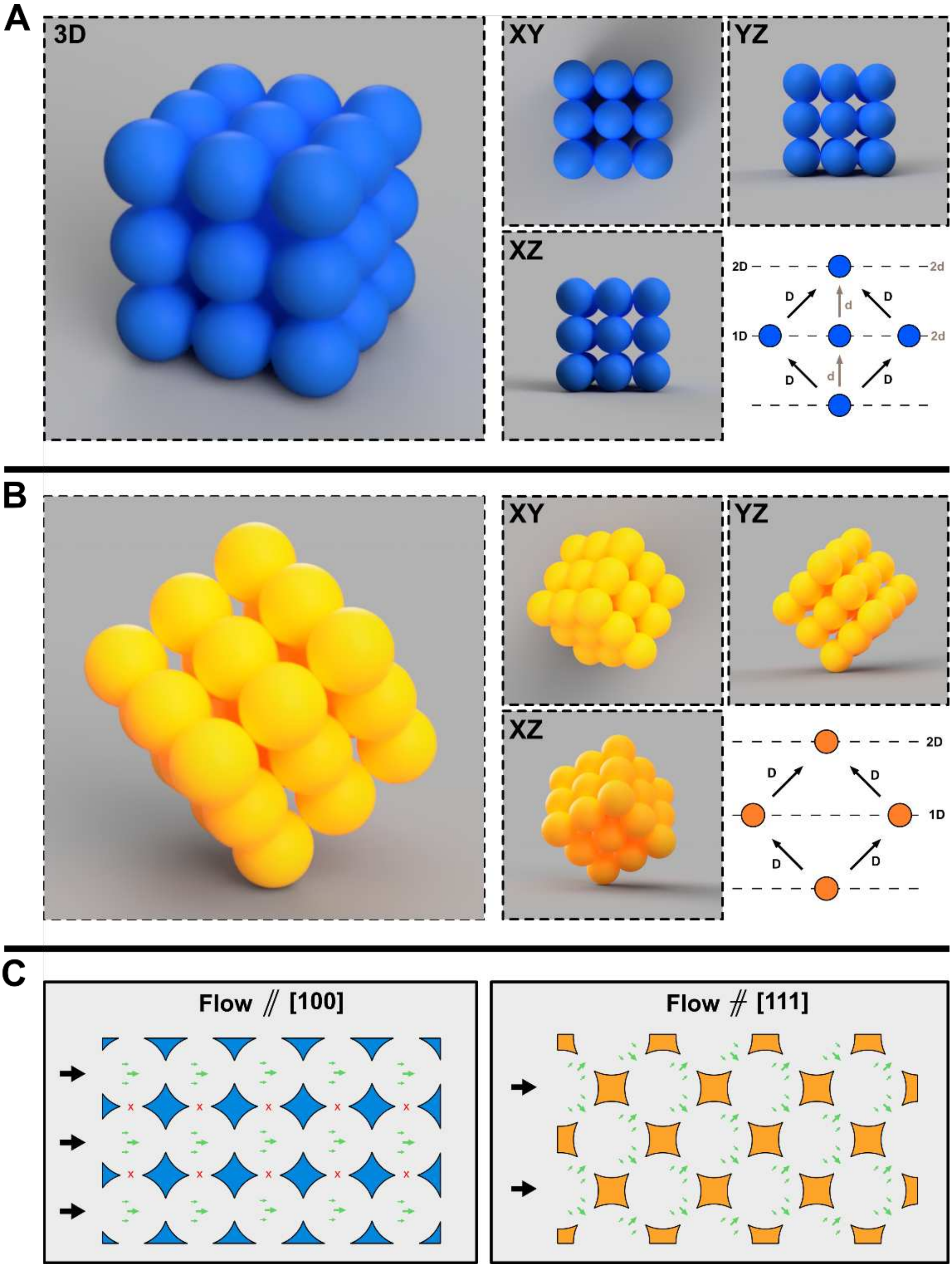

Figure 5.1. *Description of the generation of a periodic porosity architecture. The 3D structures generate the cavities of the porous architecture, or what it is called the porogen architecture.* ***(a)*** *This porosity organization privileges one path between planes due to the difference of distances between pores, creating an anisotropy in the flow.* ***(b)*** *Changing the plane orientation from the [100] to [111] the direction homogenizes the distances between the pores in two different directions, generating an isotropic distribution of communications between pores.* ***(c)*** *Representation of the flow configurations depending on the orientation of the flow regarding the structure.*

In **Table 1**, we provide a comparison between the trabecular bone replica and several designed periodic structures. The structures were produced by gradually decreasing the pore size diameter (i.e., the spheres shown in Figure 5.1) and keeping the relation between the pore diameter and the pore throat diameter constant. This produces a reduction of the pore size and an increase of the number of cavities within the cylinder, which leads to a mild variation of the porosity in the architectures and increase of the surface available. The bone scaffold presents the largest porosity, $\sim 74\ \%$ for the same volume of all the proposed structures, and the second highest surface available for cell culture, $\sim 1200\ mm^2$. In the periodic designs, we can see how the porosity ranges $\sim 55\ -\ 65\ \%$, while the surface available inversely increases with the pore size from $\sim 400\ mm^2\ to\ 2400\ mm^2$.

Table 5.1. *Different porous structures and their intrinsic properties: surface available, porosity, pore size and pore throat.*

		Surface Available	**Porosity**	**Pore Size**	**Pore Throat**
Bone replica		**1238.56 mm^2**	**73.39 %**		
Regular porosity decreasing pore size		**423.44 mm^2**	**58.06 %**	**4 mm**	**1.090 mm**
	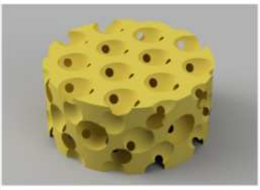	**694.97 mm^2**	**63.24 %**	**2 mm**	**0.545 mm**
	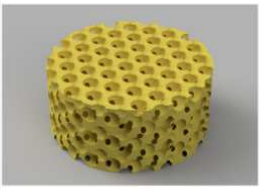	**1196.51 mm^2**	**59.60 %**	**1 mm**	**0.272 mm**
	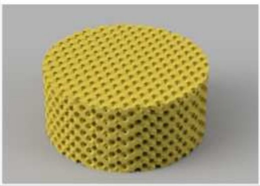	**2312.74 mm^2**	**56.24 %**	**0.5 mm**	**0.135 mm**

In the **Figure 5.2**, we can observe the resulting scaffold characterized by SEM for the different dimensions, showing a 3D view, top-view and a close-up. These structures were fabricated following the detailed **Protocol 18**. In **Chapter 1**, we described the work of Pothuaud et al. (2008) [1], who measured different regions of the skeleton, identifying the typical trabecular spacing ranging around $\sim 0.5 - 1\,mm$. The digital model obtained from that work is displayed in **Figure 5.2A.** The proposed periodic architectures are displayed in **Figure 5.2B-E.** The dimensions of the bone scaffold are better approached by the small pore size structure present in **Figure 5.2D**. In the close-up we can see how the layer-by-layer process and limited xy resolution of the printer (around 30um) impact the structures. In particular, we can see surface undulations in the borders that can be identified with light diffusion during the polymerization, creating those fuzzy borders. To conclude, **Figure 5.2E** depicts the extra small pore size version with 0.5-mm pore diameter, clearly showing a more

Protocol 18. Fabrication of 3D printed controlled-porosity architecture

We will assume previous knowledge described in **Protocol 1** about the system. This protocol is focused on the fabrication of the 10-mm diameter and 4.5-mm thickness controlled-porosity with DS3000 resin. The process is similar to the trabecular bone microarchitecture fabrication.

1. Once placed STL designs in NAUTA, manually add pillars in the down-plane XY all around but avoiding to place them inside the cavities. Fix the pillar thickness at 0.6-mm and 2-mm height, the number of pillars should be around 20. Add a base of 0.5-mm
2. Save the project and create the FICTOR file
3. In FICTOR software, add the FICTOR file and fix the material in DS3000. Modify the appeared default configuration:

Blocks:	✓ 1	✓ 2	✓ 3
To Z	0.200	1.000	0.000
Layers	4	15	∞
Slice	0.050	0.050	0.030
Contours Number	3	3	1
Indentation	0.020	0.020	0.020
Hatching	0.070	0.070	0.030
Ops	↑ ↓	✓ ↑ ✓ ↓	✓ ↑ ✓ ↓
TTT	✓	✓	✓
Z Compensation	0.120	0.120	0.120
Laser Speed	200	2800	5800

4. Once the fabrication process is finish, detach the sample using a razor blade and remove the pillars and base
5. Deep the scaffolds in a 10-mL falcon with ethanol and sonicate for 15 min. Then air-dry it
6. Post-process the samples for 15 min under UV light

crowded structure of small cavities. In terms of definition, we can see more prominently the different layers that compose the structure and through the porosity, we are able to identify the interconnected cavities of the next layer of pores. The close-up portrays as well the fuzzy borders due to the limit of the resolution of the stereolithography system. Smaller dimensions risk to result in a clogged porosity, with a large part of the structure inaccessible to cell culture. In **Table 2**, we present a brief structural analysis of the printed architecture regarding the CAD designs to ensure the proper reproducibility of the scaffolds. This measurement process was carried out on arbitrary features of the architecture and analyzed over the SEM images shown in **Figure 5.2**. We can observe that the features are adequately reproduced, with a maximum error of about ~ 5% for the smallest pore size.

Table 5.2. *Structural analysis of arbitrary features on the 3D printed structures compared with the expected dimensions as programmed on the CAD design.*

SEM images (Figure 5.2)	**Digital dimension (mm)**	**Measured dimension (mm)**	**Relative measurement**
B	2.201	2.312 ± 0.055	105 ± 2%
C	1.988	1.913 ± 0.012	96.2 ± 0.6%
D	0.699	0.693 ± 0.020	99 ± 3%
E	0.391	0.381 ± 0.18	97 ± 5%

The differences in porosity between the trabecular bone microarchitecture and the designed homogeneous architecture are due to the pore walls that are formed between the spheres that largely impact the equivalent trabecular thickness (defined as the average strut thickness of the trabeculae). This is not found in the physiological bone, where struts display a smaller ratio strut thickness/pore diameter. Modifications in the conception of the 3D architecture, for instance using a tetrahedral or woodpile designs, would allow us to reach higher porosities closer to the physiological bone.

An additional impact is expected from these regular architectures regarding the flow distribution in the context of dynamic culture experiments. Due to the decrease of the pore size and pore throat, at equal flow rate, we can expect a high shear stress field through the whole structure. This is an interesting way to modify the mechanical stimulus without altering the mass transport. These simpler structures could thus be useful to study cellular behavior in these conditions and to investigate the role of the heterogeneous architectures found in the living organisms.

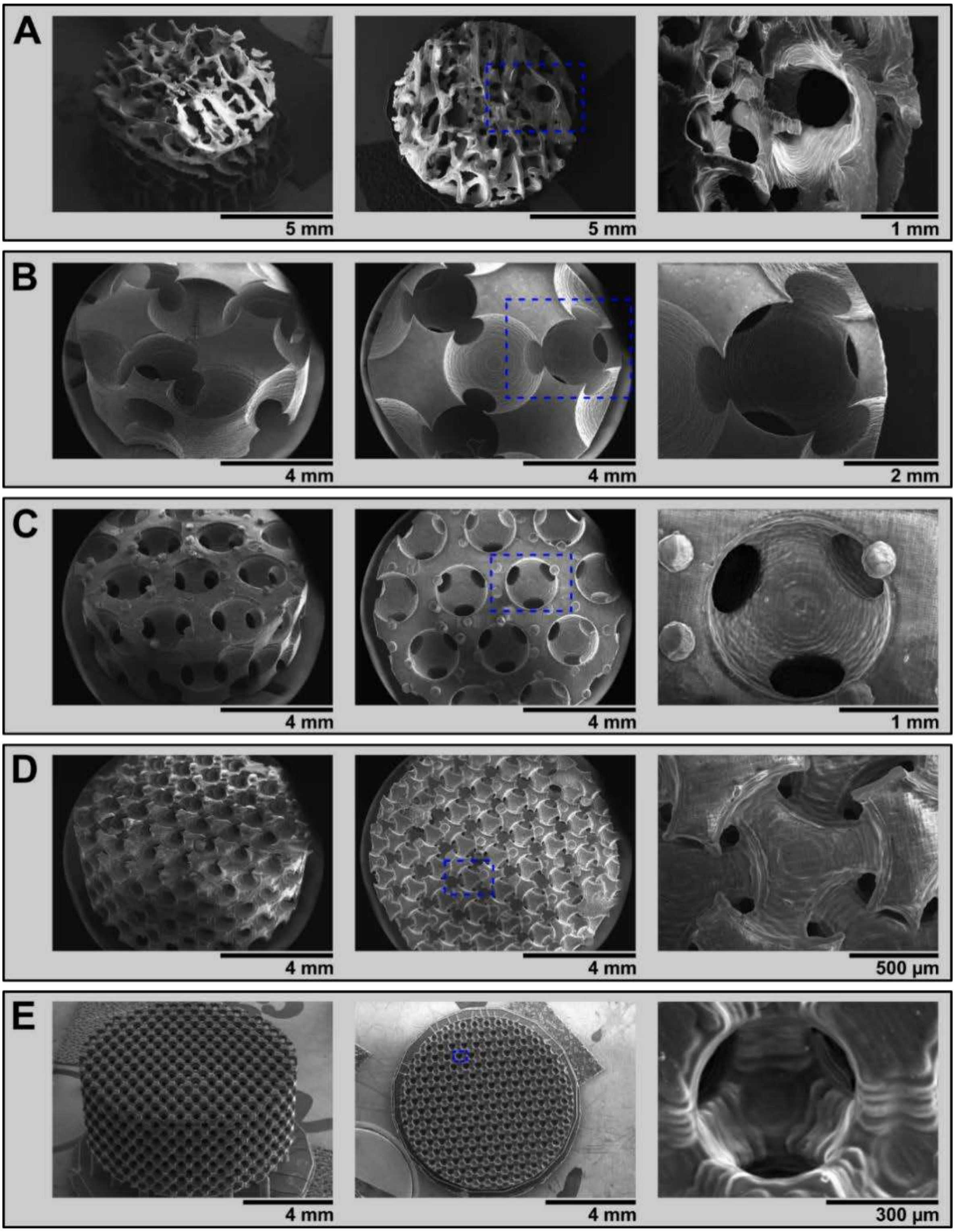

Figure 5.2. *SEM characterization images of the 3D printed architectures devoted to study the 3D cellular microenvironment and the impact of the topography in the cellular behavior.* ***(a)*** *Bone replica.* ***(b).*** *L-size 4 mm diameter pore.* ***(c)*** *M-size 2 mm diameter pore.* ***(d)*** *S-size 1 mm diameter pore.* ***(e)*** *XS-size 0.5 mm diameter pore.*

b. Miniaturized modular 3D printed bioreactor

One of the interests of the 3D printing technology is the ability to perform rapid prototyping of tailored pieces, useful to fabricate specific instrumentation. We have thus exploited this technology to fabricate a bioreactor specifically suited to our scaffold with embedded microfluidic channels, as shown in the **Figure 5.3**. The bioreactor was printed using the default parameters of the system.

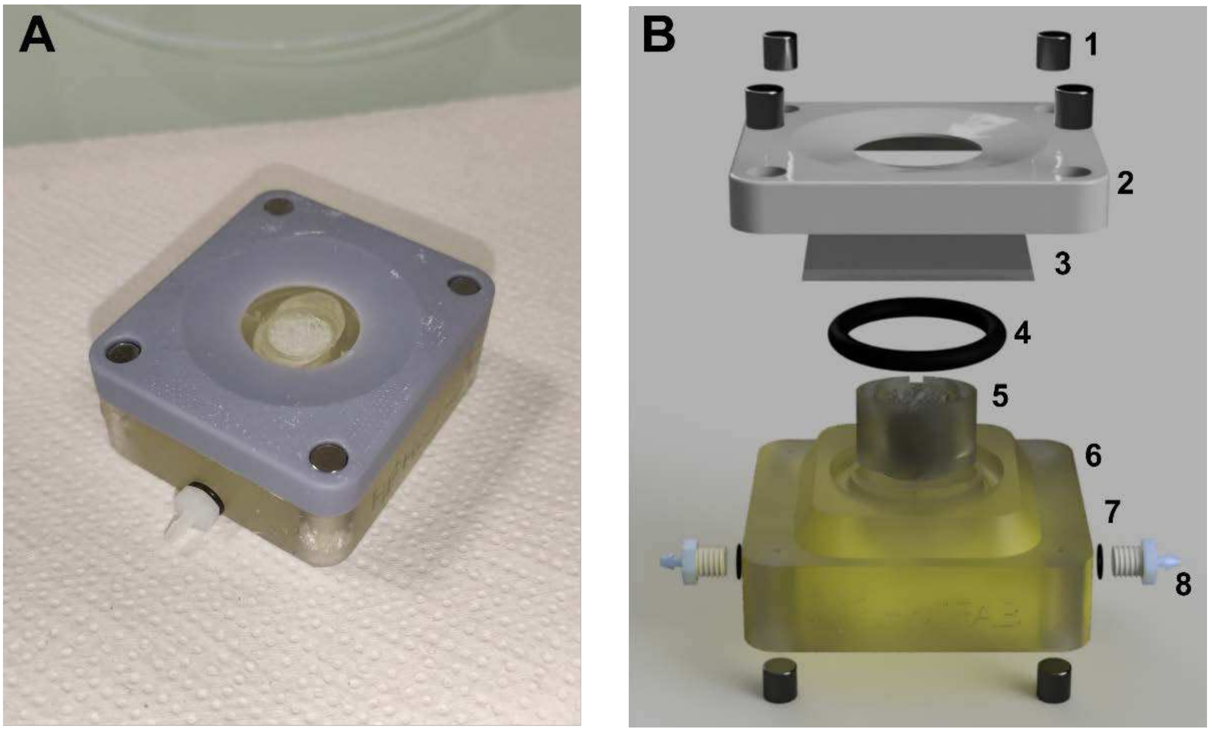

Figure 5.3. *3D printed modular micro-bioreactor.* ***(a)*** *Optical image depicting the manufactured modular micro-bioreactor.* ***(b)*** *3D digital model of the different parts of the 3D printed micro-bioreactor: 1. Magnets, 2. Micro-bioreactor microscope side, 3. Glass coverslip, 4. Toroidal joint, 5. 3D printed scaffold, 6. Micro-bioreactor microfluidic side, 7. Toroidal mini joints, 8. Commercial microfluidic connector.*

We have designed the bioreactor to include as many commercial pieces as possible in order to speed up the fabrication and simplify the maintenance. We intended as well to retain a modular design in which pieces can be modified according to punctual needs while the other parts of the system can be reused. This miniaturized bioreactor can contribute to increase our experimental capacities by facilitating multiplexed experiments. In **Figure 5.3A**, we show the resulted 3D printed bioreactor. We also present a digital deconstruction of the modular micro-bioreactor in **Figure 5.3B** with the numbered pieces that compose the system (listed on the caption). We have divided the bioreactor in two 3D printed pieces: the first one integrates a microfluidic network and is fabricated in DS3000 that ensures a high resolution and is biocompatible (since it will be in contact with cells); the second piece that enable microscope observations is fabricated in DL260 that is a stiffer material enabling the production of thinner features required to accommodate the conical shape of objective of the microscope. Both parts are held together using 8 neodymium magnets. In between both parts, a glass slide is pressed against a rubber toroidal joint to achieve tightness. The inlet and outlet connections are interfaced with commercial microfluidic connectors tight using rubber joints to link the embedded 1-mm diameter channels.

In **Figure 5.4**, we show the digital design used to fabricate the fluidic side of the micro-bioreactor with the *XY*, *XZ* and *YZ* views and crosscuts. Here, we can observe the fluidic circuit connecting the inlet and outlet to the scaffold compartment. The inlet enters the scaffold compartment from the downside and opens in a conic channel designed to homogenize the flow into the scaffold. The outlet is presented as a double exit on top of the compartment.

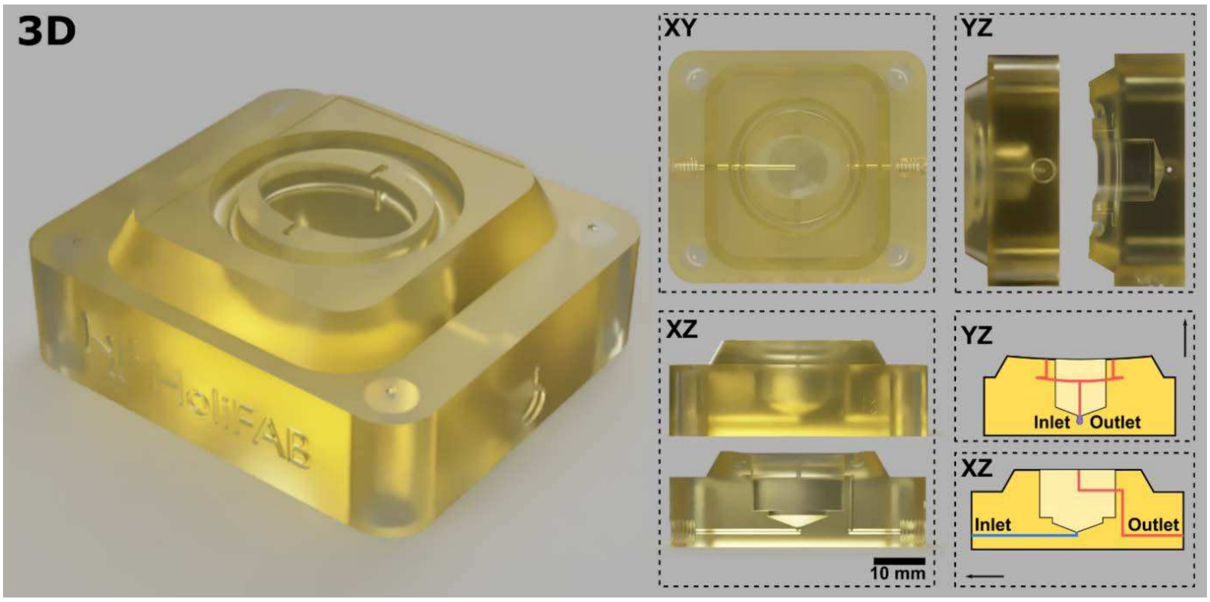

Figure 5.4. *3D digital model of the micro-bioreactor microfluidic side. The connectors in the side are directly screwed into the 3D printed piece which connects to the embedded microfluidic channels of the bioreactor.* ***Right.*** *XY, YZ and XZ-views and crosscuts to show the embedded channels of the micro-bioreactor. The fluidic circuit of the bioreactors is illustrated in the scheme.*

The scaffold compartment is designed to hold an elliptic cylindric scaffold holder. These pieces are designed to interlock themselves as construction toy blocks. In

Figure 5.5, we show the 3D digital model used for the elliptical cylindric scaffold compatible with the micro-bioreactor. This design permits the use of modular scaffolds. The potential for this sort of architectures is the possibility to create abrupt material properties gradients within the scaffold by fabricating them in different materials or providing different coatings. Another option is the use of several bioreactors in parallel with cellular monoculture to be combined later in a larger chamber to observe the interactions and migrations of each cellular type.

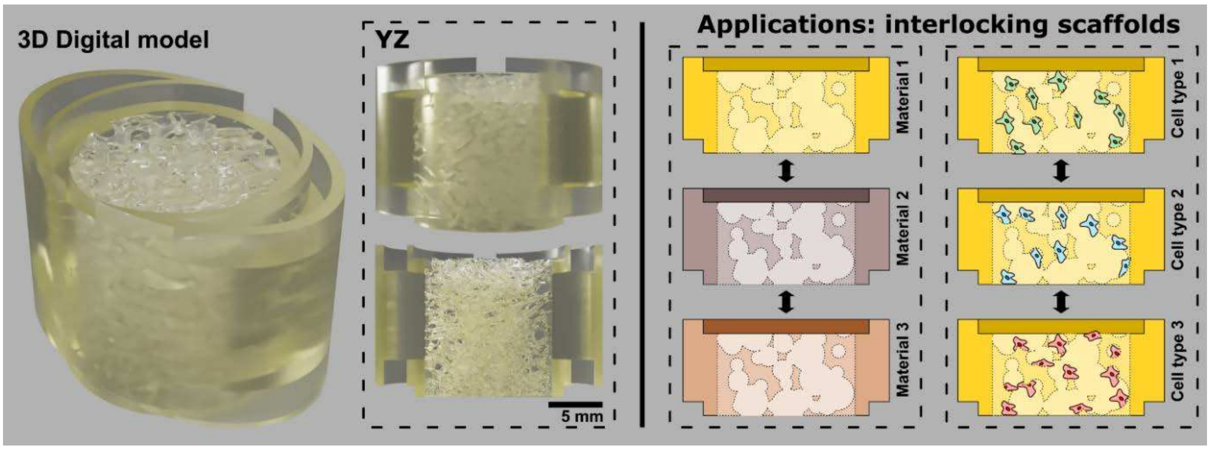

Figure 5.5. Left. *3D digital model of the trabecular bone microarchitecture embedded in an elliptical holder for the interlocking of architectures, and YZ-view and YZ-crosscut detailing the model.* ***Right.*** *Potential applications for the interlocking designed scaffolds.*

This modular configuration could be advantageous to model different kind of cellular microenvironments where we can easily identify abrupt transitions such as the transition between tendons and bone. Regarding the bone marrow, it could be an ideal configuration to study the intermedium regions between red bone marrow and yellow bone marrow as described in **Chapter 1**.

2. Perspectives regarding the free-formed porous PDMS as cellular microenvironment: mechanical stimulation

In **Chapter 4**, we have presented a fluidic device fabricated entirely in PDMS which displays a porous structure embedded in a fluidic chamber. Because of the all-PDMS nature of the bioreactor, the 3D integrated 3D scaffold can expand and deform by controlling the pressure inside the fluidic system. Hence, we plan to exploit this feature to mechanically stimulate the hosted cells in the device. Our goal is to implement a pressure-controlled fluidic circuit that can maintain a quasi-stable flow while varying the applied pressure of the liquid in the chamber. A cyclic pressure variation on the chamber is used to expand the porous PDMS in the chip and deform the surfaces onto which cells are adhering, activating them mechanically.

PDMS is a known viscoelastic material with an strain-stress curve largely characterized in the literature [2]–[4]. In **Figure 5.6**, we can observe the stress-strain curves of PDMS fabricated using different base-hardener ratios [5]. These measurements illustrate the forces exerted by the silicone when stretched at different length and aim to illustrate the hysteresis caused by the yield stress during repeated loading-unloading cycles. However, this effect is minimal when talking of cycles under 50% of strain.

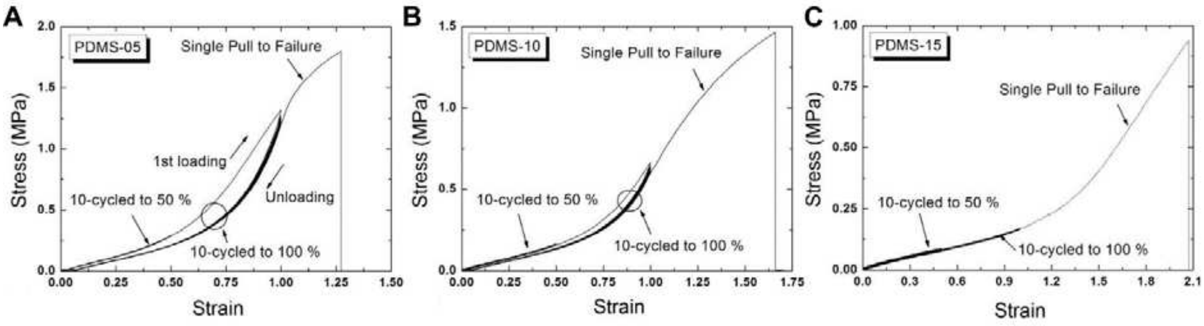

Figure 5.6. *Strain–stress curves of PDMS at 5:1, 10:1 and 15:1 base/hardener ratios. Adapted from* [5].

For our experiment, we employed a microfluidic flow control system (MFCS) of multiple pressure channels of 1 bar, from Fluigent. This instrument allows us to precisely control the applied pressure with high reproducibility. Two pressure-controlled channels were employed to create a closed pressure circuit with 2 medium reservoirs before and after the microfluidic device to generate liquid flow through the scaffold. A schematic illustration of the set-up is shown in **Figure 5.7a**. By applying pressure over the inlet and outlet of the microfluidic chip, we can tightly control the pressure inside the chip. A periodical repetition cycle of loading-unloading can be applied to the scaffold, respecting the relative pressure between them while increasing the applied pressure in both ends. This generates a constant pressure difference inside the chip that subsequently induces a flow. The absolute increase of pressure within the chip, generates the forces that stretches the porous PDMS architecture in the PDMS and swells the microfluidic device.

In **Figure 5.7b**, we present the optical images displaying the behavior of the PDMS device under applied pressure. Here, we observe the profile of the microfluidic chip at 0, 500 and 1000 mbar. By measuring the differences between these images, we were able to characterize the swelling of the microfluidic device under applied pressure. The porous PDMS chamber measures 4-mm in height and we can suppose that most of the strain is induced over the porous PDMS and not over the bulk PDMS of the microfluidic chamber. At 500 mbar, the measured elongation of the device was 2.34 ± 0.4 mm and for 1000 mbar, 3.66 ± 0.4 mm. These values correspond to strain variations of 58% and 90%, which shows the large capacity of our microfluidic device to deform, offering a large range of deformation to experiment different mechanical stress on cell culture conditions.

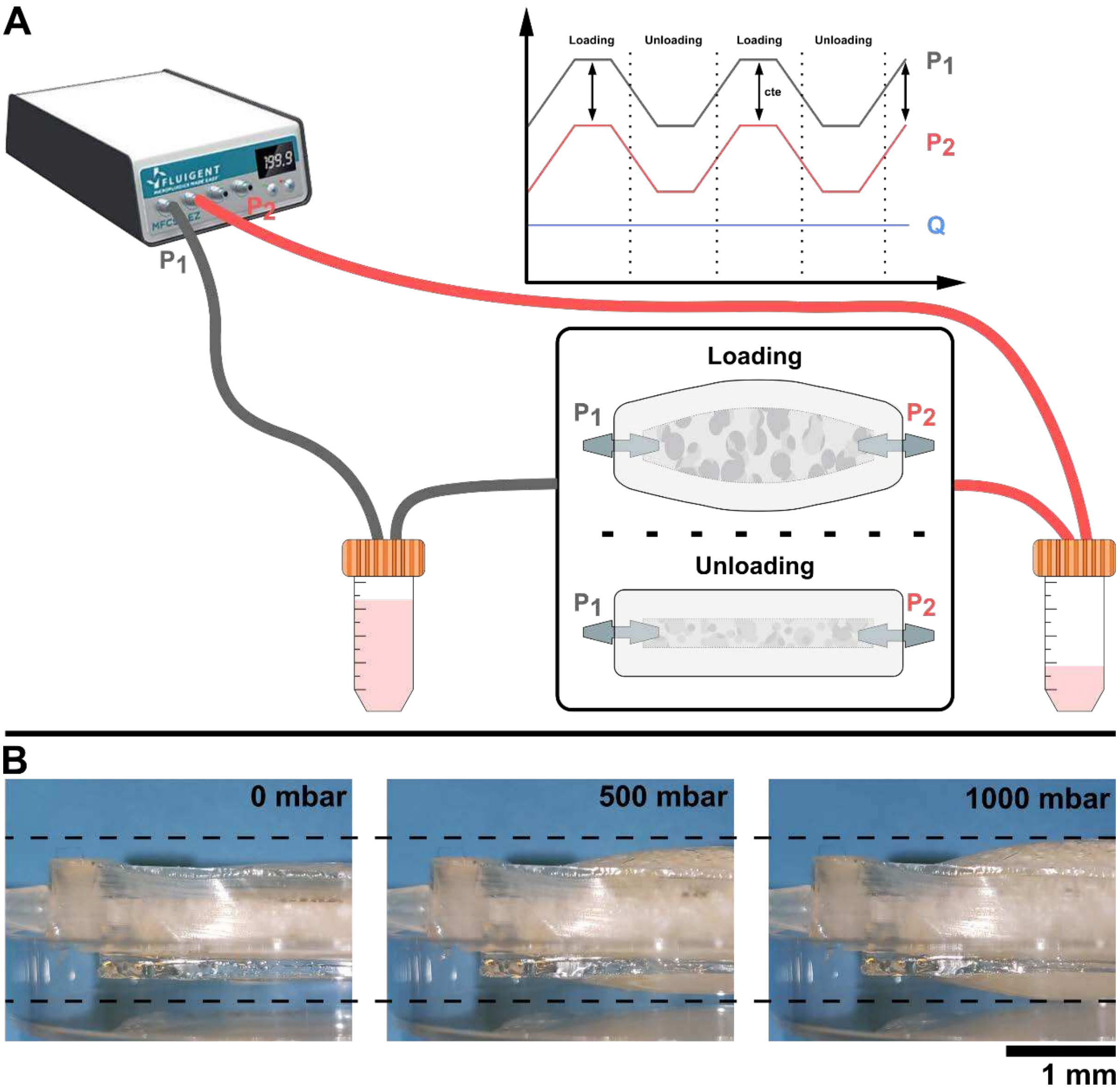

Figure 5.7.(a) *Schematic illustration of the pressure-controlled microfluidic circuit to generate deformation on the porous PDMS microfluidic device.* ***(b)*** *Optical image mosaic displaying the capabilities of the porous PDMS device to expand at different applied pressure: 0, 500 and 1000 mbar.*

A complete set of images was taken every 50-mbar increments, from 0 to 1000 mbar, to obtain the strain-pressure curve for the device. These measurements are presented in **Figure 5.8** using two image analysis, user-defined measurement and tracking particle using the brightest sport on the images. Both characterization curves present similar behavior with a slightly bias probably caused by experimenter incertitude. A breaking point test was also carried out over 3 chips, which were able to hold 4 bars before leaking.

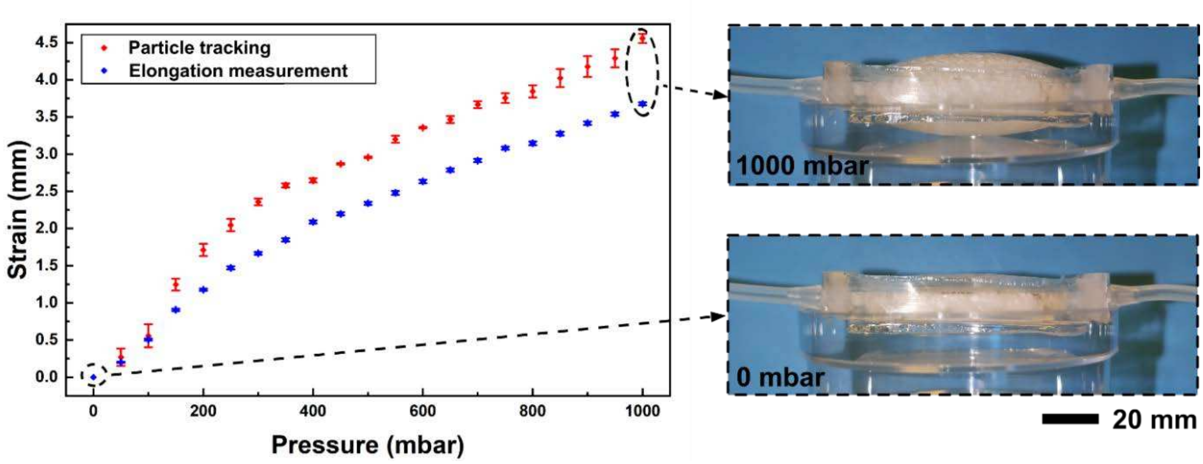

Figure 5.8. *Deformation of the porous PDMS device measured by image analysis of a sequence of optical images at different applied pressures.* ***Particle tracking*** *values was carried out by an automated tracking algorithm that monitors the position of reflection spots at the PDMS.* ***Elongation measured*** *values were obtained by tracking user-defined segments over the images.*

We have then implemented the automatization of the strain cycles. The devices was controlled using the novel software *Microfluidics Automation Tool* from Fluigent, which allows to set pressure cycles on several channels and interface it with different Fluigent devices, such as flowmeters or sensors. We have also included a flowmeter device in the inlet channel to measure the impact of the pressure variation on the flow. We applied a linear pressure gradient from 200 to 700 mbar on channel 1, and 0 to 500 mbar on channel 2, with a total cycle duration of 32 s. The pressure difference (200 mbar) was kept constant during the whole cycle. Moveover, the values of applied pressure were inverted every 7 cycles to reverse the flow and transfer liquid from the oulet reservoir to the inlet. The measurement results are shown in **Figure 5.9**. Regarding the pressure, we see reproductible curves with peaks during the changes of pressure gradient due to the viscoelastictiy of the system. The measured flow is shown in the curve underneath, where we oberve an irregular pattern. These peaks could be attributed to viscoelastic properties of the PDMS and to the reflow induced by the relaxation of the material when the pressure gradient changes. This has an impact in the PID-controller of the system, which has a latency to responde to these changes. There is also an asymmetry in the flow pattern when reverting the flow pattern that remains to be characterized. Furthermore, the maximum flow applied is about ~3000 µL/h, way above the 100 µL/h identified as optimal for cell cutlure in our previous perfusion experiments.

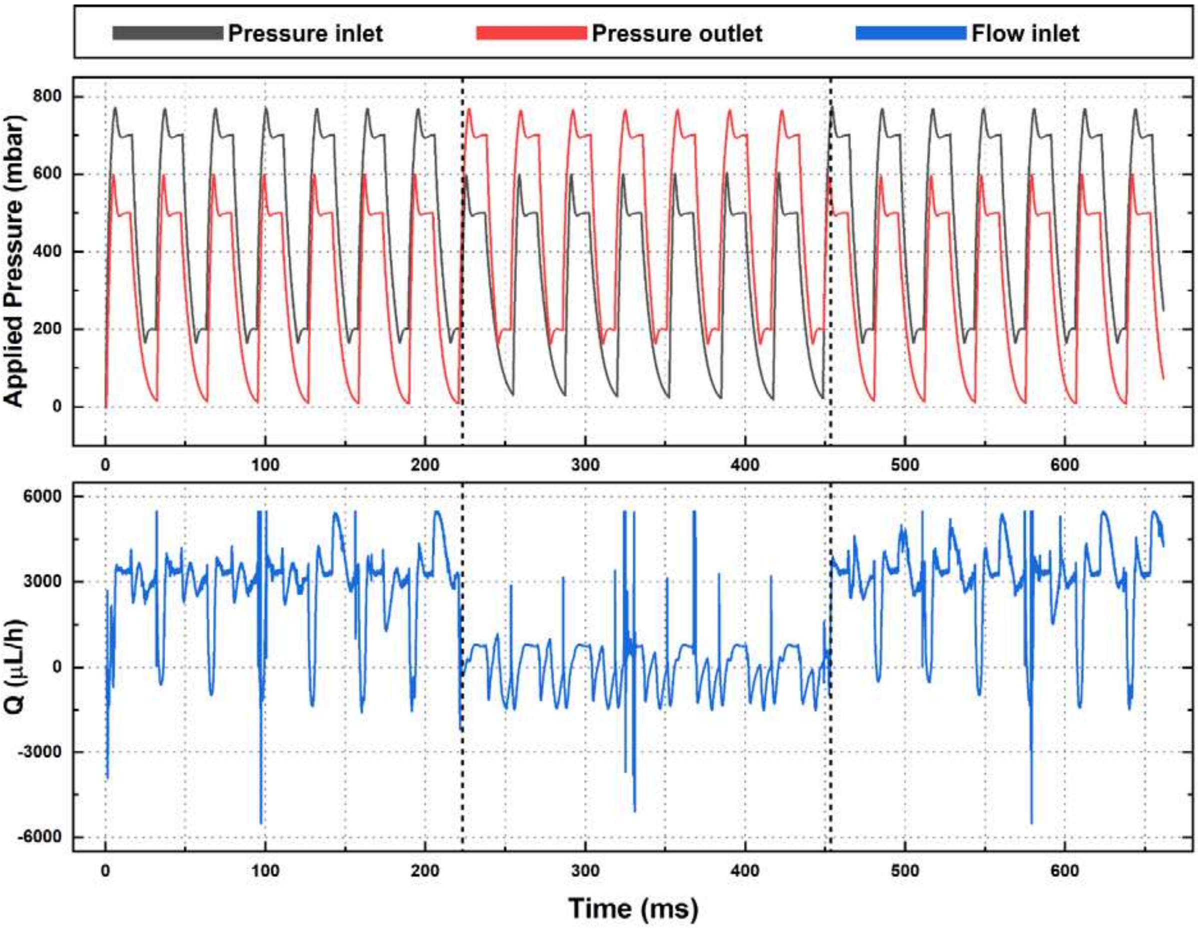

Figure 5.9. *Measurement of the PDMS device deformation by periodically applying a different of pressure between the inlet and outlet in order to maintain a perfusion. Black dashed lines demark the reverse of the flow by inverting the applied pressure in the channels.*

Providing we can solve the flow rate level and stability, this new pressure-controlled set-up should be very useful to to study the differentiation of MSCs under mechanical stress conditions.

3. PhD conclusions

In this work, we have addressed the challenges of producing cellular microenvironment models of the bone marrow. In order to achieve this goal, we have carried out a large analysis of the characteristics that such a system must possess, aiming to address the questions regarding the topology of the cellular microenvironments. One of the common limitations when fabricating 3D architectures is related to the properties of the material, which can restrain the use of certain technologies to fabricate scaffolds.

Here, we decided to pursue two complementary technological approaches which represent the main two options for generating 3D structures: designed architecture, portraying the advantages of additive manufacturing and free-form methods, representing the simplicity and versatility of physico-chemical processes.

Regarding the additive manufacturing, and more specifically stereolithography as a fabrication method, we have proven the capacity of this technology to fabricate intricate architectures that reproduce the topographic diversity of trabecular bone, obtained by X-ray tomography from a natural trabecular bone. Moreover, we aimed to exploit the possibility to reduce the structural heterogeneities found in the bone to respond to fundamental questions regarding the organization of cells over 3D architectures. The fabricated structures were characterized by diverse microscopy methods to validate the fabrication process. Regarding cell culture, we have presented a standard protocol to validate the biocompatibility of the DS3000 biomaterial commonly developed for stereolithography for cellular culture, using cell lines (SaOS-2) and bone marrow mesenchymal stromal cells (BMSCs). To complete our bone marrow microenvironment, we have adapted our 3D structures to a commercial perfusion system, which boost the versatility of additive manufacturing as a research tool. The inclusion of liquid movement in the scaffold triggered a striking cellular organization in which cells were able to completely clog millimetric pores by developing cellular constructs without additional material. The author considers these results as one of the largest success of this 3.5 years project.

3D architectures can also be obtained with technologies other than additive manufacturing. In this manuscript, we have presented an innovative and singular fabrication technique devoted to produce simple biocompatible 3D architectures. Our method takes advantage of the thermal phase transition of water and the thermal-driven gelation of PDMS, a well-known biomaterial with decades of validation regarding cell culture. The technique consists in generating an emulsion of water as internal phase in liquid PDMS, then partially reticulating the emulsion at low temperature (under the boiling point of the water) and concluding the process in a pressure-controlled oven with a temperature over 100 °C. This triggers the evaporation of water, enhanced by the low-pressure condition in the chamber, which expands the water droplet inside the partially reticulated PDMS. By controlling the PDMS reticulation point (by means of the duration of the low temperature reticulation), and the temperature and pressure of the second reticulation, we can tune the porosity of the resulting material. The porous architectures were studied by microscopy and X-ray tomography, and the scaffold function was validated using an osteosarcoma cell line, SaOS-2. These results yielded a publication in ACS Material & Interfaces [6].

The integration of perfusion in such architectures implied the modification of the fabrication process to take advantages of the injectability of the emulsion. A PDMS microfluidic device with a large central chamber was fabricated to host the porous monolith. The optimized method consisted by injecting the emulsion in the close microfluidic device and reproducing the double reticulation process *in-situ*, then interfacing a syringe pump with commercial connectors to provide the perfusion of the culture medium. With these conditions, the devices were characterized again to ensure the reproducibility of the technique using microscopy and X-ray tomography. Due to the tortuosity of the free-formed fabricated architecture, we used fluorescence nanoparticles and radiopaque solutions to study the hydrodynamic characteristics of the device with fluorescence microscopy and X-ray video-radiography. The local effects caused by the liquid movement were investigated by solving the Navier-Stokes and the diffusion equations over the digital model obtained by tomography, showing conditions compatible with cell culture. The biological capacity of the PDMS bioreactor was tested using the mentioned osteosarcoma cells and human bone marrow mesenchymal stromal cells in dynamic cell culture conditions for a few weeks. The results obtained on this project will constitute another publication in the coming weeks.

Summarizing, we have designed and fabricated two different cellular microenvironments by developing two different technical and scientific approaches. Moreover, we have proven the robustness of both technologies to fabricate three-dimensional topographies with controlled perfusion and their capacity to host human stem cells.

References

[1] L. Pothuaud, P. Carceller, and D. Hans, “Correlations between grey-level variations in 2D projection images (TBS) and 3D microarchitecture: Applications in the study of human trabecular bone microarchitecture,” *Bone*, vol. 42, no. 4, pp. 775–787, Apr. 2008, doi: 10.1016/j.bone.2007.11.018.

[2] J. Chen, K. Wright, and M. Birch, “Nanoscale viscoelastic properties and adhesion of polydimethylsiloxane for tissue engineering,” *Acta Mech. Sin.*, vol. 30, no. 1, pp. 2–6, 2014, doi: 10.1007/s10409-014-0022-0.

[3] S. Dogru, B. Aksoy, H. Bayraktar, and B. E. Alaca, “Poisson’s ratio of PDMS thin films,” *Polym. Test.*, vol. 69, pp. 375–384, Aug. 2018, doi: 10.1016/j.polymertesting.2018.05.044.

[4] Y. C. Yeh *et al.*, “Mechanically dynamic PDMS substrates to investigate changing cell environments,” *Biomaterials*, vol. 145, pp. 23–32, Nov. 2017, doi: 10.1016/j.biomaterials.2017.08.033.

[5] T. K. Kim, J. K. Kim, and O. C. Jeong, “Measurement of nonlinear mechanical properties of PDMS elastomer,” in *Microelectronic Engineering*, Aug. 2011, vol. 88, no. 8, pp. 1982–1985, doi: 10.1016/j.mee.2010.12.108.

[6] R. Riesco *et al.*, “Water-in-PDMS Emulsion Templating of Highly Interconnected Porous Architectures for 3D Cell Culture,” *ACS Appl. Mater. Interfaces*, 2019, doi: 10.1021/acsami.9b07564.

Annex: Hydrodynamic simulations

In the Chapter 4, we have presented numerical calculations to locally quantify the hydrodynamic parameters and their distribution within the porous PDMS microfluidic device. In collaboration with Omar Mokhtari and Yohan Davit (IMFT), we solved the incompressible Navier-Stokes equation using the digital model obtained by X-ray tomography (digital model presented in **Figure 4.14** and simulations presented in **Figures 4.18-20**, in **Chapter 4**). For this calculation, we selected a low flowrate similar to the one used for cell culture conditions. In this condition, Reynolds numbers is much smaller than one and we can reduce the model to the incompressible Stokes equations.

The proposed scheme to solve these set of equations combines a low order non-conforming discretization, over a locally refined staggered grid with a pressure correction algorithm. This non-conforming space consist in the adaptation of the grid to the needs, in terms of numerical resolution, of the simulation. The space discretization is based on the Marker-and-Cell (MAC) scheme known for its simplicity, efficiency and mathematical properties [1]. This discretization consists in storing the vectorial variables in the interface of the mesh while the scalar variables are stored in the center of the stagged mesh. Time discretization consists in a fractional-step of pressure-correction type.

First, the pressure gradient is ignored to determine a classical semi-implicit decoupled solution of the 2nd Newton's law, which lead to an intermediate velocity field. Second, this velocity field is corrected using an elliptic pressure-correction step to improve the solution of second partial differential equation of the Poisson law [2]. The no-slip and no-penetration conditions at the surface of the PDMS scaffold are approximated by adding a damping penalization term in the momentum transport equation [3]. The goal is to use a fast and efficient discretization on cartesian meshes in both the fluid and solid phases, rather than complex body-fitted unstructured meshes only in the fluid. The penalization term is defined through the entire volume of calculation, in both the PDMS and fluid volumes, and depends linearly upon the local velocity everywhere. By defining a very large coefficient for the solid phase, in comparation with a liquid phase, we obtain negligible velocities inside the PDMS and we recover the Navier-Stokes equations for the fluid.

The velocity field is constant and it corresponds to the previously calculated Stokes velocity field of the system. The advection equation is solved using a hybrid scheme corresponding to the blending between the first-order upwind and the centered schemes. This choice was designed to preserve the positivity due to the presence of a monotone diffusion operator. For the diffusion equation, we used a standard two-point flux approximation on conforming faces and a L-scheme for the non-conforming ones. To solve the diffusion equation, we continued using a penalization approximation defining $\mathrm{D} = 10^{-9}$ for the liquid and $\mathrm{D} = 0$ for the solid. The initial conditions were defined as $\mathrm{c} = 0$ for the domain and $\mathrm{c} = 1$ imposed in the inlet channel of the device.

References

[1] S. Patankar, “Numerical heat transfer and fluid flow: Computational methods in mechanics and thermal science,” *Hemisphere Publication Corporation,Washington, DC*. pp. 1–197, 1980.

[2] K. Schneider, “Numerical simulation of the transient flow behaviour in chemical reactors using a penalisation method,” *Comput. Fluids*, vol. 34, no. 10, pp. 1223–1238, Dec. 2005, doi: 10.1016/j.compfluid.2004.09.006.

[3] K. Khadra, P. Angot, S. Parneix, and J. P. Caltagirone, “Fictitious domain approach for numerical modelling of Navier-Stokes equations,” *Int. J. Numer. Methods Fluids*, vol. 34, no. 8, pp. 651–684, Dec. 2000, doi: 10.1002/1097-0363(20001230)34:8<651::AID-FLD61>3.0.CO;2-D.